THE UNIVERSITY *of* EDINBURGH

Stem Cell Function in the Mouse Corneal Epithelium

by

Richard L. Mort Bsc. (Hons)

Doctor of Philosophy

The University of Edinburgh, United Kingdom

Author's Declaration

Except where due acknowledgement is made, the studies undertaken in this thesis were the unaided work of the author. No part of this work has been previously accepted for, or is currently being submitted in candidature for another degree

Richard L. Mort

2007

Abstract

Limbal stem cells maintain the corneal epithelium through a process of clonal growth and ordered migration. In X-inactivation mosaic female mice, that express *LacZ* from one of their X-chromosomes, random clumps of *LacZ*-positive cells are seen in the cornea at 3-6 weeks of life. This pattern resolves between 6-10 weeks forming radial stripes thought to represent chords of clonally related, inwardly migrating cells. By measuring the number and width of stripes and correcting for the effects of different proportions of *LacZ*-positive cells, an estimate of the number of coherent stem cell clones maintaining the tissue can be derived. Analysis at 5 ages demonstrated that the estimated number of coherent stem cell clones is reduced from ~100 at 15 weeks to ~50 at 39 weeks and is then stable at least until 52 weeks. An automated method was developed using image analysis software to analyse these striping patterns. This method produced results that did not differ significantly from the above. The dosage of the transcription factor Pax6 is crucial for normal eye development. In *Pax6* heterozygous animals the estimated number of coherent stem cell clones is reduced to ~50 at 15 weeks with no further reduction up to 30 weeks. Mice hemizygous for the *PAX77* transgene over-express human *PAX6*. In *PAX77* hemizygous X-inactivation mosaics, estimated clone number was similarly reduced to ~50 with no further decline. Mice heterozygous for both *Gli3* and *Pax6* have a distinct striping phenotype, highlighted by an increase in coherent clones. When the corneal epithelium is injured the surrounding epithelial cells migrate along the corneal stroma to cover the wound. X-gal staining of healed, centrally wounded X-inactivation eyes reveals that striping patterns are reconstituted during wound healing in ex-vivo culture. In GFP mosaics the healing process can be imaged using time-lapse confocal microscopy. This technique demonstrated that clones remain contiguous throughout their migration. Healing of peripheral wounds was observed to form de-novo whorling patterns, revealing that basal cells in the epithelium can migrate both away from and towards the limbal region.

Acknowledgements

I'd like to acknowledge and thank my supervisors Dr John West and Dr Steve Morley for their support, their enthusiasm and their patience. I'd also like to thank all members of John West's research group (past and present) for their help and support, especially Thaya Ramaesh, Su-Ping Chang and Simon Chanas.

Furthermore I'd like to thank all my friends and family for helping to keep me sane. In particular Maggie and Graham Mort for their unswerving faith and encouragement. You never doubted I could do it and you were with me every step of the way. This work would not have been possible without the support of Alyssa Darrant who bore the brunt of my grumpiness and to whom I owe a massive debt of gratitude.

This PhD was supported by The University of Edinburgh College of Medicine and Veterinary Medicine PhD scholarship scheme.

Table of Contents

List of Figures

List of Tables

List of Abbreviations

ABCG2: ATP-binding cassette transporter G2

ANOVA: analysis of variance

AP: alkaline phosphatase

ARK: aniridia related keratopathy

β-Gal: β -galactosidase

bHLH: basic helix-loop-helix

BMP: bone morphogenetic protein

BrdU: bromodeoxyuridine

CAAG: cytomegalovirus/chick β-actin promoter

CMV: cytomegalovirus

EGF: epidermal growth factor

EGFR: epidermal growth factor receptor

ENU: ethylnitrosourea

ESC: embryonic stem cell

FGF: fibroblast growth factor

FGFR: fibroblast growth factor receptor

GFP: green fluorescent protein

H2B: histone 2B

H and E: haematoxylin and eosin

H-Tdr: tritiated thymidine

K: keratin

LacZ: gene encoding β-galactosidase

LCM: laser capture microdissection

LRC: label retaining cell

LSC: limbal stem cell

MMP: matrix metalloproteinase

NCC: neural crest cell

NGF: nerve growth factor

PLSD: probable least-squares difference

RCE: recurrent corneal erosions

RPE: retinal pigment epithelium

SAGE: serial analysis of gene expression

Sey: small-eye

TAC: transit/transient amplifying cell

TCA: thalamocortical axon

TGF: transforming growth factor

YAC: yeast artificial chromosome

ZAP: *LacZ*-alkaline-phosphatase

Chapter 1
Introduction

1.1 STRUCTURE AND DEVELOPMENT OF THE MOUSE EYE

1.1.1 Structure of the adult mouse eye

The eye is a highly specialised organ concerned with photoreception. This process occurs in specialised nerve cells known as rods and cones found in the retina. All the other structures in the eye have evolved to support this basic physiological process. The mouse eye is a globe of approximately 4mm in diameter (Geiss and Yoshitomi, 1999) although size varies with strain and sex. On average a mouse eye has a mass of around 18mg in the adult (Gerido et al., 2003). Figure 1.1 shows schematically the main features of the adult eye. It is encompassed by the corneoscleral envelope which comprises the sclera, mainly enclosing the vitreous cavity and the cornea enclosing the anterior chamber. This tough fibrous enclosure provides structural support and contains the intraocular pressure. The two tissues meet at the corneoscleral junction also known as the limbus (Reviewed in Forrester, 2001). The cornea is a transparent tissue that protects the eye and absorbs nutrients from the tear film and aqueous humour; a watery liquid constantly produced by the ciliary bodies. As well as its protective properties the cornea is responsible for refracting light into the lens, the cornea's refractive properties account for 75% of the eye's focusing ability. The conjunctiva starts where the cornea ends. It is thin and transparent covering part of the sclera and lining the inside of the eyelids (Michael et al., 1988; Smith, 2001). Between the corneal and conjunctival epithelia is the limbal epithelium a ring of specialised epithelium that separates the two tissues. Stem cells that replenish the corneal epithelium are said to reside in the basal limbal epithelium (Cotsarelis et al., 1989; Kruse, 1994; Lehrer et al., 1998). The iris is a contractile ring of smooth muscle that separates the anterior and posterior chambers. Its function is analogous to the diaphragm of a camera; controlling the amount of light allowed

to pass through the lens. The lens is clear and flexible; it changes shape to focus light onto the retina. It is connected to the ciliary body (containing ciliary muscles) by suspensory ligaments. The ciliary muscles contract to change the shape of the lens and thus its refractive properties. The choroid lines the back of the eye between the retina and the sclera. It contains numerous blood vessels to supply oxygen and nutrients to the retina and is highly pigmented allowing it to absorb light and prevent 'scatter' that may interfere with visual acuity. Millions of photoreceptor cells of two types, rods and cones, line the anterior surface of the retina. Around 95% of these cells are rods which are sensitive at low light levels (Soucy et al., 1998; Szel et al., 1992). The mouse retina contains two types of cones which provide higher visual acuity, this suggests that mice may have dichromatic vision (Szel et al., 1994; Szel et al., 1992; Szel et al., 1996). The central fovea is populated exclusively by cones and is the retina's most sensitive region. The optic disk is a 'blind spot' in the retina where the optic nerve exits the eye (Geiss and Yoshitomi, 1999; Szel et al., 1996).

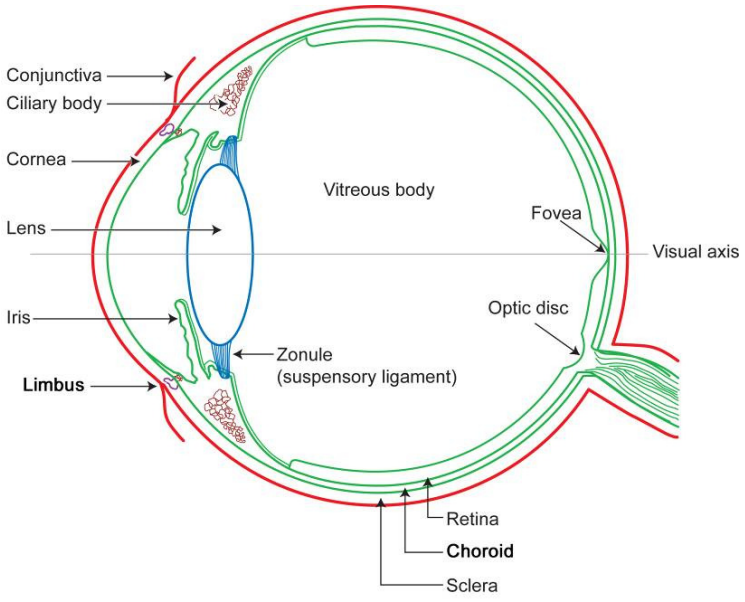

Figure 1.1: The structure of the adult eye.

The sclera encompasses the vitreous body whilst the cornea encloses the anterior chamber, these two tissues provide structure. The cornea is transparent and is responsible both for transmitting and refracting light as well as protecting the eye and absorbing nutrients. Where the cornea and sclera meet, the corneal epithelium ends and is replaced by the conjunctival epithelium a transparent epithelium that covers part of the sclera and lines the insides of the eyelids. The limbus is a ring of specialised epithelium between the corneal and conjunctival epithelia. The iris is a contractile ring that sits between the anterior and the posterior chambers and controls the amount of light allowed to pass through to the retina. The lens is clear and flexible; it changes shape to focus light onto the retina. It is connected to the ciliary body by suspensory ligaments. The choroid lines the back of the eye between the retina and the sclera. It contains numerous blood vessels to supply oxygen and nutrients. The retina contains millions of photoreceptor cells each connected to an individual nerve fibre; the fovea is its most sensitive region. The optic disk is a 'blind spot' in the retina where the optic nerve exits the eye. Diagram adapted from: www.worlinvisible.com/apologet/-humbody/eye1.htm.

1.1.2 Eye development

The mouse eye is formed through a series of inductive mechanisms involving the interaction of three embryonic tissues; the surface ectoderm, the ocular mesenchyme and the neuroepithelium of the optic vesicle (Lang, 2004). The surface ectoderm will form the lens and corneal epithelium, whilst the neuroepithelium gives rise to the retina and retinal pigment epithelium. The rest of the eye including the corneal stroma and corneal endothelium is formed from the ocular mesenchyme which is composed of cells that originate from both the mesoderm and the neural crest (Le Douarin and Kalcheim, 1999). In mice, cranial neural crest cells (NCCs) have been shown to migrate to the prospective ocular mesenchyme prior to eye development (Osumi-Yamashita et al., 1994; Serbedzija et al., 1992; Trainor and Tam, 1995). The first signs of eye development do not appear until after the fusion of the neural folds between embryonic days 8 and 8.5 (E8-8.5). At this point the optic vesicles form from evaginations of the neuroepithelium of the embryonic forebrain to which they remain connected by the optic stalks (Kaufman and Bard, 1999).

The main events in eye formation between E8 and birth (postnatal day 0, P0) are summarised schematically in Figure 1.2. The optic vesicles are visible by E8.5 (Fig 1.2 A). By E9.5 they are in contact with the head surface ectoderm, which begins to thicken at the point of contact forming the lens placode (Fig 1.2 B). A similar thickening of the neuroepithelium of the optic vesicle is fated to become the retina. The interaction between these two tissues is extremely strong and is thought to be facilitated by 'cytoplasmic extensions' between the two primordia (McAvoy, 1980). A subsequent invagination of the surface ectoderm and the optic vesicle at E10.5 (Fig 1.2 C) forms the lens pit and, surrounding it, the optic cup. During the formation of the optic cup, its outer-layer folds against the adjacent proximal layer of the optic vesicle. These two layers are fated to become the retinal pigment epithelium (RPE) and the retina. Formation of the lens vesicle is complete by E11.5 (Fig 1.2 D) at this time ocular mesenchyme begins to migrate between the lens and the future corneal epithelium, which

become completely detached. By E15.5 the corneal epithelium has synthesised extracellular matrix (ECM) components which have combined with this influx of mesenchyme to form the corneal stroma and the corneal endothelium. The lens has begun to grow and lens fibres are present although there is no lens capsule, the eyelids have begun to form from the head surface ectoderm to either side of the future corneal epithelium (Fig 1.2 E). At postnatal day 0 (P0) the lens capsule is fully formed and the cornea is intact, although the corneal stroma is composed of more cells than in the adult and the epithelium has yet to mature (Fig 1.2 F). The eyelids remain closed until P12-P14 (Smith, 2001) at this time the epithelium consists of a basal layer of cuboidal cells and a superficial layer of flattened cells (Ramaesh et al., 2003). By P42 the epithelium is fully stratified consisting of approximately five cell layers with a cuboidal basal layer and a flattened superficial layer (Kuhlman and Resnik, 1958).

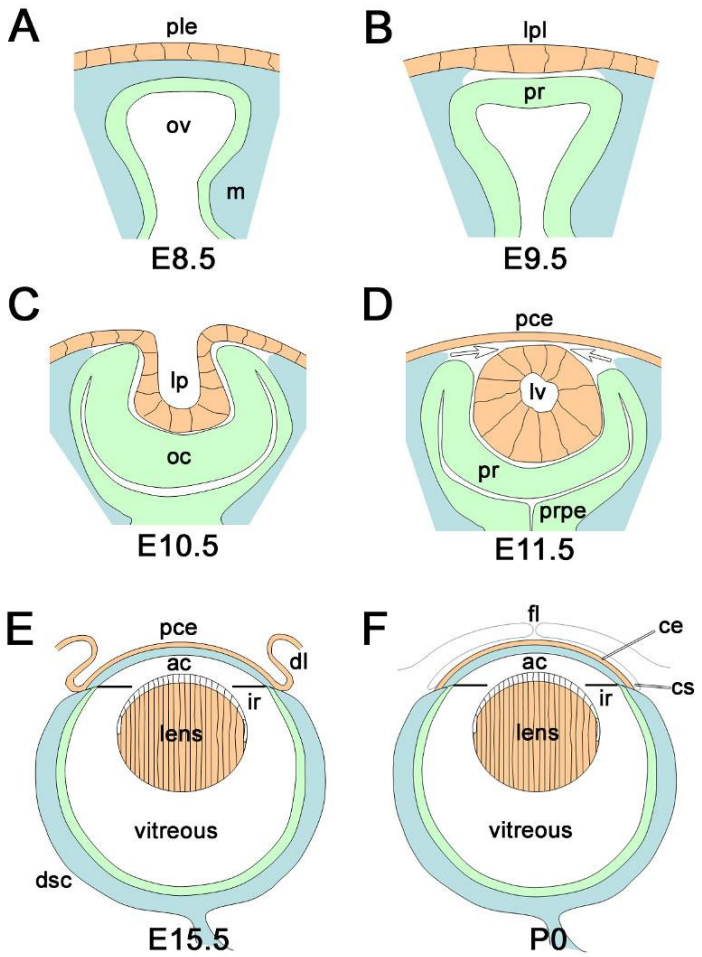

Figure 1.2: The embryonic development of the mouse eye.

The three tissue layers involved in ocular development are the surface ectoderm (brown), the mesoderm (blue) and the neuroepithelium of the optic vesicle (green). A: The first signs of eye formation are the formation of the optic vesicles from lateral evaginations of the forebrain at E8-E8.5. B: By E9.5 the optic vesicle is in contact with the surface ectoderm. The surface ectoderm begins to thicken into the lens placode and the apical neuroepithelium begins to thicken into the presumptive retina. C: By E10.5 the lens placode has developed into the lens pit and the optic cup has formed by invagination of the optic vesicle. D: By E11.5 the lens vesicle is fully formed, mesenchyme destined to become the corneal endothelium and stroma begins to migrate separating the presumptive corneal ectoderm

(epithelium) from the lens vesicle. E: The presumptive corneal ectoderm produces extra cellular matrix (ECM) components which combine with mesenchyme to form the corneal stroma. The corneal endothelium and anterior chamber are fully formed by E15.5, at this time the eyelids are beginning to develop. F: At birth (P0) the cornea is fully formed although the epithelium has yet to stratify and the stroma is more cellular than in the adult. The eyelids remain fused until P12-P14. Abbreviations; ple, presumptive lens ectoderm; ov, optic vesicle; m, ocular mesenchyme; lpl, lens placode; pr, presumptive retina; lp, lens pit; oc, optic cup; pce, presumptive corneal ectoderm; lv, lens vesicle; prpe, presumptive retinal pigment epithelium; dsc developing sclera; dl, developing eyelid; cs, conjunctival sac; ac, anterior chamber; l, lens; ce, corneal epithelium; fl, fused eye lids; ir, iris. The ciliary body is not shown. Figure adapted from Lang (2004), Smith (2001) and Forrester (2001).

1.1.3 Pax6 and ocular development

Pax6 is a homeobox gene encoding a transcription factor with two isoforms; canonical Pax6 and the Pax6(+5a) splice variant (Walther and Gruss, 1991). Figure 1.3 shows the gene and protein structure of human PAX6. Both the homeodomain and paired domain of the PAX6 protein have DNA-binding properties (Holst et al., 1997; Sheng et al., 1997). Pax6 is essential for the development of a number of tissues including the eye, central nervous system and endocrine glands of vertebrates and invertebrates (Simpson and Price, 2002). That Pax6 is essential for ocular development is highlighted by the severe ocular phenotypes of Pax6 null embryos which lack eyes in humans, mice and Drosophila (Glaser et al., 1992; Hill et al., 1991; Jordan et al., 1992; Quiring et al., 1994). Haploinsufficiency for Pax6 results in aniridia in humans and a small-eye phenotype in mice (Hill et al., 1991). Mouse small eye is characterised by aniridia, iris hypoplasia and a number of corneal defects and is a good model for the human condition, aniridia-related keratopathy (ARK) (Ramaesh et al., 2003). In mice, Pax6 expression is first observed in the head surface ectoderm and neuroectoderm at E8 (Krauss et al., 1991; Puschel et al., 1992). After invagination of the optic vesicle at E11.5, Pax6 continues to be expressed in both the lens and future corneal and conjunctival epithelia (Baulmann et al., 2002; Grindley et al., 1995; Koroma et al., 1997; Walther and Gruss, 1991). Lens placode expression of Pax6 increases during contact with the optic vesicle (Grindley et al., 1995). Regulation of Pax6 during these time-points is complex involving both its so-called ectoderm-enhancer element and the so-called SIMO enhancer element located in the final intron of an adjacent gene. Lens-placode related expression of Pax6 is dependent on an early pre-placode period of Pax6 expression. The importance of fibroblast growth factor receptor (FGFR) signalling to lens induction was demonstrated by a reduction in the transcription level and protein expression of Pax6 using small molecule inhibitors of FGFR kinase activity. Furthermore the expression of a dominant negative FGFR1IIIc receptor exclusively in the presumptive lens ectoderm showed defects in

the formation of the lens placode and reduced levels of expression for *Pax6* and *Sox2*. (Faber et al., 2001). The activity of bone-morphogenetic protein 7 (BMP7) (Wawersik et al., 1999) and the Meis transcription factor are also required. It is not clear exactly how Meis functions but it is likely that it binds directly to one or both of the enhancer elements of the *Pax6* gene (Zhang et al., 2002). In the adult, Pax6 is expressed throughout the corneal and conjunctival epithelia (Koroma et al., 1997).

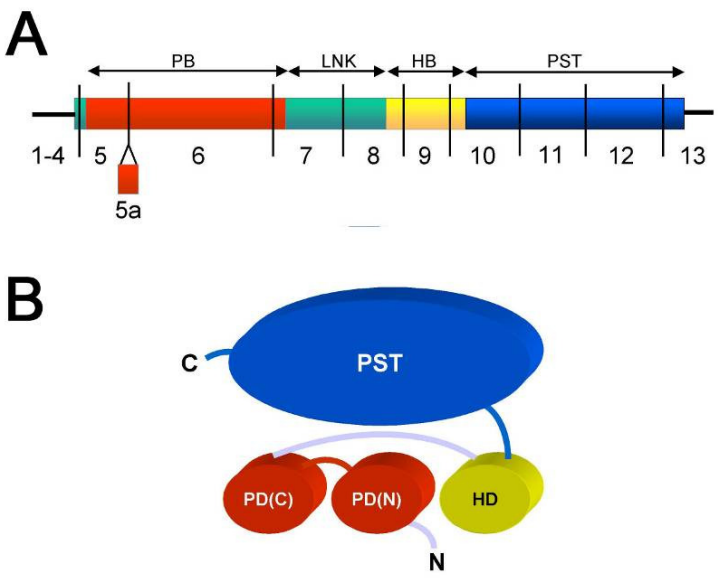

Figure 1.3: Gene and protein structure of PAX6.

A: The *PAX6* cDNA has distinct coding regions; the paired box, a linker region, the homeobox and a proline/serine/threonine-rich region. Exon boundaries are indicated by vertical black lines. Pax6(5a) is produced by alternative splicing of exon 5a leading to the insertion of 14 amino acids into the paired domain of the protein. The insertion changes PAX6's DNA binding specificity and may modify its down stream targets (Epstein et al., 1994; Kozmik et al., 1997). B: The PAX6 protein showing the different functional domains; the N-terminus of the protein, the C-terminus, the N-terminal subdomain of the paired domain, the C-terminal subdomain of paired domain, the homeodomain and the PST domain. Both the paired domain and the homeodomain have independent DNA-binding activities (Holst et al., 1997; Sheng et al., 1997). PB, pairedbox; LNK, linker region; HB, homeobox; PST, prolin/serine/threonin rich region; N, N-terminus; C, C-terminus; PB(C), C-terminal sub-domain of paired domain;p HD, homeodomain. Figure adapted from Tzoulaki et al (2005).

Pax6's function as a transcription factor regulates the expression of a broad range of molecules including other transcription factors, cell adhesion molecules, signalling molecules, hormones and structural proteins. It has wide-ranging down-stream effects on cellular processes ranging from cell cycle regulation to apoptosis. Targets include *Maf* with roles in cell death and the basic helix-loop-helix (bHLH) proteins Mash1, Math5 and Neurogenin2 which have important roles in cell determination and differentiation, as well as effects on the Pax6 regulation of retinal progenitors (Marquardt et al., 2001). Of particular importance to eye development is the interaction with the transcription factor Six3. Six3 expression regulates forebrain development and is essential for mammalian lens formation. Pax6 and Six3 have been shown to interact in a way that allows either gene to bind regulatory elements of its counterpart, their expression levels are therefore mutually regulated (Goudreau et al., 2002). However recent evidence from studies of lens cell specification suggest that Six3 may dominate this developmental network, regulating Pax6 and possibly Sox2 expression in a cell autonomous manner during early lens formation (Liu et al., 2006). The network is outlined schematically in Figure 1.4. Pax6 also regulates many eye-related structural proteins such as Keratin 12 and crystallins αA and β as well as molecules involved in cell-cell interactions (Simpson and Price, 2002). The small-eye corneal epithelium demonstrates reduction in the expression levels of β-catenin, γ-catenin and desmoglein thought to alter the structure of desmosomes and the major corneal keratin, keratin 12 (K12) (Davis et al., 2003). The crystallins are a family of proteins with roles in the structural and refractive properties of the lens and are the most numerous down-stream targets of Pax6. αA-crystallin is responsible for 25% of all soluble protein in the lens and contains a Pax6-binding site in its promoter region (Piatigorsky, 1998). β-crystallin is also expressed strongly in the lens and appears to be repressed by the Pax6 paired or homeodomain (Cvekl et al., 1995; Duncan et al., 1998).

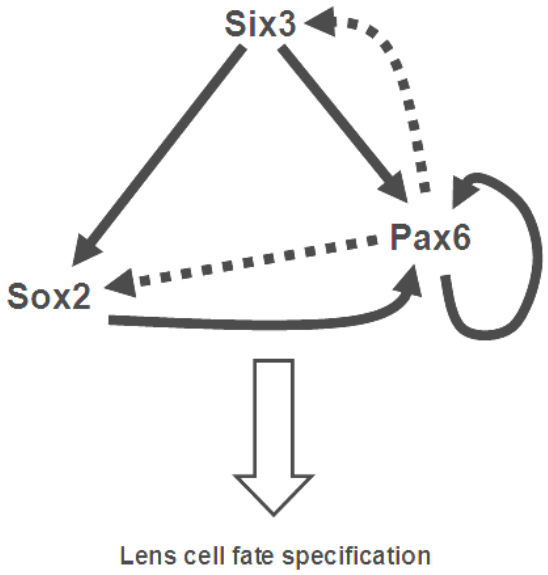

Figure 1.4: Proposed gene-regulation network for lens cell fate specification.

Solid arrows indicate direct regulation, and dashed arrows indicate potential direct regulation that has not yet been proven. Pax6 has been shown to auto-regulate by a direct interaction between the Pax6 protein and its ectoderm-enhancer element (Aota et al., 2003). Pax6 and Six3 are known to mutually regulates each other's expression levels (Goudreau et al., 2002). Six3 expression is required for Pax6 and Sox2 activation in the presumptive lens ectoderm (PLE) (Liu et al., 2006). Pax6 and SOX2 have been shown to bind cooperatively to initiate lens development (Kamachi et al., 2001). Adapted from Liu et al (2006).

Hill et al (1991) showed that the mouse small eye phenotype results from semi-dominant mutations in the *Pax6* gene. The group characterised three small-eye (*Sey*) alleles. The first arose spontaneously and was designated *Sey*. The second arose through a radiation induced mutation screen and was designated Sey^{H} and the third arose during an ethylnitrosourea (ENU)-induced screen and was designated Sey^{Neu}. They showed that in all three independent alleles *Pax6* was mutated and that the mutations could be predicted to interrupt gene function. $Pax6^{-/-}$ embryos have no eyes and there is failure of the nasal cavities to form, these animals die shortly after birth because they cannot breathe whilst suckling. $Pax6^{+/-}$ embryos are viable but they have smaller eyes than wildtype. In these animals the fissure of the optic cup is often delayed in its closure and a resultant folding at its margin results in a keyhole shaped opening. The Sey^{H} mutation, which has a more severe phenotype than the other small eye alleles, was shown to result from a chromosomal deletion. The more severe phenotype of Sey^{H} may therefore be due to the deletion of adjacent genes. The *Sey* mutation results from a base-pair change at codon 194 of the protein, resulting from a G:C ($Pax6^{+/+}$) to a T:A (in $Pax6^{-/-}$) transversion. This change converts a GGA triplet encoding glycine to an in-frame stop codon (TGA) the resultant protein terminates before the homeobox. PCR amplification of Sey^{Neu} mRNA, followed by sequence analysis of cloned PCR fragments showed that Sey^{Neu} RNA contained an additional 116 nucleotides. This was due to incorrect splicing at the +1 intronic position resulting from a change from T (in $Pax6^{+/+}$) to G (in $Pax6^{-/-}$). Due to the inclusion of an intron encoded stop-codon the resulting protein contained the paired box and the homeobox but was missing 115 amino acids from the Serine/Threonine rich (S/T-rich) C-terminus implicated in transcriptional activation (Hill et al., 1991).

1.2 STRUCTURE, FUNCTION AND DEVELOPMENT OF THE MOUSE CORNEA

1.2.1 Structure of the adult mouse cornea

The adult mouse cornea comprises 5 layers; the corneal epithelium, Bowman's layer, the corneal stroma, Descemet's membrane and the corneal endothelium (Hay, 1979). Laterally the cornea blends into the sclera at the corneoscleral junction. At this point, between the corneal epithelium and the adjacent conjunctival epithelium, is a morphological 'dent' in the ocular surface termed the limbus. LSCs that replenish the corneal epithelium are proposed to exist in the basal layer of the limbal epithelium (Cotsarelis et al., 1989; Schermer et al., 1986). As in the epidermis, Langerhans cells are present at the limbus and beneath the peripheral corneal epithelium (Klareskog et al., 1979). These cells play important roles in graft-rejection and inflammatory responses towards exogenous antigens (McLeish et al., 1989; Streilein et al., 1980).

Although the corneal and conjunctival epithelia are similar, the conjunctival epithelium is distinguished by the presence of goblet cells and the innervation of blood vessels, both absent from the corneal epithelium. Mitosis is restricted to the basal layer in both of these epithelia. Corneal epithelial cells exhibit complex interdigitations (Hazlett, 1993). Adult corneal epithelium is stratified and constitutes 4 to 6 layers of squamous non-keratinised epithelium; it is translucent and non-vascularised (Chung et al., 1992). Cells in the intermediate layers of the epithelium are termed 'wing cells' because of their characteristic shape (Hogan et al., 1971). The cornea is innervated by nerve axons that originate from the trigeminal nerve (LaVail et al., 1993), the largest of the cranial nerves responsible for sensation in the face. Corneal epithelial cells (keratinocytes) have oval nuclei and little cytoplasm and align in parallel to collagen bundles (Smith, 2001). Epithelium constitutes approximately 10% of the net corneal thickness absorbing oxygen and nutrients whilst protecting the eye (Daniels et al., 2001).

The acellular Bowman's layer beneath the epithelium is less prominent in mice than in primates. Rebinder (1978) and Hazlett (1993) contested whether a true Bowman's layer even exists in the mouse. But Smith et al (2001) showed that it can be observed under the electron microscope (EM). This layer constitutes a random arrangement of type I collagen fibrils in the adult (Beuerman and Pedroza, 1996) and type I and type XII fibrils during development (Oh et al., 1993). The corneal stroma represents around two thirds of the corneal thickness and contains sparsely distributed stromal cells (keratocytes). The acellular Descemet's membrane separates the corneal stroma from the corneal endothelium. It is a specialised basal lamina composed of laminin, fibronectin and type IV collagen produced by the corneal endothelium (Beuerman and Pedroza, 1996). The corneal endothelium consists of a single cell layer that demonstrates little or no mitosis under normal conditions.

Transparency is essential to the function of the cornea; three features ensure the tissue's transparency under normal conditions. Firstly the collagen fibres found in the tissue are of a constant, regular diameter; secondly collagen fibres are regularly spaced parallel to the surface of the tissue; thirdly the tissue is relatively dehydrated when compared for example to the sclera (Haustein, 1983). The endothelium is essential for maintaining the clarity of the corneal stroma by actively transporting fluid out of the stroma and into the anterior chamber. In this regard it demonstrates an abundance of mitochondria and pinocytotic vesicles (Rehbinder, 1978). Figure 1.5 shows the structure of the cornea. A haematoxylin and eosin (H and E) stained section of central cornea clearly shows the epithelium, stroma and endothelium (Fig 1.5 A). Confocal images of tauGFP-labelled central corneal epithelium demonstrate the change in keratocyte shape as it migrates from the basal to the superficial layer (Fig 1.5 B). The basal layer is composed of tightly packed compact cells, whereas in the superficial layer cells are squamous and more loosely packed.

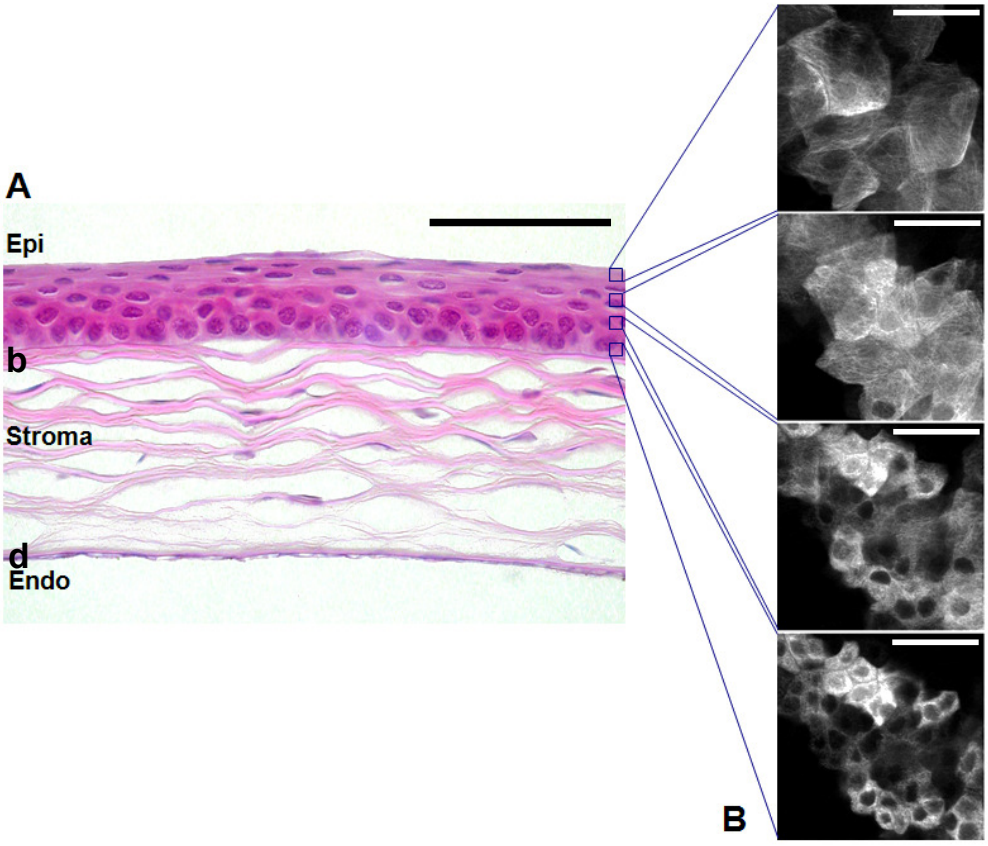

Figure 1.5 Structure of the cornea and corneal epithelium.

A: H and E staining of a section of central cornea clearly showing; a single layer of endothelium, a collagenous stroma containing sparsely distributed keratocytes and 6 layers of epithelium containing keratinocytes in various stages of differentiation. The structure of the epithelium changes from compact rounded cells in the basal layer; to wing cells in the suprabasal layers; to flattened squamous cells at the surface. **B:** Confocal images of central cornea from a CAAG-GFP animal (Pratt et al., 2000). TauGFP labelled corneal epithelial cells clearly show the change in structure from rounded compact cells in the basal layer to flattened squamous cells at the surface. Epi, epithelium; b, Bowman's layer; d, Descemet's layer; Endo, endothelium; Scale bar in A = 100 microns; Scale bars in B = 10 microns. The section provided for the photograph in A was kindly provided by Dr Thaya Ramaesh.

1.2.2 Function of the adult mouse cornea

The biochemistry of the cornea is concerned with providing a protective barrier, maintaining transparency and with the absorption and metabolism of oxygen and nutrients from the tear film and the aqueous humour. The tissue's ability to transmit light and its refractive properties are a function of the exquisite organisation of its cellular compartments and extracellular components (Haustein, 1983; LaVail et al., 1993). Keratinocytes express keratin 12 (K12), crucial to the epithelium's integrity. Whilst heterozygosity for a knock-out of K12 has no phenotype, K12 homozygous knock-out mice exhibit mild recurrent corneal erosions demonstrating that the K3-K12 keratin pair are essential for the maintenance of epithelial integrity (Kao et al., 1996). The epithelium represents an effective barrier to fluid transport and is anchored to the stroma through hemidesmosomes and type VII collagen containing many 'spot desmosomes'. The Descemet's and Bowman's layers contain many collagens that are absent from normal matrices. The Bowman's layer in humans is primarily composed of a random fibrillar network of type I collagen, but also contains type III collagen, chondroitin and dermatan sulphate (Beuerman and Pedroza, 1996). The regular arrangement of the collagen fibrils at 55nm distances and the restriction of fibril diameter to no more than 30nm are thought to be crucial in maintaining the tissue's transparency (Haustein, 1983). Lumican is a proteoglycan that has been implicated in regulating the assembly of these collagen fibrils. Lumican deficient mice homozygous for a null allele of lumican, have abnormally thick collagen fibrils in the corneal stroma and develop bilateral corneal opacification (Chakravarti et al., 1998). Descemet's layer is composed of laminin, fibronectin and type IV collagen in a fine hexagonal array providing strength and resilience to the tissue thus allowing it to contain the intraocular pressure. Parallel lamellae run at oblique angles to one another, this means that despite not being regularly arranged like the stromal collagen, the layer can maintain its transparency (Beuerman and Pedroza, 1996; Rehbinder, 1978).

The cornea's level of hydration is crucial to its transparent properties. The stroma's level of hydration is maintained precisely by the metabolic pump function of the endothelium. If the cornea becomes over-hydrated, as occurs after corneal laceration for example, the tissue becomes swollen and opaque. Because of it role in excluding water the endothelium is highly metabolically active. Two ATP dependent ion pumps exclude water from the tissue. These are a Na^+/K^+ dependent ATPase located in the plasma membrane and responsible for transporting Na^+ and HCO_3- and an HCO_3- ATPase present in mitochondria and responsible for expelling HCO_3-. The endothelium and stroma meet their energy requirements by absorbing oxygen and glucose from the aqueous humour. Keratinocytes on the other hand display a lower metabolic activity absorbing the majority of their oxygen from the tear film and their glucose from the stroma (Reviewed in Forrester, 2001).

1.2.3 Postnatal development and gene expression of the corneal epithelium

Development and maturation of the corneal epithelium continues postnatally. At birth the eyelids are sealed at which time the corneo-limbal and conjunctival epithelia constitute one to two layers of basal and suprabasal epithelium. After eye opening at postnatal day 12 the corneal epithelium begins to stratify this process being complete by 6 weeks of age in the mouse (Kuhlman and Resnik, 1958). Similarly the limbal epithelium may not be fully mature until 5-8 weeks (Collinson et al., 2002) and the size of the eye increases from around 12mg at 2-weeks to 18mg by 6-weeks (Gerido et al., 2003). These physical changes are accompanied by profound changes in gene expression. The expression of the cytokeratin pair K12/K3 is unique to all layers of the corneal epithelium. Therefore it is an indicative marker of terminally differentiated corneal epithelium (Moll et al., 1982; Schermer et al., 1986). Tanifuji-Terai et al (2006) used absence of K12 expression as a marker of undifferentiated corneo-limbal cells. The group combined a K12-Cre expressing transgenic mouse with a ZAP mouse. The ZAP transgenic contains a ubiquitously driven *LacZ* transgene flanked by loxP sites and inserted into an intron of the alkaline phosphatase (AP) gene so as to disrupt

its expression (Lobe et al., 1999). Cre-mediated recombination excises the *LacZ* gene allowing expression of AP. Therefore all K12-negative cells stained blue for *LacZ* whilst all K12 positive cells stained red for AP. They demonstrated that the K12 expression pattern changed postnatally. At P15, K12-negative *LacZ*-positive cells were found in a mosaic pattern throughout the central cornea. As the eye developed postnatally this pattern became increasingly restricted to the periphery of the tissue so that by P90 the majority of K12 negative cells were localised in the basal layer of the limbus (Tanifuji-Terai et al., 2006). Similarly Pajoosh-Ganji et al (2004) found that the distribution of α9-integrin, a proposed TAC marker, changed postnatally. At P7 α9-integrin positive cells were distributed throughout the epithelium but by P42 α9-integrin expression was restricted to the limbal epithelium. Furthermore the group described an uneven distribution of α9-integrin with higher expression in the temporal cornea at P7 and lower expression in the temporal limbus at six weeks (Pajoohesh-Ganji et al., 2004).

With the advent of high-throughput technologies such as cDNA microarrays and serial analysis of gene expression (SAGE) it has become possible to analyse gene expression on a much wider scale. Using microarrays containing 5600 human genes, Jun et al (2001) identified 6 collagen genes and 4 apoptosis-related genes that had not previously been associated with corneal expression. Additionally the work allowed the production of a human corneal gene expression database made available on line. Similarly Diehn et al (2005) used microarrays representing approximately 30,000 human genes to analyse gene expression in the cornea, lens, iris and ciliary body and were able to establish unique gene expression 'signatures' for each tissue compartment. One disadvantage of transcript profiling using cDNA microarrays is that the analysis is limited only to genes that are represented on the gene chip used, limiting it to genes where the sequence is known or a cDNA clone is available.

SAGE is a method of analysis designed to identify differentially expressed mRNA transcripts in specific tissues (Velculescu et al., 1995). The main advantage of a SAGE analysis is the ability to analyze and quantify large numbers of transcripts without prior knowledge of the genes expressed in a particular tissue (Yamamoto et al 2001). Norman et al (2004) carried out SAGE on total cornea from mice at postnatal day 9 (P9) and at 6 weeks (adult). In summary the group identified 64,272 P9 tags and 62,206 adult tags. Of these, approximately one third were expressed both at P9 and in the adult. A further third were expressed either at P9 or in the adult. When these results were corrected to exclude transcripts that only arose once (and so may be due to sequencing errors) 3,052 P9 specific transcripts, 2,394 adult specific transcripts and 3,483 common transcripts were identified. 758 transcripts from the P9 and adult SAGE libraries had no match in any public database and therefore represented novel genes. Such massive changes in gene expression between the period before and after eye opening highlight the importance of postnatal maturation. It is thought that much of this activity is associated with the changing stimuli of oxygen, light and exposure to pathogens associated with eye opening. Furthermore the identification of a novel transcript that specifically labels wing cells for the first time highlights the importance of such studies (Norman et al., 2004).

A drawback of these early studies is the use of whole corneal preparations rather then any attempt to separate the cellular compartments, making the identification of candidate genes for particular tissues much more difficult. Zhou et al (2006) addressed this by using laser capture microdissection (LCM) to separate different cellular compartments and produce transcriptional profiles of basal cells of the limbal and corneal epithelia (described in section 1.3.3 of this chapter). In the future these technologies will be hugely beneficial in characterising corneal epithelial gene expression and perhaps developing better panels of markers for its cellular compartments.

1.3 MAINTENANCE AND REPAIR OF THE ADULT CORNEAL EPITHELIUM

1.3.1 X, Y, Z hypothesis for corneal epithelial maintenance

The adult corneal epithelium is highly dynamic; cells are constantly desquamated from the corneal surface and are replaced by the progeny of LSCs (Kruse, 1994). Cells in the basal corneal epithelium proliferate, migrate centripetally and differentiate as they move to the suprabasal layers. Figure 1.6 demonstrates the X, Y, Z hypothesis of corneal maintenance first described in a letter to Investigative Ophthalmology and Visual Science by Thoft and Friend (1983). The theory supposes that as the mass of the corneal epithelium 'probably does not change under normal circumstances' the balance of proliferation migration and cell loss could be described with the simple formula X + Y = Z where X is the rate of proliferation of the basal cells, Y is the contribution to cell mass by the centripetal migration of cells and Z the rate of loss of epithelial cells from the surface of the tissue. It is generally accepted that the corneal epithelium is replenished from a pool of limbal stem cells residing in the limbal region at the edge of the cornea (Fig 1.6 A). LSCs divide to produce transient-amplifying cells (TACs) that migrate along the basal layer of the epithelium (Fig 1.6 B). As these cells leave the basal layer they differentiate and are lost from the surface of the tissue by desquamation (Fig 1.6 C). Thoft and Friend's (1983) original hypothesis makes no mention of the proliferation of limbal stem cells referring only to proliferation in the basal layers. Perhaps the hypothesis needs to be updated so that W + X + Y = Z, where W is the proliferation of LSCs as indicated in Figure 1.6 B.

1.3.1.1 X: The rate of proliferation

Beebe and Masters (1996) showed elegantly using bromodeoxyuridine (BrdU) labelling that TAC daughter cells leave the basal layer of the epithelium at variable times, and if necessary can undergo additional rounds of division. When they do leave the basal layer they invariably do this as a pair. It was subsequently shown using a double labelling technique

where cells were exposed to BrdU followed by a second pulse with tritiated thymidine (H-Tdr) that as a self-renewing tissue, the corneal epithelium can adopt three strategies to expand its cell population in response to injury by n-heptanol or stimulation by the tumour promoter TPA. Firstly the tissue may respond by recruiting of LSCs to produce additional TACs; secondly an increase in the replicative potential* of TACs was shown and thirdly TACs responded by shortening their cell cycles. The study also showed that peripheral TAC populations have a greater potential for replication then their more central counterparts (Lehrer et al., 1998).

*Lehrer et al (1998) contest that under normal circumstances not all TACs utilise their maximum ability to divide and that the decision to terminally differentiate is therefore stochastically determined. Therefore 'replicative potential' can be defined as the maximum number of cell divisions a TAC is capable of making before undergoing terminal differentiation. A TACs replicative potential may therefore be modulated by changes in the local environment (i.e wounding).

1.3.1.2 Y: The rate of migration

LSCs cycle slowly unless stimulated to proliferate by corneal insult; their progeny are transit or transient amplifying cells (TACs). TACs undergo rapid proliferation followed by differentiation, migrating centripetally along the epithelium's basal layer. Buck (1985) impregnated corneal epithelia in-vivo with India ink and then observed the results over a 7-day period. The work demonstrated that superficial and wing cells migrate at an average rate of 17μm/day. Similarly Nagasaki and Zhao (2003) used UGFP mice to track the migration of GFP-bright clusters of cells. They calculated that the average rate of migration of one of these groups of cells was 26 μm/day. As TACs differentiate they lose contact with the basal epithelium and migrate apically, eventually being desquamated from the surface layer (Ren and Wilson, 1996).

1.3.1.3 Z: The rate of desquamation

Ren and Wilson (1996) using both *in-vivo* and *in-vitro* measurements of corneal epithelial shedding rates in the rabbit calculate that on average cells are shed at a rate 5-15 cells/min/cornea.

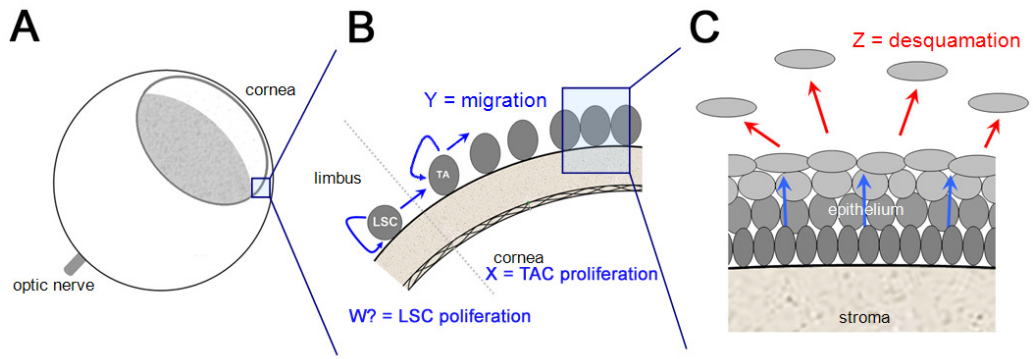

Figure 1.6: The X, Y, Z hypothesis of corneal maintenance.

Model for the maintenance of the corneal epithelium by limbal stem cells. A: Limbal stem cells (LSCs) reside in the limbal epithelium, between the corneal and conjunctival epithelia. B: LSCs cycle slowly to produce transit-amplifying cells (TACs), which undergo more rapid division and migrate centripetally along the basal layer of the corneal epithelium. C: As TACs differentiate they lose contact with the basal epithelium and migrate apically until they are desquamated from the surface layer. W, LSC proliferation; X, TAC cell proliferation; Y, cell migration; Z, desquamation.

1.3.2 Limbal stem cells and corneal epithelial maintenance

Adult stem cells, that maintain proliferative epithelia, have a high proliferative capacity but divide infrequently (Braun and Watt, 2004). H-Tdr or the thymidine analogue BrdU are incorporated into the DNA of dividing cells during S-phase of the cell cycle, and because of their slowly cycling nature, the label is retained in putative stem cells but is diluted from their more proliferative daughter cells. This approach has been used extensively in other tissues to identify label retaining cells (LRCs), a tissue's putative stem cells (Potten and Loeffler, 1990). These traditional label-retaining methods identify only a subset of functional stem cells (those that divide during the time of exposure to H-Tdr or BrdU) and do not identify quiescent stem cells.

LSCs are essential for the maintenance of the corneal epithelium and stem cell deficiency results in re-epithelialisation of the cornea by cells from the conjunctiva. This can inflict much pain, poor vision and even blindness on sufferers (Daniels et al., 2001). In humans the evidence suggests that LSCs reside in a specific anatomical location within the limbus known as the palisades of Vogt (Dua and Azuara-Blanco, 2000; Townsend, 1991). Dua et al (2005) suggest that within this region exists a 'limbal epithelial crypt' a novel anatomical structure that displays key characteristics of a stem cell niche. No such niche has been identified in the mouse. The combination of their location in the limbus and their label-retaining properties has been used to identify LSCs. Cotsarelis et al (1989) treated mouse corneas with TPA to stimulate LSCs to divide during an initial pulse of H-Tdr. Using this method they identified a population of LRCs in the basal layer of the limbal epithelium. Lehrer et al (1998) used BrdU perfusion by minipump for 7 days followed by a 6-week chase period to identify LRCs in the limbal region. This work confirmed the broader conclusions of Cotsarelis et al's (1989) study but also contradicted the finding that wounding was required to stimulate limbal stem cells to divide.

Chung et al (1992) produced a monoclonal antibody specific to adult limbal basal cells in rat, rabbit and human using a scrape of rat limbal epithelium as a source of antigen. Evidence from a postnatal time course suggested that during development 'stem-like' cells resided throughout the basal layer of the corneal epithelium until around P10. Over the next few weeks these cells became gradually restricted to the peripheral cornea and limbal region so that at 4-weeks they were entirely restricted to the basal limbal epithelium. These events occurred in conjunction with the process of stratification of the cornea which was complete by around 4 weeks in the rat (Chung et al., 1992). These early studies were useful in confirming the existence of a putative corneal stem cell located to the limbal region, subsequent studies have attempted to identify specific markers of LSCs.

1.3.3 Proposed markers

Many markers have been proposed as possible positive and negative markers of LSCs. A selection of these are outlined in Table 1.1. They can be broadly summarised into 8 groups. (1) Cytoplasmic and Nuclear markers; these include p63, nestin and vimentin (Chen et al., 2004; Kasper and Viebahn, 1992; Pellegrini et al., 2001). (2) Keratin profiles; keratin expression has been used to define cellular compartments in the epidermis. In the eye it has been suggested that LSCs are K5/K14 positive and K3/K12 negative (Chen et al., 2004; Pearton et al., 2004; Tanifuji-Terai et al., 2006). (3) Integrins; important in cell-cell adhesion, integrins have been shown to localise to the limbal epithelium postnatally (Pajoohesh-Ganji et al., 2004; Pajoohesh-Ganji and Stepp, 2005; Stepp et al., 1995). (4) Growth factor receptors; these receptors may infer competence to LSCs in order for them to respond to extracellular signals perhaps in wound healing, they include EGFR, NGFR and TGFβ-RI/II (Chen et al., 2004; Zieske and Wasson, 1993). (5) Metabolic enzymes; enzymes such as α-enolase, carbonic anhydrase and cytochrome oxidase may be more abundant in the basal layer of the corneal epithelium reflecting a high metabolic demand (Hayashi et al., 1983; Steuhl and Thiel, 1987; Zieske et al., 1992). (6) Gap junction proteins; proteins such as

connexin's 43 and 50 and involucrin are thought to be absent form basal cells of the limbal epithelium. It has been suggested that this reflects the lack of cell-cell communication between LSCs and the need to maintain a distinct intracellular compartment. (Chen et al., 2004; Matic et al., 1997). (7) Cell-cycle mediators; cell cycle components such as cyclins D and E may be important in LSCs allowing them to maintain their proliferative potential (Joyce et al., 1996). (8) Cell surface transporters; the multi-drug resistance gene ABCG2 has been proposed as a stem cell marker in other systems and may protect stem cells from exogenous damage (Chen et al., 2004; Pajoohesh-Ganji and Stepp, 2005).

As is clear from Table 1.1 despite many proposed positive and negative markers. No marker exclusive to LSCs has been identified. Alpha-enolase (Chung et al., 1992; Zieske et al., 1992) and p63 (Pellegrini et al., 2001) are much cited in the literature but it seems unlikely that they are exclusive to limbal stem cells (Boulton et al., 2004). More recently ABCG2 has been widely studied as a possible LSC marker (Chen et al., 2004). Chen et al. (2004) attempted to define a putative limbal stem cell phenotype. Their work defined the basal cells of the limbal region as p63, ABCG2 and integrin $\alpha 9$ positive and nestin, E-cadherin, connexin 43, involucrin, K3, and K12 negative, with relatively higher expression of integrin $\beta 1$, EGFR, K19 and enolase-α.

Table 1.1: Proposed positive and negative markers of LSCs

Marker	Limbal Epithelium		Corneal Epithelium		Reference
	Basal	Suprabasal	Basal	Suprabasal	
Cytoplasmic/nuclear markers					
p63	+++	±	±	-	(Pellegrini et al., 2001)
Vimentin	+++	+	+++	+++	(Kasper and Viebahn, 1992)
Nestin	-	+++	+	+++	(Chen et al., 2004)
Keratins					
Keratin 19	+++	+	+++	+++	(Chen et al., 2004)
K3/K12	-	+++	+++	+++	(Pearton et al., 2004)
K5/K14	++	+	- or +	-	(Pearton et al., 2004)
Integrins (ECM binding)					
Integrin α9	+++	±	-	-	(Stepp et al., 1995)
Integrin α6	- or +++	++	+++	++	(Pajoohesh-Ganji and Stepp, 2005)
Integrin β1	+++	++	+++	++	(Pajoohesh-Ganji and Stepp, 2005)
Integrin β4	+++	++	+++	++	(Pajoohesh-Ganji and Stepp, 2005)
Growth factor receptors					
NGF receptor	+++	++	+++	++	(Chen et al., 2004)
NGF receptor	-	+++	+++	+++	(Chen et al., 2004)
EGFR	+++	++	+++	++	(Zieske et al., 2000)
TGF-β	+++	++	+++	++	(Zieske et al., 2001)
Metabolic enzymes					
α-Enolase	+++	+	++	+	(Zieske et al., 1992)
Carbonic	+++	+	++	+	(Steuhl and Thiel, 1987)
Cytochrome	+++	+	++	+	(Hayashi et al., 1983)
Gap-junction proteins					
Connexin 43	-	+++	+	+++	(Matic et al., 1997)
Connexin 50	-	+++	-	+++	(Matic et al., 1997)
Involucrin	-	+++	+	+++	(Chen et al., 2004)
Cell-cycle					
Cyclin D	+++	+	++	-	(Joyce et al., 1996)
Cyclin E	++	+	+	-	(Joyce et al., 1996)
Cell surface transporters					
ABCG2	+++	±	-	-	(Chen et al., 2004)
Na+/K+	+++	+	++	+	(Pajoohesh-Ganji and Stepp, 2005)

NGF, nerve growth factor; EGFR, epidermal growth factor receptor; TGF, transforming growth factor; ABCG2, ATP-binding cassette transporter G2; -, no expression; ±, very weak expression; +, weak expression; ++, moderate expression; +++, strong expression.

It seems likely that one of the main difficulties in identifying a LSC specific marker is the blurring in phenotype between early TACs and LSCs. Structural proteins such as keratins and integrins, and cell surface receptors/transporters such as EGFR and ABCG2 would most likely persist at least into the first daughter of a LSC division blurring the distinction between the two populations. Better ways of distinguishing between these populations will be required to narrow down prospective markers. Zhou et al (Zhou et al., 2006) attempted to define a transcriptional profile of cell populations enriched for TAs versus LSCs by using LCM to dissect basal cells from the limbal and corneal epithelia in frozen sections. After exclusion of unknown genes they identified around 50 differentially expressed genes between these two populations. Further characterisation of randomly picked genes using semi quantitative RT-PCR showed that Epiregulin, *dachshund,* and Sry were found exclusively in limbal basal cells and not in corneal basal cells. Furthermore Diablo, cyclin M2 and multiple PDZ domain protein were expressed at significantly higher levels in corneal basal cells compared to limbal basal cells. Epiregulin-*LacZ* mice showed *LacZ*-positive staining restricted to the basal limbal epithelium (Zhou et al., 2006). Epiregulin is known to have roles in the *in-vitro* wound closure in epidermal keratinocytes (Draper et al., 2003a; Draper et al., 2003b).

1.3.4 A transgenic approach for identification of label-retaining cells

Tumbar et al (2004) have demonstrated a novel method to identify LRCs in the epidermis using the tetOff inducible system. This bi-transgenic system incorporated a transactivator protein (tetOff) driven by the Keratin 5 (K5) gene promoter. A tightly regulated cytomegalovirus promoter (mCMV) incorporating a tetracycline response element (tetRE) was then used to drive a Histone-2B-GFP (H2B-GFP) fusion protein incorporated into the chromatin of cycling cells (Gossen and Bujard, 1992; Resnitzky et al., 1994). Gene expression was constitutively active throughout the epidermis under normal conditions, where binding of tetOff to tetRE induced H2B-GFP expression. Administration of the

tetracycline analogue doxycycline inhibited tetOff binding and silenced H2B-GFP, which was then diluted from cells that underwent subsequent cell divisions. After doxycycline treatment for a chase period of up to 4 months, labelled cells were restricted to a small proportion of cells in the bulge region of the hair follicle. These label-retaining cells (putative stem cells) were isolated by flow cytometry and their transcriptional profile was shown to differ from other keratinocytes.

Although this approach is broadly equivalent to traditional BrdU label-retaining protocols there are two important differences. Firstly, only cells that express the K5 promoter will incorporate H2B-GFP into their chromatin and, according to Tumbar et al (2004), this was restricted to skin epithelium. Secondly, all cells that divided while expressing the K5-tetOFF transgene would become labelled. As K5 is first active at E9.25 (Lu et al., 2005) this effectively means the entire epidermis. In traditional BrdU protocols only a fraction of slow-cycling stem cells will incorporate BrdU into their DNA during the relatively short labelling period (typically 1-2 weeks). The massively improved efficiency of 'hitting' label retaining cells with H2B-GFP and the specificity provided by using a tissue specific promoter are major advantages. Tumbar et al's approach is therefore, a far more powerful and potentially easier to interpret system than traditional BrdU based approaches.

1.3.5 Corneal wound healing

Wound healing is essential in maintaining the corneal epithelium's barrier function, its transparency and its refractive properties. The wound healing process is dependent upon cell migration, proliferation and differentiation. The tissue must remodel itself and demonstrate considerable plasticity in its function with regard to cell-cell and cell-matrix binding in order for these processes to occur in a critical time-frame. Of the myriad of factors implicated in these processes epidermal growth factor (EGF) a small polypeptide has been shown to have responsibility for stimulating both proliferation and differentiation in the epidermis (Cohen,

1965; Cohen and Elliott, 1963). Zieske and Wasson (1993) showed that EGF is present throughout the neonatal rat corneal epithelium. However in the adult its presence in central cornea is greatly reduced whilst expression in the basal layer of the limbus is maintained. The authors speculate that the presence of EGF may allow limbal basal cells to respond rapidly in wound healing and maintain these cells in an undifferentiated 'stem cell' state.

Essential to rapid epithelialisation of corneal defects is the mobilisation of keratinocytes to migrate into the wound site. Block et al (2004) showed that epithelial cell motility can be induced by loss of spatial constraints and is not dependent on the damage of cells at the wound edge and the subsequent release of intracellular components. The group used ex-vivo culture of rabbit corneal epithelial cells in culture dishes containing agarose strips which were subsequently removed to simulate a loss of constraints. Using this technique the group demonstrated that cells could migrate to fill the void at comparable speeds to cells in mechanically wounded systems. Furthermore it was demonstrated that rapid activation of the epidermal growth factor receptor (EGFR) was required for wound healing and that by blocking this receptor, with a specific antibody, wound healing was completely abolished.

Another candidate signal for the stimulation of migration into the wound site is electrotaxis. Electrical signals have been implicated in directing the active migration of cells in wound healing in both the newt epidermis (Chiang et al., 1991) and the bovine corneal epithelium (Sta Iglesia and Vanable, 1998) among others. Reid et al (2005) showed that Cl^- and Na^+ are the major components of electrical currents in rat corneal epithelium. Na^+ is the main constituent of ionic transport under normal conditions and of the wound centre leakage current in the wounded cornea. Cl^- on the other hand is mainly concerned with the endogenous current at the wound edge. The group showed that by pharmaceutically manipulating these electrical currents they could change the rates at which corneal epithelial wounds healed. Building on this work Zhao et al (2006b) showed that this 'electrotaxis' is triggered by activation of Src and inositol-phospholipid signalling. They showed that by

deleting the phosphatidylinositol-3-OH kinase-γ (PI(3)Kγ) or the phosphatase and tensin homologue (PTEN) genes they could disrupt or enhance electrotaxis respectively. This study is the first to link electrotactic responses with specific effector genes.

As well as a myriad of growth factors, cytokines and enzymes, epithelial wound healing involves the reorganization of key structural elements of the tissue to maintain barrier integrity and facilitate migration. Migration and proliferation are key to the protection of the wound site from exogenous agents and the generation of new epithelial tissue. *In-vitro* studies of the respiratory epithelium have shown that migratory and proliferative responses differ with distance from the wound site. In culture, mitotic activity peaks around 48 hours post wounding and is greatest between 160 and 400 μm from the site of injury. In contrast the migration speed is highest in cells at the leading edge of the wound and reduces progressively in cells further from this site (Zahm et al., 1997). These early stages of wound repair require the conversion of quiescent to migratory cells and thus a requirement for actin microfilament re-organisation. Evidence from an endothelial wound repair system suggests that over a period of 6 hours post wounding there is a reduction in peripheral cellular phosphotyrosine which is associated with the loss of cell-cell adhesion sites. Simultaneously there is an increase in central phosphoytyrosine and a subsequent redistribution of microfilaments perpendicular to the wound edge. Inhibition of tyrosine kinases in this system reduced endothelial wound healing (Lee and Gotlieb, 1999). In chick and guinea pig corneal epithelial wound healing, loss of the cell adhesion-associated protein Pinin correlates with this shift from a quiescent epithelium to active migration. Pinin is associated with mature desmosomes, an integral component in cell adhesion and cytoskeletal linkage. Over expression of Pinin in cultured corneal epithelium induces a hyperstable epithelium and inhibits this transition (Shi et al., 2000).

Adherence of corneal epithelium to its basal membrane is dependent on ‘adhesion complexes’, these complexes are composed of hemidesmosomes, the lamina densa and the

lamina lucida of the basement membrane (Gipson, 1992). In order for corneal epithelial wound healing to progress, remodelling of the corneal stroma is required, these processes are modulated by MMPs which are produced by corneal keratinocytes and keratocytes and act in a carefully controlled sequence. MMP9 is specifically upregulated in corneal-epithelial wound healing and is responsible for degradation of the damaged matrix (Sivak and Fini, 2002; Wong et al., 2002). Recurrent corneal erosions (RCE) are common ocular defects characterised by repeated spontaneous recurrence of pain, photophobia, redness and tearing (Jackson, 1960). Reattachment of the corneal epithelium, after wound healing, seems to be disrupted in RCE through absence of the basement membrane and of hemidesmosomes (Brodrick et al., 1974; Rodrigues et al., 1974; Tripathi and Bron, 1972). Because of their roles in wound healing and the observation that MMP2 and MMP9 are present in elevated levels in some patients with RCE (Garrana et al., 1999), MMPs are considered an important therapeutic target for the treatment of RCE with pharmaceuticals such as doxycycline and corticosteroids (Ramamurthi et al., 2006).

It is unclear whether wound healing in the corneal epithelium induces a direct requirement for the proliferation of LSCs or whether the redundant proliferative potential of TACs in the tissue's basal layer is enough to satisfy the demand for new tissue. It seems likely that a balance between the two situations might be reached dependent on wound size. Lehrer et al (1998) used cell-cycle double-labelling techniques to show that the cornea uses three strategies for epithelial repair; firstly that stem cells can enter the cell cycle to replenish the TAC population, secondly the 'unleashing' of redundant TAC proliferative capacity and thirdly the shortening of TAC cell cycles. Changes in the distribution of proposed LSC markers have been observed in corneal epithelial wound healing systems. p63 is a protein required for the development of all stratified epithelia. p63 null embryos die postnatally and have severe limb defects and lack of development of epidermal tissues (Mills et al., 1999). The protein has been put foward as a potential LSC marker (Pellegrini et al., 2001). Six

isoforms are generated from the *p63* gene. Three isoforms from the upstream promoter have transactivating activity, whilst the three ΔN isoforms are produced by alternative splicing from a downstream intronic promoter. These three splice products have distinct C termini and are termed α, β and γ (Parsa et al., 1999; Yang and McKeon, 2000). Di Iorio et al (2005) showed that human limbal and corneal epithelial cells could contain all three ΔN isoforms. In unwounded cornea ΔNp63α is restricted to the basal cells of the limbus. Upon corneal wounding ΔNp63α containing cells migrate into the basal layer of the corneal epithelium. ΔNp63β and ΔNp63γ appear after wounding and are shown to correlate with regeneration of the epithelium and differentiation of TACs.

Similar adult expression patterns and changes in wound healing are described for the protein α9 integrin. α9 integrin is restricted to the basal cells of the limbus in the adult eye. This adult pattern is established between 6 and 8 weeks postnatally. At 1 week α9 is expressed throughout the ocular surface, its distribution begins to change progressively at 2 weeks until the adult pattern is established (Pajoohesh-Ganji et al., 2004). However localization of α9 changes during wound healing (Stepp et al., 1996). Pal-Ghosh et al (2004) describe how when a large wound is created α9 integrin is upregulated and its distribution at the limbus is altered whilst this is not the case for a small wound. Furthermore the loss of α9 integrin expression at the limbus seemed to correlate with the presence of goblet cells in the central cornea suggesting ingression of cells from the surrounding bulba-conjunctiva.

1.3.6 Analysis of corneal epithelial maintenance with mosaics and chimeras

Marking of a proportion of cells in an embryo either by the generation of *LacZ*+ ↔ *LacZ*- chimeras or by using X-inactivation mosaic mice has allowed the visualisation of clonally-related progeny in the mouse (West, 1976). In these animals 'patches' of *LacZ*-positive and negative cells can be observed in many tissues. A 'patch' may be defined as any group of cells of like genotype that are contiguous at the time of observation (Nesbitt, 1974). A

'patch' may be composed of one or more 'coherent clones'. A coherent clone is defined as a group of clonally related cells that have remained contiguous throughout development up until the point of observation. This should be distinguished from a 'descendent clone' which is defined as any group of clonally related cells, regardless of whether they have remained contiguous throughout development or not (West, 1978; West et al., 1997). So, for example, in an X-inactivation *LacZ*-mosaic mouse (Collinson et al., 2002), any clump of contiguous *LacZ* positive cells may be defined as a patch. However it cannot be directly inferred how many coherent clones of *LacZ*-positive cells such a patch may contain. This is because more than one coherent clone of *LacZ*-positive cells may be arranged adjacent to each other in a given tissue. Furthermore all the *LacZ*-positive patches in the tissue represent descendent clones.

X-gal staining of adult eyes from X-inactivation *LacZ*-mosaics revealed striking radial patterns of blue and white stripes confined to the corneal epithelium (Collinson et al., 2002). Basal cells were normally the same colour as the more apical counterparts in a stripe, implying they are clonally related. These stripes were shown to develop postnatally between weeks 5 and 8 (Collinson et al., 2002). These data are consistent with an epithelium maintained by centripetally migrating cells with little mixing. Therefore each stripe represents a patch of *LacZ*-positive or negative cells. Each stripe therefore contains one or more corneal epithelial coherent clones. It is likely that each coherent clone in the corneal epithelium is derived from a 'functional clone' of limbal stem cells, so the number of coherent corneal epithelial clones will also be equal to the number of functional LSC clones. However because each stripe may contain one or more coherent clones the number of stripes is not necessarily proportional to the number of functional clones of limbal stem cells. Nevertheless these striping patterns can be quantified to give an estimate of the number of coherent clones of limbal stem cells by correcting for the proportions of *LacZ*-positive and negative cells.

The correction factor 1/(1-*p*), where *p* is the proportion of a single cell type, was first described by Roach (1968) to estimate the extent of random clumping in a linear array of two cell types. The formula rests on the premise that as the contribution of one cell type increases so does the probability of a clump of those cells arising (Roach, 1968). It was further adapted for the analysis of clone sizes in the retinal pigment epithelium (RPE) of X-inactivation *LacZ*-mosaics and chimeras (West, 1976) and has been used successfully to correct the observed number of stripes in the corneal epithelium for the proportion of *LacZ*-positive staining (Collinson et al., 2002). This 'corrected stripe number' is an estimate of the number of coherent clones in the corneal epithelia of these animals, based on the assumption that stem cell clones are arranged randomly around the circumference of the eye and that clone sizes are normally distributed. Even if these assumptions are not true the 'corrected stripe number' is likely to be proportional to the number of coherent clones in the corneal epithelium (and hence proportional to the number of functional LSC clones). Thus the corrected stripe number provides a useful comparative measure even if absolute numbers are not accurate.

Fig 1.7 demonstrates how Collinson et al (2002) used the correction factor 1/(1-*p*) to calculate the number of corrected stripes in X-inactivation *LacZ*-mosaic mice. Using photographs of X-inactivation *LacZ*-mosaic eyes the group counted the total number and total width of the *LacZ*-positive and negative stripes. The total width of positive stripes was then expressed as a percentage of the circumference and the mean width of a *LacZ*-positive stripe calculated. This value is divided by 1/(1-*p*) to give the mean corrected stripe width, from which the number of corrected stripes can then be calculated. Analysis of X-inactivation *LacZ*-mosaics suggested that the number of coherent LSC clones maintaining the corneal epithelium decreased over time. X-inactivation mice at 10 weeks of age were shown to have around 102.39 ± 5.85 coherent clones whilst the number of clones at 20-24 weeks was 74.49 ± 5.17 (Collinson et al., 2002). The authors described a stochastic

mechanism of loss of LSC clones between 10 and 30 weeks of age and predicted that further clones may be lost as the animals aged further. A parallel was drawn with the stochastic mechanism of crypt purification in the small intestine of mosaics and chimeras (Ponder et al., 1985; Schmidt et al., 1988).

Collinson et al (2004b) investigated the effects of *Pax6*$^{+/-}$ on corneal development and LSC function. The authors compared corrected clone numbers at 15 and 28 weeks for wildtype (n= 17 and 27 respectively) and *Pax6*$^{+/-}$ (n = 12 and 27 respectively). Values for wildtype at 15 and 28 weeks were 85.04 $\pm$ 4.25 and 73.66 $\pm$ 4.32 respectively whilst values for *Pax6*$^{+/-}$ at 15 and 28 weeks were 46.43 $\pm$ 3.7 and 37.83 $\pm$ 3.97 respectively. Therefore *Pax6*$^{+/-}$ eyes had a significantly lower clone number than wildtype both at 15 and 28 weeks ($P < 0.00001$ in both cases) (Collinson et al., 2004a). This evidence implies either a change in the number of active LSC clones in the small-eye mouse or a change in their distribution, perhaps due to alterations in cell adhesion (Stoykova et al., 1997; Tyas et al., 2003), resulting in larger clones. Centripetal migration seemed to be disrupted in these animals and fewer larger coherent corneal epithelial clones were observed. However centripetal migration and striping morphology was restored in *Pax6*$^{+/+}$ $\leftrightarrow$ *Pax6*$^{+/-}$ chimeras. In these animals *Pax6*$^{+/-}$ cells were under-represented in the corneal epithelia, suggesting that these cells were cell autonomously depleted or were less efficient than *Pax6*$^{+/+}$ cells at populating the tissue. Taken together these results suggest that correct Pax6 dosage is required for clonal growth during development but that perhaps the cues that organize centripetal migration are cell nonautonomous (Collinson et al., 2004a).

A

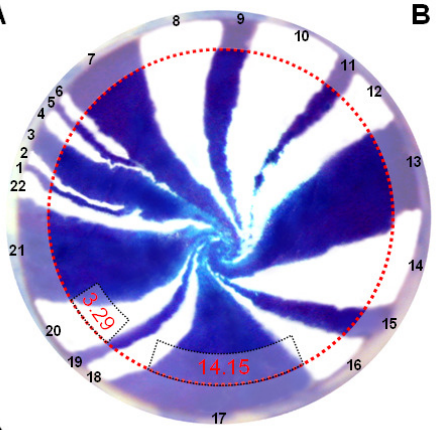

B

Measurements:

Blue Stripes		White Stripes	
Number	Width	Number	Width
1	0.58	2	1.52
3	3.24	4	0.80
5	0.89	6	1.23
7	6.26	8	0.91
9	2.93	10	6.10
11	1.94	12	7.15
13	9.19	14	3.87
15	3.14	16	7.09
17	14.15	18	4.17
19	1.15	20	3.29
21	8.70	22	4.70
Total	**52.17**	**Total**	**40.83**

C

Calculation:

Total circumference	=	52.17 + 40.83	=	93.0
Percentage of blues stripes	=	(100/93.0) x 52.17	=	56.1
Mean blue stripe width	=	56.1/11	=	5.1
1/(1-p)	=	1(1-0.561)	=	2.28
Corrected blues stripe width	=	5.1/2.28	=	2.24
Number of coherent clones	=	**100/2.24**	=	**44.7**

Figure 1.7: Calculating the number of coherent clones in the mouse corneal epithelium.

Assuming that stem cell clones are arranged randomly around the circumference of the eye and that clone sizes are normally distributed. The number of blue clones per blue stripe is predicted by the function 1/(1-p), where p is the proportion of blue clones. Using 1/(1-p), it is possible to estimate the number and width of clones from number and width of stripes, corrected for the proportion of *LacZ*-positive staining in the tissue. In this example of an eye from a 52-week old mouse, there are a total of 22 stripes with a combined circumference of 93.00 (arbitrary units). The combined length of all positive stripes is 52.17 (proportion = 0.56). As there are 11 positive stripes encompassing 56% of the circumference, the mean stripe width as a percentage of the circumference is 5.10. The value of 1/(1-p) is the reciprocal of 1-0.56 which is 2.28. The mean stripe width as a percentage of the circumference (5.10) is divided by this value to give the corrected stripe width which is 2.24. The corrected stripe number (44.7) is given by dividing the total circumference (100%) by the corrected stripe width (2.24). This is taken as an estimate of the number of coherent clones in the corneal epithelium and (by inference) an estimate of the number of active

clones of limbal stem cells. Although the estimate may not be numerically accurate it is very useful for comparing different experimental groups.

1.3.7 Effects of Pax6-depletion on maintenance of the corneal epithelium

Mice heterozygous for *Pax6* are viable but have small eyes, aniridia and a range of other ocular abnormalities including corneal opacification and cataracts in the later stages. These animals have a thinner corneal epithelium with fewer cell layers (Hogan et al., 1988). Human patients that are $PAX6^{+/-}$ suffer from a progressive corneal deterioration known as aniridia related keratopathy (ARK) causing chronic pain and leading to blindness (Mackman et al., 1979; Nishida et al., 1995). LSC deficiency has been implicated in this condition (Daniels et al., 2001), this is reinforced by the fact that transplantation treatment has better success when healthy limbal tissue rather than corneal tissue alone is transplanted (Holland et al., 2003).

Ramaesh et al (2003) evaluated corneal abnormalities in $Pax6^{+/-}$ small eye mice and compared them with human $PAX6^{+/-}$ individuals who suffered from aniridia related keratopathy (ARK). They concluded that the $Pax6^{+/-}$ small eye mouse was a good model for the features of ARK. Corneal anatomy and K12 phenotype were compared between $Pax6^{+/-}$ and $Pax6^{+/+}$ mice at foetal and postnatal time points. The group showed that prenatally and postnatally the $Pax6^{+/-}$ corneal epithelium was thinner and that the corneal stroma was thicker, hypercellular and irregular. In the $Pax6^{+/-}$ adult the ocular surface was roughened with some lens tissue evident in the stroma. Many adult corneas contained blood vessels and goblet cells. Older $Pax6^{+/-}$ animals exhibited an age related corneal degeneration with an increase in the number of goblet cells and a decrease in the level of K12 staining. This reduction in K12 staining may result in increased fragility of the epithelium, whilst the age related degeneration may result from poor wound healing responses and accumulated environmental insults (Ramaesh et al., 2003). The disrupted striping patterns reported by Collinson et al (Collinson et al., 2004a), reinforce the idea that the corneal defects described by Ramaesh et al (2003) may be a result of defective wound healing responses that divert cells from their normal centripetal migration.

1.4 AIMS

Aim 1: To refine the methods used for mosaic analysis of X-inactivation *LacZ*-mosaic mice in order to characterise the postnatal development of the corneal epithelium. In the absence of any adequate LSC markers, clonal analysis of striping patterns in the corneal epithelium may provide an insight into the arrangement and function of LSCs around the periphery of the tissue. The methods developed were used to test three hypotheses prompted by earlier work. The three central hypotheses were:

> **Hypothesis 1:** The number of active LSC clones declines throughout life.
>
> **Hypothesis 2:** Mice that express low levels of Pax6 have fewer active LSC clones and that these clones are further reduced by ageing.
>
> **Hypothesis 3:** Pax6 and Gli3 mutations interact to effect X-inactivation striping patterns.

Aim 2: To develop an accurate and reproducible image-analysis method for analysing X-inactivation *LacZ*-mosaic striping patterns in the corneal epithelium.

Aim 3: To combine the X-inactivation *LacZ*-mosaic system with an existing wound healing model in order to improve the analysis of corneal epithelial wound healing.

Aim 4: To further develop this system for imaging wound healing and striping patterns using whole-eye organ culture and time-lapse confocal microscopy in GFP mosaics.

Insights into the function of LSCs and a better understanding of corneal epithelial homeostasis and wound healing are important for the human conditions aniridia, ARK and RCE. It is only through an improved understanding of corneal epithelial dynamics that better therapeutic approaches can be developed to alleviate the considerable pain and suffering associated with these diseases.

Chapter 2
Mosaic Analysis of the Mouse Corneal Epithelium

2.1 INTRODUCTION

The mouse ocular surface is composed of corneo-limbal and conjunctival epithelia formed from the head surface ectoderm after invagination of the lens vesicle at around E11. Subsequently the corneal endothelium and then the corneal stroma are formed by two waves of neural-crest-derived mesenchymal cells that migrate centripetally between the lens vesicle and head surface ectoderm. (Smith, 2001). The fact that these tissues originate from distinct developmental lineages is highlighted by their Pax6 expression. While the ectoderm derived corneo-limbal/conjunctival epithelia, and lens express Pax6 throughout adult life, the corneal stroma and endothelium are negative for Pax6 in the adult (Koroma et al., 1997). The corneal epithelium undergoes much of its development postnatally (Collinson et al., 2002; Kuhlman and Resnik, 1958).

The conjunctival and corneo-limbal epithelia are dynamic self- renewing tissues. The conjunctival epithelium is supported by a population of stem cells whose location is still the subject of debate (Wolosin et al., 2004). However recent evidence suggests that conjunctival stem cells may be distributed throughout the tissue's basal layer (Nagasaki and Zhao, 2005). The corneo-limbal epithelium is maintained by a population of stem cells defined by their ability to retain thymidine analogues in classical label-retaining studies. These cells are confined to the basal limbus and termed limbal stem cells (LSCs), (Cotsarelis et al., 1989; Kruse, 1994; Ren and Wilson, 1996). The progeny of LSCs are TACs which undergo rapid proliferation followed by differentiation, migrating centripetally in the epithelium's basal layer (Buck, 1985; Kinoshita et al., 1981). For further background and discussion of these developmental and homeostatic mechanisms please refer to the introductory chapter.

Analysis of variegated patterns of mouse chimeras and mosaics is useful for the investigation of developmental lineages and cell mixing during development (Iannaccone et al., 1988; Ng and Iannaccone, 1992; West, 1978; West, 1999). One such system makes use of female X-inactivation mice hemizygous for an X-linked *nLacZ* transgene. These animals are mosaic in all tissues due to random X-inactivation during development (Tan et al., 1993). In the corneal epithelium of X-inactivation mosaics, a pattern of randomly dividing cells is replaced by an ordered pattern of radial stripes over the first 12 postnatal weeks (Collinson et al., 2002). This pattern is thought to represent chords of clonally related cells migrating inwards from LSCs surrounding the epithelium (Beebe and Masters, 1996; Collinson et al., 2002; Cotsarelis et al., 1989).

These X-inactivation striping patterns can be quantified to give an estimate of the number of coherent clones of limbal stem cells maintaining the corneal epithelium. This 'corrected stripe number' is an indication of the number of 'coherent clones' of LSCs maintaining the corneal epithelium and probably reflects the number of 'functional clones' of LSCs. A 'coherent clone' is a single functional group of LSCs that are derived from a single progenitor and have remained contiguous throughout development. X-inactivation mice at 10 weeks of age were shown to have around 102.39 ± 5.85 coherent clones whilst the number of clones at 20-24 weeks was 74.49 ± 5.17 (Collinson et al., 2002). It is important to emphasise that while these numbers may be proportional to the number of functional LSC clones, they do not equate to the actual number of LSCs and representation of them in this context should be discouraged. However the values are useful comparatively for comparing clonal patterns. Collinson et al's estimate of the number of functional LSC clones may deviate from the actual value because the method of derivation assumes that clones are randomly arranged around the epithelium and that the clone sizes are normally distributed. However it is still a valid method for the comparison of striping patterns in animals of different ages and genotypes (West, 1999).

Transgene silencing is thought to be a stochastic mechanism that can occur during early development perhaps due to position-effect variegation where cell intrinsic factors affect the composition and extent of heterochromatin (Dobie et al., 1997). Pratt et al (1996) describe GFP-positive embryonic stem cells (ESCs) from which they subsequently derived a transgenic mouse line displaying reportedly ubiquitous GFP expression. This transgenic mouse uses the CAAG promoter, a fusion of the chick β-actin promoter and the cytomegalovirus (CMV) immediate early enhancer, to drive expression of a fusion protein between the microtubule associated protein tau and GFP that thus marks microtubules (Pratt et al., 2000). However despite its supposedly ubiquitous expression in many tissues, in the current study the animals were found to be mosaic in the corneal epithelium presumably because of position effect variegation (unpublished).

Dr Dirk-Jan Kleinjan produced a number of mouse transgenic lines incorporating a yeast artificial chromosome (YAC) from which GFP is expressed under the control of the human *PAX6* regulatory elements (personal communication). Despite the use of a YAC intended to avoid position effect variegation, these animals also demonstrated mosaic transgene expression in the corneal epithelium. However it is not clear whether this is due to transgene silencing or mosaic expression of endogenous Pax6 in this tissue. Homozygous and heterozygous animals are mosaic which rules out any mechanism of allelic exclusion. Although useful for experiments detailed elsewhere in this thesis, these animals only became available in 2003 after the majority of the work in this chapter was produced. Using GFPU mice that express GFP ubiquitously under a ß-actin promoter, Nagasaki et al. (2003) observed the formation of radial streaks of cells in the cornea. The streaks were composed of cells that expressed different levels of GFP, vortex patterns were frequently observed towards the centre of the tissue. Additionally clusters of GFP-high expressing cells were tracked over a period of 7 weeks to yield time-lapse sequences of their centripetal movement, on average cells migrated 26μm per day (Nagasaki and Zhao, 2003).

Much of the corneal epithelium's development and maturation occurs postnatally culminating in stratification of the corneal epithelium, restriction of α9-integrin positive/K12 negative cells to the periphery of the cornea (Norman et al., 2004; Pajoohesh-Ganji et al., 2004) and the emergence of striping patterns (Collinson et al., 2002; Nagasaki and Zhao, 2003). It is likely that the onset of limbal stem cell function coincides with these events. The mass of the eye increases significantly during this period (Gerido et al., 2003) and it maybe that prior to eye opening proliferative potential is retained by all corneo-limbal basal cells. The proliferative potential of the basal layer is exhausted during postnatal development as the tissue expands, stratifies and desquamation begins. Perhaps, in order to complete stratification and growth, LSCs are stimulated to divide in order to provide a sufficiently high number of TACs for tissue growth and maintenance.

2.1.1 Experimental Aims

The aim of this chapter was to use the power of mosaic analysis to further characterise the postnatal development of the mouse corneal epithelium. First it compares two mosaic systems (*LacZ* based X-inactivation mosaics and CAAG-GFP transgenic mosaics) to assess their suitability for clonal analyses and concludes that the X-inactivation *LacZ* mosaic is the most appropriate for the study of LSC function. In the absence of any good markers these patterns provide valuable insights into the distribution and function of LSCs. The nature of striping patterns in the adult corneal epithelium is examined in detail. The study addresses the transition from randomly orientated mosaics to radial striping patterns, which provides evidence about the onset of LSC function. The postnatal growth of these eyes is also investigated. Finally the study uses numerical analyses of striping patterns in the corneal epithelium to characterise their numbers and distribution. In the absence of any adequate markers these striping patterns provide an insight into the arrangement and function of LSCs around the periphery of the corneal epithelium. The validity and implication of this model are discussed.

2.2 MATERIALS AND METHODS

2.2.1 Animals

Three transgenic mouse reporter strains were used in this study. The H253 transgenic line (Tan et al., 1993), carrying an X-linked *nLacZ* transgene under the control of the housekeeping promoter hydroxymethylglutaryl-CoA, was obtained from the MRC Mammalian Genetics Unit, Harwell, UK.

XLacZ$^{+/-}$ mice are female mice hemizygous for X-linked *LacZ*. They are progeny of crosses between hemizygous H253 males (*XLacZ*$^{+/Y}$) and (C57BL/6 x CBA/Ca)F1 females.

CAAG-GFP transgenic mice were derived through embryonic stem (ES) cells. The CAAG promoter, a fusion of the chick β-actin promoter and the cytomegalovirus (CMV) immediate early enhancer, was used to drive expression of a TauGFP fusion protein and thus mark microtubules (Pratt et al., 2000).

PAX6-GFP transgenic mice were produced by microinjection of a yeast artificial chromosome (YAC) containing the human *PAX6* locus with the GFP reporter gene inserted into its ATG start codon (Dirk-Jan Kleinjan unpublished). All mice were killed by cervical dislocation.

2.2.2 X-gal staining of adult mouse corneal epithelium

Eyes dissected at 3 to 52-weeks after birth were fixed in 0.2% Glutaraldehyde solution in 0.1M sodium phosphate buffer (pH7.3), 2mM $MgCl_2$, 5mM EGTA, for 2 hours at 4^{o}C. Samples were then washed for 3 x 20 minutes at room temperature in a detergent wash solution containing; 0.1 M sodium phosphate buffer (pH 7.3), 2 mM $MgCl_2$, 0.01% (vol/vol) sodium deoxycholate, 0.2% (vol/vol) nonidet-P40. Eyes were stained overnight at 37^{o}C in X-gal solution containing; 0.1 M sodium phosphate buffer (pH7.3), 2 mM $MgCl_2$, 5mM

$K_4Fe(CN)_6$, 5 mM $K_3Fe(CN)_6$, 0.01% (vol/vol) sodium deoxycholate, 0.02% (vol/vol) nonidet-P40, 1mg/ml 5-bromo-4-chloro-3-indolyl-beta-D-galactopyranoside (X-gal, Sigma). After staining, eyes were washed for 2 x 15 minutes in PBS, then post fixed in 4% paraformaldehyde before washing a further 2 x 15 minutes in PBS, 15 minutes in 0.9% (wt/vol) saline and 15 minutes in 50% (vol/vol) ethanol in saline. Eyes were stored in 70% (vol/vol) ethanol.

2.2.3 Sectioning of *XLacZ*$^{+/-}$ mosaic eyes

Eyes were stained for *LacZ* expression as described above and then processed for wax embedding. 7μm sections were cut on a microtome and mounted onto standard microscope slides. The sections were first dewaxed in Histoclear (2 x 5 mins) and then dipped in 95% (vol/vol) Ethanol (1min). Sections were then counterstained by dipping in Eosin for 1 min, washing in tap water (5 mins) staining in 1% (wt/vol) Neutral Red solution (3 mins), slides were then rinsed in distilled water (2 x 1min) dehydrated by dipping in a graded Ethanol series (70% vol/vol, 95% vol/vol, 100% vol/vol) followed by Xylene (2 x 1 min) cover slips were mounted with DPX mounting medium. For quantification of positive and negative cells in the basal layer of the corneal epithelium, cells were scored on a Zeiss Axioplan2 microscope to determine the average number of positive and negative patches in sections from each time point.

2.2.4 Estimation of corrected stripe number

Once fixed and stained, whole eyes were photographed with a Nikon Coolpix 995 digital camera mounted on a Wild M5A dissecting microscope so that the entire radial pattern was visible. Mice were analysed at 15-52 weeks after birth. For analysis of the striping patterns in different regions of the corneal epithelium, a small suture was placed at the nasal side of the limbus before dissection to allow orientation of the eyes.

An estimate of the actual number of clones in the corneal epithelium of *XLacZ*$^{+/-}$ mice cannot be derived directly from the observed number of stripes, as two or more blue clones may sit adjacent to each other. The 'corrected stripe number' is therefore derived from the observed number of stripes by correcting for the percentage of *LacZ*-positive staining using the function 1/(1-*p*) as described in Chapter 1 of this thesis and in Collinson et al (2002).

Using Adobe Photoshop 7.0 a circle with a diameter 80% of that of the cornea was superimposed onto a picture of the eye in question. An estimate of the proportion of positive and negative staining for the whole cornea was calculated by measuring the length of blue and white epithelium along the circumference of this circle. The number of blue and white stripes cut by the circle was counted and the circumference calculated. Because pale blue stripes are contiguous throughout the depth of the epithelium (See Fig 2.3) they were regarded as blue clones for the purposes of this analysis. Therefore a blue stripe composed of one or more lighter and darker blue stripes was regarded as a single stripe. The average width of a *LacZ*-positive stripe as a proportion of the circumference was calculated from the above measurements, this number was then divided by 1/(1-*p*), where *p* was the proportion of positive staining in the epithelium. The corrected stripe number is derived by dividing the circumference by the 'corrected stripe width' and provides an estimate of the number of coherent clones in the epithelium.

Stripes may not be distributed evenly along the circumference of the epithelium. The above analysis would not recognise such a skew in distribution, if it were consistent in a population of eyes. Therefore to analyse the corrected stripe number for different regions of the corneal epithelium a slightly different approach was used. A suture was placed in the nasal region of the conjunctival epithelium before enucleation of the eye to allow its orientation. Following X-gal staining, each stripe was counted, measured and then classed as either; nasal, temporal or nasal-temporal (stripe overlaps divide) and as either; superior, inferior or superior-inferior. Separate calculations were then made to estimate corrected stripe widths for every stripe that

fell into each of the four classes. To correct for the fact that some stripes overlapped the divide between regions, the actual circumference was halved and this figure was divided by the corrected stripe width to give the corrected stripe number per region.

2.2.5 Whole-mount images

To produce whole-mount images of the entire ocular surface the eye was enucleated with the eyelid intact, the posterior segment and lens were then removed and for *LacZ* mosaics only the eyes were stained and fixed. Several radial cuts were then made in the cornea and conjunctiva and the tissue was flattened gently by placing a cover slip over the tissue before photographing. In case of CAAG-GFP mosaic corneas, eyes were simply enucleated and corneas dissected without any processing. Four radial cuts were made in the cornea and it was mounted on a standard microscope slide in PBS under a cover slip. Whole eye images of PAX6-GFP eyes were produced by suspending fixed eyes over the inverted lens of a Leica confocal microscope. Further details are outlined in the Materials and Methods section of Chapter 6.

2.2.6 Statistical analyses

Statistical analyses were performed using Microsoft Excel in the case of χ^2 and t-tests or Statview 5.0 statistical software in the case of analysis of variance (ANOVA). Where means were compared the error bars used are 95% confidence intervals. In the case of ANOVA; where the *P*-value was greater than 0.05, pair-wise post-hoc tests were used to look for a statistical difference between individual groups. These tests were the Bonferroni/Dunn test, Fisher's PLSD test and Scheffe test. To simplify the results described, where a difference was determined to be significant the ANOVA *P*-value and the Fisher's PLSD *P*-value is tabulated as this test is intermediate in its stringency between Bonferroni/Dunn and Scheffe. A statistician (Dr Anthea Springbett, Roslin Institute) was consulted for advice.

2.3 RESULTS

2.3.1 Evaluation of mouse mosaics as a system for clonal analysis

XLacZ$^{+/-}$ mosaic eyes, PAX6-GFP and CAAG-GFP corneas were imaged to compare striping patterns. Fig 2.1 A-C demonstrates typical eyes from these three mosaic systems. When the present study was begun in 2003, only CAAG-GFP and *XLacZ*$^{+/-}$ mosaics were available (Fig 2.1 A and B). Because GFP corneas had to be flat mounted the prospect of doing a clonal analysis was viewed as too technically difficult. Furthermore because GFP expression levels vary within stripes as well as between them (Figure 2.1 B) the system is not really appropriate for conducting a clonal analysis; a GFP-negative clone could be derived from a GFP-positive LSC clone. *XLacZ*$^{+/-}$ mosaics on the other hand demonstrate clear striping patterns. There are no negative patches within positive stripes and there is very little mixing at stripe boundaries. They can be photographed easily and cheaply without the need for a fluorescent microscope and once fixed the staining does not fade. Furthermore the degree of inactivation of the *LacZ* transgene is relatively constant within a given strain (Tan et al., 1993). PAX6-GFP animals (Fig 2.1 C) became available in 2006. At this time a method of imaging whole eyes on the confocal microscope was also developed. These mosaics appear to form well demarcated clones and may be appropriate for a clonal analysis.

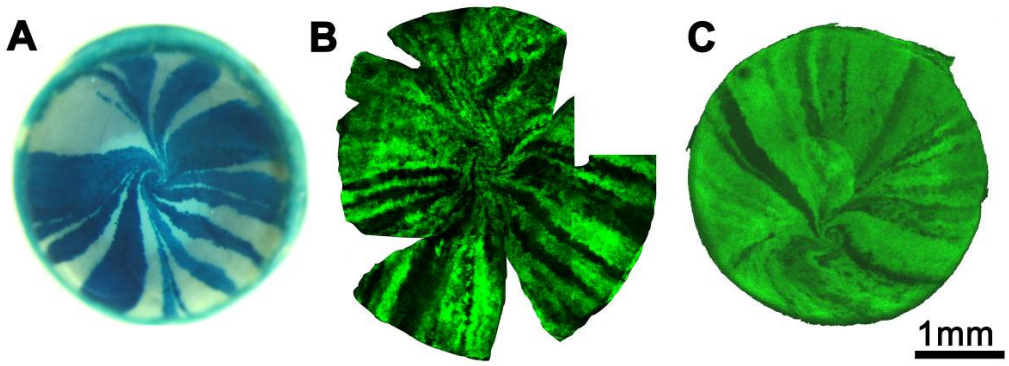

Figure 2.1 Representative images of three strains of mice exhibiting mosaic reporter expression in the corneal epithelium.

A: Female *XLacZ*$^{+/-}$ mosaic, X-Gal stained corneal epithelium. The animals are mosaic in all tissues due to random X-inactivation early in development. B: Flat-mount of a CAAG-GFP eye expressing TauGFP driven by the ubiquitous CAAG promoter. The degree of transgene expression is highly variable in the corneal epithelium. In this high expressing example individual stripes are not uniformly GFP-positive throughout. C: A PAX6-GFP eye expressing TauGFP on a yeast artificial chromosome (YAC) driven by the regulatory elements of the *PAX6* gene. While PAX6-GFP expression is mosaic in the corneal epithelium, on the whole stripes are either positive or negative although expression levels vary and the stripes are not as well demarcated as in A.

2.3.2 Striping Characteristics in *XLacZ*$^{+/-}$ mosaics

To examine the striping characteristics of *XLacZ*$^{+/-}$ eyes during their postnatal development and maturation, eyeballs were dissected between three and 52 weeks of age. Samples were stained with X-gal as outlined in the Materials and Methods section. Representative images of X-gal stained eyes from 3-52 weeks of age are shown in Fig 2.2. At 3 weeks of age eyes are composed of a randomly orientated mosaic of *LacZ*-positive and negative cells as reported previously (Collinson et al., 2002; Nagasaki and Zhao, 2003). As the eyes age striping patterns begin to arise. Orientated patches of centripetally migrating cells are first visible in the periphery of the cornea at around six weeks. By eight weeks striping patterns are much clearer and by ten weeks they are fully developed. It therefore appears to take 4-5 weeks for a stripe to become fully formed. By 15 weeks striping patterns are much clearer and are maintained at least up to 52 weeks of age. As reported previously, once stripes are fully formed, eyes often exhibit a whorl in the centre (Collinson et al., 2002; Nagasaki and Zhao, 2003).

LacZ-positive stripes have previously been shown to align vertically in the epithelium (Collinson et al., 2002). In this study a subset of eyes demonstrated paler *LacZ*-positive stripes both between two negative stripes but also within darker stripes. Figure 2.3 A demonstrates an eye with examples of a single pale blue stripe and a pale stripe within a darker patch (see asterisks in Fig 2.3 A). There could be two explanations for this variation in *LacZ* staining. It may be due to differential expression of the *LacZ* transgene within a single clone of LSCs that is then inherited along the lineage. Alternatively misalignment of the epithelial layers could allow a positive layer of cells to sit above or below a negative layer thus producing a stripe that appeared to be lighter in colour. To distinguish between these hypotheses the eye in question was sectioned and lightly counterstained with Neutral Red and Eosin. No examples of overlapping stripes were found in any of the sections.

Instead all pale blue cells appear to remain contiguous from the basal layer to the surface of the epithelium (Fig 2.3 B-D). As with the darker stained stripes all cells were closely aligned vertically and the boundaries between stripes were clear.

It is clear from previous reports that the boundary of the striping patterns is restricted to the limbal epithelium (Collinson et al., 2002). To observe this in more detail and to ascertain whether there were striping patterns in the conjunctival epithelium, whole-mount preparations of the entire ocular surface were made. Figure 2.4 demonstrates the typical staining pattern across the entire ocular surface. It is clear that striping occurs only in the corneal epithelium (Fig 2.4 B) and that stripes radiate inwards from the proposed LSCs that reside in the limbal region (Fig. 2.4 A). These data are consistent with an epithelium maintained by centripetally migrating cells with little mixing. There is no striping in the conjunctival epithelium (Fig 2.4 C) which is thought to be maintained by a separate population of stem cells present throughout its basal layer (Nagasaki and Zhao, 2005).

It is intriguing that spiral patterns are observed in *XLacZ*$^{+/-}$ eyes. In order to ascertain whether there was any prevalence of a particular striping phenotype or whether there was any agreement between the phenotype in the eyes of the same animal, a subset of eyes between 15 and 52-weeks postnatally were scored for the characteristics of their striping patterns. Fig 2.5 A demonstrates the three most common striping phenotypes. Eyes with clockwise and anticlockwise whorls were observed as well as eyes where stripes seemed to meet at a midline. Unfortunately the orientation of these eyes *in-vivo* was not recorded. A further set of eyes had striping patterns that showed none of these phenotypes clearly (for an example see Fig 2.2, 52 weeks). Fig 2.5 B demonstrates the percentage contribution of each of these 4 striping phenotypes at each time point. The predominant striping phenotype at 15 and 20 weeks was ‘unclear’. At later time-points eyes with a ‘whorl’ were the most common. Overall the majority of eyes demonstrated a clockwise or anticlockwise whorl that became more marked towards the centre of the eye. The prevalence of clockwise over anti clockwise

eyes was not significant. In a subset of eyes X-gal staining revealed stripes that appeared to meet at a midline with no obvious whorl in either direction. Figure 2.5 C demonstrates an analysis of the striping phenotypes of both eyes of individual animals. Each class (a-i) represents a different combination of phenotypes for left and right eyes. The number of animals in each class was scored and compared to predicted values calculated from the overall proportions of each phenotype. There was no significant association between the striping patterns observed in the left and right eyes.

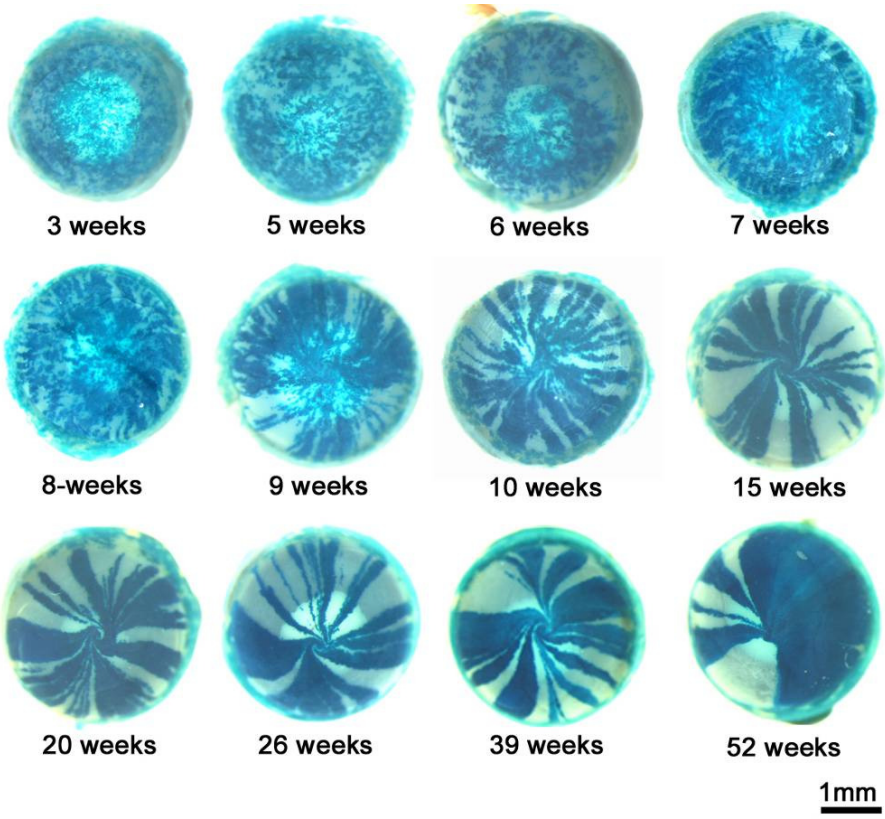

Figure 2.2: Striping patterns in *XLacZ*$^{+/-}$ mosaic corneas emerge at 6-10 weeks postnatally.

Patterns of X-gal staining in typical eyes from female *XLacZ*$^{+/-}$ mice at 3-52 weeks of age. Striping patterns begin to emerge at around 6 weeks postnatally. There is a switch from the randomly orientated positive and negative patches seen at 3-5 weeks to orientated stripes; fully formed by 10 weeks. The stripes represent chords of clonally related cells migrating centripetally from stem cells that are thought to reside in the limbal region of the eye.

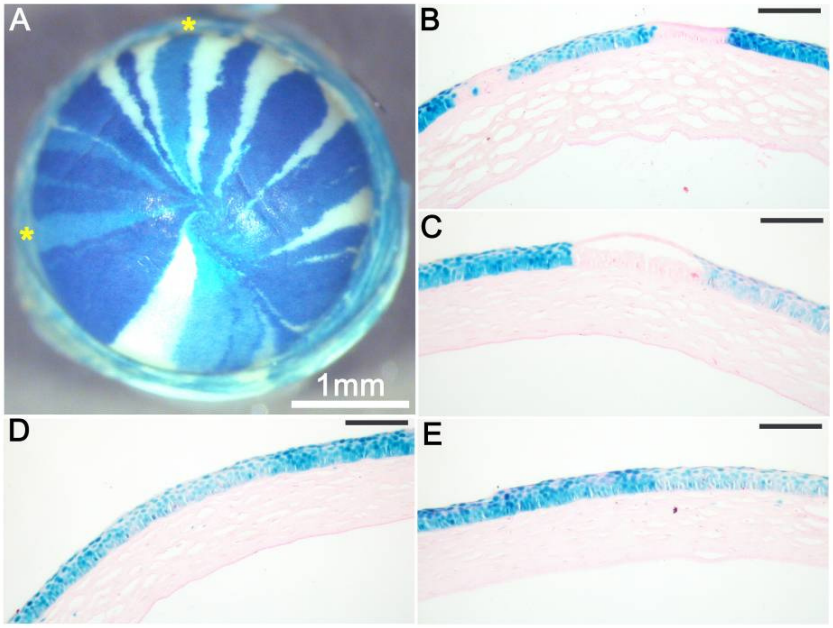

Figure 2.3: Pale *LacZ*-positive stripes observed in *XLacZ*$^{+/-}$ eyes span the entire thickness of the epithelium.

Occasionally *LacZ*-positive stripes appeared lighter. These stripes were observed between *LacZ*-negative stripes and between *LacZ*-positive but darker stripes (stars in A). The eye in A was sectioned (B-E). Sections were lightly counterstained with Neutral Red and Eosin. *LacZ*-positive stripes were aligned vertically within the epithelium (B-C). Pale stripes were observed both individually (B-C) and within darker stripes (D-E). When lightly stained stripes were located within darker stripes they still appeared to align vertically (D-E). Scale bars, 100 microns.

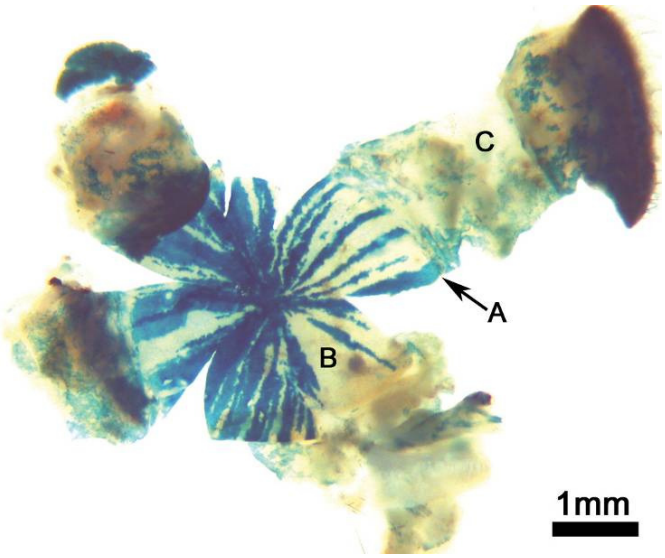

Figure 2.4: Whole-mount image of the entire ocular surface of an *XLacZ*$^{+/-}$ mosaic.

An *XLacZ*$^{+/-}$ eye was enucleated with the eyelids intact, the posterior segment and lens were then removed and several radial cuts were made in the cornea and conjunctiva to allow the tissue to be flattened. Stripes extend inwards from the edge of the limbus (A) to the centre of the corneal epithelium (B). There is no striping in any region of the conjunctival epithelium (C).

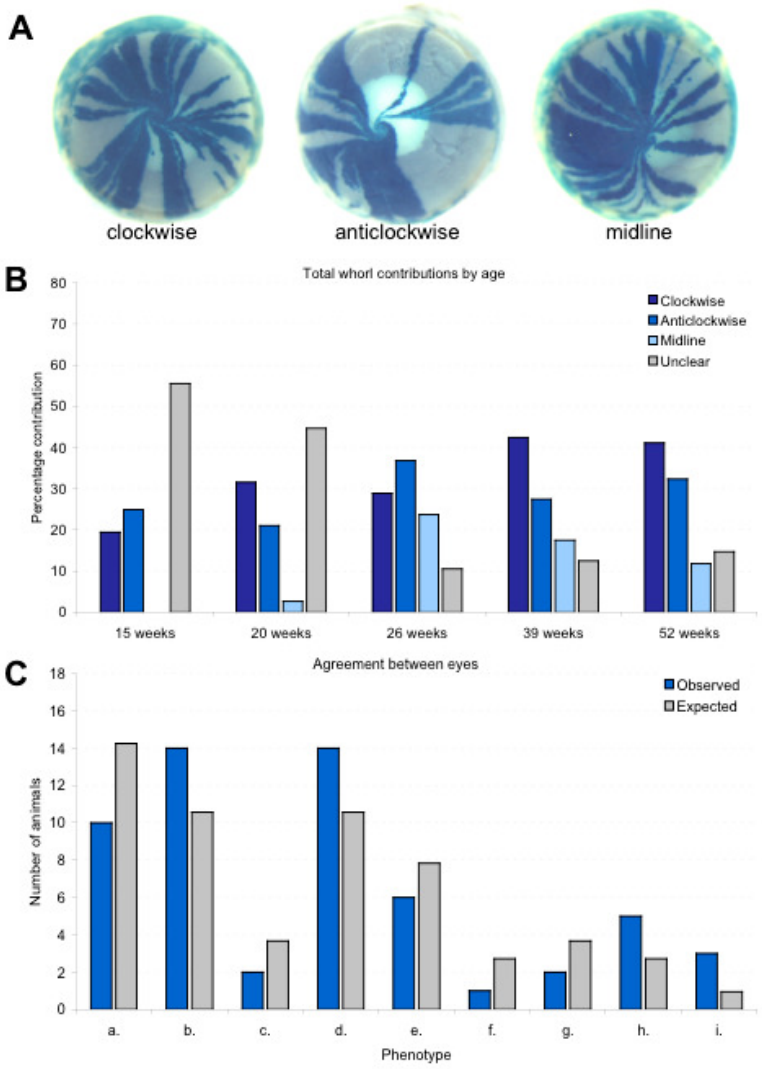

Figure 2.5: Analysis of the frequencies of striping phenotypes in *XLacZ*$^{+/-}$ mosaic corneal epithelia.

A: Eyes were classed as having either a clockwise or anticlockwise whorl, a midline or no clear pattern. B: Clockwise whorls were the most common pattern followed by anticlockwise whorls the next most common group was unclear followed by eyes with midlines. A comparison of the frequencies of clockwise and anticlockwise whorls (n = 61 and 53 eyes respectively) showed no significant difference in the prevalence of clockwise whorls ($\chi 2$ $P = 0.45$). C: Comparison of observed and expected frequencies of combinations

of whorl phenotypes in left and right eyes of all mice studied. No association was seen between the phenotypes of the left and right eye ($\chi 2$ test $P = 0.12$). a, clockwise (Left) ± clockwise (Right); b, clockwise (L) ± anti clockwise (R); c, clockwise (L) ± midline (R); d, anticlockwise (L) ± clockwise (R); e, anticlockwise (L) ± anticlockwise (R); f, anticlockwise (L) ± midline (R; g, midline (L) ± clockwise (R); h, midline (L) ± anticlockwise (R); I, midline (L) ± midline (R). Expected values were calculated from the overall proportions of clockwise, anticlockwise and midline phenotypes in all eyes. Animals with unclear patterns were excluded.

2.3.3 Postnatal growth of the *XLacZ*$^{+/-}$ mosaic mouse eye

To investigate the growth of the mouse eye, *XLacZ*$^{+/-}$ eye mass was compared at time points between 3 and 52-weeks. A growth curve was prepared by plotting mass (all *XLacZ*$^{+/-}$ mice are females) against age (Fig 2.6 A). Surprisingly mean eye weight continued to increase throughout adult life. The increase between 3-weeks and 6-weeks was the greatest. When the rate of growth was calculated between each time point it was clear that the period of fastest growth was between three and ten weeks of age. Although the pattern is clear, outliers were generated for data points that did not represent an increase in mass between time points, these are marked as red in the graph (See Fig. 2.6 B) There followed a decline in growth rate between 15 and 26 weeks of age, but the rate of growth never reached zero in the older time points. When comparing these results with the images in Figure 2.2 it becomes clear that the period of fastest growth coincides with the early postnatal period and the transition from patches to stripes. Furthermore once the stripes are fully formed by around 10 weeks the average rate of growth declines considerably.

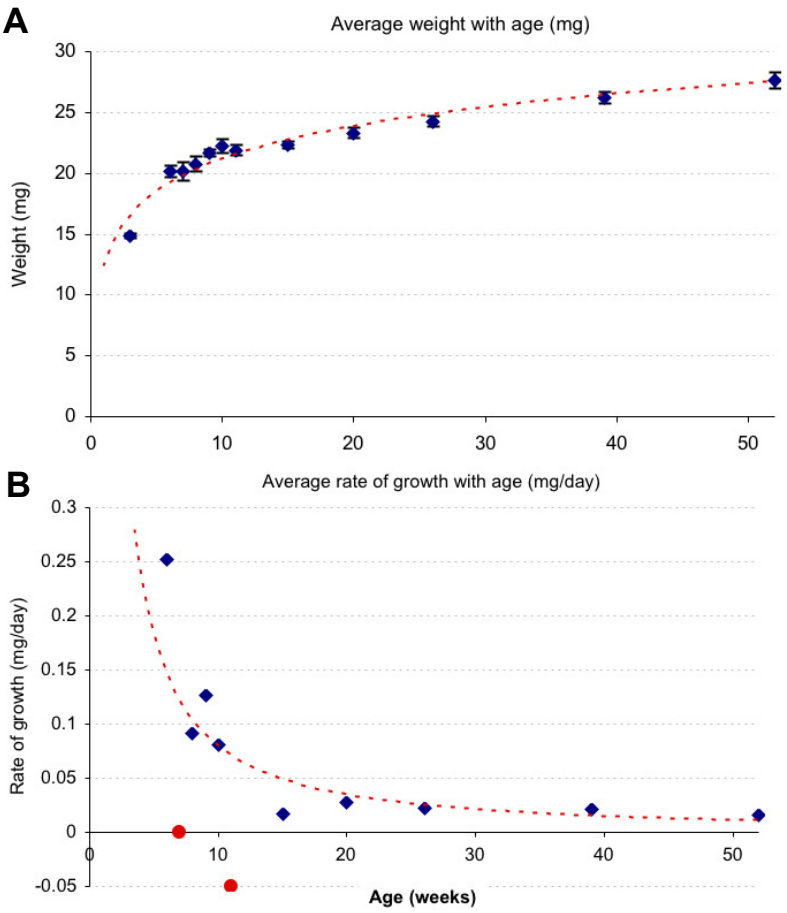

Figure 2.6: Change in average mass of *XLacZ*$^{+/-}$ mosaic eyes with age.

A: Average eye mass (wet weight) for female *XLacZ*$^{+/-}$ mosaic mice continues to increase throughout adult life; Average eye weight was 15mg at three weeks (n = 12 eyes) and 27mg at 52 weeks (n = 34), an increase of 12mg. The increase between 3-weeks and 6-weeks (n = 10) was the greatest with a change of 5mg. B: Accordingly the rate of growth is fastest between 3 and 10 weeks. Rate of growth plateaus between 26 and 52-weeks of age. Outliers are shown in red. Error bars, 95% confidence intervals.

2.3.4 The transition from patches to stripes between 3-10 weeks postnatally

In order to investigate the transition from randomly orientated patches to radial striping patterns described above, eyes were dissected and X-gal stained at 3 weeks (n = 3), 5-6 weeks (n = 3) and 10 weeks (n = 3). These eyes were then sectioned and the number of cell nuclei in basal patches of medial sections was scored for each age group. If stripes emerge in the basal layer of the tissue, the transition from random patches to stripes should be reflected by a reduction in the number of basal patches between 3 and 10 weeks. Figure 2.7 A shows a section of central cornea from a three week old *XLacZ*$^{+/-}$ mosaic with *LacZ*-positive (blue) and negative (red) nuclei in the basal layer. Figure 2.7 B demonstrates diagrammatically how we would expect the number of basal patches to decline between 3 and 10 weeks. The mean total number of basal cells in the corneal epithelium increased between 3 and 10-weeks, consistent with the tissue growth during this period shown in Figure 2.6. Over the same period the number of basal patches decreased significantly. These preliminary results are consistent with a switch from basal patches to stripes at around five to six weeks postnatally. Although time did not permit a more extensive study, the results show that this result is likely to be useful in the future. This analysis was kindly performed by Jayne Murphy (an honours student).

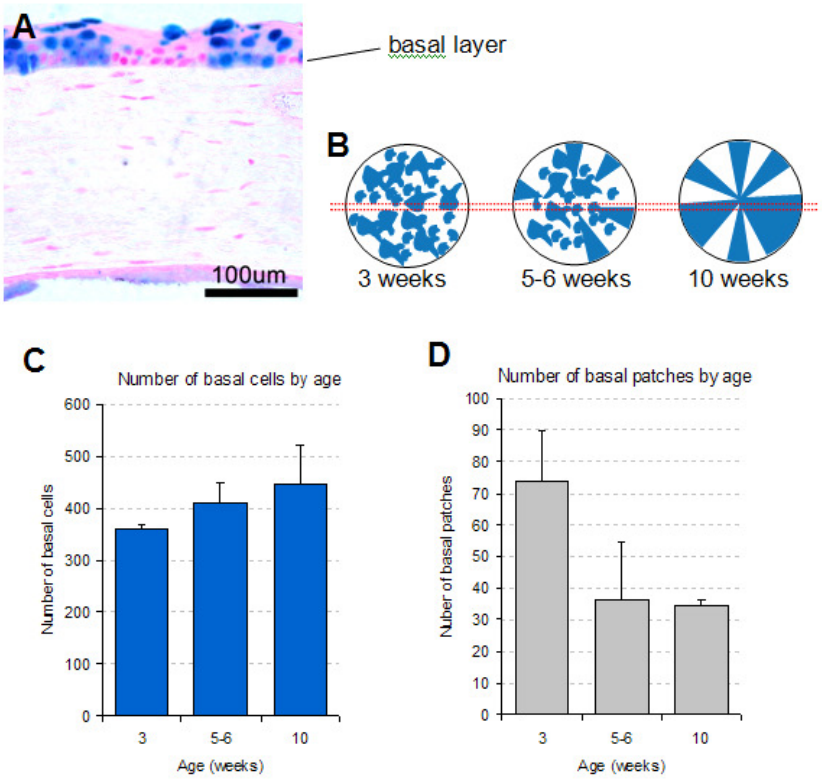

Figure 2.7: Comparison of the total number of patches and total number of cells in the basal layer of the corneal epithelia of *XLacZ*$^{+/-}$ mosaic mice.

A: A section through a 3-week *XLacZ*$^{+/-}$ mosaic. B: The middle sections were taken from eyes sectioned at 3 weeks, 5-6 weeks and 10 weeks (n = 3 for each time point). The number of cells and patches in the basal layer were scored along the entire length of the epithelium as described in the Materials and Methods section. C: The mean number of basal patches decreased from 74.00 ± 15.84 at three weeks to 36.33 ± 18.29 at five to six weeks and 34.66 ± 1.73 at ten weeks. D: The mean patch number at 3 weeks is significantly higher than the patch number at 5-6 and 10 weeks (t-test P = 0.038 and 0.0084 respectively). Error bars, 95% confidence intervals.

2.3.5 An age-related decline of corrected stripe number in *XLacZ*$^{+/-}$ mosaics

The corrected stripe number has been used previously as a method of estimating the number of active coherent clones of LSCs that replenish the corneal epithelium. It was shown previously that this number declined between 10 (n = 16) and 20-24 weeks (n = 8) from 102.39 ± 5.85 (mean ± standard error) to 74.49 ± 5.17 coherent clones (Collinson et al., 2002). To study this decline in more detail and determine whether it continues beyond 24 weeks corrected stripe numbers were calculated for female X-inactivation mice at 5 time points between 15 and 52-weeks, results are summarised in Figure 2.8. Tables 2.1-2.2 summarise the outcome of a statistical analysis of these results. If a comparison by one-way analysis of variance (ANOVA) yielded a significant result, further pair-wise, post-hoc tests were conducted as described in the Materials and Methods section. Only the Fisher's PLSD *P*-value is quoted here for simplicity. The corrected stripe numbers were calculated as described in the Materials and Methods section. Figure 2.8 A shows a marked reduction in corrected stripe number between 15 and 39 weeks of age with no further reduction up to 52 weeks. When tested by one-way ANOVA this data set showed a significant difference between values. Further post-hoc tests revealed significant differences between the 15 and 20-week groups and the 26 to 52-week groups (Table 2.1). There was no significant difference between the 39 and 52-week groups. In order to rule out differential transgene expression as an explanation for this decline, the proportions of positive and negative stripes were also calculated. Figure 2.8 B demonstrates that there was no change in the percentage of *LacZ*-positive cells contributing to the corneal epithelium over the same time points, this was confirmed by one-way ANOVA, which showed no significant difference in the data-set (Table 2.2). Note that in all cases the proportion of *LacZ*-positive cells contributing to the epithelium is greater than 50%. There are two principal reasons why this may be the case. Firstly there is an asymmetry in the ability to detect a white stripe on a blue background when compared to detecting a blue stripe on a white background that may bias the results.

Secondly X-inactivation may not be entirely random, for example the X controlling element (*Xce*) has three alleles termed Xce^a-Xce^c in mice. The relative strengths of these alleles are $Xce^a > Xce^b > Xce^c$, an X carrying a stronger allele has an increased probability of remaining active when paired with a weaker allele (Cattanach et al., 1969; Percec et al., 2002). The *Xce* genotype of the mice used in this study is not known.

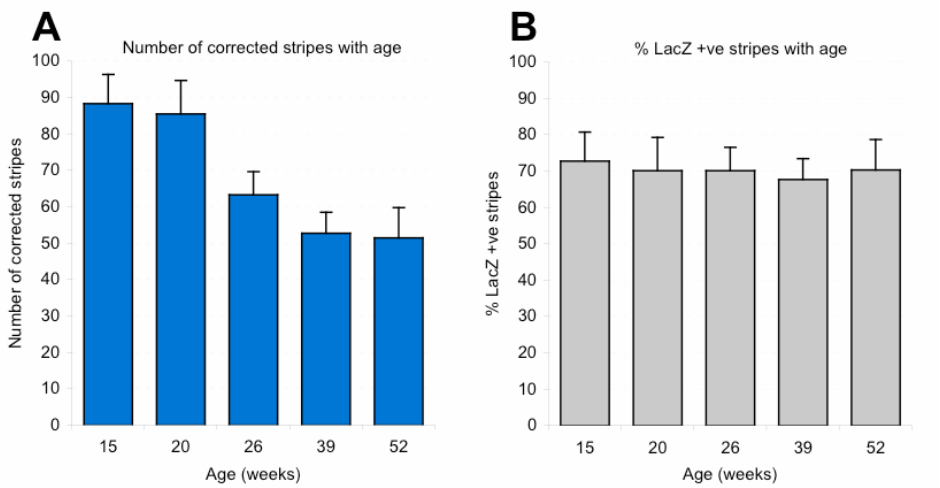

Figure 2.8: Effect of age on the corrected stripe number and the percentage contribution of *LacZ*-positive cells to the corneal epithelium.

Corrected stripe numbers at 5 time-points were calculated as described in the Materials and Methods section. A: A significant reduction is evident between 15 and 39 weeks of age form 84.33 ± 8.06 to 52.71 ± 5.79 (ANOVA P <0.0001, Fisher's PLSD P <0.0001) with no further reduction between 39 and 52 weeks of age (Fisher's PLSD P = 0.8224). B: There was no change in the percentage of *LacZ*-positive cells contributing to the corneal epithelium over the same time points (ANOVA P = 0.8194). Error bars, 95% confidence intervals.

Table 2.1: Analysis of the effects of age on corrected stripe number.

Age	Test	Corrected Stripe Number ± 95% CI	*P*-value
15-weeks (36); 20-weeks (38); 26-weeks (38); 39-weeks (40); 52-weeks (34)	One-way ANOVA	See below	<0.0001
15-weeks 'vs' 20-weeks	Fisher's PLSD	84.33 ± 8.06 'vs' 85.53 ± 9.18	0.6107
15-weeks 'vs' 26-weeks	Fisher's PLSD	84.33 ± 8.06 'vs' 63.26 ± 6.41	<0.0001
15-weeks 'vs' 39-weeks	Fisher's PLSD	84.33 ± 8.06 'vs' 52.71 ± 5.79	<0.0001
15-weeks 'vs' 52-weeks	Fisher's PLSD	84.33 ± 8.06 'vs' 51.48 ± 8.29	<0.0001
20-weeks 'vs' 26-weeks	Fisher's PLSD	85.53 ± 9.18 'vs' 63.26 ± 6.41	<0.0001
20-weeks 'vs' 39-weeks	Fisher's PLSD	85.53 ± 9.18 'vs' 52.71 ± 5.79	<0.0001
20-weeks 'vs' 52-weeks	Fisher's PLSD	85.53 ± 9.18 'vs' 51.48 ± 8.29	<0.0001
26-weeks 'vs' 39-weeks	Fisher's PLSD	63.26 ± 6.41 'vs' 52.71 ± 5.79	0.0503
26-weeks 'vs' 52-weeks	Fisher's PLSD	63.26 ± 6.41 'vs' 51.48 ± 8.29	0.0360
39-weeks 'vs' 52-weeks	Fisher's PLSD	52.71 ± 5.79 'vs' 51.48 ± 8.29	0.8224

Numbers in parentheses are the number of eyes analysed.

Table 2.2: Analysis of the effects of age on percentage contribution of *LacZ*-positive cells.

Age	Test	% *LacZ*-positive Number ± 95% CI	*P*-value
15-weeks (36); 20-weeks (38); 26-weeks (38); 39-weeks (40); 52-weeks (34)	One-way ANOVA	72.69 ± 5.14; 70.07 ± 6.8; 70.14 ± 4.75; 67.64 ± 5.67; 70.34 ± 5.88	0.8194

Numbers in parentheses are the number of eyes analysed.

2.3.6 Measurement of corrected stripe number in different regions of the eye

Recent reports of an uneven distribution of α9-integrin, a proposed TAC marker, to the nasal-temporal axis of the limbo-corneal epithelium (Pajoohesh-Ganji et al., 2004) imply a bias in the distribution of TACs and therefore perhaps LSCs. An experiment was therefore designed to determine whether this implied bias in the distribution of LSCs was reflected by a bias in the distribution of coherent clones of limbal stem cells around the circumference of the eye in *XLacZ*$^{+/-}$ mosaics. A subset of *XLacZ*$^{+/-}$ mosaic eyes (n = 15) were analysed in a way that allowed determination of the corrected stripe number for a given half of the eye in order to ascertain whether there was a bias in corrected stripe number. The corrected stripe number for the entire eye was also calculated for comparison. A suture was placed in the nasal region of the conjunctival epithelium before enucleation of the eye to allow its orientation (Figure 2.9 A). The eye was divided into 4 overlapping regions each representing half the circumference of the eye and demonstrated schematically in Fig 2.9 B. The results are summarised in Figure 2.9 and Table 2.3. There was no significant difference between corrected stripe numbers for the nasal and temporal regions or the superior and inferior groups, as expected all regions differed from the corrected stripe number for the whole eye (Table 2.3). There was no significant difference in the percentage of *LacZ*-positive cells between any group.

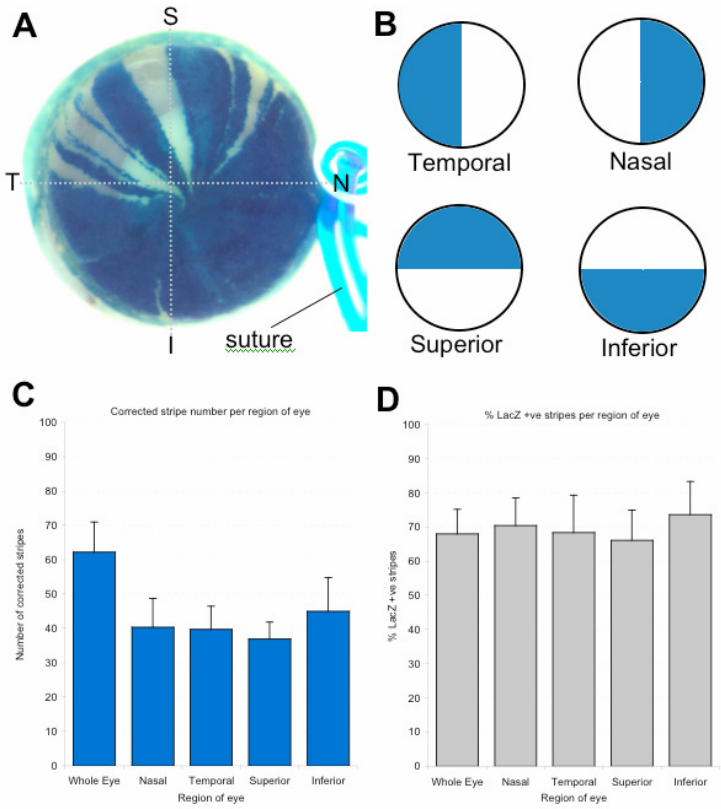

Figure 2.9: Comparison of corrected stripe number and percentage of *LacZ*-positive staining in four regions of the *XLacZ*$^{+/-}$ mosaic eye.

A: A suture was placed on the nasal side of the limbal region before dissection of *XLacZ*$^{+/-}$ mosaic eyes. B: A clonal analysis was performed on four regions of the cornea. If a stripe fell into two regions it was counted twice. C: There was no significant difference in corrected stripe number between the nasal and temporal or between the superior and inferior groups ANOVA $P = 0.0002$, Fisher's PLSD $P = 0.9126$ and 0.1615 respectively), all groups differed from the whole eye group (Fisher's PLSD $P < 0.05$ in all cases). D: There was no difference in % *LacZ*-positive cells between the nasal and temporal groups or the superior and inferior groups or between any group and the whole eye group (ANOVA $P = 0.8197$). N, Nasal; T, Temporal; S, Superior; I, Inferior; Error bars, 95% CI.

Table 2.3 Analysis of corrected stripe number in different regions of the mouse cornea

Region of Cornea	Test	Corrected Stripe Number ± 95% CI	*P*-value
Inferior (15); Superior (15); Nasal (15); Temporal (15); Whole (15)	One-way ANOVA	See below	0.0002
Inferior 'vs' Nasal	Fisher's PLSD	35.8 ± 8.8 'vs' 33.53 ± 6.36	0.4200
Inferior 'vs' Superior	Fisher's PLSD	35.8 ± 8.8 'vs' 30.37 ±4.56	0.1615
Inferior 'vs' Temporal	Fisher's PLSD	35.8 ± 8.8 'vs' 33.71 ± 5.94	0.3601
Inferior 'vs' Whole eye	Fisher's PLSD	35.8 ± 8.8 'vs' 62.29 ± 8.77	0.0036
Nasal 'vs' Superior	Fisher's PLSD	33.53 ± 6.36 'vs' 30.37 ±4.56	0.5478
Nasal 'vs' Temporal	Fisher's PLSD	33.53 ± 6.36 'vs' 33.71 ± 5.94	0.9126
Nasal 'vs' Whole eye	Fisher's PLSD	33.53 ± 6.36 'vs' 62.29 ± 8.77	0.0003
Superior 'vs' Temporal	Fisher's PLSD	30.37 ±4.56 'vs' 33.71 ± 5.94	0.6230
Superior 'vs' Whole eye	Fisher's PLSD	30.37 ±4.56 'vs' 62.29 ± 8.77	<0.0001
Temporal 'vs' Whole eye	Fisher's PLSD	33.71 ± 5.94 'vs' 62.29 ± 8.77	0.0002

Table 2.4 Analysis of percentage contribution of *LacZ*-positive cells in different regions of the mouse cornea

Region of Cornea	Test	% *LacZ*-positive Number ± 95% CI	*P*-value
Inferior (15); Superior (15); Nasal (15); Temporal (15); Whole (15)	One-way ANOVA	73.64 ± 9.73; 66.12 ± 8.83; 70.44 ± 8.11; 68.42 ± 10.91; 68.01 ± 7.20	0.8197

2.4 DISCUSSION

Following an evaluation of the *XLacZ*$^{+/-}$ mosaic and the CAAG-GFP mosaic systems, *XLacZ*$^{+/-}$ mosaics were chosen to investigate the postnatal development of the mouse corneal epithelium. Transgene silencing by X-inactivation occurs only once in a given developmental lineage thus yielding well defined clones of positive or negative cells in the corneal epithelium. This is not the case for CAAG-GFP mosaics which demonstrated distinct patches of negative cells within positive stripes in the corneal epithelium. This suggests that transgene silencing events, or fluctuations in expression levels may be common place in the adult epithelium. Such variability in expression makes CAAG-GFP mosaics less useful for studying lineage and doing clonal analysis than *XLacZ*$^{+/-}$ mosaics.

During early postnatal development *XLacZ*$^{+/-}$ mosaics show a randomly orientated patchwork of *LacZ*-positive and non-staining cells in the corneal epithelium. This pattern is replaced between 5 and 8 weeks of age with radial striping patterns that first emerge in the basal layer of the epithelium at 5-6 weeks postnatally. These patterns are fully formed by 10 weeks. The formation of radial striping patterns is consistent with previous reports in chimeras, X-inactivation *LacZ*-mosaics and GFP mosaics (Collinson et al., 2002; Nagasaki and Zhao, 2003). When *XLacZ*$^{+/-}$ eyes are sectioned, it is clear that a blue clone is aligned vertically in the epithelium consistent with the proposed mechanisms of migration and maturation for this tissue. Occasionally pale blue stripes are observed. Such stripes are entirely clonal as shown by sectioning and are probably due to differential regulation of the *LacZ* transgene in a heritable manner within that clonal lineage. Striping patterns observed in the corneal epithelia of *XLacZ*$^{+/-}$ mice are maintained into late adulthood. Patterns are always confined to the corneal epithelium and never extended into the conjunctival epithelium. The existence and emergence of these striping patterns is consistent with, and strongly supports, the maintenance of the corneal epithelium by centripetal migration from a peripherally located LSC population (Buck, 1985; Kinoshita et al., 1981). Furthermore the

temporal emergence of striping patterns indicate that LSCs become active at around 5 weeks postnatally.

The present study demonstrates that the mouse eye grows rapidly between three and ten weeks of age increasing in mass from a mean of 15mg to a mean of 21mg. These data are consistent with a previous report (although exact values may vary with strain) demonstrating an increase from 12mg at 2 weeks to 15mg at 4 weeks and 18mg at 6 weeks in control eyes (Gerido et al., 2003). The period of fastest growth is between three and ten weeks. This is consistent with growth curves of mean mouse body weight and mean tale length, which were demonstrated to increase dramatically between one and ten weeks of age at which point the rate of growth began to decline (Biggers and Papaioannou, 1991). These results are also qualitatively very similar to a growth curve of corneal diameter which demonstrated an increase from a mean diameter of 1mm at P0 to 3mm at P70 (Nagasaki and Zhao, 2003). Therefore striping patterns in the corneal epithelium become fully formed during the period of rapid eye growth.

It is of note that the patterns seen in the corneal epithelium at two to five weeks of age are qualitatively similar to the patterns observed in the adult conjunctival epithelium (See Fig 2.3), which has been shown to be maintained by a population of stem cells arranged throughout its basal layer (Nagasaki and Zhao, 2005). This suggests that between 3 and 5 weeks the cornea is expanding by random cell division throughout the tissue producing a randomly orientated mosaic and that between 5 and 10 weeks (with onset of LSC function) directional migration begins and striping patterns begin to form. No such switch appears to occur in the conjunctival epithelium. Accordingly α9-integrin a proposed early TAC marker is distributed throughout the corneal epithelium at three weeks but is restricted almost entirely to the limbal region by 10 weeks (Pajoohesh-Ganji et al., 2004). Undifferentiated cells identified through their lack of K12 expression are distributed throughout the corneal epithelium at P15 but are restricted to the limbal region by P90 (Tanifuji-Terai et al., 2006).

Furthermore EGFR (epidermal growth factor receptor) distribution changes postnatally. EGFR is an important marker of the proliferative cells in epidermis and is distributed throughout the cornea at P1 but restricted to the limbal region by P21 (Zieske and Wasson, 1993). Currently it is not known at which point LSCs are specified during development. Taken as a whole, the evidence presented here and in previous studies supports the idea of a switch from tissue maintenance by proliferation throughout the basal layer to maintenance by the progeny of LSCs at around five weeks postnatally, reflected in the subsequent emergence of striping patterns.

The whorling patterns observed in this study are consistent with earlier work both X-inactivation *LacZ*-mosaics and $LacZ^{+/+} \leftrightarrow LacZ^{-/-}$ chimeras (Collinson et al., 2002), recent work on UGFP-mice (Nagasaki and Zhao, 2003) and also hurricane and vortex keratopathy in humans, (Bron, 1973; Chong et al., 1997; Clinch et al., 1992). Hurricane keratopathy presents as a distinct whorling pattern on the corneal surface, corresponding to high cell turnover revealed by fluorescein staining. In vortex keratopathy the intracellular deposition of substances such as iron or drug metabolites reveals a similar pattern (Dua and Gomes, 2000). The recent mouse studies confirm that such patterns are a reflection of the normal apical migration of cells rather than a consequence of the disease state. The patterns seen may be dynamic and change over time, while *LacZ* staining can only reveal the pattern at one time point.

It is interesting that in the human diseases the majority of whorls seen are clockwise. In a study of hurricane keratopathy seen in eyes with corneal grafts and in contact lens wearers, 89% of whorls were clockwise (Dua and Gomes, 2000). In the current study, of 186 eyes examined 33% were clockwise and 28% were anticlockwise, if all other patterns are excluded 54% of eyes exhibited a clockwise whorl and 46% anticlockwise (although this difference was not significant). There was no prevalence of one striping pattern over another and there was no link between the patterns found in the two eyes of the same animal. This

implies a stochastic method of formation dependent on the kinetics of cell movement and their environmental modulators and determined randomly. The prevalence of unclear striping patterns at the two early time points probably reflects natural variation in the time it takes for the patterns to become fully formed. Dua et al., (1996) suggests that the whorling patterns observed are due to the influence of magnetic fields; in a culture system for human explants 11 clockwise and 4 anticlockwise whorls were induced by magnetic fields (Dua et al., 1996). However this did not represent a migration of cells but rather a reorganisation of cultured sheets of cells, it is unclear whether any such forces influence cell migration in the adult eye. It has recently been demonstrated however that wound healing responses in the adult cornea can be directed by electrical fields (Zhao et al., 2006b). Alternatively it may be that the continuous migration of progeny from the limbus with little cell mixing creates an area of collision where colliding stripes wrap around each other as originally suggested by Bron (1973).

XLacZ$^{+/-}$ mosaic mice exhibit a marked reduction in the number of corrected stripes between 15 and 39-weeks of age from around 90 to around 50, no further reduction was seen up to 52-weeks of age. This pattern suggests that the number of functional LSC clones is reduced to a level sufficient to maintain the epithelium at 39 weeks of age and that perhaps no further decline is biologically acceptable. Much pathology is associated with LSC deficiency (Daniels et al., 2001) and it seems likely that homeostatic mechanisms must have evolved to prevent loss below a threshold level which may be 50 coherent clones on this genetic background. It is not known whether the decline in corrected stripe number represents a reduction in the actual number of LSCs or perhaps an increase in the number of LSCs that remain in G0 and do not contribute TACs to the epithelium. However a reduction in the number of LSC clones that remain active is apparent.

Restricted cycling of adult stem cells may be important in preventing premature stem cell depletion. p21cip1/waf1 (p21) is a factor important for maintaining mouse haematopoietic

stem cells in a quiescent state whilst augmenting progenitor cell proliferation (Cheng et al., 2000). p21 has been shown to be present in corneal epithelium (Zieske et al., 2004). In the limbus LSCs may be preserved in G0 by p21 and only recruited into the proliferative compartment by the stress of corneal damage or depletion of the epithelium. The mixed progeny seen during the first 6-8 weeks in the mouse eye could be segregated into cells of varying proliferative potential and G0 stem cells by an increase in p21. This would drive any cell not in contact with the necessary survival factors (perhaps intrinsic to the limbus) in to the proliferative compartment. Gradually as more LSCs enter G0 the tissue will reach equilibrium where only the lowest number of LSCs required to maintain the tissue remain active. Peripheral TA populations have a greater capacity for replication than their more central counterparts. This is taken as evidence that the proliferative capacity of both stem and TACs can be modulated in response to injury (Lehrer et al., 1998). This may indicate that peripheral TACs have an important role in tissue maintenance and that the requirement of stem cells to leave G0 is an occasional event.

It may be biologically relevant for the number of active stem cells to decline in a tissue after their initial specification to avoid unnecessary cell divisions and the risk of mutation; perhaps LSCs enter replicative senescence after a certain number of cell divisions. A precedent for decline in the actual number of adult stem cells has been demonstrated in the formation of the small intestinal crypt in mice. Multi-potent progenitors make up a polyclonal intervillus region (IVR) in the foetus. However by the second postnatal week its architecture has changed to yield fully formed crypts (Calvert and Pothier, 1990). As the IVR develops into crypts a process of stem cell 'purification' occurs resulting in the conversion of polyclonal nascent crypts into monoclonal mature crypts (Schmidt et al., 1988; Winton and Ponder, 1990; Wong et al., 2000). Perhaps as the animal matures between 15 and 39 weeks of age the LSC niche becomes better defined and more restricted in a similar manner.

Evidence from other tissues suggests the finite number, as well as the competence of adult stem cells changes with age. In the human epidermis cultured keratinocytes may be classified as holoclones, paraclones or meroclones depending on their colony forming characteristics. Those with the greatest proliferative potential (holoclones) are thought to represent a population that includes putative epidermal stem cells. Paraclones on the other hand form abortive colonies and are thought to consist mainly of differentiated cells. Meroclones constitute a transitional class between stem cells and terminally differentiated cells, now thought of as TACs. Holoclones constitute around 30% of the total colonies formed when tissue is taken from a newborn child. When tissue is taken from adults over 64 years of age only 0-3% of cell colonies formed can be classed as holoclones (Barrandon and Green, 1987). This may represent a decline in the actual number of stem cells in the epidermis. However other evidence suggests that age related changes to the supporting stem cell niche or the ability of aging tissues to support renewal from otherwise healthy stem cells may also be a factor in the competence of the stem cell compartment, for review see (Rando, 2006). Similar work has been done in the corneal epithelium to demonstrate that corneo-limbal holoclones are restricted to the limbal epithelium (Pellegrini et al., 1999). In the light of the present study it would be interesting to determine whether the number of holoclones isolated from the limbus declines with age.

2.4.1 Conclusions

The current study has demonstrated that the *XLacZ*$^{+/-}$ mosaics system is appropriate for the characterisation of striping patterns in the corneal epithelium. Stripes were shown to emerge in the basal layer of the epithelium around 5-6 weeks postnatally. Such stripes are visible in whole eyes by around 8 weeks and are fully formed by 10 weeks. The majority of postnatal eye growth occurs in this 7-week period. It is likely that LSCs become active during this period to satisfy a greater demand for proliferative cells in the basal layer. When stripes are fully formed they align vertically in the epithelium. Although the majority of striping

patterns in the mouse eye are clockwise they appear to occur randomly and independently with respect to the accompanying eye. The corrected stripe number declines in a temporal manner, it takes 39-weeks of maturation for the corrected stripe number to reach the basal level of 50 at which point the decline ends. This is proposed to represent a decline in the number of functional LSC clones maintaining the epithelium.

Chapter 3
Development of a Computerised Image Analysis Method for Counting and Measuring Stripes in Mosaic and Chimeric Tissues

3.1 INTRODUCTION

The process of extracting information from an image, termed 'image analysis', is an extremely important tool for the biological sciences. Some problems can be resolved qualitatively by comparing images or critically viewing them. Human vision is excellent at determining subtle differences in shading, colour and texture. However it has not evolved to be proficient at the quantitative comparison of large numbers of similar images. It is for these purposes that computerised image analysis techniques have been developed. In the biological sciences image analysis problems are often best solved by semi-automated approaches that allow the computer to take care of the laborious quantitative tasks while allowing the operator to make key choices about the way the images are treated. Glaseby and Horgan (1994) defined image analysis in terms of five distinct sequential stages; display, filters, segmentation, mathematical morphology and measurement. Display describes the array of pixel values seen on a computer screen as a digital image. Filters are used to enhance digital images and remove noise. Segmentation is a method of dividing up an image into specific regions by grouping each pixel value into a particular class. Mathematical morphology uses specific groups of algorithms to study the size and shape of objects. Measurement is the final stage of image analysis at which quantitative information is extracted from the image. It is often particularly important to count the number of objects in an image and measure the distances between them (Glasbey and Horgan, 1994).

Tachi, C (1988) described a computerised semi-automated approach to analysing coat colour patterns in mouse chimeras. The approach was developed specifically to extract reliable quantitative information from coat pelts for statistical analysis. Images were captured on a computer from the output of a video camera mounted above the specimen. The author used software written in 8086 assembler language and Floating-point BASIC. This software allowed the extraction of data pertaining to the area and perimeter of the sample in the form of grey value histograms, profiles and maps, size distribution of connected figures in maps and mean absolute gradient as a texture measure of the image (Tachi, 1988).

As stated previously in Chapter 2, analysis of variegated patterns of mouse chimeras and mosaics have been useful both for investigations of developmental lineages and cell mixing during development (Iannaccone et al., 1988; Ng and Iannaccone, 1992; West, 1978; West, 1999) and for studies of the maintenance of the corneal epithelium by limbal stem cells (Collinson et al., 2002). A more detailed discussion of these studies is presented in Chapters 1 and 2 of this thesis. In some systems the variegated patterns appear as a 2-dimensional pattern of stripes that can be reduced to a linear array by drawing a line perpendicular to them. This approach has been used for radial stripes of descendant clones in the retinal pigment epithelium (West, 1978) and coherent clones in the corneal epithelium (Collinson et al., 2004b; Collinson et al., 2002), however no automated image analysis approach to this problem has ever been described. Collinson et al (2002) used Adobe Photoshop to measure stripe widths in the corneal epithelium and a detailed description and extension of this original analysis is described as part of the present work in Chapter 2. Briefly the method involved imposing a circle on an image of an X-inactivation *LacZ*-mosaic eye and using the ruler tool to measure the individual stripes. There are inherent difficulties in using this method and also comparing results produced by different researchers. Firstly the positioning of the circle is imprecise. Furthermore the decision as to what constitutes a positive or negative stripe is somewhat subjective and is likely to contribute to inter-user variation.

Female X-inactivation mosaics hemizygous for an X-linked *nLacZ* transgene, encoding the enzyme ß-galactosidase (In the present study termed $XLacZ^{+/-}$), are useful for analysis of such variegated patterns (Tan et al., 1993). Mosaicism occurs in all tissues due to random X-inactivation early in development. Cells expressing the ß-galactosidase enzyme appear blue after incubation with the enzyme's substrate X-gal, while non-expressing cells appear white. In the corneal epithelium distinct striping patterns form around 5-8 weeks after birth (Collinson et al., 2002). Figure 3.1 shows the right and left eyes from a typical $XLacX^{+/-}$ mosaic female at 20 weeks of age.

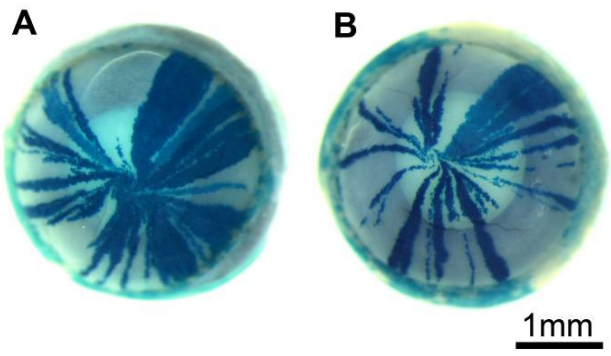

Figure 3.1: Striping patterns in X-gal stained *XLacZ*$^{+/-}$ mosaic eyes

Left (A) and right (B) eyes from a 20-week-old *XLacZ*$^{+/-}$ mosaic mouse, heterozygous for the X-linked *LacZ* transgene from strain H253. Stripes represent streams of clonally related cells migrating inwards from limbal stem cells at the periphery.

3.1.1 Patterned systems suitable for image analysis

3.1.1.1 Mosaicism in the corneal epithelium

Analysis of corneal stripes in X-inactivation mosaic mice may provide insights into limbal stem cell function because the number of coherent clones in the corneal epithelium probably reflects the number of functional clones of limbal stem cells. Previous studies used manual measurement of stripe widths in Adobe Photoshop (Collinson et al., 2004b; Collinson et al., 2002) and revealed a decrease in the corrected stripe number with age but the manual analysis was both time consuming and subjective. Chapter two describes in detail a clonal analysis of the number of coherent clones in the corneal epithelium. The number of coherent clones is reduced between 15 and 39 weeks of age with no change in the percentage of *LacZ*-positive cells contributing to the corneal epithelium over the same time points (Figure 2.8).

3.1.1.2 Mosaicism in the adrenal cortex

Morley et al., (1996) produced a transgenic mouse that expressed E. coli *LacZ* reporter gene under the control of a 6.4 kb 5'-flanking region of the 21-hydroxylase (21-OH) gene containing its promoter. As this gene is active throughout the entire adrenal cortex it was expected that *LacZ* would be expressed ubiquitously throughout the cortex. However the 21-OH/*LacZ* transgene exhibited striking variegated expression. In the adult gland, stripes extend from the outer cortex to the edge of the medulla. The authors suggested that these stripes represented cords of clonally-related cells migrating from the periphery towards the centre of the tissue (Morley et al., 1996). When these adrenals were compared to those of X-inactivation mosaics and chimeras, systems known to exhibit lineage specific expression of their transgenes, the patterns were qualitatively and quantitatively very similar (Morley et al., 2004). This work validated the 21-OH/*LacZ* mouse as a model system for the study of adrenocortical cell lineage. Furthermore a clonal analysis of striping patterns in the adrenal cortex using the method described for corneal epithelium (Collinson et al., 2002) was conducted. This analysis demonstrated that unlike the trend in the corneal epithelium (See Figure 2.8), there is no reduction in the number of corrected stripes (t-test $P = 0.2$) between 13 and 39 weeks of age, data provided by Ms S. Chang (PhD student jointly supervised by Dr J. D. West and Dr S. D. Morley). The cord-like patches observed in the adrenal glands of 21-OH/*LacZ* mice have been the subject of fractal analyses (Iannaccone et al., 2003). Having previously showed in rat aggregation chimeras that the development of liver parenchyma can be explained by iterated cell division rules (Khokha et al., 1994), the authors tested the hypothesis that cord like patches in the adrenal gland could be generated by a 'distinct but related set of iterated stereotypical cell division rules'. They demonstrated that foetal and adult adrenal patches are fractal but that they have a lower surface fractal dimension than those of adult liver. Therefore the authors conclude that adrenocortical patches are subjected to a constrained growth driven by a repetitive application of a specific stereotypical rule set.

They describe a 'nearest neighbour' mathematical model in which cell growth occurs at the edges of a patch, computer modelling using a constrained cell division algorithm produced patterns closely resembling adrenal patches (Iannaccone et al., 2003; Landini and Iannaccone, 2000).

3.1.1.3 Patterning in the somatosensory cortex

The term 'whisker barrels' was first coined by Woolsey and Van de Loos (1970). It refers to the discrete distribution of thalamocortical axon terminals (TCAs) and layer IV granule cells that form 'modules' in the primary somatosensory cortex of rodents. The spatial distribution of these patterns mirrors the spatial distribution of whisker and sinus hairs on the rodent snout (Woolsey and Van der Loos, 1970). Observations in a number of different mutant mouse models have demonstrated a disrupted organization in the distribution of TCAs, consequently these mutants do not demonstrate patterning and so barrels are absent from the neocortex (Erzurumlu and Kind, 2001). For example, animals lacking the RIIβ subunit of PKA demonstrate barrels, but the TCA densities in their walls are lower than in wildtype animals. There is a visible difference in the distribution of TCAs between RIIβ knock out (KO) and wildtype animals when tangential sections are stained for TCAs (Watson et al., 2006). Image analysis approaches to the identification and mapping of neurons in the cerebral cortex and in cell culture have been described previously (Hibbard et al., 1996; Narro et al., 2007). Hibbard et al (1996) described a suite of programs designed to digitize images of the cerebral cortex, identify immunolabelled cells and compute cell densities along local radial paths. The suite classified stained objects as cells or non-cell objects based on morphometric and grey-level texture features. Transcortical density profiles obtained by using the software suite and by manual cell counting were very similar (Hibbard et al., 1996). NeuronMetrics is software developed by Narro et al (2007) and designed to process images of primary neuronal cell cultures. It allows the quantification of 2D images of

fluorescently labelled cultured neurons. The programme uses the pre-processed image to create a Thresholded image and a Laplacian image which are then merged and skeletonised. This is followed by a number of steps to remove noise and fill in any gaps due to localised low fluorescence. The programme can then calculate, among other functions, the total neurite length, neurite branch number and the primary neurite number in a given image (Narro et al., 2007).

3.1.2 Use of ImageJ software for image analysis

This chapter describes the development of an image analysis approach (using the ImageJ software package) for the analysis of the striping patterns described in Chapter 1. Because there is very little comparable work using ImageJ to analyze striping patterns in mosaic tissues; a more general description of the application of ImageJ is included here.

ImageJ is an image processing software package designed by Wayne Rasband for the National Institute of Health (NIH), USA (Rasband, 1997-2006). It is a public domain program based around the Java programming language that can be downloaded free of charge. It handles most common image formats and can calculate area and pixel value statistics of user-defined sections. The majority of the programme's functionality is provided by separated modules called 'plugins' developed to perform specific sets of tasks and commands. Any series of core commands or commands defined in a plug-in can be recorded and then executed on demand using a 'macro'. The program can be calibrated to allow measurement in real world units such as millimetres (Rasband, 1997-2006). The reason the software is so powerful is that custom plugins for acquisition, analysis and processing can be developed using ImageJ's built in Java compiler. User-written plugins and macros make it possible to solve almost any image analysis problem. In particular the ability to record and manipulate the macro language is straightforward and highly flexible. ImageJ has been used to solve a range of image processing and analysis problems such as; point-counting of silt

particles in scanning electron micrographs (Ware, 2003), the interpretation of fluorescence resonance energy transfer (FRET) experiments (Stepensky, 2007), for the quantification of mRNA expression in osteocytes (Gluhak-Heinrich et al., 2007), to determine leukocyte adhesion to endothelial cells (Ulbrich et al., 2005) and to assess the immunolocalisation of proteins in confocal microscopy (Carmona et al., 2007).

Ware, C. I. (2003) used ImageJ to 'point count' silt in scanning electron micrographs. Briefly, silt samples from coastal dunes were impregnated with clear resin in plastic vials. The vials were then cut in half and polished. High resolution backscattered scanning electron microscope (SEM) images were recorded. The grey scale images were 'inverted' causing high atomic elements (HAE) to appear mid to dark grey and light atomic elements (LAE) to appear light grey. Areas were then calculated for HAE and LAE components. Elements touching the edge of the image were excluded. As a check of the results X-ray fluorescence was used, this showed a significant positive correlation (r^2 = 0.85) with the ImageJ-based method (Ware, 2003).

Fluorescence resonance energy transfer (FRET) allows the analysis of inter and intra-molecule interactions or intracellular processes. Stepensky et al (2007) developed an algorithm for the estimation of FRET by separating the FRET-positive pixels in an image from the background by applying user defined thresholds. The algorithm was incorporated into the FRETcalc plugin available for ImageJ for the calculation of FRET by acceptor photobleaching. The plugin's output options allow the quality and robustness of the results to be assessed using histograms and plots of donor, acceptor and FRET intensities in a particular region of interest (ROI). The resulting package offers real benefits over other FRET algorithms although its accuracy is dependent upon the shape of the organelle, degree of background noise and any image manipulations applied to the image (Stepensky, 2007).

Gluhak-Heinrich et al (2007) used a mouse tooth movement model of mechanical loading to study proteins associated with orthodontic mineralization and demineralisation. They showed that osteocyte specific mechanical stimulation of matrix extracellular phosphoglycoprotein (MEPE) was delayed when compared to dentin matrix protein 1 (DMP1). The authors used ImageJ to quantify the hybridisation signal from ^{32}P rUTP labelled RNA probes to MEPE and DMP1. The intensity of the hybridisation signal was determined in selected areas by measuring the intensity of silver grains in darkfield images. Three independent background values were averaged for normalisation. Using this method they demonstrated significant changes of MEPE mRNA in osteocytes associated with externally applied mechanical loading (Gluhak-Heinrich et al., 2007).

A rapid and easy assay for the determination of leukocyte adhesion to endothelial cells using ImageJ is described by Ulbrich et al (2005). The group adhered bovine polymorphonuclear neutrophils (PMN) and human Mono Mac 6 cells (MM6) to bovine aorta endothelial cells (BAEC) grown in monolayers on microtiter plates. They then challenged the cultures using a range of concentrations of TNFα and assessed the degree of adherence by counting the number of cells that remained adhered to the substrate. Images of the adhesion cultures were processed in ImageJ by converting the images to 8-bit greyscale, plotting the distribution of grey particles, thresholding and then counting cells using the 'particle analyzer' function. The method developed allowed high throughput screening of different test compounds (Ulbrich et al., 2005).

Carmona et al (2007) describe a simple macro developed for ImageJ that allows the visualisation of immunolocalised proteins in images taken using confocal microscopy. The macro was designed to split confocal images into red, green and blue channels using ImageJ's 'RGB split' command. The blue channel is discarded and the red and green channels merged using the application 'image calculator' with the option 'AND' finally the resulting image is inverted to produce greyscale images on a white background. This process

removes any extranuclear and background staining allowing easy visualisation of the nuclear signal. The authors propose that due to the simplicity of the method and the availability and cross platform nature of ImageJ, the method could be widely accepted as a standard for colocalisation studies (Carmona et al., 2007).

3.1.3 Experimental Aims

In this chapter the development of an image analysis tool for the one-dimensional analysis of two-dimensional tissue samples is described. This tool was designed to be a robust and easy to use method of estimating the number of patches in a mosaic tissue where the cell types are different colours. It was intended originally as a replacement for the laborious and time consuming Adobe Photoshop-based approach described in Chapter 2 and the references therein. It was designed with the user in mind, for ease of use, for increased speed and efficiency and to allow comparison of results between multiple users. Specifically it was designed to calculate the mean number of patches along a given selection in ImageJ and correct for the effects of random clumping. Although commercial solutions to some of these problems may be available it was desirable to produce a robust multiplatform approach using Freeware (ImageJ) and widely available (Microsoft Excel) software that could be used by anyone at little or no cost. Therefore the tool was developed using custom written ImageJ macros and an Excel spreadsheet. The spreadsheet was the workhorse of the system, a number of user defined modes and features allowed it to deal with many data types and produce different outputs. The application of this approach to reproduce a manually produced dataset on striping patterns in the corneal epithelium is first described. Issues of sensitivity, inter-user and intra-user variation are then discussed. Finally the system is applied to two other systems; to measure patch sizes in the adrenal cortex and to determine the degree of disorganization of TCAs in the whisker barrels of the neocortex.

3.2 MATERIALS AND METHODS

3.2.1 Animals

The H253 transgenic line, the production of *XLacZ*$^{+/-}$ mosaics and the staining of tissues from these animals are all described in the Materials and Methods section of Chapter 2.

21-OH/*LacZ* transgenic mice were produced by Morley et al (1996). The animals contain a 21-OH promoter/β-Gal reporter construct. This includes a 6.4 kb 5'-flanking region of the 21-OH gene driving *LacZ.* The mice studied here were hemizygous for the 21-OH/*LacZ* transgene and were male and female progeny of crosses between non transgenic (C57BL/6 x CBA/Ca)F1 females and 21-OH/*LacZ* homozygous males. Mice were killed by cervical dislocation and their adrenal glands were dissected and stained for β-galactosidase activity as described previously (Morley et al., 1996). Images of X-gal stained adrenal sections were kindly provided for the analyses described in this chapter by Ms Su-Ping Chang (PhD student, jointly supervised by Dr J. D. West and Dr S. D. Morley). All macros were written by the author and all analyses were done by Mr Douglas Gibson (a summer student) under the supervision of the author.

RIIβ knock out (KO) mice were produced by homologous recombination in embryonic stem cells (Brandon et al., 1997). In these animals the RIIβ regulatory subunit of the protein kinase A (PKA) gene was disrupted. The RIIβ KO mice were maintained at the University of Edinburgh on a C57BL/6J background. Mice were killed with a lethal injection of pentobarbital and then perfused with 0.1M phosphate buffered saline (PBS), pH 7.4, followed by chilled 4% (wt/vol) paraformaldehyde (PFA) in 0.1M PBS. Brains were removed post fixed for at least 6 hours in 4% (wt/vol) PFA, equilibrated in 30% (wt/vol) sucrose and then sectioned on a freezing microtome. Sections were stained with cresyl violet (Nissl) as described elsewhere (Watson et al., 2006). Images of Nissl stained sections were

kindly provided for the analyses described here by Ms Ruth Watson (PhD student, supervised by Dr Peter Kind).

3.2.2 Image capture

Ideally high quality TIFF format images would be used at all times. However as the image analysis solutions described in this chapter were applied retrospectively to banks of existing images this was not possible for images of eyes or adrenals. All images therefore were JPEG format with a resolution of 300 pixels/inch. Once fixed and stained, whole eyes were photographed with a Nikon Coolpix 995 digital camera mounted on a Wild M5A dissecting microscope so that the entire radial pattern was visible. Sections of X-gal and Neutral Red-stained adrenals were photographed with a Nikon Coolpix 995 digital camera mounted on a Leitz compound microscope, by Ms S. Chang. Nissl-stained sections of the barrel field of RIIβ KO mouse neocortex were photographed by Ms Ruth Watson at 62.5x using a Leica DMLB microscope, Leica 480 digital camera and Leica DMLB Image Manager 4.0. TIFF images were pseudo-coloured using Image Tool 3.0. It is anticipated that the use of TIFF images for all analyses would improve the accuracy of the techniques described in this chapter.

3.3 RESULTS

3.3.1 Development of a technique for measuring and counting patches

3.3.1.1 Conversion of intensity values into corrected patch numbers

All the solutions described in this chapter rely on the five stages of image analysis described by Glaseby and Horgan (Glasbey and Horgan, 1994) excluding mathematical morphology which was beyond the scope of this work. What all the solutions have in common is the need to convert the data extracted from the images (pixel intensity values) into measurements and statistics. This data consisted of a string of 'sample points' and their corresponding string of 'pixel intensities' taken along the selection (a one pixel-wide circular, linear or polygonal line) specified in ImageJ. Where specified a specific number of sample points was chosen along the selection, otherwise every pixel under the selection was sampled. It was found that the best way to implement and experiment with this approach was to design a flexible template in Microsoft Excel that allowed the analysis of a string of data points (limited to 5000 values for the purposes of this work) in a number of different ways. This 'ImageJ Patch Size Calculator' was developed as a universal tool for converting data from any ImageJ selection into patch size data, its main features are shown in Figure 3.2.

The spreadsheet was designed to import data from the clipboard, plot a graph of the values and then convert them into patch numbers, and perform the $1/(1-p)$ correction for random clumping described elsewhere (Roach, 1968; West, 1976). It also gives an estimate of the proportions of the positive and negative cell types. The spreadsheet was designed to assign a value to each data point depending upon whether it was above (output = 0) or below (output = 1) a specific threshold value in the range. The default value was the centre of the intensity range, however if required this could be overridden by the operator with a value of their choice to avoid problems of noise biasing the results. These thresholds are also plotted on the graph for ease of use. If the 'above' toggle is selected then the threshold value is set 10%

above the user entered value. If the 'below' toggle selected it is set as 10% below. This allows the user to set the threshold to the top or bottom of any noise in the graph. The computer then adds or subtracts 10% to avoid error.

The number of strings of 0's and 1's are counted to give the number of blue and white stripes. The total number of 0's gave the total width of the blue stripes and the total number of 1's gave the total width of white stripes. If the 'circular selection' toggle is selected the first and last stripes in the string are merged if they are the same colour. This take's account of the fact a circular string is being represented as a linear one and avoids the first patch to be sampled being counted twice. There are occasions when it may be appropriate to use a constant distance instead of the actual distance measured. For example if one was sampling many different images but could not control the length of each selection in ImageJ. One may want to standardize all values by asking "If the selection was of X-length how many corrected patches would there be?" If this is the case a constant value can be entered into the spreadsheet to override the actual distance measured. Finally the form also contains 4 macros assigned to buttons for ease of use. The first 3 are concerned with importing data into (Paste), saving the values in (Save) and clearing (Clear) the data input and summary sections. The 4th (Compile) exports a summary of all values calculated to a separate spreadsheet in the next available empty column. It is therefore possible to analyse many images in a series without the need to save any separate files, greatly speeding up the entire process.

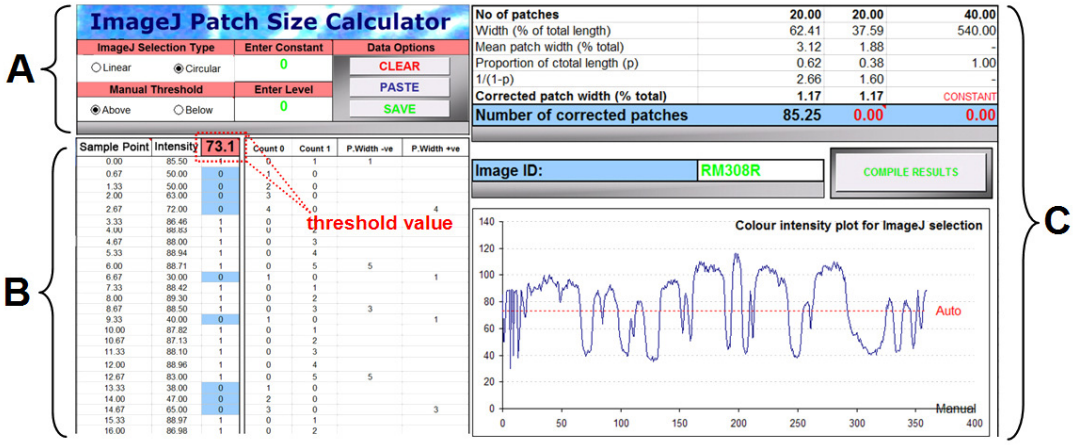

Figure 3.2: Screen shots of the main features of the ImageJ Patch Size Calculator.

A: Input section. Data is imported from the clipboard by clicking 'Paste'. At this point the data type is specified as being generated by a linear or circular selection in ImageJ. The option of using a constant value instead of the actual sample length is also available. Finally rather than relying on the spreadsheets automatic options the spreadsheet allows a researcher to threshold manually if required. B: The threshold value is automatically set as the middle of the intensity range (in this case 73.1). Each individual data-point is classed as blue or white depending on the threshold value. Finally these strings are counted. C: The output section calculates and displays the corrected patch number. An intensity plot is also produced to compare to the original ImageJ plot. The results can be 'compiled' to a second spreadsheet without leaving this window, enabling high throughput analysis of many images.

3.3.1.2 Analysis of Images of the corneal Epithelium with ImageJ

Each image was processed individually using ImageJ, a shareware image analysis software package (Rasband, 1997-2006). Figure 3.3 summarises the approach. The marquee tool was used to define a square that touched the edge of the epithelium at four points. This first step proved extremely important in providing reproducible results. Originally an automatic method of positioning the image was used, but this proved unreliable. Manual selection of the edge of the epithelium produced more accurate results with less variation.

One of 4 custom written macros was then used to convert the image to 8-bit greyscale and enhance the contrast. The macros then automatically cropped and resized the image, imposed a circle in the centre of the image, with a diameter equal to 80% of its width, and ran the 'Oval Profile Plot' plug-in (O'Connell, 2002). The 'Oval Profile Plot' plug-in takes the image region bounded by an oval region and samples at N equal angles around the oval. It can generate a number of plots, the one that is relevant here contains pixel values along the oval. The output of this sequence was a table of colour intensities around the circle's circumference, because the images were converted to 8-bit greyscale a value of 0 = black and a value of 255 = white. The number of sample points used around the circumference was varied from 180 (i.e. one measurement every 2 degrees) to 720 in the 4 separate macros (macro180 to macro720).

Macro180:

```
run("8-bit");

run("Enhance Contrast", "saturated=0.5  ");

run("Size...", "width=1000 height=1000 constrain ");

makeOval(100, 100, 800, 800);

run("Oval Profile" , "number=180 analysis='Along Oval' show");

run("Close");
```

Macro360:

```
run("8-bit");

run("Enhance Contrast", "saturated=0.5  ");

run("Size...", "width=1000 height=1000 constrain ");

makeOval(100, 100, 800, 800);

run("Oval Profile" , "number=360 analysis='Along Oval' show");

run("Close");
```

Macro540:

```
run("8-bit");

run("Enhance Contrast", "saturated=0.5  ");

run("Size...", "width=1000 height=1000 constrain ");

makeOval(100, 100, 800, 800);

run("Oval Profile" , "number=540 analysis='Along Oval' show");

run("Close");
```

Macro720:

```
run("8-bit");

run("Enhance Contrast", "saturated=0.5  ");

run("Size...", "width=1000 height=1000 constrain ");

makeOval(100, 100, 800, 800);

run("Oval Profile" , "number=720 analysis='Along Oval' show");

run("Close");
```

The corrected patch numbers were calculated from this data using the 'ImageJ Patch Size Calculator' described above. 'ImageJ Selection Type' was toggled to 'circular', the 'Manual Threshold' and 'Constant Fields' were left blank. Statistical analyses of the corrected stripe numbers were done using ANOVA in Statview 5.0 (Abacus Concepts Inc., Berkeley, USA). Statistical advice was kindly provided by Dr Anthea Springbett.

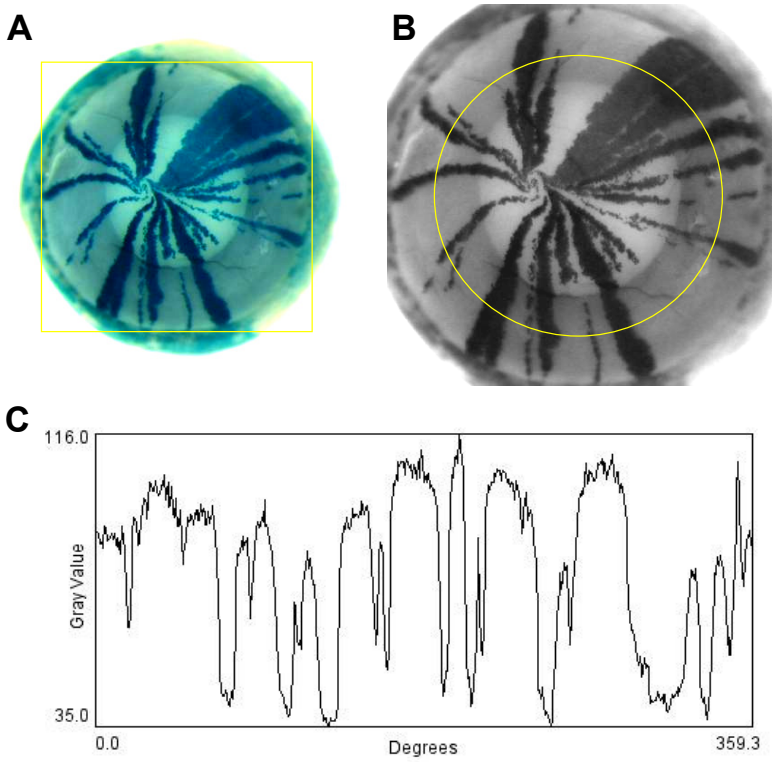

Figure 3.3: Analysis of *XLacZ*$^{+/-}$ mosaic corneal epithelial striping patterns in ImageJ.

A: The 'Rectangular Selection' tool was used to define the edge of the epithelium. B: The image was cropped, converted to 8-bit greyscale and the contrast enhanced, a circle was imposed at 80% of the cornea's diameter. C: Running the 'Oval Profile Plot' command gave an intensity plot along this circle. The data from the resulting graph was copied into the ImageJ Patch Size Calculator.

3.3.1.3 Analysis of images of the adrenal cortex with ImageJ

Because the size and shape of the adrenal gland varies so much between sections the approach described for analysis of the corneal epithelium is not appropriate. Instead, two macros were used to process and then extract data from the image. Figure 3.5 summarises the process. To introduce some consistency in the way the images were treated, the user manually orientated the adrenal gland so that its longest axis was horizontal. Then the marquee tool was used to define the edges of the gland (Fig 3.4 A). The image was cropped and re-sized so that the width was 1000 pixels, converted to 8-bit greyscale and the contrast enhanced (Fig 3.4 B). The user then defined the adrenal capsule with the 'polygon selection' tool (Fig 3.4 B). A second macro was run which then shrunk the polygon by 25 pixels so that it was far enough into the cortex not to impose on the junction between the zona-glomerulosa (zG) and the zona-fasiculata (zF) (Fig 3.4 C). It was then converted into a 'polyline' and the plot profile function was run (Fig 3.4 D). In contrast to the corneal epithelial work this method analysed every pixel under the selection due to the constraints of the ImageJ software. As no adrenal work on the corrected stripe number has yet been published it was not felt that a need to match the actual numbers measured by eye was necessary for comparison between different groups. The corrected patch numbers were calculated from this data using the 'ImageJ Patch Size Calculator' described above. 'ImageJ Selection Type' was toggled to 'circular', the 'Manual Threshold' and 'Constant Fields' were left blank.

Adrenal Macro1:

```
run("Crop");

run("8-bit");

run("Enhance Contrast", "saturated=0.5");

setTool(2);
```

Adrenal Macro2:

```
run("Enlarge...", "enlarge=-25");

getSelectionCoordinates(x,y);

makeSelection("polyline", x, y);

run("Plot Profile");
```

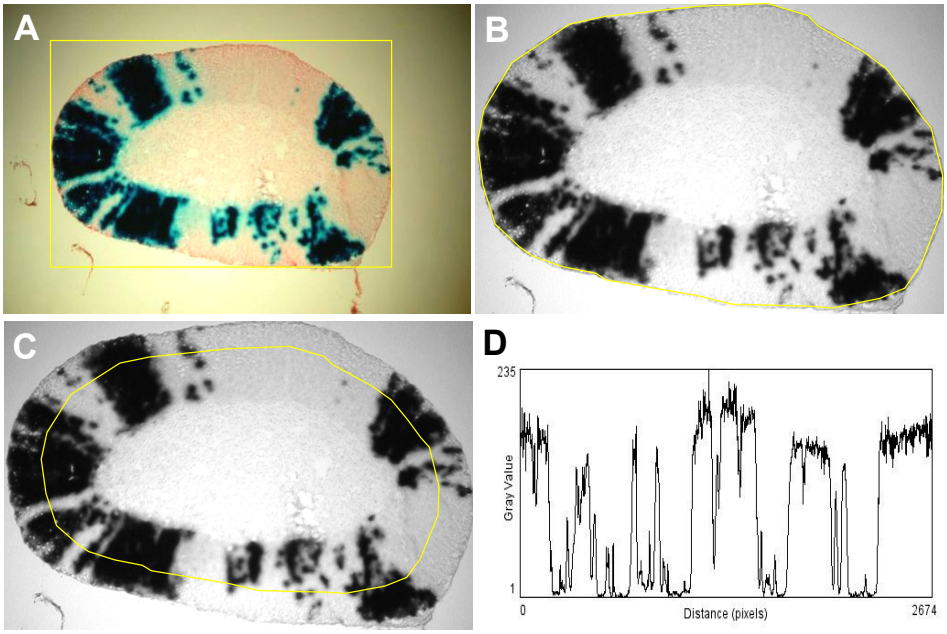

Figure 3.4: Image analysis of stripes in the 21-OH/*LacZ* adrenal cortex.

A: The 21-OH/*LacZ* hemizygous mouse exhibits radial striping patterns in the adult adrenal. ImageJ was used to define the capsule. B: The edge of the capsule was then defined. C: This shape was then shrunk by 25 pixels and converted into a 'polyline'. D: A profile plot was then made using ImageJ's "profile plot" command.

3.3.1.4 Analysis of Images of whisker barrels with ImageJ

Pseudo-coloured TIFF images were analysed without the need for a macro. Using ImageJ's segmented line selection tool a line was drawn through the centre of row 5 of the whisker barrels (Fig 3.6 5 and B). The 'plot profile' command was then run and the data copied into the 'ImageJ Patch Size Calculator'. The patch numbers were calculated from this data without 1/(1-p) correction, as actual estimates of the number of patches were required. 'Circular' selection was toggled to 'linear', the 'Manual Threshold' level was set to 75 and the 'Constant' field was left blank. An artificially high threshold value was used to cut out noise. This was possible because estimates of the widths of patches were not required. Instead the number of peaks over the threshold value with no correction was a sufficient statistic to compare the degree of disorganisation in the tissue.

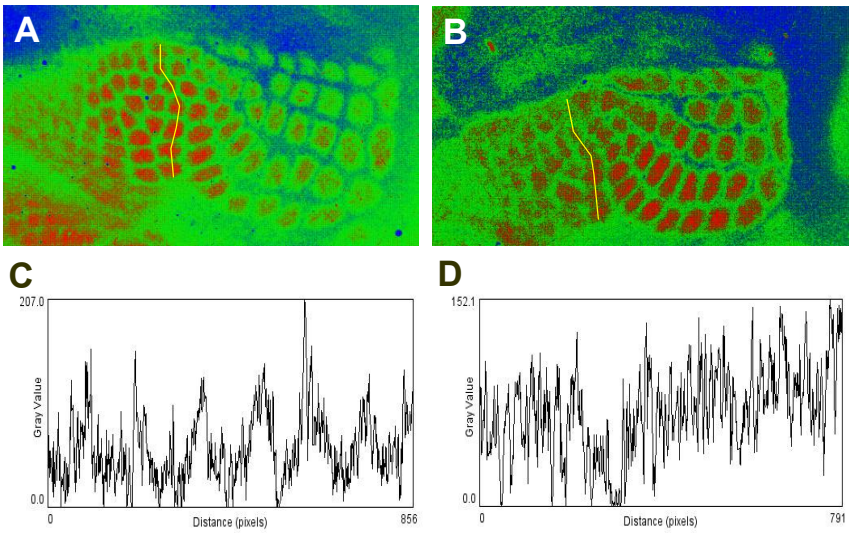

Figure 3.5: Image analysis of wildtype and RII*β* KO whisker barrels.

A and B: Segmented lines were superimposed on pseudo-coloured images of nissl-stained whisker barrels from wildtype and RIIβ KO mice, the lines were converted to polylines and the plot profile command was executed. Whereas wildtype animals have well defined whisker barrels (A), RIIβ KO animals have disorganised patches in the same region. C and D: Profile plots of wildtype (C) and RIIβ mutants (D). The RIIβ plot is much noisier representing reduced organisation of the whisker barrels.

3.3.2 Application of the image analysis technique developed

3.3.2.1 Comparison of manual and semi-automated image analysis of the corneal epithelium

To determine whether accurate and comparable results could be produced using the semi-automated approach described above, results were compared to an existing dataset produced by manual analysis of corneal striping patterns using Adobe Photoshop (See figure 2.8). Because it was observed that altering the number of sample points used in the 'Oval profile plot' plug-in affected the number of corrected stripes, a series of four macros were compared that sampled at 180, 360, 540 and 720 points per selection (termed 'macro180' to 'macro720' and described above). Figure 3.6 and Tables 3.1-3.4 outline the results. One way ANOVA conducted on each individual dataset for corrected stripe numbers revealed that the results were significant for each analysis (Table 3.1). A similar analysis for percentage contribution of *LacZ*-positive cells revealed that the contribution differed significantly between time-points when macro180 and macro720 were used. The contribution differed with marginal significance for macro540 and not al all for macro360 (Table 3.2).

A two-way ANOVA comparing each complete analysis with the original dataset showed that only corrected stripe numbers generated using macro180 differed significantly from the original dataset (Fig 3.6 A-D, Table 3.3). Macro720 produced results that were overall closest to the manual results with macro540 next and then macro360. However the 95% confidence interval also increased with the number of sample points. Average confidence intervals for macro180, macro360, macro540 and macro720 were 6.41, 9.38, 10.32 and 12.60 respectively (the original, manual method produced a 95% confidence interval of 5.65). Comparison of percentage *LacZ*-positive stripes for all macros and the original dataset showed that no method differed significantly from the manually produced results (Fig 3.6 E, Table 3.4). Macro180 was ruled out as the results for corrected stripe number and percentage

LacZ-positive cells differed significantly from the original analysis. Macro720 was also ruled out, despite the corrected stripe data being a good fit, because it was felt that the increased confidence intervals might mask significant results in other datasets and the *LacZ* results differed significantly from the original dataset. Either macro360 or macro540 would be suitable, but macro540 was chosen for this analysis as it gave the best fit for corrected stripe number qualitatively to the original analysis.

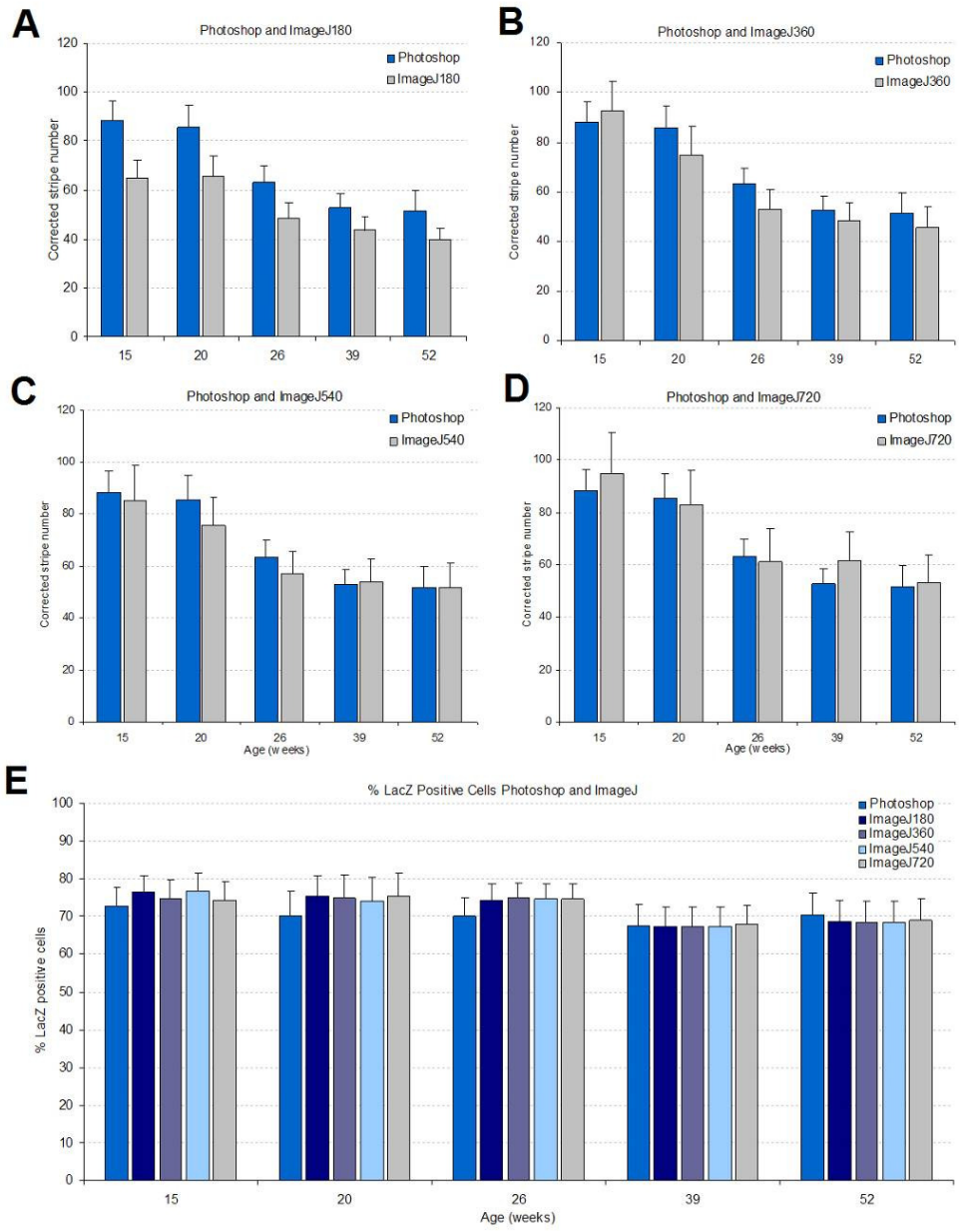

Figure 3.6: Comparison of corrected stripe numbers produced manually and by image analysis.

Relationship between mean corrected stripe number and age derived from manual measurements of stripe widths using Adobe Photoshop and automated analysis using ImageJ. A reduction in the mean corrected number of stripes in the corneal epithelium occurs

between 15-52 weeks of age. A-D: Comparison of mean corrected stripe numbers produced using macro180, macro360, macro540 and macro720 in ImageJ with the original manually produced dataset. Macro180 differed significantly from the original dataset (ANOVA $P < 0.0001$). Macro720 produced results that were overall closest to the manual results. E: Comparison of percentage *LacZ*-positive stripes for all macros and the original dataset. No method differed significantly form the manually produced results (ANOVA $P > 0.05$ in all cases).

Table 3.1: Analysis of the effects of method of analysis on corrected stripe number.

Method of Analysis and Age	Test	Corrected Stripe Number ± 95% CI	*P*-value
Macro180; 15 (36), 20 (38), 26 (38), 39 (40) and 52-weeks (34)	One-way ANOVA	64.70 ± 7.47; 65.80 ± 8.26; 48.50 ± 6.20; 43.58 ± 5.50; 39.90 ± 4.60	<0.0001
Macro360; 15 (36), 20 (38), 26 (38), 39 (40) and 52-weeks (34)	One-way ANOVA	92.64 ± 12.13; 74.83 ± 11.62; 53.15 ± 7.71; 48.43 ± 7.15; 45.41 ± 8.29	<0.0001
Macro540; 15 (36), 20 (38), 26 (38), 39 (40) and 52-weeks (34)	One-way ANOVA	85.03 ± 13.36; 75.41 ± 10.81; 56.87 ± 8.64; 53.57 ± 9.17; 51.41 ± 9.63	<0.0001
Macro720; 15 (36), 20 (38), 26 (38), 39 (40) and 52-weeks (34)	One-way ANOVA	94.92 ± 15.93; 82.93 ± 13.07; 61.29 ± 12.35; 61.73 ± 11.00; 53.03 ± 10.63	<0.0001

Numbers in parentheses are the number of eyes analysed.

Table 3.2: Analysis of the effects of method of analysis on of *LacZ*-positive cells.

Method of Analysis and Age	Test	% *LacZ*-positive Number ± 95% CI	*P*-value
Macro180; 15 (36), 20 (38), 26 (38), 39 (40) and 52-weeks (34)	One-way ANOVA	76.67 ± 4.22; 75.38 ± 5.49; 74.44 ± 4.14; 67.34 ± 5.17; 68.69 ± 5.77	0.0304
Macro360; 15 (36), 20 (38), 26 (38), 39 (40) and 52-weeks (34)	One-way ANOVA	74.67 ± 5.10; 75.03 ± 6.15; 74.90 ± 4.01; 67.42 ± 5.16; 68.52 ± 5.51	0.0894
Macro540; 15 (36), 20 (38), 26 (38), 39 (40) and 52-weeks (34)	One-way ANOVA	76.90 ± 4.55; 74.05 ± 6.14; 74.57 ± 4.08; 67.36 ± 5.19; 68.57 ± 5.58	0.0486
Macro720; 15 (36), 20 (38), 26 (38), 39 (40) and 52-weeks (34)	One-way ANOVA	74.34 ± 4.81; 75.57 ± 5.73; 74.66 ± 4.07; 67.79 ± 5.21; 68.89 ± 5.74	0.0223

Numbers in parentheses are the number of eyes analysed.

Table 3.3: Analysis of the effects of method of analysis on corrected stripe number.

Method of Analysis	Test	Corrected Stripe Number ± 95% CI	*P*-value
Photoshop 'vs' Macro180 (n = 36, 38, 38, 40 and 34 as above)	Two-way ANOVA	88.33 ± 8.06; 85.53 ± 9.18; 63.26 ± 6.41; 52.71 ± 5.79; 51.48 ± 8.29 'vs' Macro180 above	<0.0001
Photoshop 'vs' Macro360 (n = 36, 38, 38, 40 and 34 as above)	Two-way ANOVA	Photoshop above 'vs' Macro360 above	0.0552
Photoshop 'vs' Macro540 (n = 36, 38, 38, 40 and 34 as above)	Two-way ANOVA	Photoshop above 'vs' Macro540 above	0.1973
Photoshop 'vs' Macro720 (n = 36, 38, 38, 40 and 34 as above)	Two-way ANOVA	Photoshop above 'vs' Macro720 above	0.4574

Numbers in parentheses are the number of eyes analysed.

Table 3.4: Analysis of the effects of method of analysis on contribution of *LacZ*-positive cells.

Method of Analysis	Test	% *LacZ*-positive Number ± 95% CI	*P*-value
Photoshop 'vs' Macro180 (n = 36, 38, 38, 40 and 34 as above)	Two-way ANOVA	72.69 ± 5.14; 70.07 ± 6.8; 70.14 ± 4.75; 67.64 ± 5.67; 70.34 ± 5.88 'vs' Macro180 above	0.1804
Photoshop 'vs' Macro360 (n = 36, 38, 38, 40 and 34 as above)	Two-way ANOVA	Photoshop above 'vs' Macro360 above	0.2756
Photoshop 'vs' Macro540 (n = 36, 38, 38, 40 and 34 as above)	Two-way ANOVA	Photoshop above 'vs' Macro540 above	0.2301
Photoshop 'vs' Macro720 (n = 36, 38, 38, 40 and 34 as above)	Two-way ANOVA	Photoshop above 'vs' Macro720 above	0.1061

Numbers in parentheses are the number of eyes analysed.

3.3.2.2 Reproducibility of Method

Having selected macro540 as the most appropriate method for analysing corneal striping patterns the reproducibility of the technique was assessed. Briefly three researchers analysed the same image 5 times using the manual method (Photoshop) and with macro540 in ImageJ (ImageJ). Figure 3.7 summarises the results. 5 individual measurements of eye RM24L were made with both methods (Figure 3.7 A). Firstly the mean results for all researchers were compared (Figure 3.7 B). For measurement of corrected clone number the inter-quartile range was higher for the automated ImageJ method than for the manual Photoshop approach. For percentage *LacZ*-positive stripes the inter-quartile ranges were similar. However when the variances were compared they did not differ significantly. Figure 3.7 C-D shows the mean clone numbers and standard deviations for each researcher using Photoshop and ImageJ. In two out of three cases when researchers were compared separately the standard deviation of the mean clone number was lower for ImageJ versus Photoshop. However the variance between researchers for clone number never differed significantly. Figure 3.7 E-F shows the mean percentage *LacZ*-positive stripes and standard deviations for each researcher. In this case the standard deviations were always higher for the Photoshop than ImageJ. However the variance between researchers never differed significantly. This data implies that ImageJ may produce better results than Photoshop but overall the results are inconclusive.

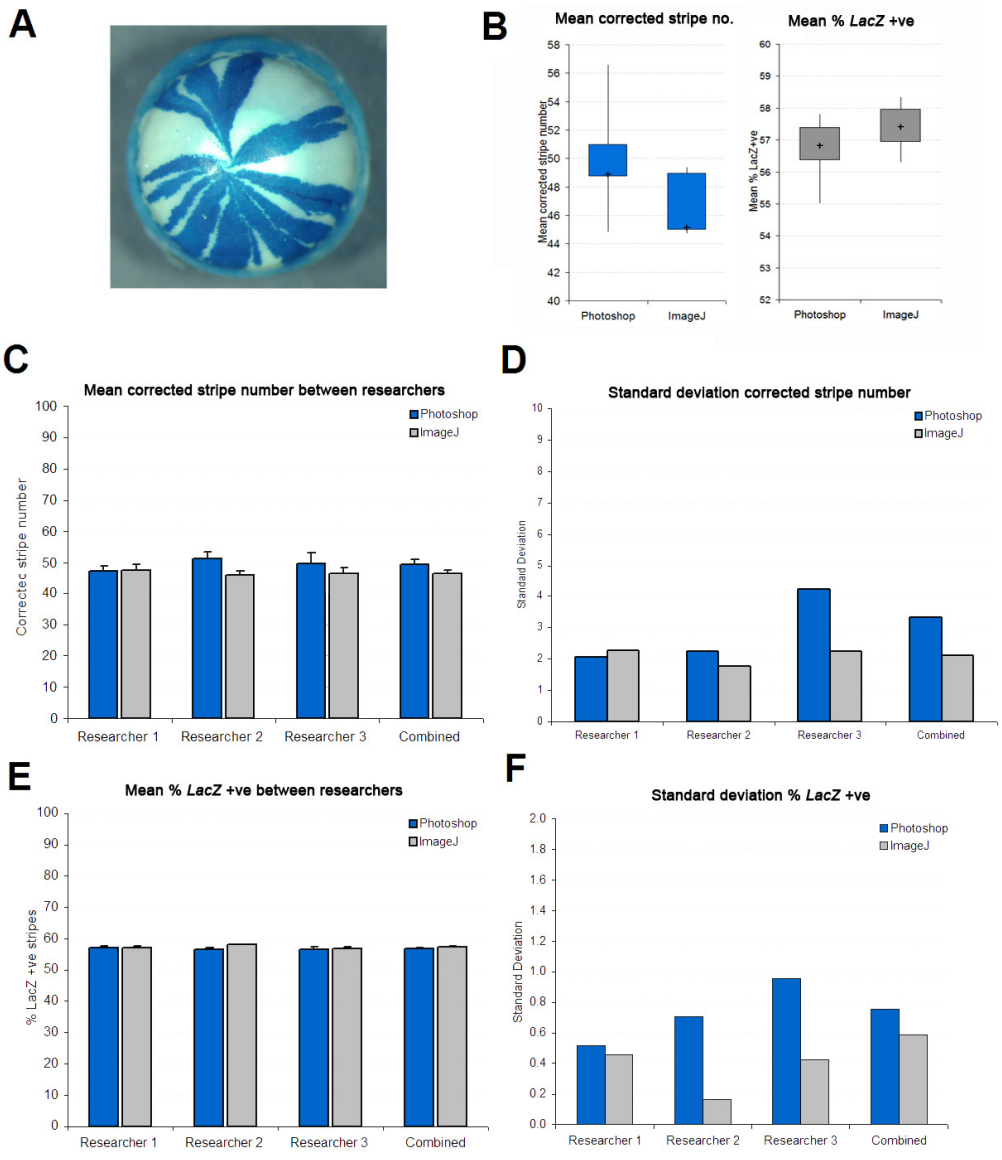

Figure 3.7: Reproducibility of results between manual and automated approaches.
Data produced by five repeated measurements of the same eye using manual (Photoshop) and automated (ImageJ) methods by three separate researchers. A: Five separate analyses of image RM24L were carried out both manually and by an automated approach by each researcher. B: Box and whisker plots; whiskers represent minimum and maximum values, box represents 1st and 3rd quartile (q1 and q3), cross equals median value. Plots show the

spread of the combined results for all three researchers, for both corrected stripe number and % *LacZ* the difference in variance is not significant (F-Test $P > 0.4$ in both cases). C: Comparison of mean clone number between researchers. D: Comparison of standard deviation in corrected stripe number between researchers, there is no significant difference between researchers (F-Test $P > 0.05$). E: Comparison of mean % *LacZ*-positive stripes between researchers. F: Comparison of the variance in % *LacZ*-positive stripes between researchers, there is no significant difference between researchers (F-Test $P > 0.05$).

3.3.2.3 Application of method for the adrenal gland

In order to ascertain whether the methods described above could be applied to other systems, the 21-OH/*LacZ* hemizygous adrenal mosaic was chosen as a model system. These animals express *LacZ* from the 21-OH promoter which is active throughout the adrenal cortex. However for unknown reasons 21-OH/*LacZ* transgene expression is mosaic (Morley et al., 1996). The adrenal gland is thought to be maintained by centripetal migration of cells arising near the periphery and accordingly in the adult gland *LacZ*-positive patches appear to form orientated patches of cells extending from the periphery to the centre of the tissue. These patterns have been previously subjected to a manual method of clonal analysis between 13 and 39 weeks of age by Ms Su-Ping Chang (PhD student jointly supervised by Dr J. D. West and Dr S. D. Morley). It was demonstrated that over this period there is no apparent decline in the corrected stripe number. (Chang, S. unpublished). The methods described above were modified to analyze mosaic 21-OH/*LacZ* transgene expression in the adrenal gland. Briefly, a selection corresponding to the shape of the outline of an adrenal gland was shrunk and imposed on the adrenal cortex. Crucially rather then altering the number of sample points taken along this line (as described for the cornea above) the intensity value of every pixel was measured. As no data has yet been published on this system it was felt that there was no need to match the previously described data. Figure 3.8 summarises the results. No change in corrected stripe number was seen between 13 and 39 weeks of age when using the semi-automated results. The manual and semi-automated results differed significantly. Although the actual values were different there was no decline between 13 and 39 weeks for the computer generated results. There was no change in proportion of *LacZ*-positive cells between 13 and 39 weeks for the semi-automated results or for the manual method. However the proportion of *LacZ*-positive cells values did differ significantly between methods.

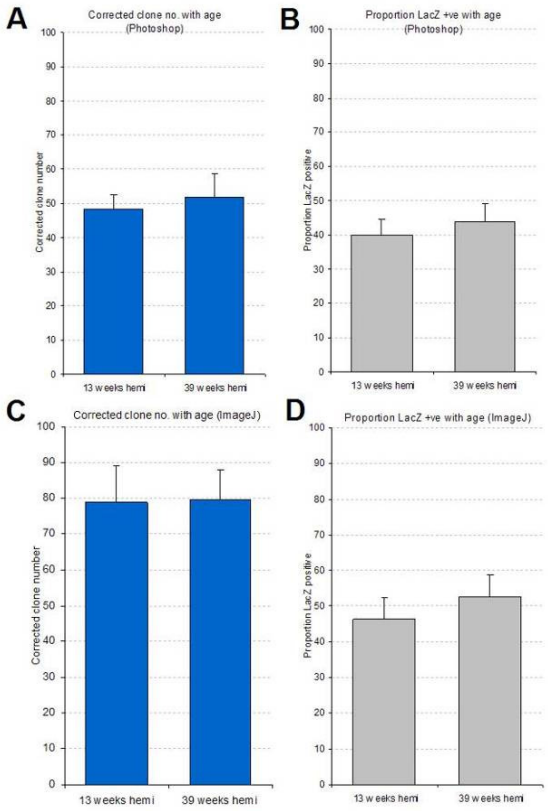

Figure 3.8: Image analysis of 21-OH/*LacZ* adrenal cortex.

A: Manual analysis of hemizygous 21-OH/*LacZ* adrenal mosaics was previously shown to show no change in clone number between 13 (51.8 ± 7.0) and 39 (48.1 ± 4.3) weeks of age (t-test $P = 0.4$). B: There was no change in contribution of *LacZ*-positive cells to the tissue at the same time points (t-test $P = 0.3$). C: Analysis of the same tissue sections using a semi-automated approach gave results of that didn't differ significantly (78.8 ± 10.5 and 79.5 ± 8.4 at 13 and 39 weeks respectively, t-test $P = 0.9$). These values were significantly different from those produced manually at 13 and 39 weeks (t-test $P < 0.0001$ in both cases). D: The automated *LacZ*-positive results were not significantly different at 13 and 39 weeks (t-test $P = 0.2$). However these values did differ significantly from the manual approach (t-test $P = 0.04$). Data for A and B were provided by Ms S. P. Chang who performed the manual analysis.

3.3.2.4 Application for whisker barrels

In order to address the flexibility of the methods described, a different kind of problem was chosen for analysis. Instead of measuring patch sizes in mosaic tissues, an estimate of the distribution of TCAs in the mouse neocortex was generated. If TCAs were distributed randomly throughout the neocortex then a very high number of distinct peaks could be counted with ImageJ using a linear selection. However if the TCAs were organised into barrels (as seen in the wildtype) fewer positive peaks would be generated, representing larger aggregation of cells. For the purpose of measuring the degree of disorganisation in the tissue, the number of peaks were counted using an artificially high threshold value in the 'ImageJ patch size calculator'. This number represented the degree of disorganisation; the more disorganisation the higher the number of peaks. 5 measurements of a wildtype row of whisker barrels and a RIIβ KO row were made and the mean values compared Figure 3.9 shows the results. There were significantly fewer patches in the wildtype than the RIIβ KO row suggesting it is possible to discriminate between the two genotypes using an analysis of the barrel field in ImageJ.

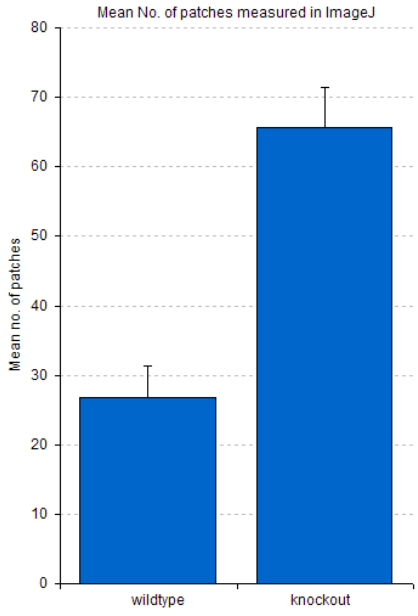

Figure 3.9: Image analysis of wildtype and RII*β* KO whisker barrels.

Measurement of the number of discrete patches in the whisker barrels of wildtype and RIIβ KO whisker barrels using image analysis. Analysis of a wildtype row of barrels yielded a patch count of 65 $\pm$ 5.0 whereas the RII*β* KO rows yielded a patch number of 27 $\pm$ 5.0. The difference in the mean patch number is statistically significant (t-test $P = 0.0004$).

3.4 DISCUSSION

This chapter describes the development of a rapid semi-automated method for analysing striped patterns in mosaic mice using freely available image analysis software and Microsoft Excel. The Excel spreadsheet conferred flexibility and ease of use to the system. It allowed the analysis of straight line and circular selections in ImageJ. It allowed thresholding both manually and automatically, extrapolation by changing the sample length to a constant and the compilation of multiple reports into a single exterior spreadsheet. It performed correction for the effects of random clumping using the 1/(1-p) method defined by Roach and modified by West (Roach, 1968; West, 1976). Combined with simple ImageJ macros this tool is a very efficient method of producing large numbers of results and summary statistics very quickly. What once would take many minutes to complete can now be done in two or three mouse clicks. When there are hundreds of images to analyse this is hugely advantageous.

3.4.1 The mosaic corneal epithelium

The results for the corneal epithelium were comparable to those produced by a laborious and time consuming manual method and faithfully reproduced an age-dependent effect on corrected stripe numbers described in Chapter 2. In determining which macro best suited the needs of this study several factors had to be considered. The resulting data had to be as close as possible to data generated using a manual method as to be broadly comparable. It was especially important that the numerical results were equivalent to previously published and accepted results from this research group (Collinson et al 2002, 2003) so that new studies could be compared to published results. The pattern described had to be qualitatively similar to the original analysis and the statistical significance of the original analysis needed to be maintained. Macro540 represented a good compromise between these factors. Using macro540 a set of results were produced that fell within the 95% confidence intervals of the previous dataset. The two datasets did not differ significantly when compared using two-way

ANOVA. They both demonstrate a significant decline in clone number from around 80 at 15 weeks to around 50 at 39 weeks with no further decline up to 52 weeks of age. Although the confidence intervals are slightly increased using this semi-automated approach, the reproducibility as demonstrated by the size of the inter-quartile range was suitably improved so that researchers can be confident of comparing their own results without laboriously re-analysing them. It is proposed then that this analysis is appropriate and accurate enough to replace the manual approach. Therefore all striping data described in the following chapters has been generated in this manner. By custom-writing ImageJ macros, the Excel tool described above can be used to analyse other systems.

3.4.2 The mosaic adrenal cortex

The adrenal is particularly appropriate because the radial stripes observed in the 21-OH/*LacZ* mouse are qualitatively similar to striping patterns seen in the eye (Morley et al., 2004). The biggest challenge in adapting this system to the adrenal was the wide variation in the size and shape of sections. Because the eye is broadly circular it is easy to automatically position a circular selection on an image by defining the edge of the epithelium. To solve a similar problem for the adrenal, slightly more user input is required to first orientate and define the edge of the gland. This allows sizing to a standard width in pixels. The outline of the adrenal gland is defined by the user, this shape is shrunk by a set number of pixels so as to sample within the adrenal cortex. The size of the image must be standardised in order to make shrinking of this selection consistent so that each image is sampled in broadly the same position. Once these steps were defined it was possible to analyze larger numbers of adrenal images in the same manner as with *XLacZ*$^{+/-}$ mosaic eyes. The results although not numerically similar, were broadly comparable with those of a manual analysis (kindly provided by Ms Su-Ping Chang) showing the same trend with acceptable confidence intervals. In some ways the adrenal images were ideal for computerised analysis due to the excellent contrast produced from transmitted images of 7μm sections. As the stripe

boundaries however are not as well defined in the adrenal it is to be expected that an unbiased automated approach may 'see' stripes that the naked eye might disregard as insignificant.

The chords of cells apparent in the 21OH/*LacZ* mouse (Morley et al., 1996) are consistent with previous work in support of the 'centripetal migration theory of adrenocortical maintenance'. A putative stem cell population is proposed to exist in the outer adrenal cortex and the progeny of these cells migrate centripetally towards the medulla where they are removed by apoptosis (Bertholet, 1980; McNicol and Duffy, 1987; Zajicek et al., 1986). The whereabouts of this stem cell population is still a matter of debate. The mammalian adrenal cortex constitutes three functional zones the zona glomerulosa (zG), zona fasiculata (zF) and zona reticularis (zR). In the mouse the zR is less apparent and an 'x-zone' is also initially present adjacent to the medulla. The x-zone regresses in male mice after postnatal day 35 (P35), but persists in females until their first pregnancy. The zG produces mineralocorticoids such as aldosterone. The zF and zR produce glucocorticoids such as corticosterone (reviewed in Keegan and Hammer, 2002). The undifferentiated zone (zU) is an area between the zG and zF that is devoid of characteristic corticosteroid-synthesizing enzymes in the rat (Mitani et al., 1994). It was proposed to be the adrenocortical stem cell zone by Mitani et al (1998; 2003) who used BrdU labelling to demonstrate the principal areas of cell division in the adrenal cortex are the zU and the areas immediately adjacent to it. Using chase periods of 1h-20 days (post-BrdU injection) the work also demonstrated a migration of cycling cells centripetally over time from the outermost part of the zF to its inner portion. The group inferred from these results that the zU was a stem cell zone in the rat adrenal cortex. However the study only labelled the actively dividing cell population rather than labelling any stem cells present.

That the corrected clone number does not change between 13 and 39 weeks of age in the adrenal probably reflects the differences between adrenal and corneal biology. As describe in

Chapter 1 the corneal epithelium turns over relatively quickly with cell constantly shed from the tissue's surface (Kruse, 1994). In the adrenal gland on the other hand BrdU labelling studies have demonstrated that cells migrate relatively slowly from the outer gland towards its centre. Zajiceck et al (1986) showed that H-Tdr labelled cells persisted in the cortex for up to 60 days post injection. The group also speculated that the average cell cycle time of a progenitor cell might be as high as 32 days. It may be that because the tissue turns over so slowly under normal conditions there is no requirement for a specialised stem cell compartment. However the adrenal has remarkable regenerative capacity when it is surgically enucleated (Perrone et al., 1986; Skelton, 1959), suggesting that sub-capsular cells are capable of regenerating the gland at least under such extreme conditions. Although the mechanism by which the mosaicism in this system is established is not known, the fact that there is no change in the proportions of *LacZ*-positive and negative cells between 13 and 39 weeks shows that it must occur in a stable manner in the early embryo.

3.4.3 Whisker barrels

The methods used to analyse stripes was also adapted to characterise whisker barrel phenotype in the somatosensory cortex. Barrelless (*Adcy1*^{brl}) mice are homozygous for a defect in the Adenyl Cyclase 1 (AC1) gene and exhibit no segregation of TCAs or layer IV granule cells despite the normal topological organisation of the S1 region of the somatosensory cortex. They therefore do not have the characteristic whisker barrels seen in the same region in wildtype animals after Nissl staining (Welker et al., 1996). AC1 is responsible for converting ATP to cAMP and PKA is therefore a candidate for a role in whisker barrel formation because cAMP is its best known downstream target (Abdel-Majid et al., 1998; Laurent et al., 2002). The role of PKA was studied further by knocking out its subunits and observing the whisker barrel phenotype. When the RIIβ subunit of PKA was removed by homologous recombination in ES cells the resulting transgenic mice exhibited disrupted organisation of TCAs in the barrel field when compared to wildtype. Specifically

barrels are visible but cells appear less well segregated and there are few barrels in the anterior snout region of the barrel field (Brandon et al., 1997; Watson et al., 2006).

It is demonstrated here that when information about stripe widths is not required, the ImageJ 'Patch Size Calculator' can be used with an artificially high threshold value. This allows the user to essentially count the number of positive and negative patches traversed by the ImageJ selection. This made it possible to produce an index of disorganisation from images of whisker barrels in wildtype and RIIβ KO mice. Here it is shown that the disruption of TCAs demonstrated qualitatively and by morphometric analyses by Watson et al (2006) can be quantified simply using an ImageJ macro and that there is a clear difference between wildtype and RIIβ KO animals.

This RIIβ KO phenotype represents the only whisker barrel-specific phenotype in 5 viable PKA subunit specific knockouts correlating with a 40% reduction in PKA activity associated with these animals (Brandon et al., 1998; Watson et al., 2006). The RIIβ subunit was immunolocalised to dendrites in the barrelfield suggesting that the site of action is postsynaptic. However because these animals do have barrels, unlike *Adcy1*^{brl} mice, PKA cannot be the downstream target of AC1 in barrel formation. Therefore these disrupted patterns reflect an AC1 independent postsynaptic role for PKA in barrel formation (Watson et al., 2006). The method described here may prove beneficial for screening multiple image sets without the need for complicated morphometric analyses in order to distinguish between subtle changes in the TCA/barrel field phenotype that may not be evident qualitatively.

Chapter 4
Effects of *PAX77* Transgene, *Pax6* and Combined *Pax6* and *Gli3* Mutations on Corneal Epithelial Phenotype and Striping Patterns

4.1 INTRODUCTION

The mouse ocular surface is derived from a primordium of Pax6 positive cells of the head surface ectoderm. These cells are the endpoint of a series of inductive mechanisms that specify the lens. It is not surprising that mutation of the 'master gene' of eye development would have many severe implications on structure and function. However what is perhaps more surprising is that the same mutations can contribute to other chronic and progressive conditions such as aniridia related keratopathy (ARK) in humans. That master genes of development also have a role in maintenance of tissue homeostasis in the adult, probably reflects the complex nature in which they interact and are regulated. Pax6 for example has many downstream targets involved in proliferation, differentiation and tissue homeostasis. It encodes two isoforms, shown to regulate gene expression differentially, that are themselves regulated in a complex manner. Progressive tissue specific phenotypes suggest a defect in the propagation or maintenance of a tissue or a cell lineage essential to that tissue. In the case of the corneal epithelium, where only one cell lineage is involved, the limbal stem cell (LSC) is the likely target of such a mechanism. But it is unclear whether the defect is a cell autonomous defect of LSCs or a direct consequence of a developmental aberration with consequences for the entire tissue. Here a number of mouse genetic backgrounds with ocular phenotypes are probed for limbal stem cell function using mosaicism for *LacZ* as a lineage marker.

The *PAX6* gene is a highly conserved paired-like homeobox-containing gene encoding the transcription factor PAX6. PAX6 is essential for development of the eye, brain, spinal cord

and pancreas (Simpson and Price, 2002). In humans the *PAX6* gene was first cloned during the genetic analysis of WAGR syndrome (Wilms tumour, aniridia, genitourinary abnormalities and mental retardation) a disease caused by a hemizygous deletion of chromosome 11p13 removing a single copy of the genes *PAX6* and *WT1* (Ton et al., 1991). It was subsequently demonstrated that haploinsufficiency for *PAX6* alone, by loss-of-function of one allele by truncation of the protein, results in aniridia (absence of the iris) and related developmental eye diseases (Hanson et al., 1993; Martha et al., 1994; Ton et al., 1991; Vincent et al., 2003). It has been proposed that a LSC deficiency is the principle cause of deterioration of the ocular surface in aniridia patients (Nishida et al., 1995; Puangsricharern and Tseng, 1995).

The small-eye $Pax6^{Sey\text{-}Neu}$ mutation is semi-dominant in nature, it represents a single base pair change from G to T resulting in the conversion of a GGA (glycine codon) into a TGA (stop codon) thus encoding a truncated form of the Pax6 protein. Homozygosity for the $Pax6^{Sey\text{-}Neu}$ mutation results in a complete lack of eyes and nasal primordia. Mice heterozygous for $Pax6^{Sey\text{-}Neu}$ (here termed $Pax6^{+/-}$) are viable but have small eyes, aniridia and a range of other ocular abnormalities (Hogan et al., 1988). $Pax6^{+/-}$ X-inactivation mosaics have disrupted striping patterns and fewer coherent corneal epithelial clones. (Collinson et al., 2004a). Values for wildtype at 15 and 28 weeks were 85.04 ± 4.25 and 73.66 ± 4.32 respectively whilst values for $Pax6^{+/-}$ at 15 and 28 weeks were 46.43 ± 3.7 and 37.83 ± 3.97 respectively. The difference between $Pax6^{+/-}$ and wildtype was significant ($P < 0.00001$) in both cases (Collinson et al., 2004a).

Gli3 encodes a zinc finger protein, important for craniofacial development (Theil et al., 1999; Tole et al., 2000). It is a transcriptional repressor that is activated in response to signalling through sonic hedgehog (Shh) and patched (Ptc), its receptor (Marigo et al., 1996; Wang et al., 2000). GLI3 null embryos demonstrate a number of ocular defects including microphthalmia (Franz, 1994; Johnson, 1967). The $Gli3^{XtJ}$ mutation results from a 51.5-kb

deletion of the coding sequence of the *Gli3* gene (Maynard et al., 2002). This deletion results in a non functional fusion transcript of *Gli3* that lacks the DNA binding elements required for normal activity (Buscher et al., 1998). Homozygosity for the $Gli3^{Xt J}$ allele results in severe developmental defects including polydactyly, craniofacial abnormalities, brain defects and various defects in organs such as the lungs (Franz, 1994; Grindley et al., 1997; LaMantia, 1999). The $Gli3^{Xt J}$ heterozygous (here termed $Gli3^{+/-}$) eye is on the whole normal with occasional minor iris and retinal abnormalities whilst $Pax6^{+/-}/Gli3^{+/-}$ double heterozygous animals exhibit a range of mild to severe defects of the retina, iris, lens and cornea much more extensive than could be predicted by addition of the two phenotypes (Zaki et al., 2006).

Because eye development is extremely susceptible to reductions in Pax6 expression it was hypothesised that an increase in expression may also effect development. To test this Schedl et al (1996) over expressed the human form of Pax6 (PAX6) in the mouse. This was achieved by insertion of a 420kb yeast artificial chromosome (YAC) containing *PAX6* into the mouse genome. Standard genetic approaches were not thought to be appropriate to create a functional locus in the mouse as the regulation of PAX6 expression is complex (Fantes et al., 1995; Plaza et al., 1995). Furthermore the *PAX6* locus is alternatively spliced to produce two protein products of (at that time) unknown significance (Glaser et al., 1992; Walther and Gruss, 1991).The use of a YAC allows insertion of a genetic locus into the mouse in an almost natural chromosomal context, thus allowing normal regulation of the locus and avoiding the problems of position effect variegation often reported in addition transgenics. By using the human form of *PAX6* in the mouse it was possible to distinguish between endogenous and transgenic copies of the gene. Because the *PAX6* sequence and expression pattern is so well conserved between species the risk of aberrant expression patterns induced by the transgene was small (Schedl et al., 1996).

Of the mouse lines produced by injection of a 420bp transgene, strain PAX77 was shown to have integrated 5-7 copies of the transgene (here termed the *PAX77* transgene) and to over-express PAX6 in a manner that mimicked the endogenous gene. In complementation studies, animals positive for *PAX77* (here termed $PAX77^{+ve}$) completely rescued the ocular phenotype in both *Pax6* hetero and homozygotes. Eye size, formation of a normal pupil and the formation of a properly developed iris spanning the lens was completely restored. Interestingly $PAX77^{+ve}$ mice exhibited multiple eye abnormalities ranging from normally sized eyes to severe microphthalmia. $PAX77^{+ve}$ transgenics showed a reduction in corneal size. The lens did not protrude beneath the cornea effecting the formation of the iris. Some mice demonstrated unilateral microphthalmia with the other eye appearing normal. In animals with apparently normal eyes iris abnormalities were apparent. In microphthalmic eyes lens phenotype included improperly arranged fibres or severe cataracts. The retina was fused to the lens. (Schedl et al., 1996).

4.1.1 Experimental Aims

It is known that the dosage of Pax6 is essential for proper development of the eye and the structure of the corneal epithelium. Here the effects of different doses of Pax6 and the synergistic effects of another transcription factor Gli3 are investigated in $XLacZ^{+/-}$ mosaics. Effects on eye mass, epithelial structure, striping patterns and clone numbers are summarised. Chapter 3 outlines a computerized method for analyzing striping patterns in the $XLacZ^{+/-}$ mouse eye. This chapter uses this method to analyse striping patterns in $XLacZ^{+/-}$ mice with different genetic backgrounds. Firstly striping phenotypes and corrected stripe numbers are compared in animals heterozygous for the $Pax6^{Sey\text{-}Neu}$ mutation ($Pax6^{+/-}$) and their wildtype littermates. As illustrated in chapter 2 there is a decline in wildtype stripe number between 15 and 39-weeks. Therefore comparisons were also made at 15 and 30-weeks of age. The same comparisons are made between $XLacZ^{+/-}$ animals hemizygous and for the *PAX77* transgene and wildtype littermates (termed $PAX77^{+ve}$ and wildtype

respectively) at 15 and 30-weeks of age. Because *Pax6* and *Gli3* may be linked through Sonic Hedgehog (*Shh*) and earlier studies have demonstrated animals heterozygous for both *Pax6* and *Gli3* (termed $Pax6^{+/-}/Gli3^{+/-}$) have distinct and wider ranged ocular defects, these animals were compared here at 15 weeks of age.

4.2 MATERIALS AND METHODS

4.2.1 Animals

The H253 transgenic line, the production of *XLacZ*$^{+/-}$ mosaics and the staining of tissues from these animals are all described in the Materials and Methods section of Chapter 2. Three strains of *XLacZ*$^{+/-}$ mosaic mice were used in this study.

XLacZ$^{+/-}$/*Pax6*$^{+/-}$ animals heterozygous for *Pax6*, were female progeny of crosses between H253 males and *Pax6*$^{+/-}$ females. The animals were compared with *XLacZ*$^{+/-}$ (wildtype) littermates at 15 and 30-weeks.

XLacZ$^{+/-}$/*PAX77*$^{+ve}$ animals hemizygous for *PAX77*, were female progeny of crosses between H253 males and *PAX77* hemizygous females. The animals were compared with *XLacZ*$^{+/-}$ (wildtype) littermates at 15 and 30-weeks.

XLacZ$^{+/-}$/*Pax6*$^{+/-}$ animals heterozygous for *Pax6*, *XLacZ*$^{+/-}$/*Gli3*$^{+/-}$ animals heterozygous for *Gli3* and *XLacZ*$^{+/-}$/*Pax6*$^{+/-}$/*Gli3*$^{+/-}$ animals heterozygous for both *Pax6* and *Gli3*, were female progeny of crosses between *Gi3*$^{+/-}$ males hemizygous for X-linked *nLacZ* and *Pax6*$^{+/-}$ females. The animals were compared with *XLacZ*$^{+/-}$ (wildtype) littermates at 15 weeks.

Because all the animals in this chapter were *XLacZ*$^{+/-}$ females, for simplicity the *XLacZ*$^{+/-}$ part of the genotype has been dropped. For example *XLacZ*$^{+/-}$ animals are termed 'wildtype' and *XLacZ*$^{+/-}$/*Pax6*$^{+/-}$ animals are termed *Pax6*$^{+/-}$. Eyes were dissected, stained and photographed as described in Chapter 2. Images were analysed using macro540 in ImageJ. The corrected patch numbers were calculated from this data using the 'ImageJ Patch Size Calculator' described in Chapter 3. 'ImageJ Selection Type' was toggled to 'circular', the 'Manual Threshold' and 'Constant Fields' were left blank. Statistical analyses were done using Statview 5 (Abacus Concepts Inc., Berkeley, USA) and Microsoft Excel.

4.2.2 Genotyping

Genomic DNA was extracted from tale tip material. Tail tips were incubated overnight at 55^{o}C in 0.6mg/ml Proteinase K (50mM Tris, 250mM Kcl, 25mM MgCl pH 7.8, 2.25% v/v IGEPAL, 2.25% v/v TWEEN 20, 0.5mg/ml Gelatin). After incubation the Proteinase K was denatured by heating to 100^{o}C for ten minutes and then cooling on ice. The samples were briefly centrifuged at 13,000 rpm to form a pellet and the solution removed to a clean tube.

To identify animal heterozygous for the *Pax6*$^{Sey\text{-}Neu}$ mutation, PCR was carried out on genomic DNA to amplify a 223 bp fragment of the *Pax6* gene that contains the base effected in the *Sey-Neu* mutation. The sequences of the primers used in *Sey-Neu* genotyping reactions were; 5'-GCAACACTCCTAGTCACATTCC-3' and 5'-ATGGAACCTGATGTGAAGG-AGG-3' for the forward and reverse primers respectively. The resulting PCR products were digested with the restriction enzyme HindII to yield a 223bp (wildtype), 141bp and 82bp (mutant) fragments which were resolved by electrophoresis on a 4% agarose gel.

To identify animals positive for the *PAX77* transgene a duplex PCR reaction was used that amplified a 282 bp region of the human *PAX6* gene and a 398 bp region of the mouse Pax6 gene, as an internal control. This was resolved using agarose gel electrophoresis. The sequences of the primers used to amplify the mouse *Pax6* region were; 5'-GAGGGTTTCCTGGATCTGG-3' and 5'-CGCAAATACACCTTTGCTCA-3' for the forward and reverse primers respectively. The sequences of the primers used to amplify the human *Pax6* transgene were 5'- CACGGTTTACTGGGTCTGG-3' and 5'-CCGTGTGCCTCAACCGTA-3' for the forward and reverse primers respectively.

To identify animals carrying the *Gli3*^{XtJ} mutation PCR was carried out on genomic DNA using a duplex reaction to amplify a 580 bp region of the *XtJ* allele and a 193 bp region of the wildtype-*Gli3* allele which were resolved using agarose gel electrophoresis. The

sequences of the primers used to amplify the *XtJ* region were; 5'-TACCCCAGCAGGAGACTCAGATTAG-3' and 5'-AAACCCGTGGCTCAGGACAAG-3' for the forward and reverse primers respectively. The sequences of the primers used to amplify the wildtype-*Gli3* region were; 5'- GGCCCAAACATCTACCAACACATA-3' and 5'-GTTGGCTGCTGCATGAAGACTGAC-3' for the forward and reverse primers respectively (See Maynard M. T. et al (2002).

4.3 RESULTS

4.3.1 Effect of *Pax6*$^{+/-}$ on eye mass and striping phenotype

Effects of *Pax6*$^{+/-}$ on eye size and striping phenotype have been previously documented (Collinson et al., 2004a) the original analysis is extended here. Eye mass in milligrams was compared for wildtype and *Pax6*$^{+/-}$ females at 15 and 30-weeks of age Figure 4.1 and Table 4.1 outline the results. Average wildtype eye mass was significantly greater than *Pax6*$^{+/-}$ eye mass at both time points. The increase in eye mass between 15 and 30-weeks was also significant for both genotypes.

Stripes do not form correctly in *Pax6*$^{+/-}$ mice. Figure 4.2 shows typical striping patterns for wildtype and *Pax6*$^{+/-}$ eyes at 15 and 30-weeks of age. Consistent with the eye mass data, *Pax6*$^{+/-}$ animals have smaller eyes, when compared to wildtype. Whereas wildtype animals exhibit a 'normal' radial striping phenotype consistent with the eyes describe in Chapter 2, *Pax6*$^{+/-}$ animals exhibit disrupted striping patterns in the corneal epithelium. Although whole stripes can occasionally be observed, the majority of eyes exhibit 'orientated patches' rather than stripes. This is true both at 15 and 30-weeks of age. It was observed in wildtype animals that stripes were aligned vertically in the corneal epithelium (See Chapter 2 Figure 2.3), to see whether this was the case in *Pax6*$^{+/-}$ animals a typical eye was sectioned. Figure 4.3 shows sections from a *Pax6*$^{+/-}$ mosaic eye. As shown previously the *Pax6*$^{+/-}$ corneal epithelium is thinner than wildtype (Collinson et al., 2004a). It is typically 2-cells thick. Striping patterns span the entire corneal thickness, however cell mixing is evident at stripe boundaries (Figure 3 B). *LacZ* staining is more prominent in the corneal stroma than in wildtype animals.

As demonstrated in Chapter 2 there is a decline in wildtype corrected stripe number between 15 and 39 weeks of age. For this reason corrected stripe numbers were calculated for wildtype and *Pax6*$^{+/-}$ littermates at 15 and 30-weeks to see whether there is a similar effect in

the *Pax6*$^{+/-}$ animals. The results are summarised in Figure 4.4 and Table 4.2. Whereas the difference in corrected stripe number between the wildtype 15-week group and the *Pax6*$^{+/-}$ 30-week group was significant the difference between the *Pax6*$^{+/-}$ 15 and 30-week groups was not. The difference in the percentage of *LacZ*-positive staining between the wildtype and *Pax6*$^{+/-}$ groups was significant (Table 4.3). Although these results were not significant they reflect the general finding of the work presented by Collinson et al (2004a).

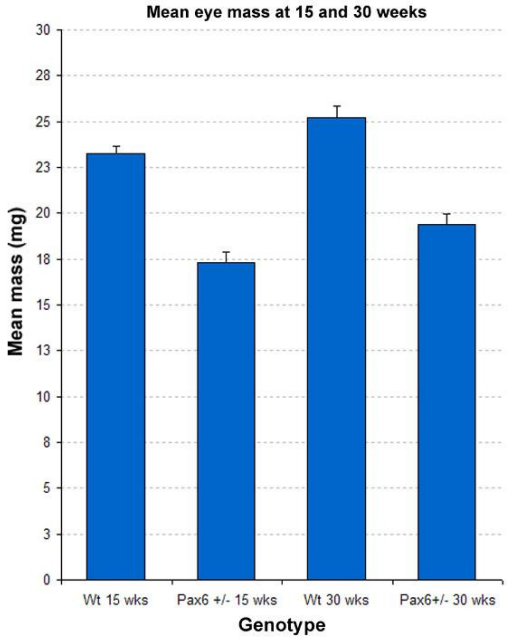

Figure 4.1: Comparison of eye mass in wildtype and *Pax6*$^{+/-}$ mice at 15 and 30 weeks. Average wildtype eye mass increased significantly between 15 and 30-weeks from 23.3 ± 0.4 mg to 25.2 ± 0.7 mg (ANOVA P = <0.0001, Fisher's PLSD P = <0.0001). Average *Pax6*$^{+/-}$ eye mass increased between 15 and 30-weeks from 17.3 ± 0.6 mg to 19.4 ± 0.6 mg (ANOVA P = <0.0001, Fisher's PLSD P = <0.0001). Wildtype eye mass was greater than *Pax6*$^{+/-}$eye mass at both time-points (Fishers PLSD P < 0.0001 in both cases). Error bars, 95% confidence intervals; Wt, wildtype.

Table 4.1: Analysis of the effects of *Pax6* genotype and age on eye mass.

Genotype and Age	Test	Eye Mass ± 95% CI (mg)	*P*-value
Wildtype 15-weeks (16); Wildtype 30-weeks (18); *Pax6*$^{+/-}$ 15-weeks (18); *Pax6*$^{+/-}$ 30-weeks (18)	One-way ANOVA	See below	<0.0001
Wildtype 15-weeks 'vs' Wildtype 30-weeks	Fisher's PLSD	23.3 ± 0.4 'vs' 25.2 ±0.7	<0.0001
Wildtype 15-weeks 'vs' *Pax6*$^{+/-}$ 15-weeks	Fisher's PLSD	23.3 ± 0.4 'vs' 17.3 ± 0.6	<0.0001
Wildtype 15-weeks 'vs' *Pax6*$^{+/-}$ 30-weeks	Fisher's PLSD	23.3 ± 0.4 'vs' 19.4 ± 0.6	<0.0001
Wildtype 30-weeks 'vs' *Pax6*$^{+/-}$ 15-weeks	Fisher's PLSD	25.2 ± 0.7 'vs' 17.3 ± 0.6	<0.0001
Wildtype 30-weeks 'vs' *Pax6*$^{+/-}$ 30-weeks	Fisher's PLSD	25.2 ± 0.7 'vs' 19.4 ± 0.6	<0.0001
Pax6$^{+/-}$ 15-weeks 'vs' *Pax6*$^{+/-}$ 30-weeks	Fisher's PLSD	17.3 ± 0.6 'vs' 19.4 ± 0.6	<0.0001

Numbers in parentheses are the number of eyes analysed.

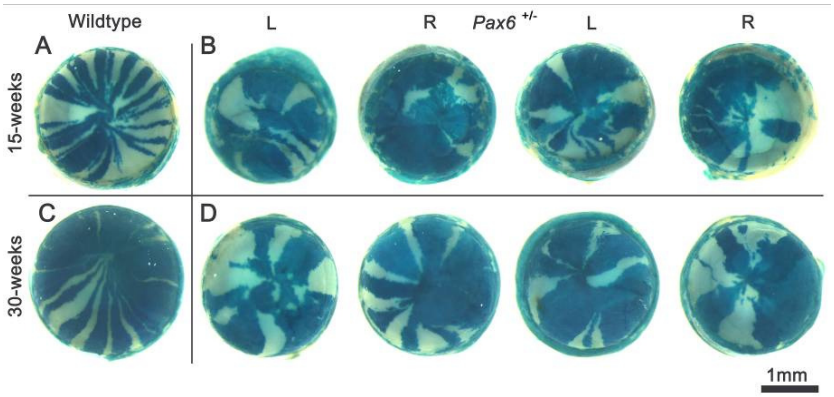

Figure 4.2: Striping patterns in wildtype and *Pax6*$^{+/-}$ littermates at 15 and 30 weeks.
A: A typical 15-week old wildtype eye. B: A selection of eyes from *Pax6*$^{+/-}$ mice. C: A typical 30-week old wildtype eye. D: A selection of *Pax6*$^{+/-}$ eyes at 30-weeks. *Pax6*$^{+/-}$ have smaller eyes, when compared to wildtype. These eyes also exhibit disrupted striping patterns in the corneal epithelium. Although whole stripes can occasionally be observed, the majority of eyes exhibit 'orientated patches' rather than stripes. This is true both at 15 and 30-weeks of age.

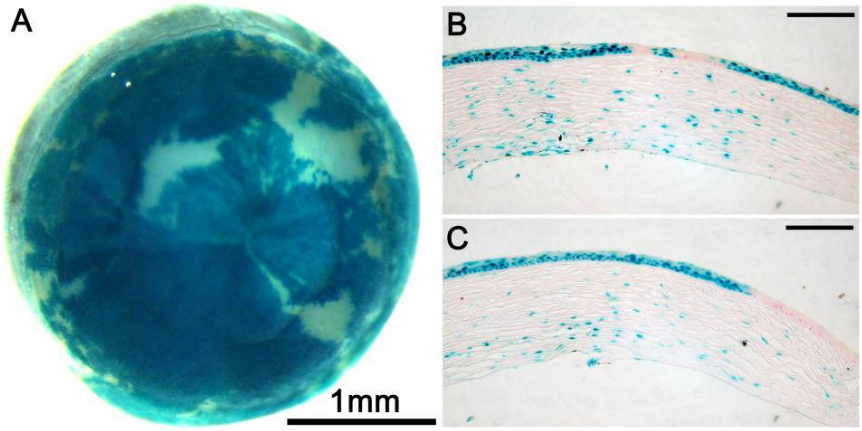

Figure 4.3: Typical sections from a *Pax6*$^{+/-}$ mosaic.

A: A typical *Pax6*$^{+/-}$ eye was sectioned. B-C: *Pax6*$^{+/-}$ corneal epithelium is thinner (typically 2-cells thick). Striping patterns span the entire corneal thickness, however cell mixing is evident at stripe boundaries. *LacZ*-positive staining is more prominent in the corneal stroma than in wildtype animals (See Chapter 2, Figure 2.3). Scale bars in B-C = 100 microns.

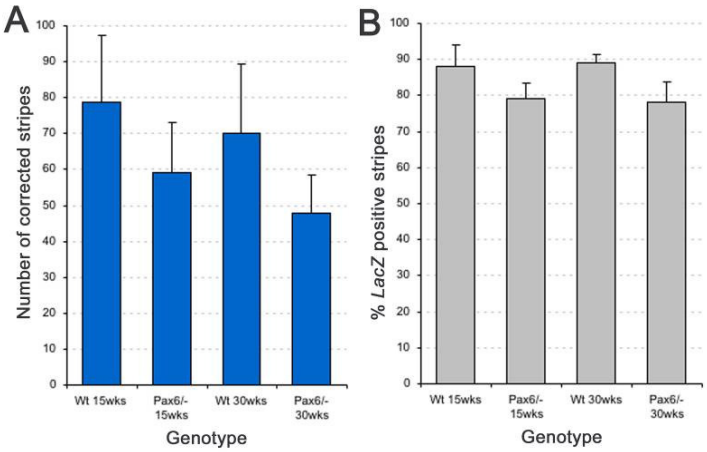

Figure 4.4: Effect of *Pax6* genotype on the corrected stripe number and the percentage contribution of *LacZ*-positive cells to the corneal epithelium.

Pax6$^{+/-}$ mice show no decrease in corrected stripe number between 15 and 30-weeks of age (ANOVA P = 0.03, Fisher's PLSD P = 0.2842) however neither did wildtype in this comparison (Fisher's PLSD P = 0.4523). *Pax6*$^{+/-}$ did not differ from wildtype at 15-weeks (Fisher's PLSD P = 0.1076) but did differ from wildtype at 30-weeks (Fisher's PLSD P = 0.0340). The proportion of *LacZ*-positive cells is significantly reduced in *Pax6*$^{+/-}$ 15 and 30-weeks (ANOVA P = 0.0020, Fisher's PLSD P = 0.0240 and 0.0015 respectively). Error bars, 95% confidence intervals; Wt, wildtype.

Table 4.2: Analysis of the effects of *Pax6* genotype and age on corrected stripe.

Genotype and Age	Test	Corrected Stripe Number ± 95% CI	*P*-value
Wildtype 15-weeks (16); Wildtype 30-weeks (18); *Pax6*$^{+/-}$ 15-weeks (18); *Pax6*$^{+/-}$ 30-weeks (18)	One-way ANOVA	See below	0.0300
Wildtype 15-weeks 'vs' Wildtype 30-weeks	Fisher's PLSD	78.82 ± 18.44 'vs' 69.96 ± 19.25	0.4523
Wildtype 15-weeks 'vs' *Pax6*$^{+/-}$ 15-weeks	Fisher's PLSD	78.82 ± 18.44 'vs' 59.25 ± 13.79	0.1076
Wildtype 15-weeks 'vs' *Pax6*$^{+/-}$ 30-weeks	Fisher's PLSD	78.82 ± 18.44 'vs' 47.84 ± 10.7	0.0060
Wildtype 30-weeks 'vs' *Pax6*$^{+/-}$ 15-weeks	Fisher's PLSD	69.96 ± 19.25 'vs' 59.25 ± 13.79	0.3493
Wildtype 30-weeks 'vs' *Pax6*$^{+/-}$ 30-weeks	Fisher's PLSD	69.96 ± 19.25 'vs' 47.84 ± 10.7	0.0340
Pax6$^{+/-}$ 15-weeks 'vs' *Pax6*$^{+/-}$ 30-weeks	Fisher's PLSD	59.25 ± 13.79 'vs' 47.84 ± 10.7	0.2842

Numbers in parentheses are the number of eyes analysed.

Table 4.3: Analysis of the effects of *Pax6* genotype and age on percentage contribution of *LacZ*-positive cells.

Genotype and Age	Test	% *LacZ*-positive Number ± 95% CI	*P*-value
Wildtype 15-weeks (16); Wildtype 30-weeks (18); *Pax6*$^{+/-}$ 15-weeks (18); *Pax6*$^{+/-}$ 30-weeks (18)	One-way ANOVA	See below	0.0020
Wildtype 15-weeks 'vs' Wildtype 30-weeks	Fisher's PLSD	88.23 ± 5.79 'vs' 89.09 ± 2.4	0.8223
Wildtype 15-weeks 'vs' *Pax6*$^{+/-}$ 15-weeks	Fisher's PLSD	88.23 ± 5.79 'vs' 79.24 ± 4.04	0.0240
Wildtype 15-weeks 'vs' *Pax6*$^{+/-}$ 30-weeks	Fisher's PLSD	88.23 ± 5.79 'vs' 78.15 ± 5.28	0.0059
Wildtype 30-weeks 'vs' *Pax6*$^{+/-}$ 15-weeks	Fisher's PLSD	89.09 ± 2.4 'vs' 79.24 ± 4.04	0.0093
Wildtype 30-weeks 'vs' *Pax6*$^{+/-}$ 30-weeks	Fisher's PLSD	89.09 ± 2.4 'vs' 78.15 ± 5.28	0.0015
Pax6$^{+/-}$ 15-weeks 'vs' *Pax6*$^{+/-}$ 30-weeks	Fisher's PLSD	79.24 ± 4.04 'vs' 78.15 ± 5.28	0.7520

Numbers in parentheses are the number of eyes analysed.

4.3.2 Effect of the *PAX77* transgene on eye mass and striping phenotype

Eye mass in milligrams was compared for wildtype and $PAX77^{+ve}$ mosaic females at 15 and 30-weeks of age. Figure 4.5 and Table 4.4 outline the results. Average wildtype eye mass increased significantly between 15 and 30 weeks. The increase in $PAX77^{+ve}$ eye mass was not significant. $PAX77^{+ve}$ eye mass only differed from wildtype at 30-weeks. This may reflect an increase in amount of variation in the $PAX77^{+ve}$ sample.

Figure 4.6 shows typical striping patterns for wildtype and $PAX77^{+ve}$ eyes at 15 and 30-weeks of age. Eyes mass data suggested that wildtype and $PAX77^{+ve}$ did not differ at 15-weeks, however it is obvious that $PAX77^{+ve}$ eyes are smaller with small flattened corneas. $PAX77^{+ve}$ eyes exhibit striping patterns at 15 and 30-weeks of age, these patterns are qualitatively similar to those observed in wildtype animals. Because $PAX77^{+ve}$ eyes had smaller flatter corneas in comparison to wildtype despite the similarity in actual size, an analysis of corneal diameter was conducted (Figure 4.7, Table 4.5). The overall diameter and the corneal diameter of wildtype and $PAX77^{+ve}$ eyes were measured. The corneal diameter was then expressed as a percentage of total diameter to avoid problems of scale, the results are summarised in Table 4.5. This value did not differ significantly for either genotype between 15 and 30-weeks. However it was also significantly less for $PAX77^{+ve}$ than wildtype showing that despite having similar sized eyes $PAX77^{+ve}$ mice have a developmental defect in the formation of the corneal epithelium.

To ascertain whether the stripes seen in $PAX77^{+ve}$ eyes were aligned vertically in the epithelium a typical $PAX77^{+ve}$ eye was sectioned, Figure 4.8 shows typical sections from a $PAX77^{+ve}$ mosaic. $PAX77^{+ve}$ corneal epithelium is similar in thickness to wildtype epithelium (See Chapter 2, Figure 2.3). Striping patterns span the entire corneal thickness. Although stripes align vertically some cell mixing is evident at stripe boundaries.

Corrected stripe numbers were calculated for wildtype and *PAX77*$^{+ve}$ mice at 15 and 30-weeks of age, the results are shown in Figure 4.9 and Table 4.6. Wildtype corrected stripe number declined significantly between 15 and 30-weeks. At 15-weeks *PAX77*$^{+ve}$ corrected stripe umber was significantly less than wildtype. Furthermore no such decline was observed for *PAX77*$^{+ve}$ corrected stripe number between these time-points. The difference in the percentage of *LacZ*-positive staining between the wildtype and *PAX77*$^{+ve}$ groups was significant at both time-points (Table 4.7).

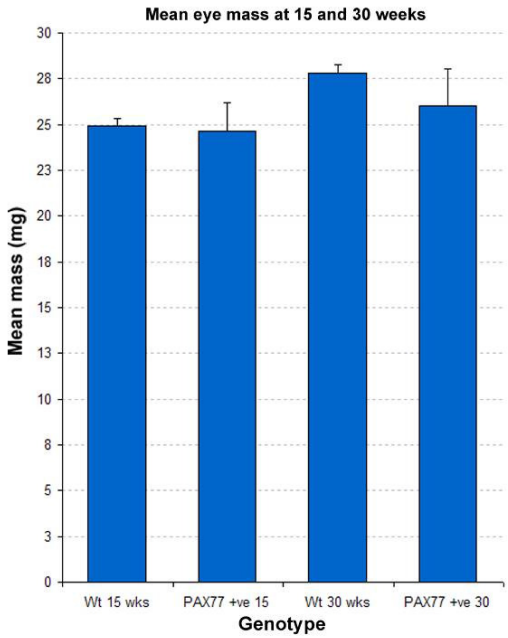

Figure 4.5: Comparison of eye mass in wildtype and *PAX77*$^{+ve}$ mice at 15 and 30 weeks. Average wildtype eye mass increased significantly between 15 and 30 weeks from 24.0 ± 0.4 mg to 27.8 ± 0.4 mg ANOVA P <0.0001, Fisher's PLSD P <0.0001). Average *PAX77*$^{+ve}$ eye mass increased between 15 and 30 weeks from 24.7 ± 1.5 mg to 26.0 ± 2.0 mg. However this increase was not significant (Fisher's PLSD P = 0.1232). *PAX77*$^{+ve}$ eye mass only differed significantly from wildtype at 30-weeks (Fisher's PLSD P = 0.0145). Error bars, 95% confidence intervals; Wt, wildtype.

Table 4.4: Analysis of the effects of *PAX77* genotype and age on eye mass.

Genotype and Age	Test	Eye Mass ± 95% CI (mg)	*P*-value
Wildtype 15-weeks (22); Wildtype 30-weeks (36); and $PAX77^{+ve}$ 15-weeks (14); $PAX77^{+ve}$ 15-weeks (20)	One-way ANOVA	See below	<0.0001
Wildtype 15-weeks 'vs' Wildtype 30-weeks	Fisher's PLSD	24.9 ± 0.4 'vs' 27.8 ± 0.4	<0.0001
Wildtype 15-weeks 'vs' $PAX77^{+ve}$ 15-weeks	Fisher's PLSD	24.9 ± 0.4 'vs' 24.7 ± 1.5	0.7504
Wildtype 15-weeks 'vs' $PAX77^{+ve}$ 30-weeks	Fisher's PLSD	24.9 ± 0.4 'vs' 26.0 ± 2.0	0.1644
Wildtype 30-weeks 'vs' $PAX77^{+ve}$ 15-weeks	Fisher's PLSD	27.8 ± 0.4 'vs' 24.7 ± 1.5	0.0002
Wildtype 30-weeks 'vs' $PAX77^{+ve}$ 30-weeks	Fisher's PLSD	27.8 ± 0.4 'vs' 26.0 ± 2.0	0.0145
$PAX77^{+ve}$ 15-weeks 'vs' $PAX77^{+ve}$ 30-weeks	Fisher's PLSD	24.7 ± 1.5 'vs' 26.0 ± 2.0	0.1232

Numbers in parentheses are the number of eyes analysed.

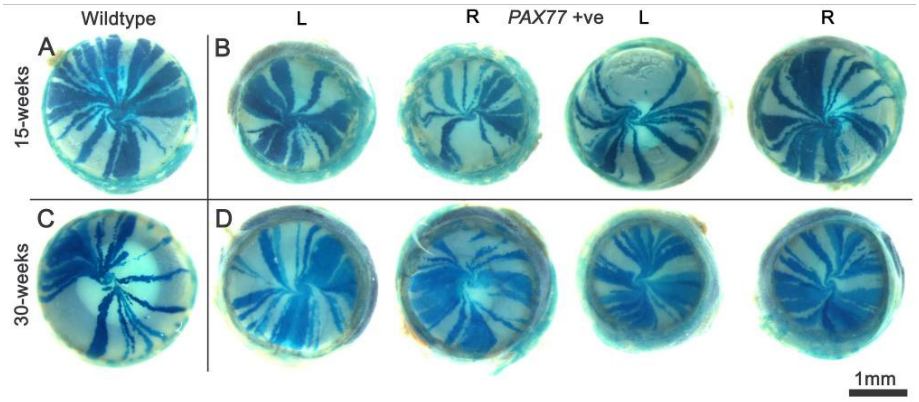

Figure 4.6: Striping patterns in wildtype and *PAX77*$^{+ve}$ mice at 15 and 30 weeks.

A: A typical 15-week old wildtype eye. B: A selection of eyes from 15-week old *PAX77*$^{+ve}$ mice. C: A typical 30-week old wildtype eye. D: A selection of eyes from 30-week old *PAX77*$^{+ve}$ mice. *PAX77*$^{+ve}$ eyes have smaller flattened corneas. *PAX77*$^{+ve}$ eyes exhibit striping patterns at 15 and 30-weeks of age, these patterns are qualitatively similar to those observed in wildtype animals.

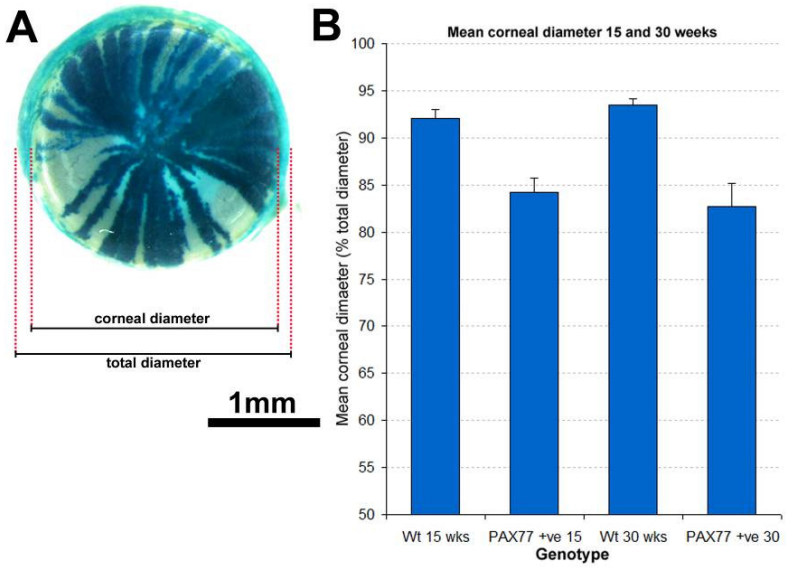

Figure 4.7: Comparison of corneal diameter in wildtype and *PAX77*$^{+ve}$ animals.

A: The total diameter and the corneal diameter of wildtype and *PAX77*$^{+ve}$ eyes were measured. B: The corneal diameter as a percentage of total diameter was plotted at 15 and 30 weeks. This value did not significantly differ between 15 and 30 weeks for either genotype. Furthermore wildtype and *PAX77*$^{+ve}$ values differed significantly at both 15 and 30 weeks (ANOVA P <0.0001, Fisher's PLSD P <0.0001 in all cases). Error bars, 95% confidence intervals; Wt, wildtype.

Table 4.5: Analysis of the effects of *PAX77* genotype and age on corneal diameter.

Genotype and Age	Test	Corneal Diameter ± 95% CI (%Total)	*P*-value
Wildtype 15-weeks (22); Wildtype 30-weeks (36); and $PAX77^{+ve}$ 15-weeks (14); $PAX77^{+ve}$ 15-weeks (20)	One-way ANOVA	See below	<0.0001
Wildtype 15-weeks 'vs' Wildtype 30-weeks	Fisher's PLSD	92.09 ± 0.91 'vs' 93.47 ± 0.64	0.4925
Wildtype 15-weeks 'vs' $PAX77^{+ve}$ 15-weeks	Fisher's PLSD	92.09 ± 0.91 'vs' 84.22 ± 1.55	<0.0001
Wildtype 15-weeks 'vs' $PAX77^{+ve}$ 30-weeks	Fisher's PLSD	92.09 ± 0.91 'vs' 82.69 ± 2.45	<0.0001
Wildtype 30-weeks 'vs' $PAX77^{+ve}$ 15-weeks	Fisher's PLSD	93.47 ± 0.64 'vs' 84.22 ± 1.55	<0.0001
Wildtype 30-weeks 'vs' $PAX77^{+ve}$ 30-weeks	Fisher's PLSD	93.47 ± 0.64 'vs' 93.47 ± 0.64	<0.0001
$PAX77^{+ve}$ 15-weeks 'vs' $PAX77^{+ve}$ 30-weeks	Fisher's PLSD	84.22 ± 1.55 'vs' 82.69 ± 2.45	0.6150

Numbers in parentheses are the number of eyes analysed.

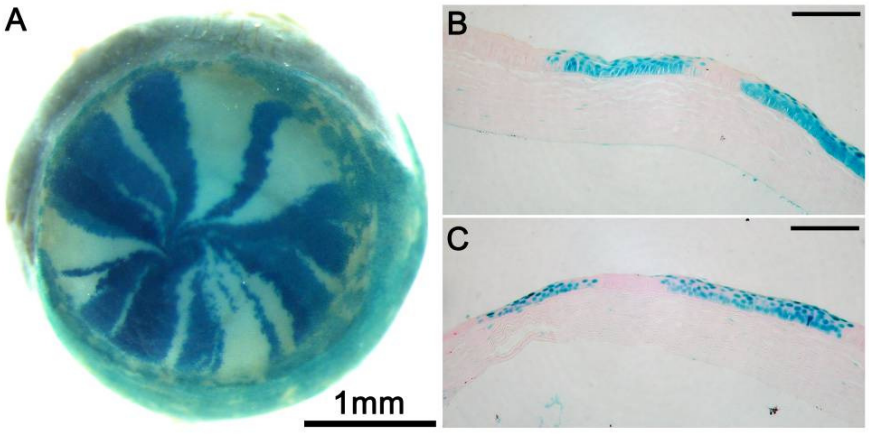

Figure 4.8: Typical sections from a *PAX77*$^{+ve}$ mosaic.

A: A typical *PAX77*$^{+ve}$ eye (sectioned in B-C). B-C: The *PAX77*$^{+ve}$ epithelium is similar in thickness to wildtype epithelium (See Chapter 2, Figure 3). Striping patterns span the entire corneal thickness. Some cell mixing is evident at stripe boundaries. Scale bars in B-C = 100 microns.

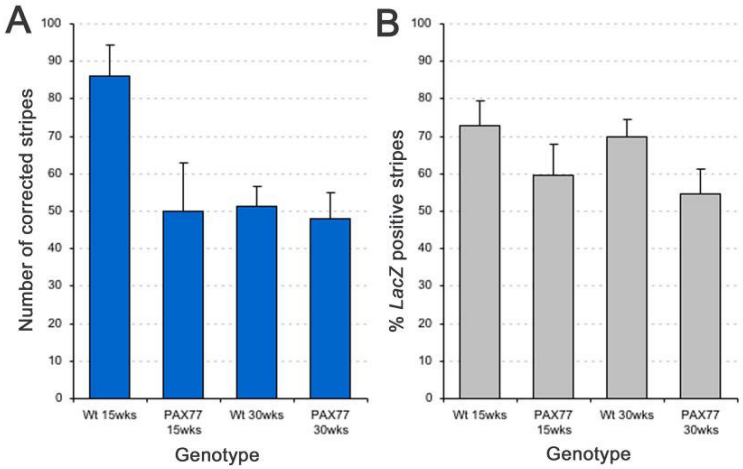

Figure 4.9: Effect of *PAX77* genotype on the corrected stripe number and the percentage contribution of *LacZ*-positive cells to the corneal epithelium.

A: $PAX77^{+ve}$ mice have a significantly reduced corrected stripe number compared to wildtype littermates at 15-weeks (ANOVA P <0.0001, Fisher's PLSD P <0.0001. There is no reduction in corrected stripe number between 15 and 30 weeks in $PAX77^{+ve}$ animals (Fisher's PLSD P = 0.7493). Wildtype corrected stripe number declines between 15 and 30-weeks (Fisher's PLSD P <0.0001). B: The proportion of *LacZ*-positive cells is reduced in $PAX77^{+ve}$ animals at 15 and 30-weeks (ANOVA P = 0.0002, Fisher's PLSD P = 0.0116 and 0.0003 respectively. Error bars, 95% confidence intervals; Wt, wildtype.

Table 4.6: Analysis of the effects of *PAX77* genotype and age on corrected stripe number.

Genotype and Age	Test	Corrected Stripe Number ± 95% CI	*P*-value
Wildtype 15-weeks (22); Wildtype 30-weeks (36); and $PAX77^{+ve}$ 15-weeks (14); $PAX77^{+ve}$ 15-weeks (20)	One-way ANOVA	See below	<0.0001
Wildtype 15-weeks 'vs' Wildtype 30-weeks	Fisher's PLSD	86.05 ± 8.46 'vs' 51.32 ± 5.34	<0.0001
Wildtype 15-weeks 'vs' $PAX77^{+ve}$ 15-weeks	Fisher's PLSD	86.05 ± 8.46 'vs' 50.12 ± 12.66	<0.0001
Wildtype 15-weeks 'vs' $PAX77^{+ve}$ 30-weeks	Fisher's PLSD	86.05 ± 8.46 'vs' 48.05 ± 6.98	<0.0001
Wildtype 30-weeks 'vs' $PAX77^{+ve}$ 15-weeks	Fisher's PLSD	51.32 ± 5.34 'vs' 50.12 ± 12.66	0.8386
Wildtype 30-weeks 'vs' $PAX77^{+ve}$ 30-weeks	Fisher's PLSD	51.32 ± 5.34 'vs' 48.05 ± 6.98	0.5296
$PAX77^{+ve}$ 15-weeks 'vs' $PAX77^{+ve}$ 30-weeks	Fisher's PLSD	50.12 ± 12.66 'vs' 48.05 ± 6.98	0.7493

Numbers in parentheses are the number of eyes analysed.

Table 4.7: Analysis of the effects of *PAX77* genotype and age on percentage contribution of *LacZ*-positive cells.

Genotype and Age	Test	% *LacZ*-positive Number ± 95% CI	*P*-value
Wildtype 15-weeks (22); Wildtype 30-weeks (36); and $PAX77^{+ve}$ 15-weeks (14); $PAX77^{+ve}$ 15-weeks (20)	One-way ANOVA	See below	0.0002
Wildtype 15-weeks 'vs' Wildtype 30-weeks	Fisher's PLSD	72.83 ± 6.63 'vs' 70.01 ± 4.55	0.4868
Wildtype 15-weeks 'vs' $PAX77^{+ve}$ 15-weeks	Fisher's PLSD	72.83 ± 6.63 'vs' 59.69 ± 8.11	0.0116
Wildtype 15-weeks 'vs' $PAX77^{+ve}$ 30-weeks	Fisher's PLSD	72.83 ± 6.63 'vs' 54.5 ± 6.64	0.0001
Wildtype 30-weeks 'vs' $PAX77^{+ve}$ 15-weeks	Fisher's PLSD	70.01 ± 4.55 'vs' 59.69 ± 8.11	0.0306
Wildtype 30-weeks 'vs' $PAX77^{+ve}$ 30-weeks	Fisher's PLSD	70.01 ± 4.55 'vs' 54.5 ± 6.64	0.0003
$PAX77^{+ve}$ 15-weeks 'vs' $PAX77^{+ve}$ 30-weeks	Fisher's PLSD	59.69 ± 8.11 'vs' 54.5 ± 6.64	0.3207

Numbers in parentheses are the number of eyes analysed.

4.3.3 Effects of combined *Pax6* /*Gli3* mutations on eye mass and striping phenotype

Mean eye mass in milligrams was compared for wildtype, $Pax6^{+/-}$, $Gli3^{+/-}$, and $Pax6^{+/-}/Gli3^{+/-}$ X-inactivation females at 15-weeks of age. Figure 4.10 and Table 4.8 outline the results. The wildtype and $Gli3^{+/-}$ groups did not differ significantly. The $Pax6^{+/-}$ group differed significantly from the wildtype and $Gli3^{+/-}$ groups. Furthermore the $Pax6^{+/-}/Gli3^{+/-}$ group differed significantly from the $Gli3^{+/-}$ and wildtype groups. These results suggest that $Gli3^{+/-}$ has no effect on eye mass and that $Pax6^{+/-}/Gli3^{+/-}$ animals have a $Pax6^{+/-}$ eye mass phenotype.

Figure 4.11 shows typical striping patterns for wildtype, $Pax6^{+/-}$, $Gli3^{+/-}$ and $Pax6^{+/-}/Gli3^{+/-}$ eyes at 15 weeks of age. As demonstrated above $Pax6^{+/-}$ eyes are smaller with disrupted striping patterns. The weight data suggested that $Gli3^{+/-}$ eyes did not differ from wildtype and these eyes appeared normal with striping patterns qualitatively similar to wildtype. In the compound heterozygote the striping phenotype is highly varied. Stripes are highly disrupted and may look similar to $Pax6^{+/-}$, or may demonstrate much smaller tighter disorganised patches reminiscent of the striping patterns of eyes at 6-weeks shown in Figure 2.2 of Chapter 2. Eyes D3 and D4 are left and right eyes from the same animal demonstrating markedly different striping patterns. To understand how these patterns may have arisen typical $Gli3^{+/-}$ and $Pax6^{+/-}/Gli3^{+/-}$ eyes (Figure 4.12 A and D) were sectioned. $Gli3^{+/-}$ corneal epithelium appears qualitatively similar to wildtype in section (See Chapter 2 Figure 3). $Pax6^{+/-}/Gli3^{+/-}$ corneal epithelium is qualitatively similar to $Pax6^{+/-}$ (See Figure 3).

Corrected stripe numbers were calculated for wildtype, $Pax6^{+/-}$, $Gli3^{+/-}$ and $Pax6^{+/-}/Gli3^{+/-}$ groups at 15-weeks of age The results are summarised in Figure 4.13 and Table 4.9. There was no statistical difference between corrected stripe numbers for the wildtype and $Gli3^{+/-}$ groups. The $Pax6^{+/-}$ group was significantly reduced when compared to the wildtype group. Furthermore the $Pax6^{+/-}/Gli3^{+/-}$ group differed significantly form both the $Pax6^{+/-}$ and the

wildtype groups. The *Pax6*$^{+/-}$/*Gli3*$^{+/-}$ group did not differ significantly form the *Gli3*$^{+/-}$ group. The difference in the percentage of *LacZ*-positive staining between the wildtype and *Pax6*$^{+/-}$ and the wildtype and *Pax6*$^{+/-}$/*Gli3*$^{+/-}$ groups was significant and the difference in the percentage of *LacZ*-positive staining between the *Gli3*$^{+/-}$ and *Pax6*$^{+/-}$ and the *Gli3*$^{+/-}$ and *Pax6*$^{+/-}$/*Gli3*$^{+/-}$ groups was also significant (Table 4.10).

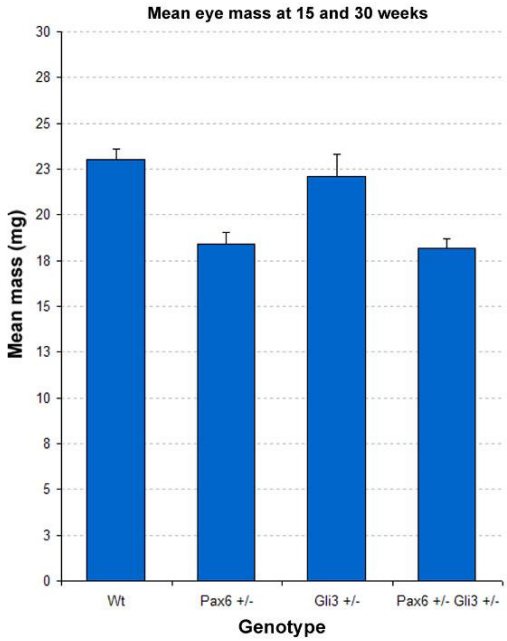

Figure 4.10: Comparison of eye mass in wildtype, *Pax6*$^{+/-}$, *Gli3*$^{+/-}$and combined *Pax6*$^{+/-}$ */Gli3*$^{+/-}$ littermates at 15 weeks.

Average eye weights at 15-weeks for wildtype, *Pax6*$^{+/-}$, *Gli3*$^{+/-}$ and *Pax6*$^{+/-}$/*Gli3*$^{+/-}$ groups were 23.0 ± 0.5 mg, 18.5 ±. 0.7, 22.1 ±. 1.2 mg and 18.2 ± 0.5 mg respectively. The *Pax6*$^{+/-}$ group differed significantly form the wildtype and *Gli3*$^{+/-}$ groups (ANOVA P <0.0001, Fishers PLSD P <0.0001 in both cases. Furthermore the *Pax6*$^{+/-}$/*Gli3*$^{+/-}$ group differed significantly from the wildtype *and Gli3*$^{+/-}$ groups (Fisher's PLSD P <0.0001 in both cases) but not the *Pax6*$^{+/-}$ group (Fisher's PLSD P = 0.6980). The wildtype and *Gli3*$^{+/-}$ groups did not differ significantly (Fisher's PLSD P = 0.1211). Error bars, 95% confidence intervals; Wt, wildtype.

Table 4.8: Analysis of the effects of *Pax6* and *Gli3* genotype on eye mass.

Genotype (all genotypes are 15-weeks old)	**Test**	**Eye Mass ± 95% CI (mg)**	***P*-value**
Wildtype (18): *Pax6*$^{+/-}$ (28); *Gli3*$^{+/-}$ (20); *Gli3*$^{+/-}$/*Pax6*$^{+/-}$ (40)	One-way ANOVA	See below	<0.0001
Wildtype 'vs' *Pax6*$^{+/-}$	Fisher's PLSD	23.0 ± 0.5 'vs' 18.4 ± 0.7	<0.0001
Wildtype 'vs' *Gli3*$^{+/-}$	Fisher's PLSD	23.0 ± 0.5 'vs' 22.1 ± 1.2	0.1211
Wildtype 'vs' *Gli3*$^{+/-}$/*Pax6*$^{+/-}$	Fisher's PLSD	23.0 ± 0.5 'vs' 18.2 ± 0.5	<0.0001
Wildtype 'vs' *Gli3*$^{+/-}$	Fisher's PLSD	18.4 ± 0.7 'vs' 22.1 ± 1.2	<0.0001
Pax6$^{+/-}$ 'vs' *Gli3*$^{+/-}$/*Pax6*$^{+/-}$	Fisher's PLSD	18.4 ± 0.7 'vs' 18.2 ± 0.5	0.6980
Gli3$^{+/-}$ 'vs' *Gli3*$^{+/-}$/*Pax6*$^{+/-}$	Fisher's PLSD	22.1 ± 1.2 'vs' 18.2 ± 0.5	<0.0001

Numbers in parentheses are the number of eyes analysed.

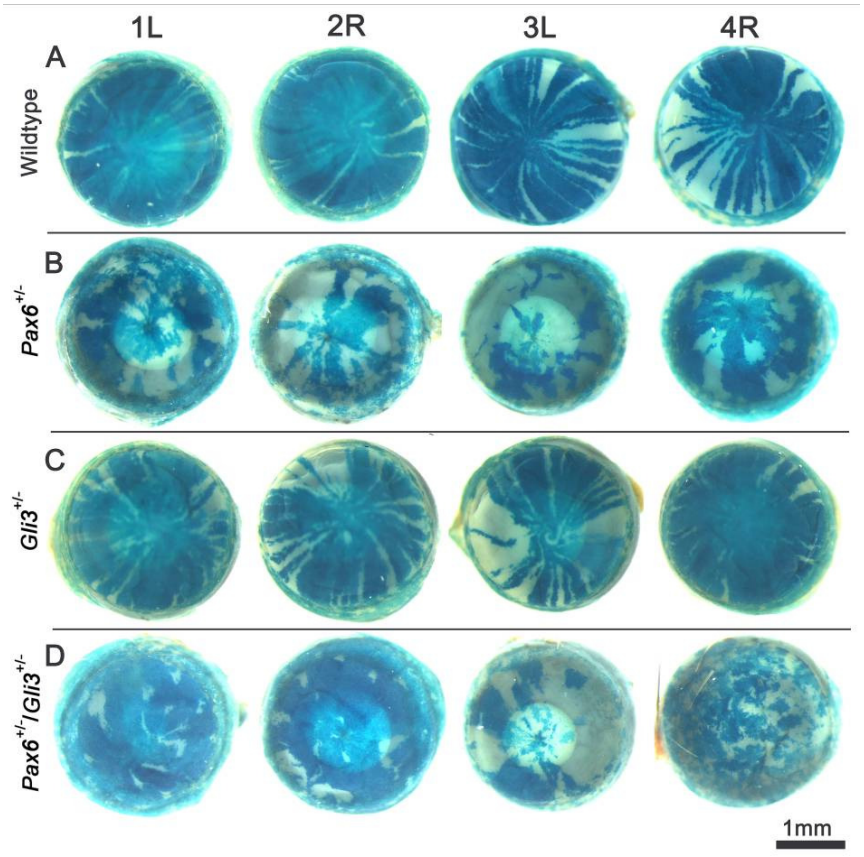

Figure 4.11: Striping patterns in the corneal epithelia of wildtype, *Pax6*$^{+/-}$, *Gli3*$^{+/-}$ and *Pax6*$^{+/-}$/*Gli3*$^{+/-}$ littermates at 15-weeks.

A: A selection of 15-week old wildtype eyes. B: A selection of 15-week old eyes from *Pax6*$^{+/-}$ mice. C: A selection of eyes from 15-week old *Gli3*$^{+/-}$ mice. D: A selection of eyes from 15-week old *Pax6*$^{+/-}$/*Gli3*$^{+/-}$ mice. *Pax6*$^{+/-}$ eyes are smaller with disrupted striping patterns. *Gli3*$^{+/-}$ eyes appear normal with striping patterns qualitatively similar to wildtype. In *Pax6*$^{+/-}$/*Gli3*$^{+/-}$ eyes the striping phenotype is highly varied. Stripes are highly disrupted and may look similar to *Pax6*$^{+/-}$ eyes or may demonstrate much smaller tighter disorganised patches. Eyes D3 and D4 are left and right eyes from the same animal demonstrating markedly different striping patterns.

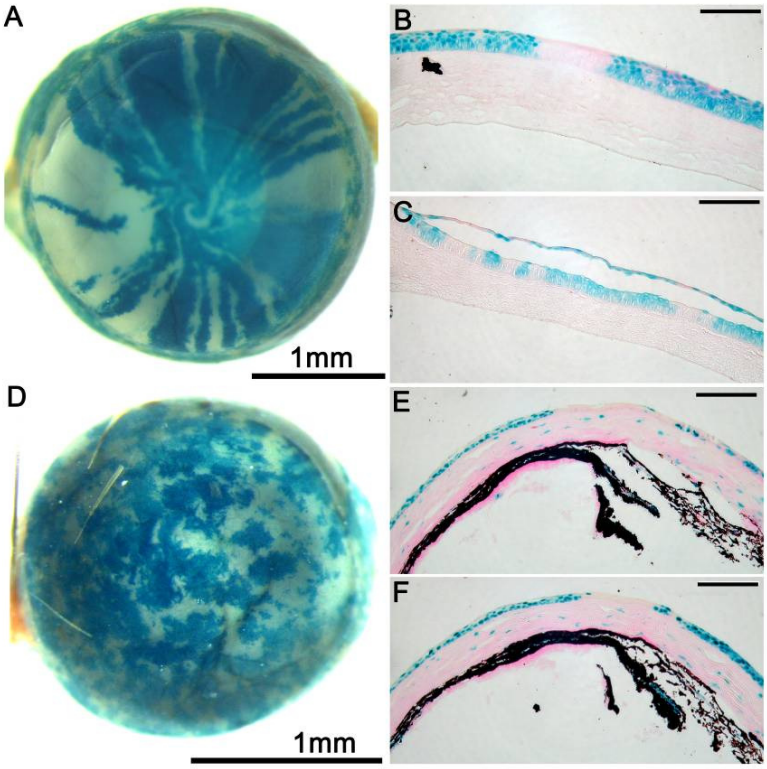

Figure 4.12: Typical sections from a *Gli3*$^{+/-}$ and *Pax6*$^{+/-}$*/Gli3*$^{+/-}$ mosaic eyes.

A and D: *Gli3*$^{+/-}$ and *Pax6*$^{+/-}$*/Gli3*$^{+/-}$ eyes were sectioned. B-C: *Gli3*$^{+/-}$ corneal epithelium appears qualitatively similar to wildtype in section (See Chapter 2 Figure 3). E-F: *Pax6*$^{+/-}$*/Gli3*$^{+/-}$ corneal epithelium is qualitatively similar to *Pax6*$^{+/-}$ (See Figure 3). Scale bars in B-F = 100 microns.

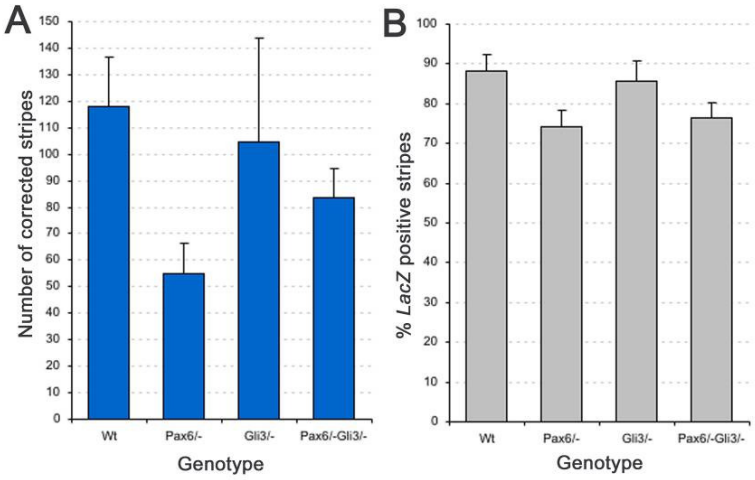

Figure 4.13: Effect of *Pax6* and *Gli3* genotype on the corrected stripe number and the percentage contribution of *LacZ*-positive cells to the corneal epithelium.

A: The number of corrected stripes in the eyes of $Pax6^{+/-}/Gli3^{+/-}$ animals is significantly greater than $Pax6^{+/-}$ (ANOVA P <0.0001, Fisher's PLSD P = 0.0126). Mice harbouring the $Gli3^{+/-}$ mutation show no significant difference in corrected stripe number when compared to wildtype littermates (Fisher's PLSD P = 0.3912). B: The proportion of *LacZ*-positive cells is significantly reduced in all $Pax6^{+/-}$ and $Pax6^{+/-}/Gli3^{+/-}$ animals compared with wildtype (ANOVA P <0.0001, Fisher's PLSD P = 0.0001 and 0.0004 respectively). Error bars, 95% confidence intervals; Wt, wildtype.

Table 4.9: Analysis of the effects of *Pax6* and *Gli3* genotype on corrected stripe number.

Genotype (all genotypes are 15-weeks old)	**Test**	**Corrected Stripe Number ± 95% CI**	***P*-value**
Wildtype (18): *Pax6*$^{+/-}$ (28); *Gli3*$^{+/-}$ (20); *Gli3*$^{+/-}$/*Pax6*$^{+/-}$ (40)	One-way ANOVA	See below	<0.0001
Wildtype 'vs' *Pax6*$^{+/-}$	Fisher's PLSD	118.01 ± 18.74 'vs' 54.97 ± 11.55	<0.0001
Wildtype 'vs' *Gli3*$^{+/-}$	Fisher's PLSD	118.01 ± 18.74 'vs' 104.61 ± 39.08	0.3912
Wildtype 'vs' *Gli3*$^{+/-}$/*Pax6*$^{+/-}$	Fisher's PLSD	118.01 ± 18.74 'vs' 83.48 ± 11.30	0.0088
Wildtype 'vs' *Gli3*$^{+/-}$	Fisher's PLSD	54.97 ± 11.55 'vs' 104.61 ± 39.08	0.0007
Pax6$^{+/-}$ 'vs' *Gli3*$^{+/-}$/*Pax6*$^{+/-}$	Fisher's PLSD	54.97 ± 11.55 'vs' 83.48 ± 11.30	0.0126
Gli3$^{+/-}$ 'vs' *Gli3*$^{+/-}$/*Pax6*$^{+/-}$	Fisher's PLSD	104.61 ± 39.08 'vs' 83.48 ± 11.30	0.1193

Numbers in parentheses are the number of eyes analysed.

Table 4.10: Analysis of the effects of *Pax6* and *Gli3* genotype on percentage contribution of *LacZ*-positive cells.

Genotype and Age	**Test**	**% *LacZ*-positive Number ± 95% CI**	***P*-value**
Wildtype (18): *Pax6*$^{+/-}$ (28); *Gli3*$^{+/-}$ (20); *Gli3*$^{+/-}$/*Pax6*$^{+/-}$ (40)	One-way ANOVA	See below	<0.0001
Wildtype 'vs' *Pax6*$^{+/-}$	Fisher's PLSD	88.18 ± 4.14 'vs' 74.36 ± 4.11	0.0001
Wildtype 'vs' *Gli3*$^{+/-}$	Fisher's PLSD	88.18 ± 4.14 'vs' 85.58 ± 5.26	0.5087
Wildtype 'vs' *Gli3*$^{+/-}$/*Pax6*$^{+/-}$	Fisher's PLSD	88.18 ± 4.14 'vs' 76.35 ± 3.99	0.0004
Wildtype 'vs' *Gli3*$^{+/-}$	Fisher's PLSD	74.36 ± 4.11 'vs' 85.58 ± 5.26	0.0022
Pax6$^{+/-}$ 'vs' *Gli3*$^{+/-}$/*Pax6*$^{+/-}$	Fisher's PLSD	74.36 ± 4.11 'vs' 76.35 ± 3.99	0.4834
Gli3$^{+/-}$ 'vs' *Gli3*$^{+/-}$/*Pax6*$^{+/-}$	Fisher's PLSD	85.58 ± 5.26 'vs' 76.35 ± 3.99	0.0075

Numbers in parentheses are the number of eyes analysed.

4.4 DISCUSSION

Changes in the basal level of PAX6 can have dramatic effects on ocular phenotype in mice. *Pax6*$^{+/-}$ mice exhibit small-eye and a plethora of other ocular defects. These animals exhibit thinner corneal epithelia and, in X-inactivation mosaics, striping patterns are disrupted. It has been suggested that this could be due to a cell non-autonomous diversion of epithelial migration or a LSC deficiency (Collinson et al., 2004a). Interestingly over expression of PAX6 also yields a range of effects from almost normal eye size to severe microphthalmia. It should be noted that the variation between eyes of the same animal is great in this group. For this reason the authors suggest that effects other than genetic background may be interfering with eye specification (Schedl et al., 1996). Recent evidence shows that as well as having mild effects on ocular phenotype *Gli3*$^{+/-}$ can interact with *Pax6*$^{+/-}$ to produce an ocular phenotype more severe than would be expected just by addition of the two phenotypes (Zaki et al., 2006).

This study has demonstrated that *Pax6*$^{+/-}$ eye mass is consistently lower than in wildtype littermates. Whilst *Pax6*$^{+/-}$ eyes are smaller at 15 and 30-weeks of age, like wildtype they increase in mass over these time points. Mean *Pax6*$^{+/-}$ eye mass increases from ~17 mg to ~19 mg between 15 and 30 weeks whilst wildtype mass increases from ~23 mg to ~25 mg. As shown previously the *Pax6*$^{+/-}$ eye has a thinner corneal epithelium. *LacZ*-positive cells may appear to be more prominent in the stroma of these corneas because the thinner epithelium allows more efficient penetration of the X-gal substrate. It is also the case that wildtype corneas have a largely acellular stroma whilst *Pax6*$^{+/-}$ animals exhibit hypercellularity of the corneal stroma associated with infiltration by inflammatory cells (Ramaesh et al., 2003). Therefore as well as possible increased X-gal penetration there are more cells present in the stroma to be stained in the first place. As well as effects on eye mass and epithelial thickness, *Pax6*$^{+/-}$ have disrupted X-inactivation striping patterns. Although some striping is still apparent the majority of staining reveals orientated patches

rather than stripes. This may result, as suggested by Collinson et al (2004), from a disruption of non cell autonomous guidance. Or it may be due to migration of epithelial cells to heal wounds, more common because of the increased fragility of the *Pax6*$^{+/-}$ epithelium (Ramaesh et al., 2003). Combined with the fact the *Pax6*$^{+/-}$ epithelium is thinner this implies a requirement for a much more dramatic reorganisation of the epithelium including the basal layer in order to heal a wound. Wounding may not have the same effect on striping patterns in the wildtype cornea because a wound would be less likely to extend to the basal layer (wildtype epithelium is 6-8 cells thick). Thus in wildtype cornea, TACs may be left intact in the basal layer and could modulate their proliferative potential (Pellegrini et al., 1999) and expand rapidly to heal the wound clonally. This would avoid the disruption of striping patterns seen in *Pax6*$^{+/-}$ animals because cells from adjacent clones must be diverted to heal the wound.

PAX77^{+ve} eyes do not have lower eye mass when compared to wildtype littermates. Whereas the increase in mean eye mass in wildtype littermates is significant (~25 mg to ~28 mg) the increase in mean eye mass for *PAX77*$^{+ve}$ animals is not. This may represent greater variability in eye size at older ages or be due to the small sample size (n = 14 and 20 for *PAX77*$^{+ve}$ at 15 and 30 weeks compared to n = 22 and 36 for wildtype). Despite the similarity in eye mass, corneal diameter (% of total diameter) is significantly reduced in *PAX77*$^{+ve}$ animals (~ 83% in *PAX77*$^{+ve}$ animals compared to ~93% in wildtype animals). It is interesting that whilst under expression of Pax6 reduces total eye size. Over expression only appears to effect corneal size on this background. Corneal thickness appears normal in these animals and striping patterns are also qualitatively similar to wildtype. Taken together with the results for *Pax6*$^{+/-}$ animals these data again suggest that there is an implied link between epithelial thickness and integrity of striping patterns. There appears to be little variation between the eyes of the same animal in these data. This suggests that unlike in the original

Schedl paper (1993) where unilateral defects were described, on this background corneal defects are predominantly bilateral.

Gli3$^{+/-}$ animals do not have defects in eye mass, corneal thickness or striping patterns however *Pax6*$^{+/-}$ and *Pax6*$^{+/-}$/*Gli3*$^{+/-}$ littermates have a reduced eye size at 15 weeks (~18 mg compared with ~23 mg for wildtype). Eye mass and corneal thickness is reduced in all animals that are *Pax6*$^{+/-}$. These features would be expected from the *Pax6*$^{+/-}$ phenotype alone. However striping patterns are more heavily disrupted in a subset of *Pax6*$^{+/-}$/*Gli3*$^{+/-}$ corneas than in animals that have *Pax6*$^{+/-}$ alone. As in previous studies (Zaki et al 2006) it is demonstrated here that there are additional aspects to the *Pax6*$^{+/-}$/*Gli3*$^{+/-}$ phenotype that suggest an interaction between Pax6 and Gli3. In the corneal epithelium this genotype has phenotypic effects on tissue homeostasis.

X-inactivation mosaics have been used previously to conduct clonal analyses on striping patterns in wildtype (Collinson et al., 2002) and *Pax6*$^{+/-}$ (Collinson et al., 2004a) corneal epithelium. Building on this work, clonal analyses were conducted here on all *Pax6*$^{+/-}$ and *PAX77*$^{+ve}$ animals and their wildtype littermates at 15 and 30 weeks of age. Furthermore *Pax6* and *Gli3* mutations were combined in a complementation study and clonal analyses conducted at 15 weeks. The results demonstrate that both *Pax6*$^{+/-}$ (on both backgrounds) and *PAX77*$^{+ve}$ animals exhibit corrected stripe numbers of around 50 at 15-weeks of age and that there is no apparent reduction up to 30-weeks (as might be expected from the results summarised in chapter 2). Although in the data discussed here the difference between *Pax6*$^{+/-}$ and wildtype littermates was not significant (this maybe due to the combined factors of a small sample size and very high contribution of *LacZ*-positive cells to the tissue) the results from the *Pax6*$^{+/-}$/*Gli3*$^{+/-}$ group help highlight the general pattern first described by Collinson et al (Collinson et al., 2004a) where the *Pax6*$^{+/-}$ genotype reduces the number of coherent corneal epithelial clones.

The clone numbers quoted here and in previous reports (Collinson et al., 2004a; Collinson et al., 2002) do not represent actual numbers of limbal stem cells, they are a comparative measure of the number of coherent clones present in the tissue (thought to be proportional to the actual number of limbal stem cell clones). However it is still striking that the numbers of coherent clones seen in *Pax6*$^{+/-}$, *Pax6*$^{+/-}$/*Gli3*$^{+/-}$ and *PAX77*$^{+ve}$ animals seems to stabilise at ~50 and show no decline with age. In Chapter 2 it was suggested that ~50 coherent clones was the lowest number sufficient to maintain the epithelium in wildtype animals. The evidence presented here further implicates this number as a crucial sufficient number to maintain an intact epithelium. In these mutant animals the stripe number has either dramatically declined before 15 weeks of age or the arrangement of clones has been altered so that fewer are initially specified during development. One way that this may happen is due to changes in cell-cell adhesion which increase the likelihood of cells remaining adjacent to each other after cell division, thus leading to larger 'clumps' of a given lineage. It has been demonstrated that *Pax6*$^{-/-}$ and *Pax6*$^{+/-}$ cells have different cell adhesion properties than wildtype cells in the developing brain. In *Pax6*$^{+/-}$ mice the segregation of cortical and striatal cells into aggregates in the developing forebrain is lost due to changes in the expression of the homophillic adhesion molecule R-cadherin. (Stoykova et al., 1997). Furthermore when *Pax6*$^{-/-}$ embryonic cortical cells were transplanted into wildtype embryonic cortex (in explant cultures) they were seen to segregate from wildtype cells and form dense clusters (Tyas et al., 2003).

To investigate whether the apparent reduction in corrected clone number in *Pax6*$^{+/-}$ animals could be due to an effect on the randomness of clumping before the formation of stripes, an analysis of clumping in *Pax6*$^{+/-}$ and wildtype animals was performed using the same method of clonal analysis (analysis kindly performed by Jayne Murphy an honours student). These data suggest that rather than an increase in the size of clumps in the embryonic tissue there are actually more clumps in the *Pax6*$^{+/-}$ corneas (n = 15) than in wildtype (n = 12). A centred

circular selection 80% of the corneal diameter spanned 140.3 $\pm$ 26.72 corrected patches in the *Pax6*$^{+/-}$ cornea compared to 90.85 $\pm$ 18.76 in the wildtype, this difference was statistically significant (T-test P = 0.0046, data not shown). This strengthens the evidence that the striping defect is due to a reduction in the actual number of LSCs specified during development rather than a change in the 'randomness' of cell clumping during this period. As the number of wildtype corrected clones at 3-weeks is similar to the number of corrected clones at 15 weeks, it follows that a single coherent stem cell clone is specified for every coherent clone that spans the limbus at three weeks. However in the *Pax6*$^{+/-}$ group despite there being around 140 patches close to the limbus (a greater number than in wildtype), the adult tissue contains only around 30% of this number in coherent clones, further strengthening the hypothesis that a LSC deficiency is causal in the epithelial defects observed. The LSC deficiency may be due to a cell autonomous defect restricting the ability of cells to occupy the available stem cell niche. Equally it may be due to changes in the micro architecture of the stem cell niche restricting the number of clones it can support, or the number of stem cells that remain quiescent. This may mean that less stem cells are sequestered to the niche during development or that the number of stem cells allowed to proliferate is restricted.

Mice heterozygous for both *Pax6*$^{+/-}$/*Gli3*$^{+/-}$ exhibit a partially rescued stripe number when compared to *Pax6*$^{+/-}$ and wildtype littermates. This does not represent a true rescue of phenotype but rather the presence of a distinct ocular phenotype in a subset of these eyes that demonstrate highly disrupted striping patterns. It has been suggested that Pax6 and Gli3 may interact through the sonic hedgehog (*Shh*) signalling pathway (Zaki et al., 2006). Gli3 is a known modulator of Shh signalling (Ruiz i Altaba, 1999) whilst *Pax6* null animals exhibit disrupted Shh signalling in the telencephalon (Stoykova et al., 2000). Interaction of these genes may be particularly important for stem cell populations in the eye. Pax6 and Gli3 are both expressed in the retinal stem cells of *Xenopus*, fish and chick where they are thought to

have roles in multipotencey and proliferation (Fischer and Reh, 2000; Hitchcock et al., 1996; Perron et al., 2003; Perron et al., 1998). Recent insights into Pax6 function in the retina suggest that it controls the multipotent state of retinal progenitors, conditional mutation of *Pax6* restricts the lineage of these progenitors so that they only generate amacrine cells (Marquardt et al., 2001) similarly it could act here to restrict the numbers of LSCs. Gli3 is a marker of retinal stem cells; it may interact with Shh to increase the proliferation rate of mouse retinal embryonic precursors. (Jensen and Wallace, 1997). Furthermore it is thought that Hh signalling from ganglion cells to the retinal pigment epithelium (RPE) may instruct stem cells to maintain a proliferative state (Perron et al., 2003). So perhaps a change in Shh signalling modulated by combined *Pax6/Gli3* defects allows basal cells of the corneal epithelium to retain their proliferative potential at least up to 15-weeks of age meaning that, in a subset of eyes at least, the X-inactivation patterns remain juvenile in nature rather than maturing into the orientated patches observed in littermates.

4.4.1 Conclusions

This study provides evidence that under-expression of Pax6 has effects on eye size, corneal thickness and striping phenotype. Whilst over-expression of PAX6 in the mouse has effects on corneal size but not on eye mass, corneal thickness or striping patterns. Furthermore combining $Pax6^{+/-}$ and $Gli3^{+/-}$ genotypes gives the general features of $Pax6^{+/-}$ but with the addition of a more severe striping defect. This implies an interaction between Gli3 and Pax6. Whilst Pax6 and Gli3 are not thought to interact directly, the Shh pathway, into which both genes feed, is an excellent candidate to mediate this interaction. Shh signalling has roles in modulating the wound healing response in the mouse corneal epithelium. Corneal epithelial debridement has been shown to cause a transient up-regulation of Shh expression resulting in activation of Shh/Gli3 signalling during the wound healing response (Saika et al., 2004). Evidence is provided here that $Pax6^{+/-}$ animals have a LSC deficiency. However the mechanism causing reduced corneal thickness seems to be distinct from the LSC defect as

PAX77^{+ve} animals have a reduced corrected stripe number but intact epithelia. Furthermore work in *Pax6*$^{+/-}$ ↔ wildtype chimeras shows that whilst under represented in the corneal epithelium, *Pax6*$^{+/-}$ cells can contribute to a full thickness epithelium (Collinson et al., 2004a). As wildtype animals have a similar clone number at 30-weeks it is clear that other factors as well as LSC deficiency must contribute to the corneal defects in these animals.

Chapter 5
Wound Healing Responses and Their Effects on Striping Patterns in the Mouse Corneal Epithelium

5.1 INTRODUCTION

The corneal epithelium is an excellent model system for the study of epithelial wound healing because it is a discrete epithelium with well defined cellular compartments and a regionalised stem cell population. The corneal epithelium is responsible for the protection of the anterior segment of the eye preventing the penetration of exogenous agents and pathogens. In order to maintain the visual properties of the eye it must also maintain a continuous, smooth refractive surface. To do this the epithelium is constantly replenished by TACs that migrate inwards from limbal stem cells at the periphery of the tissue (For a more detailed discussion of these processes please see Chapter 1). As well as responding quickly to injury the wound healing process must be scar-free as this would compromise the refractive properties of the tissue. Many factors have been implicated specifically in corneal epithelial wound healing. These include proposed stem cell markers such as p63 (Di Iorio et al., 2005) and α9β1 integrin (Pal-Ghosh et al., 2004), modulators of stromal remodelling such a matrix metalloproteinase's (MMPs) (Ramamurthi et al., 2006), changes in calcium signalling (Leiper et al., 2006), modulation of electrical signals (Reid et al., 2005; Zhao et al., 2006b) and the effects on these processes by mutations in the so-called master gene of eye development *Pax6* (Kucerova et al., 2006; Ramaesh et al., 2006; Sivak and Fini, 2002; Sivak et al., 2000). The ability to culture corneal epithelium *ex-vivo* in a whole-organ culture system opens the possibility of imaging these wound healing processes using time-lapse microscopy.

Corneal epithelial wound healing proceeds through 3 stages; an initial migratory stage to cover the wound, a proliferative stage to restore the epithelial thickness and a period of

differentiation to restore the epithelium's complex structure (Suzuki et al., 2003). After a corneal insult, neighbouring undamaged cells begin to migrate to cover the wound with a monolayer of cells. Kuwabara et al (1976) Describe how this re-epithelialisation of a corneal wound is facilitated by 'epithelial sliding' a mechanism first observed by Peters (1885). They describe the way epithelial cells migrate in an amoebic fashion without the need for mitotic activity. Each cell spreads out from its leading edge extending fan shaped lamellipodia. This initial sliding, ruffling monolayer has been observed by time-lapse, phase-contrast imaging (Murakami et al., 1992). Zhao et al (2003) used a novel approach that combined Hoffman modulation optics with digital photography allowing 3-dimensional time-lapse imaging of corneal epithelial wound healing. Wounds were created in human and bovine eyes by scratching with a scalpel blade. Live cells were imaged *ex-vivo* using a whole eye culture system for up to 2 days. The group showed that in its early stages, epithelial wound healing proceeds predominantly through an 'epithelial sliding' mechanism. Only 5% of cells changed layers as the wounds healed with equal proportions moving up and down within the epithelial layer (Zhao et al., 2003). After this initial sheet-like movement of cells there is a landslide like movement of the remaining epithelium en-masse to completely cover the wound. Once the wound has been completely covered cells begin to proliferate in order to restore the typical epithelial thickness, After a number of weeks, cells in the wound area begin to differentiate restoring the epithelium to a smooth well layered structure (Suzuki et al., 2003).

Crosson et al (1986) showed that healing of wounds in the rabbit cornea involved a biphasic response. They showed that an initial latent phase lasted around 5 hours in which epithelial migration was negligible. Following this they describe a 'linear healing phase' in which cells migrated at a constant rate until the wound was completely healed. Epithelial wound closure occurs in an essentially linear manner. This means it is possible to calculate the wound healing rate by linear regression analysis (Ubels et al., 1982). However when conducting

wound healing experiments careful control of the wound size is required (Matsuda et al., 1985; Ramaesh et al., 2006). Matsuda et al (1985) showed *in-vivo* that larger wounds heal at a faster rate in the rabbit corneal epithelium. The authors found that there was a strong correlation between the wound healing rate and the initial wound area. Similarly Ramaesh et al (2006) found that larger wounds healed at a faster rate in both wildtype ($Pax6^{+/+}$) and $Pax6^{+/-}$ eyes in ex-vivo organ culture.

The *Pax6* gene is essential for normal development of the eye and the corneal epithelium (For detailed discussion see Chapter 1). Pax6 activity is known to be upregulated during re-epithelialisation of the cornea and it has been shown to interact with the promoter region of the MMP9 gene (Sivak et al., 2000). Furthermore it is known that suppression of Pax6 activity is required for EGF induced proliferation in corneal epithelial cells (Li and Lu, 2005). Ramaesh et al (2006) showed that the rate of wound healing in whole eye organ culture was greater for $Pax6^{+/-}$ eyes and for those with larger wounds. The authors also showed that $Pax6^{+/-}$ eyes exhibit greater stromal cell apoptosis and that cultured $Pax6^{+/-}$ cells had a lower MMP-9 activity than $Pax6^{+/+}$ cells. Kucerova et al (2006) used lectin cytochemistry to demonstrate that $Pax6^{+/-}$ corneal epithelial cells have a partial defect in glycoprotein trafficking. Disruption of carbohydrate moieties on the surface of corneal epithelial cells produced similar wound healing delays to those observed in $Pax6^{+/-}$ cells. Taken together these evidence suggest that the altered cell surface glycoconjugate signature of $Pax6^{+/-}$ cells may underlie the restriction in the ability of cultured cells to initiate a migratory wound healing response. Calcium (Ca^{2+}) signalling is an important intracellular signalling mechanism with effects on wound healing rates. Walker et al (2004) showed that wound healing rates in low Ca^{2+} conditions were double the rate of those in normal Ca^{2+}. Furthermore defective calcium signalling in $Pax6^{+/-}$ corneal epithelial cells has been implicated in the wound healing delay observed in these cells. Leiper et al (2006) showed

that the degree of propagation of the intracellular calcium wave in *Pax6*$^{+/-}$ cells was reduced and that this defective response could be restored by exogenous EGF.

A number of systems exhibit striping in the corneal epithelium, including X-inactivation mosaics, GFP mosaics and chimeras (Collinson et al., 2002; Nagasaki and Zhao, 2003; West, 1999). To date no group has investigated how striping patterns in the corneal epithelium are disrupted by wounding and the wound healing process. By imaging how stripes behave in a wound healing context it may be possible to develop a better understanding of how individual cells and individual clones of cells behave in such a context. As cells migrate to heal an epithelial defect they must modulate their stromal and cell-cell interactions in a cycle that allows them to migrate but also to maintain a degree of adherence to the underlying stroma and neighbouring cells, essential to preserve the integrity of the epithelium (Suzuki et al., 2003). These processes may have implications for the degree in which cells are able to mingle laterally. Specifically it would be interesting to ascertain whether the cells in a single epithelial stripe, migrate in a clonal manner or whether the change in cell-cell binding properties allows mixing between clones so that a wound is covered by a mixed population of cells rather than by an extension of the existing striping patterns.

5.1.1 Experimental Aims

This chapter looks at the effects on striping patterns of wound healing in the adult corneal epithelium. Given the proposed mechanism of stripe formation by migration of TACs along the epithelium's basal layer with little cell mixing between clones, it asks whether stripes can be reconstituted by wound healing after complete removal of the central cornea. This question is first addressed using whole-eye organ culture of X-inactivation eyes. Subsequently the ability to image wound healing and striping patterns using whole-eye organ culture and time-lapse confocal microscopy in GFP mosaics is evaluated. The chapter attempts to address whether clones of cells remain contiguous during the wound healing process. Occasionally wildtype (*Pax6*$^{+/+}$) X-inactivation eyes exhibit disrupted striping patterns and demonstrate two whorls of blue and white cells. The whole eye organ culture system described here is used to demonstrate whether these patterns may be formed by healing of an off centre wound in the corneal epithelium. Furthermore given the disruption of striping patterns in *Pax6*$^{+/-}$ eyes (described in Chapter 4) wound healing in these eyes is also investigated. ImageJ is a flexible freeware image analysis package available online and described in Chapter 3 of this thesis. Here its usefulness in constructing and analysing time-lapse sequences is assessed. It is used to construct AVI files of confocal time lapse sequences, to measure the rate of migration of individual stripes and the rate of closure of epithelial wounds and to enhance images so that individual stripes can be viewed in isolation.

5.2 MATERIALS AND METHODS

5.2.1 Animals

The H253 transgenic line, the production of *XLacZ*$^{+/-}$ mosaics and the staining of tissues from these animals are all described in the Materials and Methods section of Chapter 2. Wound healing experiments were also done using PAX-GFP-transgenic mice on a *Pax6*$^{+/+}$ background and small eye (*Pax6*$^{+/-}$) backgrounds. These animals are described in more detail in Chapter 2 and 4.

5.2.2 Fluorescein and X-gal staining

Female X-inactivation mice were killed by cervical dislocation and both eyes were wounded in-situ. The outline of the wound was marked on the corneal epithelium using a 1mm trephine. The full thickness of the epithelium within this region was then removed using an Algerbrush rust ring remover with a 0.5 mm burr (ALTOMED). Wounds were kindly made by Dr Thaya Ramaesh. After wounding the eye was enucleated and placed in warm MEM containing 10% (vol/vol) FBS, 0.5% glutamine (vol/vol) and 0.5% (vol/vol) antibiotic/mycotic. Eyes were stained with fluorescein 1.0% wt/vol (Chauvin Pharmaceuticals Ltd, Surrey, UK) and photographed under blue light with a Nikon Coolpix 995 digital camera mounted on a Wild M5A dissecting microscope. Eyes were then briefly washed in PBS containing 1% (vol/vol) antibiotic/mycotic, followed by 2 washes in PBS. Eyes were cultured pointing upwards in a multiwell culture dish in MEM containing 10% (vol/vol) FBS, 0.5% glutamine (vol/vol) and 0.5% (vol/vol) antibiotic/mycotic. Eyes were cultured overnight at 37^{o}C and then photographed again with fluorescein. After staining the eyes were lightly fixed for 2 hours in 0.2% (vol/vol) glutaraldehyde solution in 0.1M sodium phosphate buffer (pH7.3), 2mM $MgCl_2$, 5mM EGTA, for 2 hours at 4^{o}C. Eyes were subsequently X-gal stained as described in the Materials and Methods section of Chapter 2.

5.2.3 Time-lapse microscopy

To take time-lapse images of wound healing in the corneal epithelium, PAX6-GFP eyes on both *Pax6*$^{+/+}$ and *Pax6*$^{+/-}$ backgrounds were wounded as described above. After wounding the eye was enucleated and placed in warm clear (without phenol red) MEM containing 10% (vol/vol) FBS, 0.5% glutamine (vol/vol) and 0.5% (vol/vol) antibiotic/mycotic. The dish was placed on a heat pad in an environmental chamber containing 5% CO_2 (95% air) on the stage of a Leica inverted confocal microscope. Figure 5.2 shows schematically the equipment used. Eyes were suspended on a specially designed stand formed from a black-plastic coated paper clip (Woolworths). Z-stack images of a PAX6-GFP eye imaged with the inverted scope. Z-stacks were merged into single files and enhanced using the following macro in ImageJ (National Institute of Health, USA); there are 24 images in the stack in this example but this number varied with overall diameter of the eye:

Time Lapse Macro 1:

```
run("8-bit");
run("Z Project...", "start=1 stop=24 projection=[Max Intensity]");
run("Despeckle");
run("Enhance Contrast", "saturated=0.5");
run("Size...", "width=512 height=512 constrain interpolate");
saveAs("Tiff", "C:\\.....);
close();
close();
```

8-bit black and white images were used because of the superior contrast obtained. Image resolution was converted to 512 x 512 pixels to reduce the overall size of the AVI files. Once

all stacks were converted to single images they were opened as an ‘Image Sequence’ (File>Import>Image Sequence) and converted into an AVI file (File>Save As>AVI..). Although more time consuming than using software such as Imaris this process allowed a lot more flexibility in cutting together different frames and synchronising multiple experiments, initially taken using different time intervals. Using the ‘linear selection’ tool and the ‘measure’ command in ImageJ it is possible to make frame by frame measurements of the rate of migration of a point on the edge of a wound within the resulting AVI file.

In order to track individual stripes in ImageJ the “Manual Tracking” plugin (Fabrice Cordelières, Institut Curie, Orsay, France) was used to produce overlays of dots and lines on the AVI files produced. This plugin is also an excellent way of tracking movements and measuring distances, however because the whole eyes were moving between frames as well as the wound healing movement these measurements were made manually instead. In order to define stripe edges and produce AVI files of individual stripes an ImageJ plugin was used that incorporated a median filter and the ‘find edges’ command. Advice on ImageJ macros was kindly provided by Dr Gabriel Landini (University of Birmingham):

Time Lapse Macro 2:

```
run("Median...", "radius=1 stack");

run("Find Edges", "stack");

setMinAndMax(0, 127);
```

The surrounding stripes were then masked off so that the movement of the stripes of interest could be observed in isolation.

5.3 RESULTS

5.3.1 Stripes reform in whole eye organ culture after wounding

To determine whether corneal wounds heal in a clonal manner, eyes from *XLacZ*$^{+/-}$ mosaic mice were wounded. After wounding eyes were stained with fluorescein to visualize the wound margin. Fluorescein fluoresces under blue light when it is in contact with the underlying stroma, it does not fluoresce in contact with intact epithelium. Eyes were cultured for 0, 6 and 24 hours before being stained with fluorescein again and then fixed and X-gal stained to visualize striping patterns. Fig 5.1 (C and F) shows clearly that after 24-hours of culture a central wound is completely healed (as shown by the complete lack of florescence) and that striping patterns extend from the edge of the wound to its centre. It is clear from these images that stripes remain contiguous throughout the wound healing process.

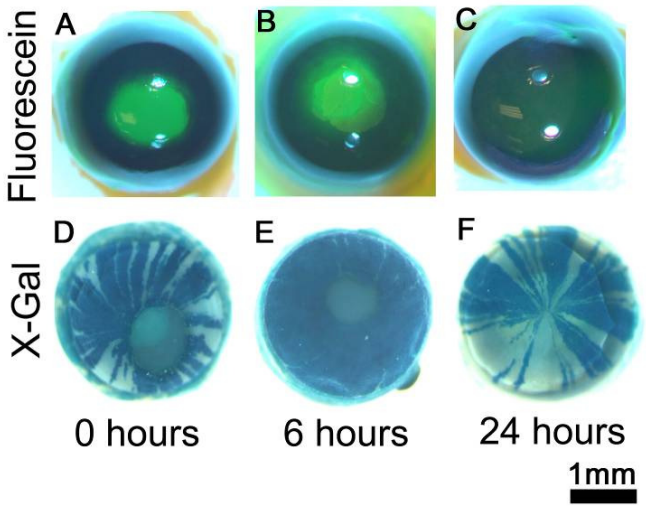

Figure 5.1: Stripes reform in culture after wound healing.

Dissected eyes were cultured for 0, 6 and 24 hours after removal of a 1mm piece of central cornea. Wound margins were visualised using fluorescein staining (A-C) and striping patterns visualised by subsequent X-gal staining (D-F). A: A 1mm central wound was made through the depth of the epithelium. B: After 6 hours some healing was evident. C: By 24 hours the wound as visualised by fluorescein staining was completely healed. F: X-gal staining revealed that stripes extended to the centre of the wound by 24 hours.

5.3.2 Confocal imaging of GFP-positive corneas

The X-inactivation, *LacZ* system described in detail in chapters 2-4 of this thesis is not appropriate for studying stripes in an *ex-vivo* time-lapse culture system. For these purposes it was decided to attempt to develop a GFP-based system so that eyes could be wounded and then imaged using a confocal microscope. Figure 5.2 A shows the set up used. Eyes were wounded as described in the Materials and Methods section. In order to balance the wounded eye so that it could be viewed by the inverted scope it was placed on a carefully designed stand (Figure 5.2 B) fashioned from a black paperclip. Z-Stacks could then be taken and merged to produce images of the GFP positive eyes. Figure 5.2 C shows a Z-stack produced by imaging a fixed PAX6-GFP eye using the above set up. Unlike in other GFP systems previously evaluated (See Chapter 1), whole stripes were clearly visible and it was felt that such a system would be ideal for time-lapse imaging of wound healing in the corneal epithelium. It was not until the PAX6-GFP mice became available that this was possible, as the GFP transgenics available previously did not demonstrate good enough striping patterns. This was partly because GFP expression in the lens was too high interfering with confocal images of the cornea.

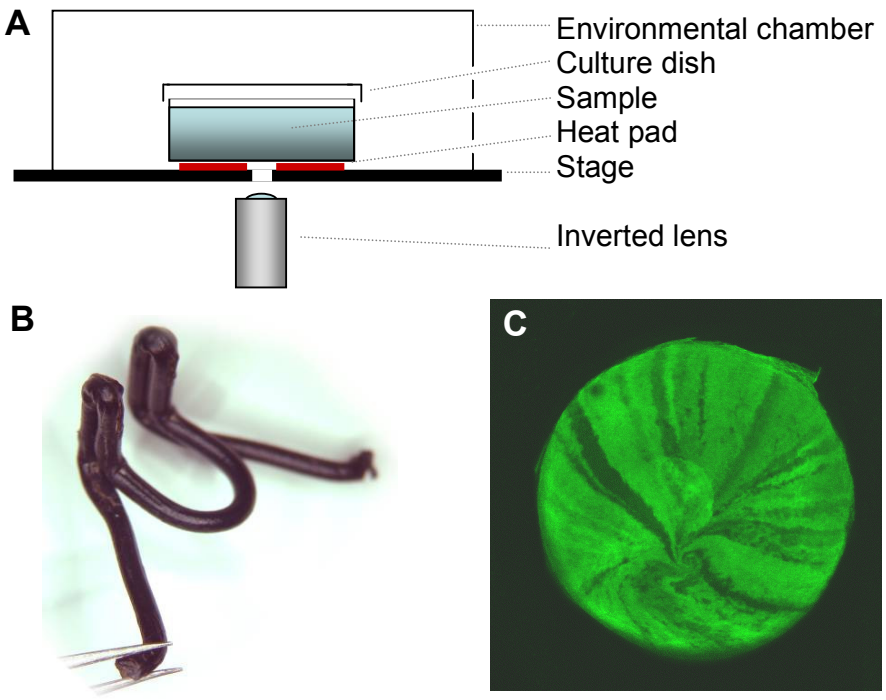

Figure 5.2: Time-lapse imaging of Pax6-GFP eyes in culture.

A: Time-lapse organ culture setup. Eyes were placed in a culture dish in clear culture medium. The dish was placed on a heat pad in an environmental chamber containing 5% CO_2 (95% air) on the stage of a Leica inverted confocal microscope. B: Eyes were suspended on a specially designed stand formed from a black-plastic coated paper clip. C: Z-stack image of a PAX6-GFP eye imaged with the inverted microscope.

5.3.3 Time-lapse ex-vivo confocal imaging of the corneal epithelium

Having shown that a centrally wounded *XLacZ*$^{+/-}$ mosaic eye heals to recapitulate striping patterns, the time-lapse system described above was used to show how this mechanism proceeds in more detail. A PAX6-GFP eye on a *Pax6*$^{+/+}$ background (Eye 1) was wounded centrally and cultured for 24 hours. Very occasionally in *XLacZ*$^{+/-}$ animals on a *Pax6*$^{+/+}$ background disrupted striping patterns are observed these may sometimes appear like a double vortex. Figure 5.3 shows such an eye. These patterns may be formed by the divergence of cells to heal an epithelial wound forming a second whorl in the process. To test whether this may be the cause of such patterns, a second eye (Eye 2) on a *Pax6*$^{+/+}$ background was wounded in a peripheral position so that the central vortex would not be disrupted. *Pax6*$^{+/-}$ eyes have disrupted striping patterns (See Chapter 4), such patterns could be caused by a migratory defect that could contribute to abnormal wound healing. To test whether *Pax6*$^{+/-}$ eyes heal abnormally a third PAX6-GFP eye on a *Pax6*$^{+/-}$ background (Eye 3) was also wounded centrally. Unfortunately the third eye demonstrated a very high level of GFP positive cells in the cornea making it impossible to see individual patches of positive and negative cells around the wound edge.

Z stacks were taken every 45 minutes and the images were converted into an AVI file using the ImageJ software package. Figure 5.4 shows time-lapse confocal images of this experiment. Figure 5.4 A shows clearly that 5.25 hours post-wounding the margins of the wound are clearly evident in all three eyes. Wound healing is visualised through migration of GFP positive cells towards the centre of the wound, in eyes 1 and 2 stripes are also visible. By 18.75 hours the wound is completely healed in eyes 1 and 3 whilst it is only partially healed in eye 2 (peripherally wounded). GFP positive stripes are seen to extend towards the centre of the previously wounded region in eyes 1 and 2. No such striping is evident in eye 3. In eyes 1 and 2 stripes remain contiguous throughout the wound healing response. The time-

points used in Figure 5.4 and in the following analyses, were chosen as the best compromise for comparing the three experiments described. The results of these experiments can be more clearly visualised when watching supplementary videos 1- 3. Here we see that in a *Pax6*$^{+/+}$ background stripes remain contiguous as they migrate to heal a wound. When a wound is made peripherally cells migrate to form de-novo striping patterns. Video 3 demonstrates wound healing on a *Pax6*$^{+/-}$ background. The wound appears to heal in an uneven manner. Furthermore once the wound appears completely covered in GFP positive cells, there appears to be migration back out from the wound centre.

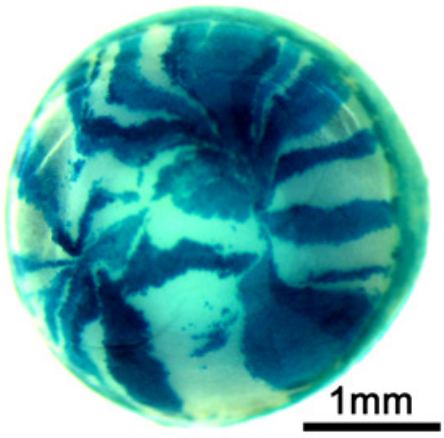

Figure 5.3: A double-vortex in a wildtype (*Pax6*$^{+/+}$) eye.

Disrupted striping pattern in an *XLacZ*$^{+/-}$ mosaic eye. Occasionally on a *Pax6*$^{+/+}$ background eyes are observed that demonstrate disrupted striping patterns, in this case reminiscent of a double vortex. Perhaps such patterns are created by the divergence of migrating cells to heal a wound in the corneal epithelium.

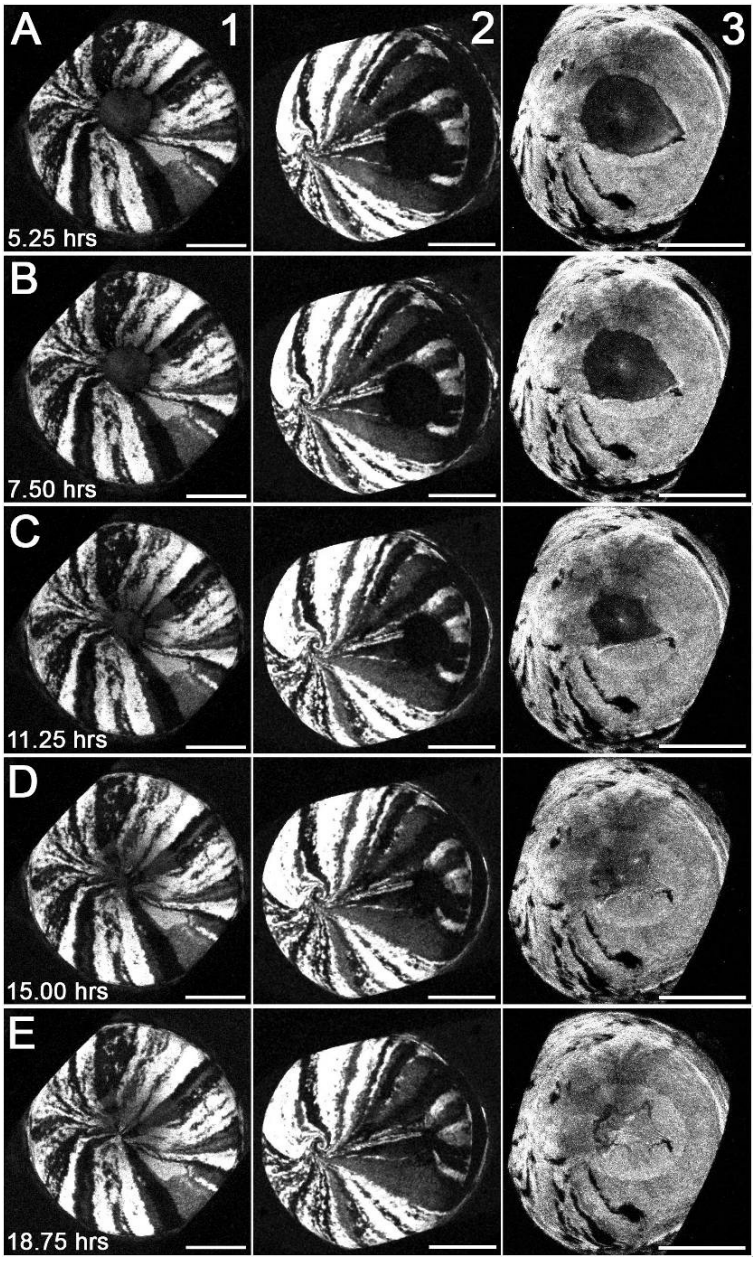

Figure 5.4: Time-lapse images of wound healing in the corneal epithelium.

Time-lapse confocal images of wound healing in GFP mosaic eyes. Columns 1, 2 and 3 show a central wound on *Pax6*$^{+/+}$ background (eye 1), a peripheral wound on *Pax6*$^{+/+}$ background (eye 2) and a central wound on a *Pax6*$^{+/-}$ background (eye 3). Rows A-E represent time points between 5.25 and 18.75 hrs post-wounding. Five hours post-wounding the margins of the wound are clearly evident in all eyes (A). Wound healing is visualised

through migration of GFP-positive cells (which appear white in Fig 5.4) towards the centre of the wound (B-E). By 18.75 hours central wounds are completely healed (E1 and E3), GFP positive stripes are seen to meet at the centre of the previously wounded region. However the eye wounded peripherally is not fully healed (E2). Scale bars, 1mm.

5.3.4 Tracking and Isolation of stripes using ImageJ

To investigate the movement of stripes more carefully the images created for eye 1 were investigated in more detail. Firstly using ImageJ's manual tracking plug-in, six GFP positive stripes were tracked and a composite AVI file of the original images plus the 'dots and lines' added by the plug-in was created. The resulting images are represented in Figure 5.5 A-C in which it is clear that the majority of stripes migrate towards the centre of the wound. However it is also clear that the stripes do not meet in the centre of the wounded area, consequently some stripes must either move at different speeds or start moving at different times. The results are more clearly followed when watching supplementary video 4. To analyse in detail two stripes from the faster and slower moving sides of the wound, an ImageJ macro was run on the videos to enhance two stripe edges (indicated as 1* and 2* in Figure 5.5 A and D; the lower stripe 2* moves faster). The rest of the image was then masked off and an AVI file created. Figure 5.5 D-E shows three frames from this sequence showing the convergence of two stripes from different sides of the wound. By watching supplementary video 5 the effect is much more striking. From watching these videos it appears that all stripes begin to migrate at roughly the same time. However it is clear from Video 4 that some stripes migrate much further in the 19-hour period than others and so must be moving at a greater speed.

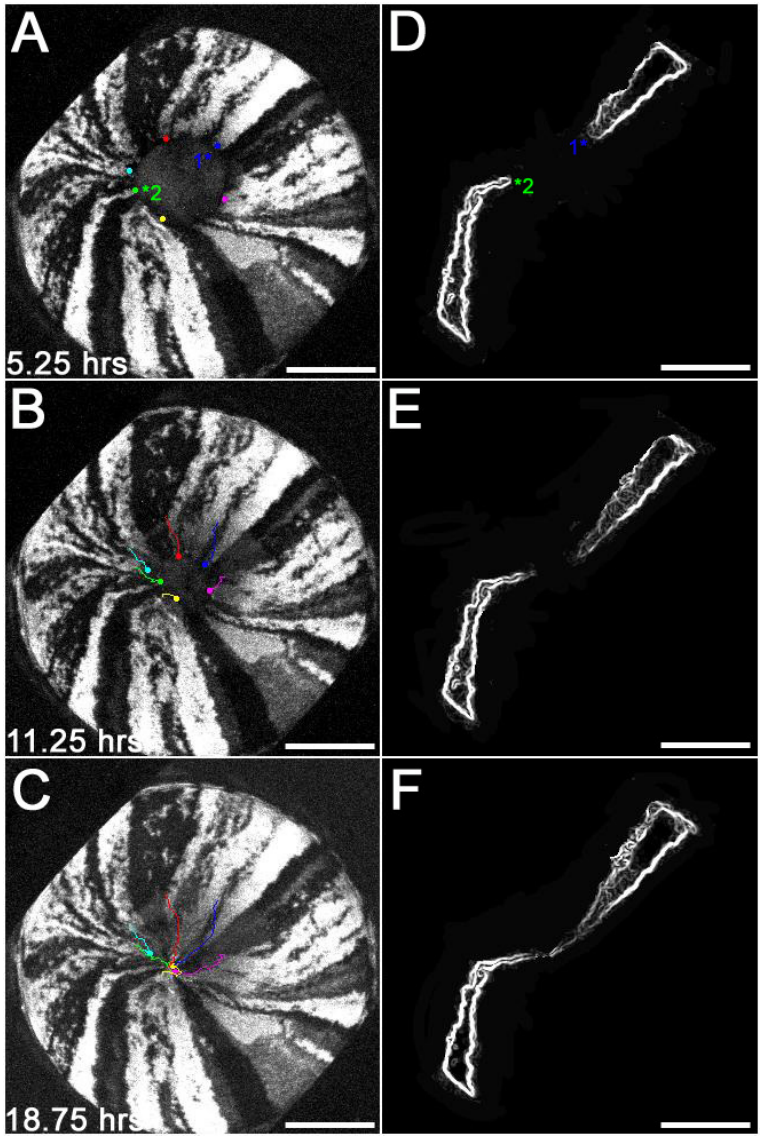

Figure 5.5: Tracking and enhancement of stripes during wound healing.

Time-lapse confocal images of wound healing in GFP mosaic eyes. Stripes were tracked using the 'Manual Tracking' plug-in in ImageJ (A-C). They are represented by coloured dots and lines. It is apparent from the migration of the stripes that they do not meet in the centre of the wound. In order to address this, two GFP-positive stripes (indicated as 1* and 2* in A and D) were isolated in ImageJ (D-E). It is clear that stripe *1 migrates further than stripe *2.

5.3.5 Wound Healing Rates

Using the 'linear selection' tool and the 'measure' command in ImageJ it is possible to make frame by frame measurements of the rate of migration of a point on the edge of a wound. In the *Pax6*$^{+/+}$ background eye wounded centrally, it was observed that not all stripes migrated at the same rate. Figure 5.5 shows measurements of healing rate in two roughly opposing stripes from the sides of the wound perceived to be 'faster and slower'. Figure 5.6 A demonstrates the two stripes chosen (indicated as *1 and *2). The mean distance migrated per time-point by stripes one and two differed significantly. Figure 5.6 C shows that the combined rate of wound closure was 1.18 microns per minute. Although these data are preliminary it is intriguing to consider whether there is a predetermined point at which the stripes meet near the centre of the eye. Although this eye was wounded centrally, it is technically difficult to wound exactly in the centre. Perhaps the stripes are meeting at the original point of convergence which is 'off centre' with the wound.

When a *Pax6*$^{+/+}$ background eye was wounded peripherally there did not appear to be any difference in the rate of migration of the surrounding stripes. Unfortunately this analysis was confounded by the degree to which the eye moved in culture (See Additional Video 2). Because the eye is not clamped into position and the confocal laser locally heats the culture medium, currents of medium can induce the eye to move around in the culture dish between time points. Figure 5.7 A shows two stripes that roughly oppose each other (indicated as *1 and *2). The mean distance migrated per time-point by stripes one and two did not differ significantly. Figure 5.7 C indicates that the combined rate of wound closure was 0.84 microns per minute. As well as being slower than the closure of a central wound (the wound is not fully closed by 18.75 hours post-wounding). The stripes seem to converge at roughly the same rate.

A *Pax6*$^{+/-}$ eye was wounded centrally and confocal time-lapse videos were made by taking Z-stacks every 45 minutes. Figure 5.8 A Shows two points on the wound edge roughly opposing each other (indicated as *1 and *2). The mean distance migrated per time-point by stripes one and two did not differ significantly. Figure 8 C demonstrates that the combined rate of wound closure was 1.35 μm/min. The rate of closure here is marginally greater than the centrally wounded *Pax6*$^{+/+}$ background eye. There is no bias in the rate of closure for the two converging points chosen here.

The mean rates of wound closure and mean distances migrated (per time point) for the three wound healing experiments described above are compared in Figure 5.9. Figure 5.9 A shows the points that were tracked in the three experiments (indicated as *1 and *2 in Figure 5.8 A-C). The speed at which these two points converged over the time series was compared. Figure 5.9 B shows the mean distances migrated per time-point (every 45-minutes) for central *Pax6*$^{+/+}$, peripheral *Pax6*$^{+/+}$ and central small-eye (*Pax6*$^{+/-}$) wounds respectively. The difference between small-eye and peripheral wounds was significant. However the differences between small-eye and central and central and peripheral were not significant. **C:** The central wound closed at an overall rate of 1.18 μm/min, the peripheral wound closed at a rate of 0.84 μm/min and the small eye wound closed at a rate of 1.35 μm/min. These preliminary data indicate that a 1mm wound in *Pax6*$^{+/-}$ eyes may heal significantly faster than peripheral wounds in *Pax6*$^{+/+}$ eyes.

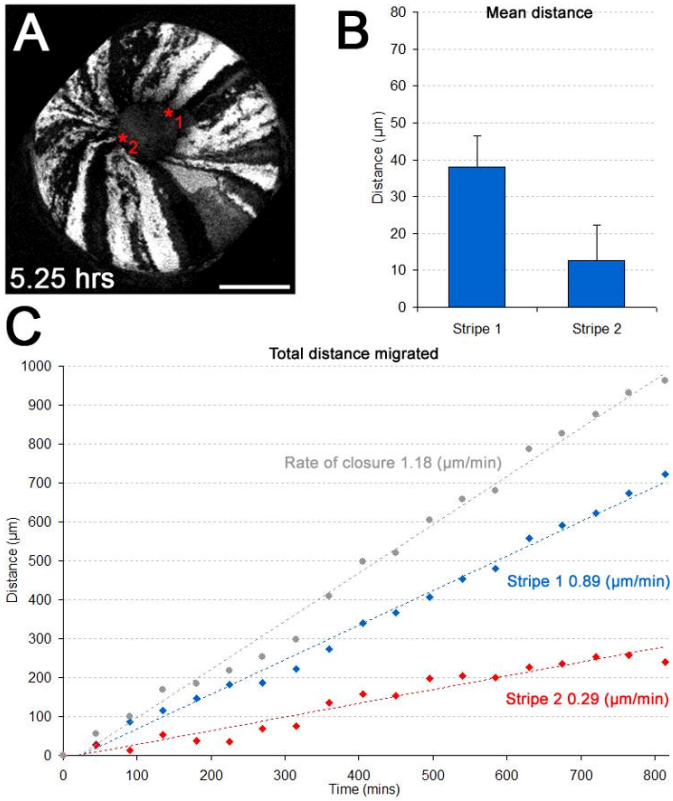

Figure 5.6: Rate of wound closure in two opposing stripes of a central wound.

It was observed that not all stripes migrate at the same rate. Confocal time-lapse videos were made by taking Z-stacks every 45 minutes. A: Two stripes that roughly opposed each other were chosen (*1 and *2). The distance migrated between each time-point was measured. B: The mean distances (± 95% CI) migrated per time-point (every 45 minutes) were 40.17 ± 7.85 and 13.32 ± 10.10 for stripes one and stripe two respectively. The difference between these values was highly significant (t-test $P = 0.000696$). C: Stripe 1 migrated at an overall rate of 0.34 microns per minute. Stripe 2 migrated at a rate of 0.84 microns per minute. The combined rate of wound closure was 1.18 microns per minute. Scale bar in A, 1mm; Error bars in B, 95% confidence intervals.

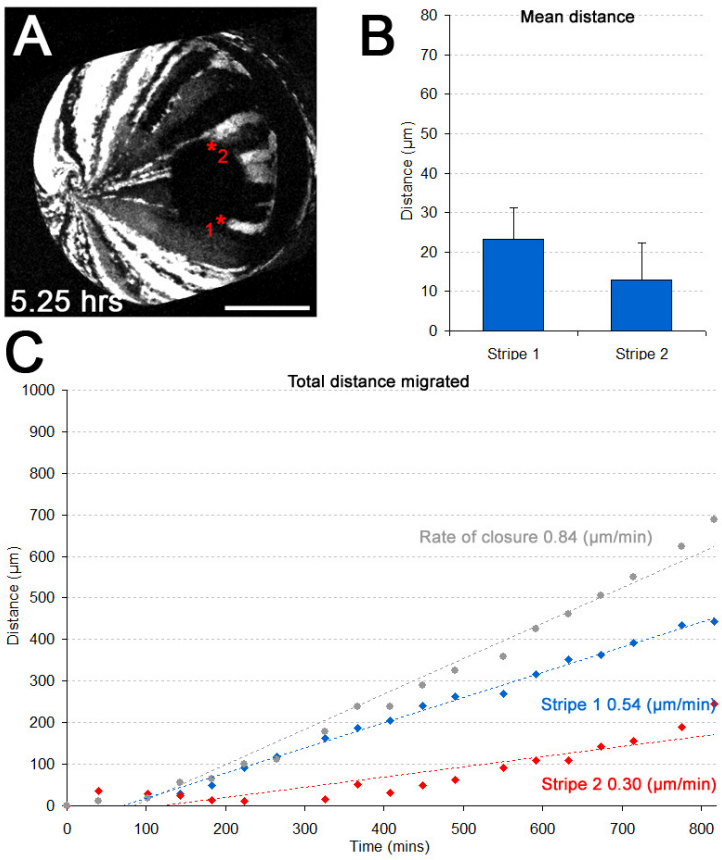

Figure 5.7: Rate of wound closure in two opposing stripes of a peripheral wound.
When a *Pax6*$^{+/+}$ background eye was wounded peripherally there did not appear to be any difference in the rate of migration of the surrounding stripes. A: Two stripes that roughly opposed each other were chosen (*1 and *2). The distance migrated between each time-point was measured. B: The mean distances migrated per time-point (every 45 minutes) were 24.57 ± 8.04 and 13.63 ± 9.70 µm for stripes one and stripe two respectively. The difference between these values was not significant (t-test P = 0.149). C: Stripe one migrated at an overall rate of 0.54 microns per minute. Stripe two migrated at a rate of 0.30 microns per minute. The combined rate of wound closure was 0.84 microns per minute. Scale bar in A, 1mm; Error bars in B, 95% confidence intervals.

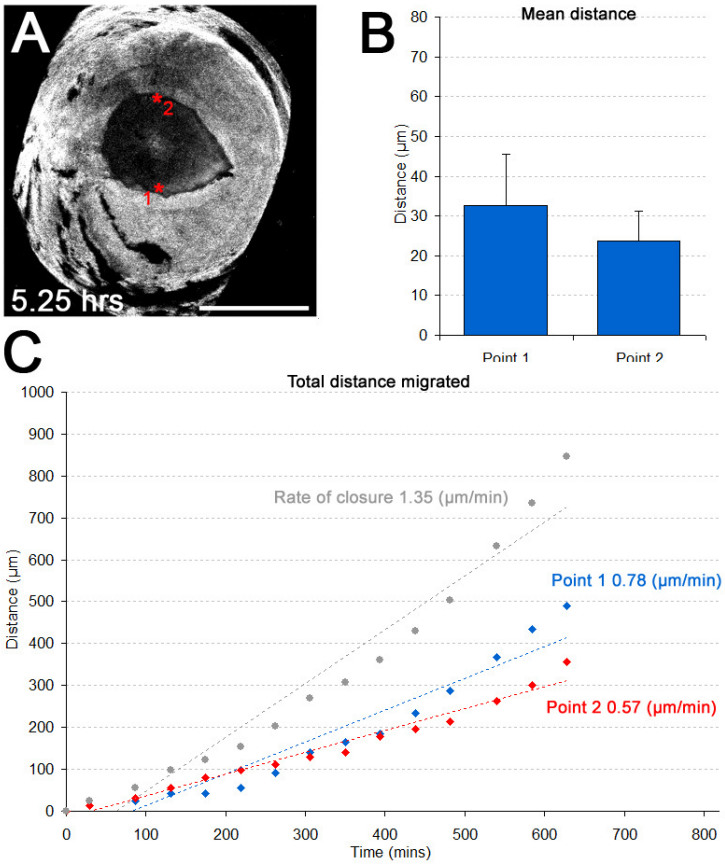

Figure 5.8: Rate of wound closure in two opposing wound edges of a *Pax6*$^{+/-}$ central wound.

A *Pax6*$^{+/-}$ eye was wounded and confocal time-lapse videos were made by taking Z-stacks every 45 minutes. A: Two points on the wound edge roughly opposing each other were chosen (*1 and *2). The distance migrated between each time-point was measured. B: The mean distances (± 95% CI) migrated per time-point (every 45 minutes) were 35.04 ± 12.76 µm and 25.42 ± 7.25 µm for point one and point two respectively. The difference between these values was not significant (t-test $P = 0.107$). C: Point one migrated at an overall rate of 0.78 µm/min. Point two migrated at a rate of 0.57 µm/min. The combined rate of wound closure was 1.35 µm/min. Scale bar in A, 1mm; Error bars in B, 95% confidence intervals.

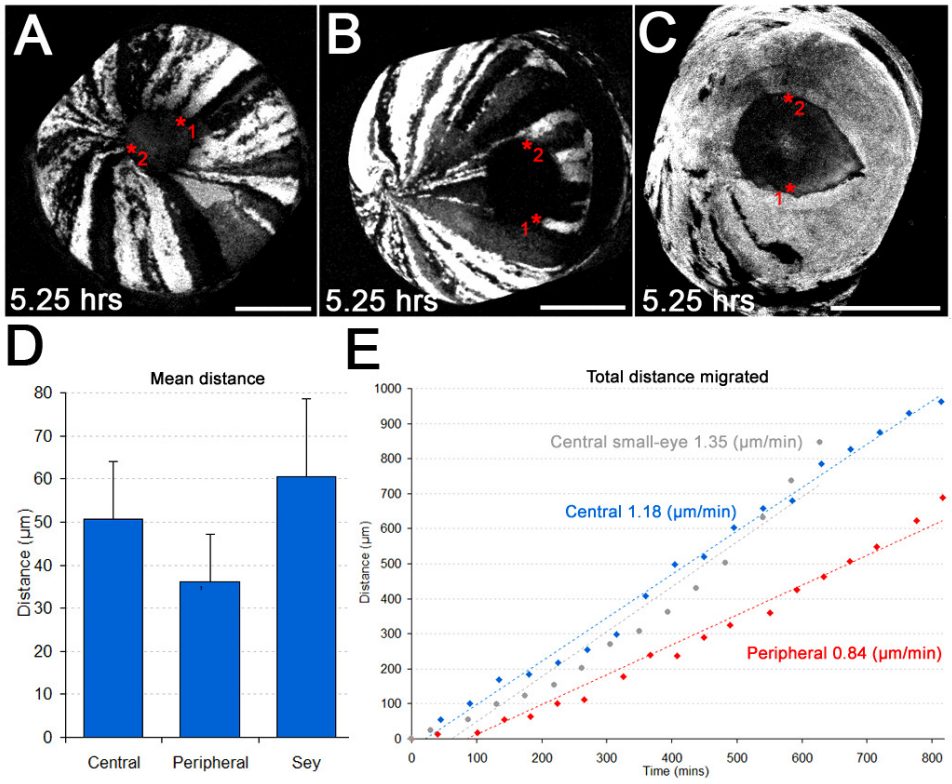

Figure 5.9: Rate of central, peripheral and small-eye (*Pax6*$^{+/-}$) central wound closure. Wound healing was compared in *Pax6*$^{+/+}$ background eyes wounded centrally and peripherally and a *Pax6*$^{+/-}$ eye wounded centrally. Confocal time-lapse videos were made by taking z-stacks every 45 minutes. A: Two points that roughly opposed each other were chosen (*1 and *2) at the wound edge in each time series. The distance migrated between each time-point was measured. B: The mean distances (± 95% CI) migrated per time-point (every 45 minutes) were 53.50 ± 12.85 µm, 38.20 ± 10.76 µm and 60.46 ± 17.66 µm for central, peripheral and small-eye wounds respectively. The difference between small-eye and peripheral wounds was significant (t-test $P = 0.006965$). C: The central wound closed at an overall rate of 1.18 µm/min, the peripheral wound closed at a rate of 0.84 µm/min and the small eye wound closed at a rate of 1.35 µm/min. Scale bar in A-C, 1mm; Error bars in D, 95% confidence intervals.

5.4 DISCUSSION

Here it is demonstrated for the first time that striping patterns in X-inactivation mosaic eyes are recapitulated as a central wound heals in whole eye culture. A 1mm central epithelial wound is fully closed by 24 hours with stripes extending to the centre of the previously wounded area, indicating that corneal epithelial wounds heal in a clonal manner. Even in this wound healing context there is very little cell mixing at the edge of a stripe. This may be because cells are migrating in the same direction as they do under normal conditions *in-vivo* as proposed by Thoft and Friend (1983) and confirmed by Nagasaki and Zhao (2003) who showed *in-vivo* that GFP positive cells in the intact, unwounded mouse corneal epithelium migrate at an average rate of 26μm a day under normal conditions. In the current study, cells migrated 500μm in a 24 hour period but stripes still remained contiguous. This suggests that removal of spatial constraints inducing epithelial cells to migrate apically does not promote lateral cell mixing. Furthermore despite the requirement for changes in cell-cell adhesion (Lee and Gotlieb, 1999) and remodelling of adhesion complexes (Ramamurthi et al., 2006) required to close a wound, the constraints that inhibit cell mixing between stripes must still be preserved.

To study stripe dynamics during wound healing more carefully, a GFP-based imaging system was developed. This system allowed confocal time lapse imaging of the wound healing process in PAX6-GFP mosaics. Results were promising, with eyes surviving well in the culture conditions provided. Although images produced were of a relatively low resolution (1024 x 1024 pixels for a field of view approximately 4mm x 4mm) they were good enough to view changes in striping patterns as a wound healed. With future improvements to the system (which was somewhat make-shift, in its prototype form), it is anticipated that much higher quality time-lapse sequences could be produced. The main limitation of the current method is in the way a wounded eye is held in place in the culture. A more sophisticated container that clamps the eye in place whilst allowing access for the

culture medium, is currently being custom-made. By using a better clamp with a glass bottomed culture dish it should be possible to image at a much higher magnification, perhaps even making it possible to view microtubule organisation at the wound edge (the GFP mosaics used here express a tauGFP fusion protein). Zhao et al (2006a) have developed a three dimensional organ culture system for the study of wound healing and corneal transplantation in a bovine model. The system uses bovine corneoscleral buttons in an ex-vivo culture system that maintains artificial intra ocular pressure by perfusing the endothelial layer and also separately irrigates the corneal surface and exposes it to air. The system was shown to maintain the corneal epithelium, limbus, corneal stroma and endothelium in good condition for up to 10-days. Although not directly translatable to the mouse eye due to the presumptive size constraints, much may be learned by comparing this system with the one described here.

To evaluate the confocal system developed in this study a 1mm central wound was made in a *Pax6*$^{+/+}$ eye, after which the wound healing process was then imaged overnight. Imaging of stripes of GFP-positive cells revealed that cells migrated in such a fashion that stripes remained contiguous throughout the healing process. Analysis of the migration of a number of stripes using ImageJ demonstrated that not all stripes migrated at the same rate and that they therefore did not meet in the centre of the eye. This suggested perhaps that the stripes were meeting at a pre-determined point. It is intriguing to speculate that this may be the point at which the original stripes coincided before wounding. However this is only a preliminary result and needs to be substantiated with further analyses of greater numbers of eyes. There have been no previous reports of different rates of migration occurring at different parts of the wound edge in similar systems. This may be because most wound healing culture systems of this type measure the rate of closure by imaging the size of the wound area at different time points. It is clear from the work presented here that imaging striping patterns

has a clear advantage over such methods. By tracking individual cells the subtleties in the way epithelial wounds heal can be studied more carefully.

Very occasionally *Pax6*$^{+/+}$ eyes are observed that appear to have two whorling patterns instead of the typical central pattern described in Chapter 2. One might speculate that this may be due to wound healing processes diverting the original stripes to heal a wound. To test this hypothesis a peripheral wound was made in a *Pax6*$^{+/+}$ eye. Stripes migrated in a contiguous manner to heal this defect, meeting close to the centre of the wound. It was tempting to predict a greater bias in the rates of migration for a peripheral wound, with the majority of cells migrating from the side of the wound nearest the limbus where TACs with the highest proliferative capacity reside. However this was not the case as stripes met at the wound centre, suggesting that if an organisational centre is involved in centripetal migration it was not disrupted in this experiment and does not have long range effects on cells more than 0.5mm away. In this experiment a *de-novo* whorl at the centre of the wound reminiscent of the double whorls observed previously was produced. This strongly implicates wound healing in the disruption of normal striping patterns in these eyes. This is the first such report of the generation of *de-novo* striping patterns in a wound healing system and proves that as well as migrating to reconstitute a central whorl, corneal epithelial cells can migrate in the opposite direction to generate a unique pattern.

Because striping patterns are disrupted in *Pax6*$^{+/-}$ eyes, a central wound was made in a GFP mosaic eye on a *Pax6*$^{+/-}$ background. This experiment was less successful because in this particular case, the proportion of GFP-positive cells was too high. Further investigation is required to determine whether this is a problem caused by an interaction between the PAX6-GFP construct and the *Pax6*$^{+/-}$ genetic background that has altered GFP expression. For this reason a different mosaic system such as a GFP X-inactivation mosaic (Hadjantonakis et al., 1998) with a more balanced contribution of positive and negative cells may be more appropriate. Interestingly the wound in this experiment appeared to heal faster than either

wound on the *Pax6*$^{+/+}$ background. Furthermore when the wound had fully healed cells appeared to migrate outwards from the centre of the wound towards its edge. At the same time GFP negative patches in the epithelium begin to appear, it is not clear whether these are epithelial lesions similar to those observed in recurrent epithelial erosions (RCE) (Ramamurthi et al., 2006) or areas where GFP expression has been turned off and this requires further investigation.

The wound healing rates calculated in this study represent only preliminary results and are multiple measurements made on only 3 eyes. However the results are broadly consistent with other reports of cell migration in response to wound healing both *in-vivo*, *ex-vivo* and *in-vitro*. In the current study a central epithelial wound on a *Pax6*$^{+/+}$ background closed at a rate of 1.18μm/min, giving a rate of individual cell migration of 0.59μm/min. By comparison a peripheral wound closed at a rate of 0.84 μm/min giving a mean rate of migration of 0.42μm/min. Although the sample size is too small to draw any firm conclusions, it is encouraging that for all points tracked, the rate of wound healing was broadly linear. Crosson et al (1986) first described this linear migration, and also showed that in the 'linear healing phase' of the wound healing process, rabbit cornea cells would migrate at a constant rate of 1.06μm a minute. Also in rabbit corneal epithelial cells Kuwabara et al (1976) describe epithelial cells *in-vitro* migrating at a rate of 0.43 microns/min. Zahm et al described the migration of respiratory epithelial cells *in-vitro* as being in the range of 0.58-0.75μm/min in an in-vitro wound healing system. *In-vivo* Matsuda et al (1985) demonstrated that regardless of initial wound area, the wound diameter decreased at a rate of approximately 1.66μm/min (an average speed of 0.83μm/min). The faster rate of migration in a *Pax6*$^{+/-}$ eye shown here is consistent with a previous report for wounds $\geq$ 1mm, using the same culture conditions, that showed an increased rate of migration in *Pax6*$^{+/-}$ eyes (Ramaesh et al., 2006). The linear regression models proposed by the authors imply that the

mean rate of migration for a 1mm central wound in a *Pax6*$^{+/+}$ eye would be 0.24μm/min whilst the rate for *Pax6*$^{+/-}$ would be 0.27μm/min.

As well as developing an ex-vivo confocal time lapse imaging approach, the capabilities of the software package ImageJ were assessed. ImageJ's main attractions are its open framework (it is a freeware distribution) and the ability to easily write macros with which to process multiple images. It was found that ImageJ was very useful for constructing AVI files especially when different numbers of sections and different time points had been used between each series. It is also extremely easy to construct montages of the video frames. The 'manual tracking' plug-in (Fabrice Cordelières, Institut Curie, Orsay, France) was used to good effect in showing the routes and distances of migration of individual stripes. It is anticipated that once a better way to stabilise the eyes in culture is developed, this will be an extremely useful tool for analysing stripe dynamics. Although not attempted in the work described here, the capability to track movement in 3D using this plug-in should allow for correction for the curvature of the tissue in future experiments. Using a simple macro and some masking it was possible to show the migration of two individual stripes in isolation. This opens the possibility of making much more accurate detailed analyses of individual stripe migration, perhaps even allowing computer modelling and a fractal analysis (Iannaccone et al., 2003) of shape over time.

5.4.1 Conclusions

In summary, a time-lapse confocal system for imaging corneal epithelial wound healing, ex-vivo in GFP mosaics was developed. Using this system it was possible to image the migration of GFP positive stripes to heal a central wound. Where stripes were present, wound healing proceeded in a way that allowed them to remain contiguous. Using the freeware software package ImageJ allowed detailed analysis of stripe dynamics and the production of time-lapse videos. Analysis of cell migration using this system yielded rates of

migration comparable with previous reports in multiple systems. Consistent with previous reports with similar sized wounds, it was observed that *Pax6*$^{+/-}$ eyes heal at a faster rate than *Pax6*$^{+/+}$. It was observed for the first time that healing of peripheral wounds can form *de-novo* whorling patterns, revealing that basal cells in the epithelium can migrate both away from and towards the limbal region. In the future it is anticipated this system will be extremely useful in analysing the movement of cells during wound healing and in screening for the effects of pharmaceutical modulators of MMP signalling as potential treatments for RCE.

Chapter 6
General Discussion

6.1 THE ONSET OF LIMBAL STEM CELL FUNCTION

6.1.1 Postnatal development and gene expression

The evidence presented here combined with the conclusions of Collinson et al (2002) suggest that LSCs become active around 5-weeks postnatally when stripes first begin to form. It is not known when in development limbal stem cells are specified. One possibility is that LSCs are drawn from a compartment of cells that are present in the limbal region at a specific point postnatally. It may be that all the basal cells in the corneo-limbal epithelium initially have the proliferative potential to maintain the tissue, however only those cells in contact with the limbal basement membrane at a specific point during development are fated to become LSCs. In support of this theory changes in EGFR and α9-integrin expression in the ocular surface appear to be restricted to the limbal region postnatally (Pajoohesh-Ganji et al., 2004; Zieske and Wasson, 1993). Furthermore Tanifuji-Terai et al (2006) showed, using a *K12*$^{Cre/Cre}$*/ZAP* bitransgenic mouse, that undifferentiated K12 negative cells are present throughout the corneal epithelial basal layer at 2 weeks and become restricted to the limbal basal epithelium gradually until around 12-weeks postnatally, although some negative cells persisted to 24-weeks postnatally.

Figure 6.1 summarises these studies in conjunction with the current evidence on size and striping patterns. The key time points for each series are highlighted with an asterisk. The earliest of these changes is the distribution of EGFR (Figure 6.1 A). The receptor is distributed throughout the corneal epithelium at 1-week postnatally but has become more restricted to the limbal region by 3-weeks (Zieske and Wasson, 1993). In a similar manner α9-integrin is expressed throughout the basal layer up to three weeks postnatally and is

restricted to the limbal region by 10-weeks (Figure 6.1 B) at which point its expression levels are also higher in the limbal nasal region than the temporal region (Pajoohesh-Ganji et al., 2004). K12-negative cells become restricted to the limbal epithelium by 12 weeks postnatally (Figure 6.1 C). The expression patterns of EGFR, K12 and α9-integrin in *Pax6*$^{+/-}$ mice have not been investigated. Figure 6.1 D shows how striping patterns develop in the corneal epithelium. There is a reduction from ~90 corrected patches to ~50 between 15 and 39 weeks. Furthermore preliminary evidence presented here suggests that from around ~90 corrected patches present in the limbal region at 3 weeks a similar number of coherent clones of limbal stem cells are specified.

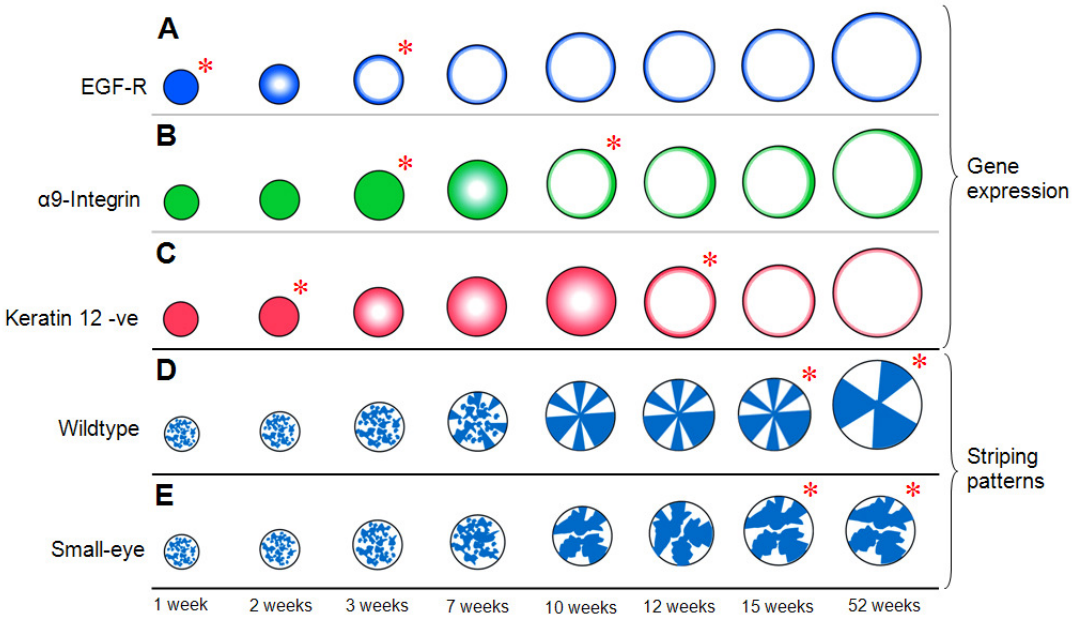

Figure 6.1: Comparison of changes in gene expression, striping patterns and size.

The change in size for the time points indicated is shown schematically in **A-E. A:** EGFR is expressed throughout the ocular surface at 1-week but is restricted to the basal limbal region by 3-weeks (Zieske and Wasson, 1993). **B:** α9-Integrin expression is expressed throughout the ocular surface until 3-weeks, it is restricted to the limbal region by 10-weeks, expression is thought to be higher in the nasal region than the temporal (Pajoohesh-Ganji et al., 2004). **C:** Cells negative for Keratin 12 are present throughout the ocular surface at 2-weeks but are restricted to the limbal region by 12-weeks (Tanifuji-Terai et al., 2006). **D:** Striping patterns in wildtype animals begin to form around 5-weeks and are fully formed by 10-weeks. There is a reduction in the number of corrected stripes between 15 and 52 weeks. **E:** *Pax6*$^{+/-}$ animals have smaller eyes, there are fewer corrected patches at 10-weeks than at 3-weeks. There is no reduction in the corrected patch size with age.

These changes in gene expression may represent three key stages in the maturation of the embryonic to adult tissue. These could be broadly outlined as changes in the competence, functionality and structure of the tissue allowing its compartmentalisation into distinct populations. The first change is in the competence of cells to respond to growth factors through EGFR (Zieske and Wasson, 1993). Initially all basal cells in the tissue may be responsive but by three weeks LSCs have been specified perhaps by changes in the niche of the basal limbal epithelium. It is only in these cells that the competence is preserved. Secondly, functional changes occur, perhaps here reflected by α9-integrin expression (Pajoohesh-Ganji et al., 2004) and allowing remodelling of the tissue architecture to allow the centripetal migration necessary to maintain the tissue. The third is the Keratin switch from K5/K14 to K12/K3 (Tanifuji-Terai et al., 2006) reflecting structural changes and the stratification of the tissue.

Stem cells must be specified prior to the formation of striping patterns. As its expression pattern changes the earliest, perhaps EGFR expression is the most informative about when this may happen. EGFR is linked with proliferative potential and the ability to respond to growth factors both inherent stem cell attributes. Fig 6.2 outlines a possible model for stem cell specification. In the randomly orientated mosaic of the early tissue all basal cells may have similar proliferative potential. However by 3 weeks only cells in contact with the basal limbal region (red dotted line) are fated to become LSCs and retain EGFR expression while it is lost in the cells of the central cornea. Identification of the LSC niche architecture and a proper understanding of its function will be important in understanding how effectively the tissue can support a stem cell population in health and disease.

6.1.2 Perspectives from the small-eye mouse

Centripetal migration is disrupted in *Pax6*$^{+/-}$ animals and fewer, larger coherent corneal epithelial clones are observed (Collinson et al., 2004a). However centripetal migration and

striping morphology was restored in *Pax6*$^{+/+}$ ↔ *Pax6*$^{+/-}$ chimeras. In these animals *Pax6*$^{+/-}$ cells were under-represented in the corneal epithelia, suggesting that these cells were cell autonomously depleted or were less efficient than *Pax6*$^{+/+}$ cells at populating the tissue. Taken together these results suggest that correct Pax6 dosage is required for clonal growth during development but that perhaps the cues that organize centripetal migration are cell nonautonomous (Collinson et al., 2004a).

Pax6$^{+/-}$, small-eye mice have corneal defects in the adult tissue proposed to be caused by a LSC deficiency. The present study demonstrates that in *Pax6*$^{+/-}$, *PAX77*$^{+ve}$ *and Pax6*$^{+/-}$*/Gli3*$^{+/-}$ X-inactivation mosaic animals the estimated number of coherent stem cell clones is reduced to ~50 at 15-weeks (compared to ~100 in wildtype) with no further reduction up to 30 weeks (wildtype declines to ~50 by 30 weeks). This suggests that not only are LSC numbers depleted by a reduction in Pax6 expression but also by an increase in PAX6. In wildtype animals the number of corrected stripes present at 15 weeks is roughly similar to the number of corrected patches present near the limbal region at 3 weeks. However in the *Pax6*$^{+/-}$ animals fewer LSC clones (and perhaps fewer LSCs) are initially specified or there is a subsequent loss before 15 weeks. It is not known how patch shapes change or are lost during the period between 3 and 10 weeks indicated in Figure 6.2 B. Mice heterozygous for both *Gli3*$^{+/-}$ and *Pax6*$^{+/-}$ have a distinct striping phenotype.

These data suggest that the specification or maintenance of LSC populations is sensitive to Pax6 dosage. This may suggest that changes in the stem cell niche are responsible for the LSC deficiency rather than a cell autonomous LSC defect. Perhaps in order for them to persist at the limbus, potential LSCs need to both interact with the niche through adhesion molecules such as α9-integrin and also be stimulated to proliferate through EGFR. Because Pax6 interacts with both EGF/EGFR and MMP9 (Leiper et al., 2006; Li and Lu, 2005; Sivak et al., 2000), the haploinsufficiency or over-expression of Pax6 may disrupt this balance

allowing putative stem cells to instead remodel their stromal interactions through MMP9 and migrate from the niche.

Figure 6.3 is adapted from Simpson and Price (2002) and outlines some of the key interactions of Pax6. Shh, Gli3, EGF/EGFR and MMP9 (Fig 6.3 A, all relevant to the current discussion) have been added along with the cellular compartments of the limbo-corneal epithelium (Fig 6.3 C). EGF/EGFR interact with both Pax6 and MMP9 to modulate wound healing in the cornea and Shh interacts with Gli3 (Jensen and Wallace, 1997; Marigo et al., 1996; Wang et al., 2000). Pax6 is known to respond to graded Shh signalling in the ventral spinal cord and hindbrain (Ericson et al., 1997). Pax6 is a bottleneck through which a spectrum of cellular outcomes must pass. Its effects are relevant in all cellular compartments of the ocular surface. It regulates genes with roles in the cell cycle, proliferation, differentiation and cell death and so potentially affects LSCs, TACs, wing cells and differentiated cells. These are genes that come up time and time again in developmental and adult contexts. Further investigation of the effects of haploinsufficiency for Pax6 in *Pax6*$^{+/-}$ mice is required to understand its effects on these cellular compartments in the adult corneo-limbal epithelium.

The evidence presented here suggests that different components of this network are sensitive to different levels of Pax6. Under-expression effects embryonic development of the entire eye as well as maintenance of the corneal epithelium, over-expression on the other hand does not affect eye size but does effect embryonic development of the corneal epithelium. If LSC numbers are indeed depleted in both genotypes, then LSC deficiency itself does not effect corneal epithelial integrity (*PAX77*$^{+ve}$ corneas are normal in thickness and have normal striping patterns). It is proposed therefore that *PAX77*$^{+ve}$ may be useful as a tool for dissecting reduced LSC function from the other phenotypes observed in ARK.

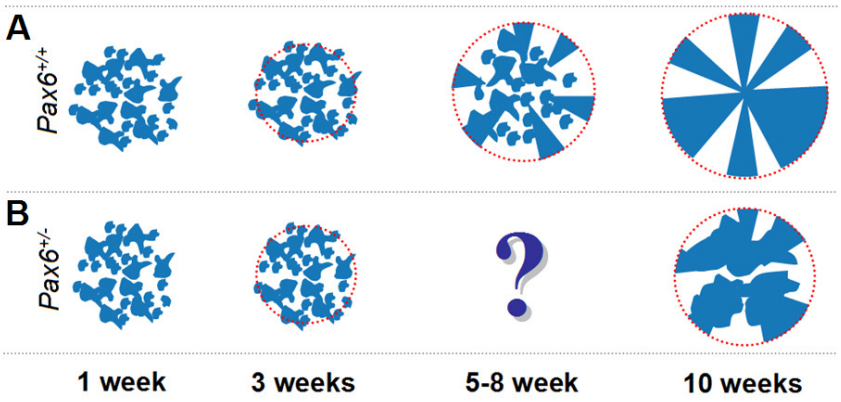

Figure 6.2: LSC specification and onset of stripes.

Preliminary evidence suggests that in *Pax6*$^{+/+}$ *XLacZ*$^{+/-}$ mosaic animals LSCs are specified from patches of *LacZ*-positive and *LacZ*-negative cells overlapping the limbal region at or before 3 weeks. These patches give rise to a similar number of stripes at 10 weeks. In *Pax6*$^{+/-}$ animals however fewer stripes are formed from a greater number of patches. It is unclear whether this is due to a reduction in the number of cells specified or a loss of LSCs during the intervening period.

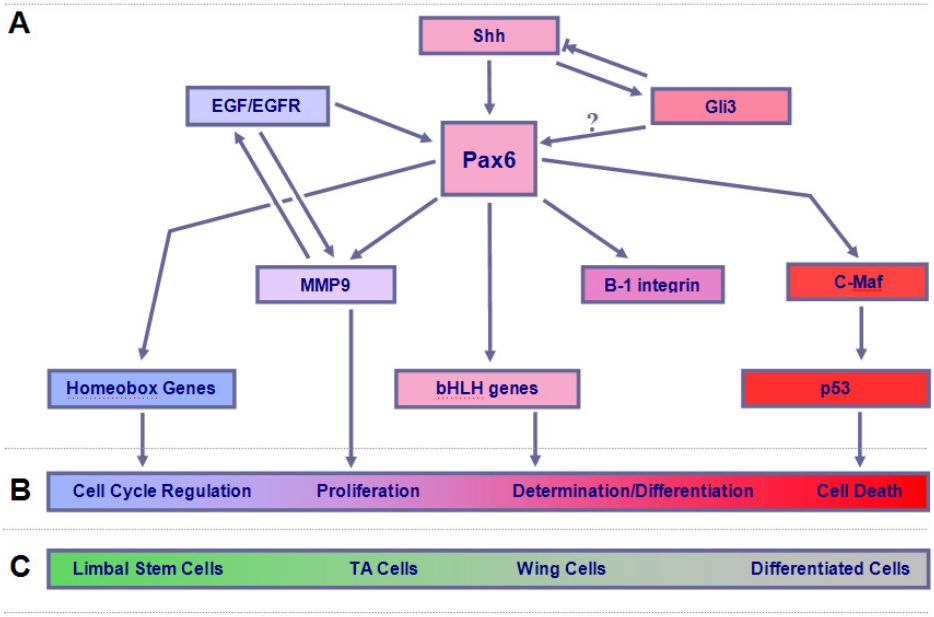

Figure 6.3: The *Pax6* network.

Schematic representing the complexity of the *Pax6* network adapted from Simpson and Price (2002). A: *Shh* interacts with both *Pax6* and *Gli3*, it is not known whether there is a direct interaction between *Pax6* and *Gli3*. Genes such as *EGF* and *MMP9* have direct effects on corneal epithelial wound healing. B: Pax6 has downstream targets with roles in the cell cycle, proliferation, differentiation and cell death. C: The range of outcomes from this network may translate into the cellular compartments of the limbo-corneal epithelium.

6.2 ASSAYS OF LIMBAL STEM CELL NUMBER

6.2.1 Age related decline in coherent clones of limbal stem cells

Analysis at 5 ages demonstrated that the estimated number of coherent clones of LSCs maintaining the corneal epithelium is reduced from ~90 at 15 weeks to ~50 at 39-weeks and is then stable at least until 52-weeks. Because there are no good markers with which to identify LSCs, retention of cell cycle labels such as H-Tdr and BrdU have been used (Cotsarelis et al., 1989; Lehrer et al., 1998). In order to address whether the actual number of limbal stem cells at the limbus declines in the same way as the number of coherent clones, a BrdU-based system and a transgenic approach were evaluated. These were only preliminary studies and so are not presented in the main Results chapters. The approaches are summarised below.

6.2.2 BrdU label retaining approach to identifying limbal stem cells

Two ages of mice were implanted with osmotic mini-pumps charged with 50mg/ml BrdU at 15 and 30 weeks of age. After 7-days the pumps were removed and the animals were sacrificed following a further 12-week 'chase' period. Figure 6.4 shows the preliminary results of this study. Whole mount tissue sections were kindly stained by Mr Douglas Gibson (a summer student). Label retaining cells could be identified in the 30 week cohort as a clearly defined ring of positive cells elongated along the length of the limbal region (Fig 6.4 C and D). However in the 15 week group no BrdU positive cells could be identified, therefore it was not possible to make a meaningful comparison between the two time points. This is perhaps because the rate of tissue turnover is greater at the earlier time point and so BrdU is cleared from the tissue at a faster rate. Further work is thus required to determine appropriate chase times for different ages before this work can be completed. It may be beneficial to also study cell cycle times at the same time points. If the tissue was turning over at a faster rate in younger animals, the proliferative potential of LSCs may become exhausted

more quickly thus explaining the decline in coherent LSC clones in wildtype animals up to 39 weeks.

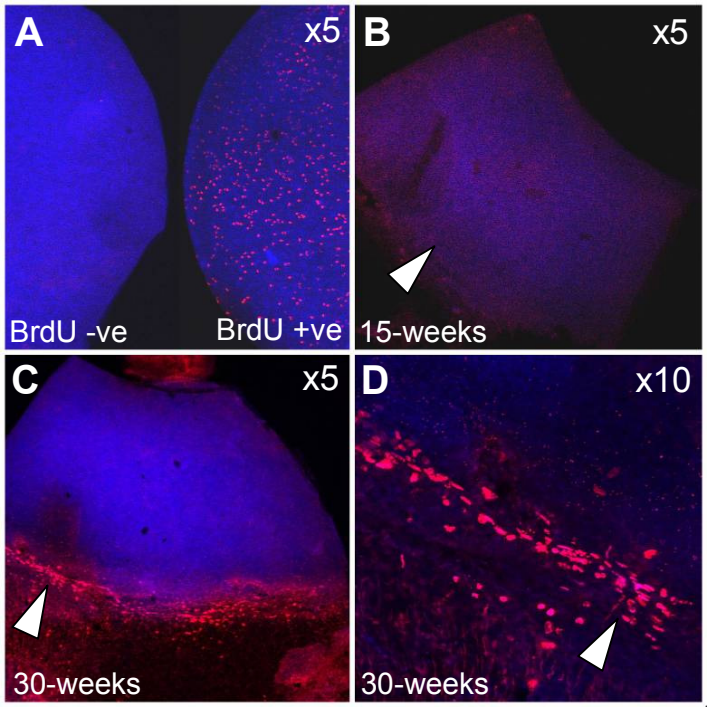

Figure 6.4: BrdU labelling in whole-mounts of the corneo-limbal epithelium.

A: Positive and negative controls of central cornea from two mice, one injected with BrdU and sacrificed four hours later, the other negative for BrdU. Positive cells are clearly evident in the BrdU treated cornea. **B:** Peripheral cornea from a label retaining experiment. A 15-week old mouse was implanted with an osmotic mini-pump delivering BrdU for 7 days followed by a 12-week chase. The limbal region is indicated by the arrow. No positive cells were detected in the whole mount section. **C:** When 30-week mice were treated identically BrdU positive cells were confined to the limbal region. **D:** Higher magnification of the cells indicated in **C**. BrdU positive cells appear to be orientated longitudinally along the circumference of the limbus.

6.2.3 Transgenic label retaining approach to identifying limbal stem cells

In Chapter 1 a transgenic system for identifying label retaining cells in the epidermis is described (Tumbar et al., 2004). The group used K5-tetOff to drive expression of H2B-GFP in the skin. Gene expression was constitutively active throughout the epidermis under normal conditions. Administration of doxycycline inhibited tetOff and silenced H2B-GFP, which was then diluted from cells that underwent subsequent cell divisions in the same way as BrdU. After doxycycline treatment for a chase period of up to 4 months, labelled cells were restricted to a small proportion of cells in the bulge region of the hair follicle.

Although tissue specificity is an important advantage of this approach, use of a ubiquitous promoter to drive tetOff (rather than the K5 promoter used by Tumbar et al) may yield results similar to BrdU based experiments but with the added advantage of hitting all stem cells in a tissue. By driving tetOff from a ubiquitous promoter every cell in the animal will express H2B-GFP until doxycycline is administered. The CMV/chick β-actin promoter (CAAG) has previously been used to drive GFP ubiquitously in the mouse (Pratt et al., 2000). This was utilised to evaluate the feasibility of using a ubiquitous promoter in conjunction with tetOff in collaboration with Professor Bob Hill (MRC Human Genetics Unit, Edinburgh). Figure 6.5 outlines the approach used. TetOff was sub-cloned into the multiple cloning region of pZErO-1 (Invitrogen, shown in Figure 6.5 A). An artificial polylinker containing NotI and KpnI restriction sites was inserted into pCAGiP (a kind gift from Dr Tom Pratt) (Figure 6.5 B). TetOff was then cloned directly from pZErO-1 into this polylinker region as a NotI/KpnI fragment (Figure 6.4 C). The CAG-tetOff construct was isolated with a PvuII/SfiI digest.

Transgenics were generated through standard pronuclear injection techniques at the MRC Human Genetics Unit, Edinburgh however no positive founders were obtained. After an exhaustive search of the literature it became clear that this is most likely because the VP16

domain of the TetOff protein is toxic to preimplantation embryos at the transition from the 2-cell to the 4-cell stage (Yueh et al., 2000). For this reason the use of a ubiquitous promoter that is active early in development is not appropriate. This approach has been re-designed to incorporate a Cre based system to activate tetOff in a tissue specific manner in the ocular surface and is the focus of a grant proposal to the BBSRC.

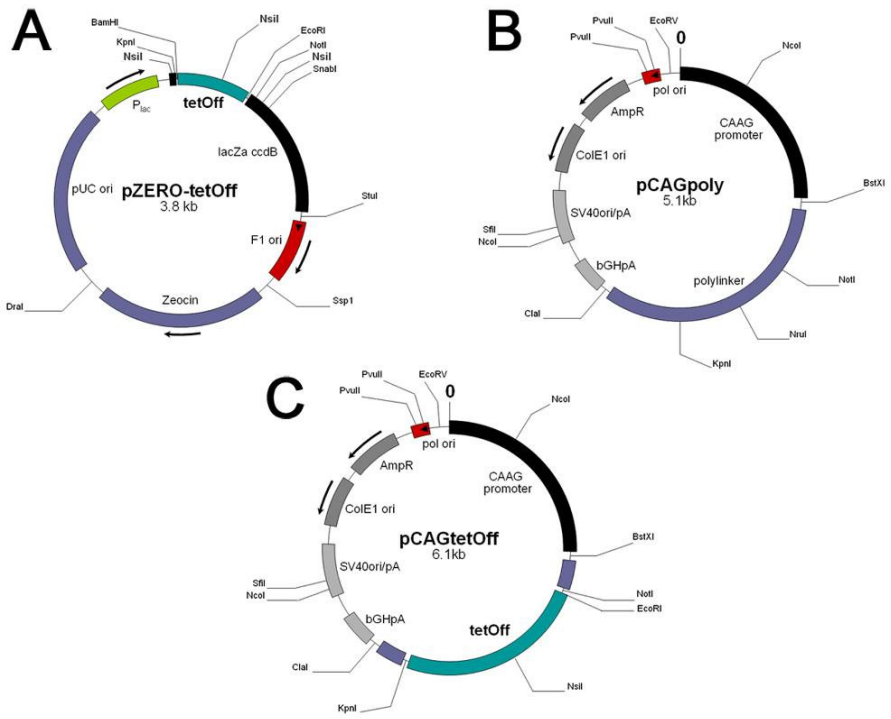

Figure 6.5: Production of CAAG-TetOff mice.

A: TetOff was sub-cloned into the multiple cloning region of the pZErO-1 cloning vector (Invitrogen) as a BamHI/EcoRI fragment. **B:** Subsequently a polylinker containing NotI and KpnI restriction sites was inserted into the pCAGiP plasmid (a kind gift from Dr Tom Pratt) to yield pCAGpoly. This step resulted in 1.8kb deletion replacing the BstXI stuffer region, the IRES and the Puromycin resistance gene of pCAGiP with the polylinker. **C:** TetOff was then cloned into pCAGpoly as a NotI/KpnI fragment. The CAAG-tetOff construct was then excised using a PvuII/SfiI digest. After gel-electrophoresis the construct was electroeluted from the excised gel fragment and purified through an Elutip column (Schleicher and Schuell) by Dr Laura Lettice, (MRC, Human Genetics Unit, Edinburgh). Transgenics were generated through standard pronuclear injection techniques.

6.3 WOUND HEALING RESPONSES AND STRIPING PATTERNS

When the corneal epithelium is injured the surrounding epithelial cells migrate along the corneal stroma to cover the wound. X-gal staining of healed, centrally wounded X-inactivation eyes revealed for the first time that striping patterns are reconstituted during wound healing in ex-vivo culture. A time-lapse imaging system to view wound healing in GFP mosaics using confocal microscopy was developed. This technique demonstrated that clones remain contiguous throughout their migration. Healing of peripheral wounds was observed to form de-novo whorling patterns, revealing that basal cells in the epithelium can migrate both away from and towards the limbal region. The work presented in Chapter 5 was all of a preliminary nature; nevertheless it raised some interesting questions. Figure 6.5 shows a number of proposed further experiments, firstly the experiments described here must be repeated (Figure 6.5 A and B). C: By making wounds off-centre that disrupt the centre of an eye's whorl it may be possible to ascertain whether the results described for a central wound in Chapter 4 are accurate. D: Ring like wounds will be helpful in ascertaining whether cells move more quickly towards the centre of the tissue than towards the periphery. This may be because there is a greater requirement for structural re-organisation in order for cells to migrate centrifugally rather than the usual centripetal migration. If this is the case perhaps wound healing response times would be different for wounds made at 3 weeks compared to those made at 10 weeks (before and after migration has started). This may help identify whether cells are attracted to the centre or pushed from the periphery.

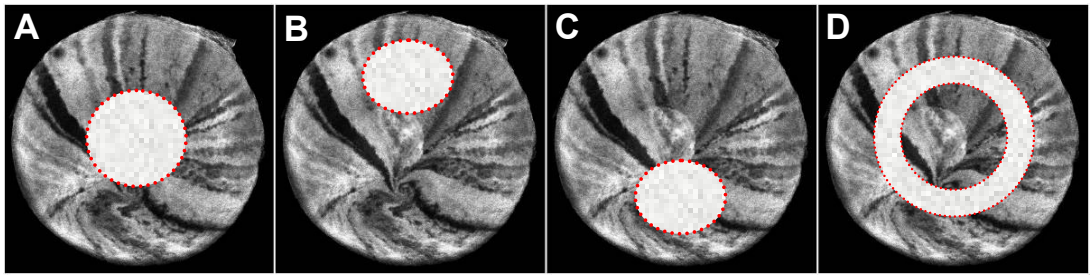

Figure 6.6: Proposed wound healing experiments.

Schematic of proposed experiments. **A:** Further central wounds to study the dynamics of wound healing. **B:** Additional peripheral wounds. **C:** Wounds that involve the centre of the original whorl but are 'off-centre' may help to clarify whether there is a specific point where stripes meet if this part of the cornea is involved **D:** A ring like wound around the central pattern to try and determine where the predominant migration occurs and whether migration rates and response time are equal when cells are moving centripetally or centrifugally.

6.4 CONCLUSIONS

This thesis has raised important issues about corneal epithelial development, stem cell specification, tissue maintenance, and wound healing. Its findings are broadly applicable to any tissue maintained by a population of adult stem cells. In particular it has raised the following points:

6.4.1 Mosaic clonal analysis can be used as an assay for stem cell function

Changes in mosaic patterns can yield information about changes in the distribution of adult stem cells. This demonstrates the usefulness of mosaic analysis to the study of tissue maintenance as well as morphogenesis. The application of clonal analyses is currently undergoing a resurgence fuelled by the availability of sophisticated transgenic reporter systems that can label rare clones such as *LaacZ* (Bonnerot and Nicolas, 1993) or that can activate markers in a spatiotemporal manner such as Cre-ERt (Feil et al., 1997). Recent work in the mouse epidermis using a tamoxifen regulatable enhanced yellow fluorescing protein (EYFP) has suggested that day to day tissue maintenance is achieved through the division of TA cells and that stem cells may not have a major input into the tissue under normal conditions (Clayton et al., 2007). This thesis has produced evidence that LSCs may decline with age. A precedent for the decline of epidermal holoclones was first suggested by Barrandon and Green (1987). It is not known whether changes in stem cell function are due to cell autonomous changes to the stem cells themselves or are a result in change of the capacity of the niche to support these cells in a functional state (for a review see Rando, 2006). A method of quantifying actual stem cell numbers in the limbus is required to understand more closely how these numbers relate to striping patterns and whether the age related decline implied by the coherent clone data holds up. In order to achieve this, a better understanding of tissue cell cycle times, turnover and maintenance will also be required.

6.4.2 Onset of adult stem cell function is postnatal and may be niche dependent

The model for specification and activation of adult stem cells shown here may have implications for the way that other tissues are maintained. Little is currently known about the switch from growth and development of a tissue in the embryo to tissue maintenance in the adult. Identifying the window in which adult stem cells are specified and localised to their niche will be crucial in understanding how they function in normal conditions and how to target a niche therapeutically. Without an understanding of how cells will engraft to a vacant, existing niche or a strategy to expand such a niche to accommodate more cells, stem cell therapies will not be successful in the future. The importance of timing in the derivation of mouse ES cell lines highlights how subtle differences between cell populations at different developmental time points may have far reaching implications for the properties of those cells (Brons et al., 2007; Tesar et al., 2007). Furthermore tissue recombination studies demonstrating the ability of the corneal epithelium to transdifferentiate into epidermis highlight the importance of the niche, to which a donor cell is engrafted, rather than a cell's autonomous properties in controlling its eventual fate (Pearton et al., 2005).

6.4.3 Over-expression of *Pax6* may represent a better model for LSC deficiency

The importance of Pax6 to the adult eye as well as in ocular development is underlined by disruption of striping patterns, corneal defects and modulation of corneal wound healing (this thesis and Collinson et al., 2004a; Ramaesh et al., 2003; Ramaesh et al., 2006). The postnatal development of striping patterns and the specification of LSCs needs to be studied in greater detail. The current study demonstrates that the difference in development between wildtype and *Pax6*$^{+/-}$ corneo-limbal epithelium in the 3-10 week window, prior to LSC activation, may be especially important. *PAX77*$^{+ve}$ eyes exhibit a full thickness epithelium and demonstrate radial striping patterns similar in appearance to wildtype eyes. However the reduction in the

number of corrected stripes at 15-weeks shown here suggests a reduction in the number of functional LSC clones. Therefore the *PAX77*$^{+ve}$ mouse may be a better model of LSC deficiency as it does not exhibit many of the corneal abnormalities associated with the *Pax6*$^{+/-}$ genotype. Research into the development and maintenance of the wildtype and *Pax6*$^{+/-}$ corneal epithelium will yield invaluable information about the tissue in health and disease. Such insights are required to develop a new understanding of the corneal defects implicated in ARK and RCE and the LSC deficiency observed in human patients with aniridia.

6.4.4 Mosaics represent a better model system for wound healing

The advantages of using a mosaic system to study wound healing are clear and are on the whole the same reasons such systems have been so beneficial in the study of growth and development. Specifically that the way clones of different cell types interact as a tissue responds to injury are informative. Existing methods of quantifying corneal epithelial wound healing could not have picked up the differences in the rate of migration at the wound edge shown in this thesis. The wound healing culture and imaging system described here requires further development. With improvements it should be an ideal system for studying cell dynamics and stromal interactions and perhaps for making measurements needed to computer-model these processes. Furthermore the system may prove useful for screening pharmaceuticals for the treatment of RCE.

Bibliography

Abdel-Majid, R. M., Leong, W. L., Schalkwyk, L. C., Smallman, D. S., Wong, S. T., Storm, D. R., Fine, A., Dobson, M. J., Guernsey, D. L. and Neumann, P. E. (1998). Loss of adenylyl cyclase I activity disrupts patterning of mouse somatosensory cortex. *Nat Genet* **19**, 289-91.

Aota, S., Nakajima, N., Sakamoto, R., Watanabe, S., Ibaraki, N. and Okazaki, K. (2003). Pax6 autoregulation mediated by direct interaction of Pax6 protein with the head surface ectoderm-specific enhancer of the mouse Pax6 gene. *Dev Biol* **257**, 1-13.

Barrandon, Y. and Green, H. (1987). Three clonal types of keratinocyte with different capacities for multiplication. *Proc Natl Acad Sci U S A* **84**, 2302-6.

Baulmann, D. C., Ohlmann, A., Flugel-Koch, C., Goswami, S., Cvekl, A. and Tamm, E. R. (2002). Pax6 heterozygous eyes show defects in chamber angle differentiation that are associated with a wide spectrum of other anterior eye segment abnormalities. *Mech Dev* **118**, 3-17.

Beebe, D. C. and Masters, B. R. (1996). Cell lineage and the differentiation of corneal epithelial cells. *Invest Ophthalmol Vis Sci* **37**, 1815-25.

Bertholet, J. Y. (1980). Proliferative activity and cell migration in the adrenal cortex of fetal and neonatal rats: an autoradiographic study. *J Endocrinol* **87**, 1-9.

Beuerman, R. W. and Pedroza, L. (1996). Ultrastructure of the human cornea. *Microsc Res Tech* **33**, 320-35.

Biggers, J. D. and Papaioannou, V. E. (1991). Postnatal compensatory growth of manipulated mouse embryos. *Hum Reprod* **6**, 36-44.

Block, E. R., Matela, A. R., SundarRaj, N., Iszkula, E. R. and Klarlund, J. K. (2004). Wounding induces motility in sheets of corneal epithelial cells through loss of spatial constraints: role of heparin-binding epidermal growth factor-like growth factor signaling. *J Biol Chem* **279**, 24307-12.

Bonnerot, C. and Nicolas, J. F. (1993). Clonal analysis in the intact mouse embryo by intragenic homologous recombination. *C R Acad Sci III* **316**, 1207-17.

Brandon, E. P., Idzerda, R. L. and McKnight, G. S. (1997). PKA isoforms, neural pathways, and behaviour: making the connection. *Curr Opin Neurobiol* **7**, 397-403.

Brandon, E. P., Logue, S. F., Adams, M. R., Qi, M., Sullivan, S. P., Matsumoto, A. M., Dorsa, D. M., Wehner, J. M., McKnight, G. S. and Idzerda, R. L. (1998). Defective motor behavior and neural gene expression in RIIbeta-protein kinase A mutant mice. *J Neurosci* **18**, 3639-49.

Braun, K. M. and Watt, F. M. (2004). Epidermal label-retaining cells: background and recent applications. *J Investig Dermatol Symp Proc* **9**, 196-201.

Brodrick, J. D., Dark, A. J. and Peace, G. W. (1974). Fingerprint dystrophy of the cornea. A histologic study. *Arch Ophthalmol* **92**, 483-9.

Bron, A. J. (1973). Vortex patterns of the corneal epithelium. *Trans Ophthalmol Soc U K* **93**, 455-72.

Brons, I. G., Smithers, L. E., Trotter, M. W., Rugg-Gunn, P., Sun, B., Chuva de Sousa Lopes, S. M., Howlett, S. K., Clarkson, A., Ahrlund-Richter, L., Pedersen, R. A. et al. (2007). Derivation of pluripotent epiblast stem cells from mammalian embryos. *Nature*.

Buck, R. C. (1985). Measurement of centripetal migration of normal corneal epithelial cells in the mouse. *Invest Ophthalmol Vis Sci* **26**, 1296-9.

Buscher, D., Grotewold, L. and Ruther, U. (1998). The XtJ allele generates a Gli3 fusion transcript. *Mamm Genome* **9**, 676-8.

Calvert, R. and Pothier, P. (1990). Migration of fetal intestinal intervillous cells in neonatal mice. *Anat Rec* **227**, 199-206.

Carmona, R., Macias, D., Guadix, J. A., Portillo, V., Perez-Pomares, J. M. and Munoz-Chapuli, R. (2007). A simple technique of image analysis for specific nuclear immunolocalization of proteins. *J Microsc* **225**, 96-9.

Cattanach, B. M., Pollard, C. E. and Perez, J. N. (1969). Controlling elements in the mouse X-chromosome. I. Interaction with the X-linked genes. *Genet Res* **14**, 223-35.

Chakravarti, S., Magnuson, T., Lass, J. H., Jepsen, K. J., LaMantia, C. and Carroll, H. (1998). Lumican regulates collagen fibril assembly: skin fragility and corneal opacity in the absence of lumican. *J Cell Biol* **141**, 1277-86.

Chen, Z., de Paiva, C. S., Luo, L., Kretzer, F. L., Pflugfelder, S. C. and Li, D. Q. (2004). Characterization of putative stem cell phenotype in human limbal epithelia. *Stem Cells* **22**, 355-66.

Cheng, T., Rodrigues, N., Shen, H., Yang, Y., Dombkowski, D., Sykes, M. and Scadden, D. T. (2000). Hematopoietic stem cell quiescence maintained by p21cip1/waf1. *Science* **287**, 1804-8.

Chiang, M. C., Cragoe, E. J., Jr. and Vanable, J. W., Jr. (1991). Intrinsic electric fields promote epithelization of wounds in the newt, Notophthalmus viridescens. *Dev Biol* **146**, 377-85.

Chong, E. M., Campbell, R. J. and Bourne, W. M. (1997). Vortex keratopathy in a patient with multiple myeloma. *Cornea* **16**, 592-4.

Chung, E. H., Bukusoglu, G. and Zieske, J. D. (1992). Localization of corneal epithelial stem cells in the developing rat. *Invest Ophthalmol Vis Sci* **33**, 2199-206.

Clayton, E., Doupe, D. P., Klein, A. M., Winton, D. J., Simons, B. D. and Jones, P. H. (2007). A single type of progenitor cell maintains normal epidermis. *Nature* **446**, 185-9.

Clinch, T. E., Goins, K. M. and Cobo, L. M. (1992). Treatment of contact lens-related ocular surface disorders with autologous conjunctival transplantation. *Ophthalmology* **99**, 634-8.

Cohen, S. (1965). The stimulation of epidermal proliferation by a specific protein (EGF). *Dev Biol* **12**, 394-407.

Cohen, S. and Elliott, G. A. (1963). The stimulation of epidermal keratinization by a protein isolated from the submaxillary gland of the mouse. *J Invest Dermatol* **40**, 1-5.

Collinson, J. M., Chanas, S. A., Hill, R. E. and West, J. D. (2004a). Corneal development, limbal stem cell function, and corneal epithelial cell migration in the Pax6(+/-) mouse. *Invest Ophthalmol Vis Sci* **45**, 1101-8.

Collinson, J. M., Hill, R. E. and West, J. D. (2004b). Analysis of mouse eye development with chimeras and mosaics. *Int J Dev Biol* **48**, 793-804.

Collinson, J. M., Morris, L., Reid, A. I., Ramaesh, T., Keighren, M. A., Flockhart, J. H., Hill, R. E., Tan, S. S., Ramaesh, K., Dhillon, B. et al. (2002). Clonal analysis of patterns of growth, stem cell activity, and cell movement during the development and maintenance of the murine corneal epithelium. *Dev Dyn* **224**, 432-40.

Cotsarelis, G., Cheng, S. Z., Dong, G., Sun, T. T. and Lavker, R. M. (1989). Existence of slow-cycling limbal epithelial basal cells that can be preferentially stimulated to proliferate: implications on epithelial stem cells. *Cell* **57**, 201-9.

Crosson, C. E., Klyce, S. D. and Beuerman, R. W. (1986). Epithelial wound closure in the rabbit cornea. A biphasic process. *Invest Ophthalmol Vis Sci* **27**, 464-73.

Cvekl, A., Kashanchi, F., Sax, C. M., Brady, J. N. and Piatigorsky, J. (1995). Transcriptional regulation of the mouse alpha A-crystallin gene: activation dependent on a cyclic AMP-responsive element (DE1/CRE) and a Pax-6-binding site. *Mol Cell Biol* **15**, 653-60.

Daniels, J. T., Dart, J. K., Tuft, S. J. and Khaw, P. T. (2001). Corneal stem cells in review. *Wound Repair Regen* **9**, 483-94.

Davis, J., Duncan, M. K., Robison, W. G., Jr. and Piatigorsky, J. (2003). Requirement for Pax6 in corneal morphogenesis: a role in adhesion. *J Cell Sci* **116**, 2157-67.

Di Iorio, E., Barbaro, V., Ruzza, A., Ponzin, D., Pellegrini, G. and De Luca, M. (2005). Isoforms of DeltaNp63 and the migration of ocular limbal cells in human corneal regeneration. *Proc Natl Acad Sci U S A* **102**, 9523-8.

Diehn, J. J., Diehn, M., Marmor, M. F. and Brown, P. O. (2005). Differential gene expression in anatomical compartments of the human eye. *Genome Biol* **6**, R74.

Dobie, K., Mehtali, M., McClenaghan, M. and Lathe, R. (1997). Variegated gene expression in mice. *Trends Genet* **13**, 127-30.

Draper, B. K., Komurasaki, T., Davidson, M. K. and Nanney, L. B. (2003a). Epiregulin is more potent than EGF or TGFalpha in promoting in vitro wound closure due to enhanced ERK/MAPK activation. *J Cell Biochem* **89**, 1126-37.

Draper, B. K., Komurasaki, T., Davidson, M. K. and Nanney, L. B. (2003b). Topical epiregulin enhances repair of murine excisional wounds. *Wound Repair Regen* **11**, 188-97.

Dua, H. S. and Azuara-Blanco, A. (2000). Limbal stem cells of the corneal epithelium. *Surv Ophthalmol* **44**, 415-25.

Dua, H. S. and Gomes, J. A. (2000). Clinical course of hurricane keratopathy. *Br J Ophthalmol* **84**, 285-8.

Dua, H. S., Shanmuganathan, V. A., Powell-Richards, A. O., Tighe, P. J. and Joseph, A. (2005). Limbal epithelial crypts: a novel anatomical structure and a putative limbal stem cell niche. *Br J Ophthalmol* **89**, 529-32.

Dua, H. S., Singh, A., Gomes, J. A., Laibson, P. R., Donoso, L. A. and Tyagi, S. (1996). Vortex or whorl formation of cultured human corneal epithelial cells induced by magnetic fields. *Eye* **10 (Pt 4)**, 447-50.

Duncan, M. K., Haynes, J. I., 2nd, Cvekl, A. and Piatigorsky, J. (1998). Dual roles for Pax-6: a transcriptional repressor of lens fiber cell-specific beta-crystallin genes. *Mol Cell Biol* **18**, 5579-86.

Epstein, J., Cai, J., Glaser, T., Jepeal, L. and Maas, R. (1994). Identification of a Pax paired domain recognition sequence and evidence for DNA-dependent conformational changes. *J Biol Chem* **269**, 8355-61.

Ericson, J., Rashbass, P., Schedl, A., Brenner-Morton, S., Kawakami, A., van Heyningen, V., Jessell, T. M. and Briscoe, J. (1997). Pax6 controls progenitor cell identity and neuronal fate in response to graded Shh signaling. *Cell* **90**, 169-80.

Erzurumlu, R. S. and Kind, P. C. (2001). Neural activity: sculptor of 'barrels' in the neocortex. *Trends Neurosci* **24**, 589-95.

Faber, S. C., Dimanlig, P., Makarenkova, H. P., Shirke, S., Ko, K. and Lang, R. A. (2001). Fgf receptor signaling plays a role in lens induction. *Development* **128**, 4425-38.

Fantes, J., Redeker, B., Breen, M., Boyle, S., Brown, J., Fletcher, J., Jones, S., Bickmore, W., Fukushima, Y., Mannens, M. et al. (1995). Aniridia-associated cytogenetic rearrangements suggest that a position effect may cause the mutant phenotype. *Hum Mol Genet* **4**, 415-22.

Feil, R., Wagner, J., Metzger, D. and Chambon, P. (1997). Regulation of Cre recombinase activity by mutated estrogen receptor ligand-binding domains. *Biochem Biophys Res Commun* **237**, 752-7.

Fischer, A. J. and Reh, T. A. (2000). Identification of a proliferating marginal zone of retinal progenitors in postnatal chickens. *Dev Biol* **220**, 197-210.

Forrester, J. V., Dick, A. D., McMenamin, P. G., Lee, W. R. (2001). The Eye: Basic Sciences In Practice: Saunders.

Franz, T. (1994). Extra-toes (Xt) homozygous mutant mice demonstrate a role for the Gli-3 gene in the development of the forebrain. *Acta Anat (Basel)* **150**, 38-44.

Garrana, R. M., Zieske, J. D., Assouline, M. and Gipson, I. K. (1999). Matrix metalloproteinases in epithelia from human recurrent corneal erosion. *Invest Ophthalmol Vis Sci* **40**, 1266-70.

Geiss, V. and Yoshitomi, K. (1999). Pathology of the mouse; reference and atlas, (ed. R. R. Maronpot): Cache River Press.

Gerido, D. A., Sellitto, C., Li, L. and White, T. W. (2003). Genetic background influences cataractogenesis, but not lens growth deficiency, in Cx50-knockout mice. *Invest Ophthalmol Vis Sci* **44**, 2669-74.

Gipson, I. K. (1992). Adhesive mechanisms of the corneal epithelium. *Acta Ophthalmol Suppl*, 13-7.

Glasbey and Horgan. (1994). Image Analysis for the Biological Sciences: John Wiley & Sons.

Glaser, T., Walton, D. S. and Maas, R. L. (1992). Genomic structure, evolutionary conservation and aniridia mutations in the human PAX6 gene. *Nat Genet* **2**, 232-9.

Gluhak-Heinrich, J., Pavlin, D., Yang, W., MacDougall, M. and Harris, S. E. (2007). MEPE expression in osteocytes during orthodontic tooth movement. *Arch Oral Biol* **52**, 684-90.

Gossen, M. and Bujard, H. (1992). Tight control of gene expression in mammalian cells by tetracycline-responsive promoters. *Proc Natl Acad Sci U S A* **89**, 5547-51.

Goudreau, G., Petrou, P., Reneker, L. W., Graw, J., Loster, J. and Gruss, P. (2002). Mutually regulated expression of Pax6 and Six3 and its implications for the Pax6 haploinsufficient lens phenotype. *Proc Natl Acad Sci U S A* **99**, 8719-24.

Grindley, J. C., Bellusci, S., Perkins, D. and Hogan, B. L. (1997). Evidence for the involvement of the Gli gene family in embryonic mouse lung development. *Dev Biol* **188**, 337-48.

Grindley, J. C., Davidson, D. R. and Hill, R. E. (1995). The role of Pax-6 in eye and nasal development. *Development* **121**, 1433-42.

Hadjantonakis, A. K., Gertsenstein, M., Ikawa, M., Okabe, M. and Nagy, A. (1998). Non-invasive sexing of preimplantation stage mammalian embryos. *Nat Genet* **19**, 220-2.

Hanson, I. M., Seawright, A., Hardman, K., Hodgson, S., Zaletayev, D., Fekete, G. and van Heyningen, V. (1993). PAX6 mutations in aniridia. *Hum Mol Genet* **2**, 915-20.

Haustein, J. (1983). On the ultrastructure of the developing and adult mouse corneal stroma. *Anat Embryol (Berl)* **168**, 291-305.

Hay, E. D. (1979). Development of the vertebrate cornea. *Int Rev Cytol* **63**, 263-322.

Hayashi, T., Amino, M. and Ikoma, Y. (1983). Changes of metabolism and substrate-binding spectrum of emorfazone between immature and mature guinea-pigs. *Xenobiotica* **13**, 461-6.

Hazlett, L. D. (1993). Corneal and ocular surface histochemistry. *Prog Histochem Cytochem* **25**, 1-60.

Hibbard, L. S., McCasland, J. S., Brunstrom, J. E. and Pearlman, A. L. (1996). Automated recognition and mapping of immunolabelled neurons in the developing brain. *J Microsc* **183**, 241-56.

Hill, R. E., Favor, J., Hogan, B. L., Ton, C. C., Saunders, G. F., Hanson, I. M., Prosser, J., Jordan, T., Hastie, N. D. and van Heyningen, V. (1991). Mouse small eye results from mutations in a paired-like homeobox-containing gene. *Nature* **354**, 522-5.

Hitchcock, P. F., Macdonald, R. E., VanDeRyt, J. T. and Wilson, S. W. (1996). Antibodies against Pax6 immunostain amacrine and ganglion cells and neuronal progenitors, but not rod precursors, in the normal and regenerating retina of the goldfish. *J Neurobiol* **29**, 399-413.

Hogan, B. L., Hirst, E. M., Horsburgh, G. and Hetherington, C. M. (1988). Small eye (Sey): a mouse model for the genetic analysis of craniofacial abnormalities. *Development* **103 Suppl**, 115-9.

Hogan, M. J., Alvardo, J. A. and Weddell, J. E. (1971). Histology of the human eye. Philadelphia: W. B. Saunders.

Holland, E. J., Djalilian, A. R. and Schwartz, G. S. (2003). Management of aniridic keratopathy with keratolimbal allograft: a limbal stem cell transplantation technique. *Ophthalmology* **110**, 125-30.

Holst, B. D., Wang, Y., Jones, F. S. and Edelman, G. M. (1997). A binding site for Pax proteins regulates expression of the gene for the neural cell adhesion molecule in the embryonic spinal cord. *Proc Natl Acad Sci U S A* **94**, 1465-70.

Iannaccone, P., Morley, S., Skimina, T., Mullins, J. and Landini, G. (2003). Cord-like mosaic patches in the adrenal cortex are fractal: implications for growth and development. *Faseb J* **17**, 41-3.

Iannaccone, P. M., Howard, J. C. and Berkwits, L. (1988). Mosaic pattern and lineage analysis in chimeras. *Cell Differ Dev* **25 Suppl**, 77-90.

Jackson, H. (1960). Effect of eye-pads on healing of simple corneal abrasions. *Br Med J* **2**, 713.

Jensen, A. M. and Wallace, V. A. (1997). Expression of Sonic hedgehog and its putative role as a precursor cell mitogen in the developing mouse retina. *Development* **124**, 363-71.

Johnson, D. R. (1967). Extra-toes: anew mutant gene causing multiple abnormalities in the mouse. *J Embryol Exp Morphol* **17**, 543-81.

Jordan, T., Hanson, I., Zaletayev, D., Hodgson, S., Prosser, J., Seawright, A., Hastie, N. and van Heyningen, V. (1992). The human PAX6 gene is mutated in two patients with aniridia. *Nat Genet* **1**, 328-32.

Joyce, N. C., Meklir, B., Joyce, S. J. and Zieske, J. D. (1996). Cell cycle protein expression and proliferative status in human corneal cells. *Invest Ophthalmol Vis Sci* **37**, 645-55.

Jun, A. S., Liu, S. H., Koo, E. H., Do, D. V., Stark, W. J. and Gottsch, J. D. (2001). Microarray analysis of gene expression in human donor corneas. *Arch Ophthalmol* **119**, 1629-34.

Kamachi, Y., Uchikawa, M., Tanouchi, A., Sekido, R. and Kondoh, H. (2001). Pax6 and SOX2 form a co-DNA-binding partner complex that regulates initiation of lens development. *Genes Dev* **15**, 1272-86.

Kao, W. W., Liu, C. Y., Converse, R. L., Shiraishi, A., Kao, C. W., Ishizaki, M., Doetschman, T. and Duffy, J. (1996). Keratin 12-deficient mice have fragile corneal epithelia. *Invest Ophthalmol Vis Sci* **37**, 2572-84.

Kasper, M. and Viebahn, C. (1992). Cytokeratin expression and early lens development. *Anat Embryol (Berl)* **186**, 285-90.

Kaufman, M. H. and Bard, J. B. L. (1999). The anatomical basis of mouse development. San Diego: Harcourt Brace.

Keegan, C. E. and Hammer, G. D. (2002). Recent insights into organogenesis of the adrenal cortex. *Trends Endocrinol Metab* **13**, 200-8.

Khokha, M. K., Landini, G. and Iannaccone, P. M. (1994). Fractal geometry in rat chimeras demonstrates that a repetitive cell division program may generate liver parenchyma. *Dev Biol* **165**, 545-55.

Kinoshita, S., Friend, J. and Thoft, R. A. (1981). Sex chromatin of donor corneal epithelium in rabbits. *Invest Ophthalmol Vis Sci* **21**, 434-41.

Klareskog, L., Forsum, U., Tjernlund, U. M., Rask, L. and Peterson, P. A. (1979). Expression of Ia antigen-like molecules on cells in the corneal epithelium. *Invest Ophthalmol Vis Sci* **18**, 310-3.

Koroma, B. M., Yang, J. M. and Sundin, O. H. (1997). The Pax-6 homeobox gene is expressed throughout the corneal and conjunctival epithelia. *Invest Ophthalmol Vis Sci* **38**, 108-20.

Kozmik, Z., Czerny, T. and Busslinger, M. (1997). Alternatively spliced insertions in the paired domain restrict the DNA sequence specificity of Pax6 and Pax8. *Embo J* **16**, 6793-803.

Krauss, S., Johansen, T., Korzh, V., Moens, U., Ericson, J. U. and Fjose, A. (1991). Zebrafish pax[zf-a]: a paired box-containing gene expressed in the neural tube. *Embo J* **10**, 3609-19.

Kruse, F. E. (1994). Stem cells and corneal epithelial regeneration. *Eye* **8 (Pt 2)**, 170-83.

Kucerova, R., Ou, J., Lawson, D., Leiper, L. J. and Collinson, J. M. (2006). Cell surface glycoconjugate abnormalities and corneal epithelial wound healing in the pax6+/- mouse model of aniridia-related keratopathy. *Invest Ophthalmol Vis Sci* **47**, 5276-82.

Kuhlman, R. E. and Resnik, R. A. (1958). Quantitative histochemical changes in the development of the rat lens and cornea. *Am J Ophthalmol* **46**, 47-55.

Kuwabara, T., Perkins, D. G. and Cogan, D. G. (1976). Sliding of the epithelium in experimental corneal wounds. *Invest Ophthalmol* **15**, 4-14.

LaMantia, A. S. (1999). Forebrain induction, retinoic acid, and vulnerability to schizophrenia: insights from molecular and genetic analysis in developing mice. *Biol Psychiatry* **46**, 19-30.

Landini, G. and Iannaccone, P. M. (2000). Modeling of mosaic patterns in chimeric liver and adrenal cortex: algorithmic organogenesis? *Faseb J* **14**, 823-7.

Lang, R. A. (2004). Pathways regulating lens induction in the mouse. *Int J Dev Biol* **48**, 783-91.

Laurent, A., Goaillard, J. M., Cases, O., Lebrand, C., Gaspar, P. and Ropert, N. (2002). Activity-dependent presynaptic effect of serotonin 1B receptors on the somatosensory thalamocortical transmission in neonatal mice. *J Neurosci* **22**, 886-900.

LaVail, J. H., Johnson, W. E. and Spencer, L. C. (1993). Immunohistochemical identification of trigeminal ganglion neurons that innervate the mouse cornea: relevance to intercellular spread of herpes simplex virus. *J Comp Neurol* **327**, 133-40.

Le Douarin, N. and Kalcheim, C. (1999). The Neural Crest. Cambridge: Cambridge University Press.

Lee, T. Y. and Gotlieb, A. I. (1999). Early stages of endothelial wound repair: conversion of quiescent to migrating endothelial cells involves tyrosine phosphorylation and actin microfilament reorganization. *Cell Tissue Res* **297**, 435-50.

Lehrer, M. S., Sun, T. T. and Lavker, R. M. (1998). Strategies of epithelial repair: modulation of stem cell and transit amplifying cell proliferation. *J Cell Sci* **111 (Pt 19)**, 2867-75.

Leiper, L. J., Walczysko, P., Kucerova, R., Ou, J., Shanley, L. J., Lawson, D., Forrester, J. V., McCaig, C. D., Zhao, M. and Collinson, J. M. (2006). The roles of calcium signaling and ERK1/2 phosphorylation in a Pax6+/- mouse model of epithelial wound-healing delay. *BMC Biol* **4**, 27.

Li, T. and Lu, L. (2005). Epidermal growth factor-induced proliferation requires down-regulation of Pax6 in corneal epithelial cells. *J Biol Chem* **280**, 12988-95.

Liu, W., Lagutin, O. V., Mende, M., Streit, A. and Oliver, G. (2006). Six3 activation of Pax6 expression is essential for mammalian lens induction and specification. *Embo J* **25**, 5383-95.

Lobe, C. G., Koop, K. E., Kreppner, W., Lomeli, H., Gertsenstein, M. and Nagy, A. (1999). Z/AP, a double reporter for cre-mediated recombination. *Dev Biol* **208**, 281-92.

Lu, H., Hesse, M., Peters, B. and Magin, T. M. (2005). Type II keratins precede type I keratins during early embryonic development. *Eur J Cell Biol* **84**, 709-18.

Mackman, G., Brightbill, F. S. and Optiz, J. M. (1979). Corneal changes in aniridia. *Am J Ophthalmol* **87**, 497-502.

Marigo, V., Johnson, R. L., Vortkamp, A. and Tabin, C. J. (1996). Sonic hedgehog differentially regulates expression of GLI and GLI3 during limb development. *Dev Biol* **180**, 273-83.

Marquardt, T., Ashery-Padan, R., Andrejewski, N., Scardigli, R., Guillemot, F. and Gruss, P. (2001). Pax6 is required for the multipotent state of retinal progenitor cells. *Cell* **105**, 43-55.

Martha, A., Ferrell, R. E., Mintz-Hittner, H., Lyons, L. A. and Saunders, G. F. (1994). Paired box mutations in familial and sporadic aniridia predicts truncated aniridia proteins. *Am J Hum Genet* **54**, 801-11.

Matic, M., Petrov, I. N., Chen, S., Wang, C., Dimitrijevich, S. D. and Wolosin, J. M. (1997). Stem cells of the corneal epithelium lack connexins and metabolite transfer capacity. *Differentiation* **61**, 251-60.

Matsuda, M., Ubels, J. L. and Edelhauser, H. F. (1985). A larger corneal epithelial wound closes at a faster rate. *Invest Ophthalmol Vis Sci* **26**, 897-900.

Maynard, T. M., Jain, M. D., Balmer, C. W. and LaMantia, A. S. (2002). High-resolution mapping of the Gli3 mutation extra-toes reveals a 51.5-kb deletion. *Mamm Genome* **13**, 58-61.

McAvoy, J. W. (1980). Cytoplasmic processes interconnect lens placode and optic vesicle during eye morphogenesis. *Exp Eye Res* **31**, 527-34.

McLeish, W., Rubsamen, P., Atherton, S. S. and Streilein, J. W. (1989). Immunobiology of Langerhans cells on the ocular surface. II. Role of central corneal Langerhans cells in stromal keratitis following experimental HSV-1 infection in mice. *Reg Immunol* **2**, 236-43.

McNicol, A. M. and Duffy, A. E. (1987). A study of cell migration in the adrenal cortex of the rat using bromodeoxyuridine. *Cell Tissue Kinet* **20**, 519-26.

Michael, M. I., Khalil, S. H., Matta, C. A. and Rizk, T. A. (1988). Normal postnatal development of the mouse eye. *Folia Morphol (Praha)* **36**, 125-32.

Mills, A. A., Zheng, B., Wang, X. J., Vogel, H., Roop, D. R. and Bradley, A. (1999). p63 is a p53 homologue required for limb and epidermal morphogenesis. *Nature* **398**, 708-13.

Mitani, F., Mukai, K., Miyamoto, H. and Ishimura, Y. (1998). Localization of replicating cells in rat adrenal cortex during the late gestational and early postnatal stages. *Endocr Res* **24**, 983-6.

Mitani, F., Mukai, K., Miyamoto, H., Suematsu, M. and Ishimura, Y. (2003). The undifferentiated cell zone is a stem cell zone in adult rat adrenal cortex. *Biochim Biophys Acta* **1619**, 317-24.

Mitani, F., Suzuki, H., Hata, J., Ogishima, T., Shimada, H. and Ishimura, Y. (1994). A novel cell layer without corticosteroid-synthesizing enzymes in rat adrenal cortex: histochemical detection and possible physiological role. *Endocrinology* **135**, 431-8.

Moll, R., Franke, W. W., Schiller, D. L., Geiger, B. and Krepler, R. (1982). The catalog of human cytokeratins: patterns of expression in normal epithelia, tumors and cultured cells. *Cell* **31**, 11-24.

Morley, S. D., Chang, S. P., Tan, S. S. and West, J. D. (2004). Validity of the 21-OH/LacZ transgenic mouse as a model for studying adrenocortical cell lineage. *Endocr Res* **30**, 513-9.

Morley, S. D., Viard, I., Chung, B. C., Ikeda, Y., Parker, K. L. and Mullins, J. J. (1996). Variegated expression of a mouse steroid 21-hydroxylase/beta- galactosidase transgene suggests centripetal migration of adrenocortical cells. *Mol Endocrinol* **10**, 585-98.

Murakami, J., Morimoto, K., Nishida, T. and Otori, T. (1992). Movement of corneal epithelium of rats in situ observed by time-lapse cinematography. *Current Aspects in Ophthalmology* **1**, 315-319.

Nagasaki, T. and Zhao, J. (2003). Centripetal movement of corneal epithelial cells in the normal adult mouse. *Invest Ophthalmol Vis Sci* **44**, 558-66.

Nagasaki, T. and Zhao, J. (2005). Uniform distribution of epithelial stem cells in the bulbar conjunctiva. *Invest Ophthalmol Vis Sci* **46**, 126-32.

Narro, M. L., Yang, F., Kraft, R., Wenk, C., Efrat, A. and Restifo, L. L. (2007). NeuronMetrics: software for semi-automated processing of cultured neuron images. *Brain Res* **1138**, 57-75.

Nesbitt, M. N. (1974). Chimeras vs X inactivation mosaics: significance of differences in pigment distribution. *Dev Biol* **38**, 202-7.

Ng, Y. K. and Iannaccone, P. M. (1992). Experimental chimeras: current concepts and controversies in normal development and pathogenesis. *Curr Top Dev Biol* **27**, 235-74.

Nishida, K., Kinoshita, S., Ohashi, Y., Kuwayama, Y. and Yamamoto, S. (1995). Ocular surface abnormalities in aniridia. *Am J Ophthalmol* **120**, 368-75.

Norman, B., Davis, J. and Piatigorsky, J. (2004). Postnatal gene expression in the normal mouse cornea by SAGE. *Invest Ophthalmol Vis Sci* **45**, 429-40.

O'Connell, W. (2002). Oval Profile Plot, (ed.

Oh, S. P., Griffith, C. M., Hay, E. D. and Olsen, B. R. (1993). Tissue-specific expression of type XII collagen during mouse embryonic development. *Dev Dyn* **196**, 37-46.

Osumi-Yamashita, N., Ninomiya, Y., Doi, H. and Eto, K. (1994). The contribution of both forebrain and midbrain crest cells to the mesenchyme in the frontonasal mass of mouse embryos. *Dev Biol* **164**, 409-19.

Pajoohesh-Ganji, A., Ghosh, S. P. and Stepp, M. A. (2004). Regional distribution of alpha9beta1 integrin within the limbus of the mouse ocular surface. *Dev Dyn* **230**, 518-28.

Pajoohesh-Ganji, A. and Stepp, M. A. (2005). In search of markers for the stem cells of the corneal epithelium. *Biol Cell* **97**, 265-76.

Pal-Ghosh, S., Pajoohesh-Ganji, A., Brown, M. and Stepp, M. A. (2004). A mouse model for the study of recurrent corneal epithelial erosions: alpha9beta1 integrin implicated in progression of the disease. *Invest Ophthalmol Vis Sci* **45**, 1775-88.

Parsa, R., Yang, A., McKeon, F. and Green, H. (1999). Association of p63 with proliferative potential in normal and neoplastic human keratinocytes. *J Invest Dermatol* **113**, 1099-105.

Pearton, D. J., Ferraris, C. and Dhouailly, D. (2004). Transdifferentiation of corneal epithelium: evidence for a linkage between the segregation of epidermal stem cells and the induction of hair follicles during embryogenesis. *Int J Dev Biol* **48**, 197-201.

Pearton, D. J., Yang, Y. and Dhouailly, D. (2005). Transdifferentiation of corneal epithelium into epidermis occurs by means of a multistep process triggered by dermal developmental signals. *Proc Natl Acad Sci U S A* **102**, 3714-9.

Pellegrini, G., Dellambra, E., Golisano, O., Martinelli, E., Fantozzi, I., Bondanza, S., Ponzin, D., McKeon, F. and De Luca, M. (2001). p63 identifies keratinocyte stem cells. *Proc Natl Acad Sci U S A* **98**, 3156-61.

Pellegrini, G., Golisano, O., Paterna, P., Lambiase, A., Bonini, S., Rama, P. and De Luca, M. (1999). Location and clonal analysis of stem cells and their differentiated progeny in the human ocular surface. *J Cell Biol* **145**, 769-82.

Percec, I., Plenge, R. M., Nadeau, J. H., Bartolomei, M. S. and Willard, H. F. (2002). Autosomal dominant mutations affecting X inactivation choice in the mouse. *Science* **296**, 1136-9.

Perron, M., Boy, S., Amato, M. A., Viczian, A., Koebernick, K., Pieler, T. and Harris, W. A. (2003). A novel function for Hedgehog signalling in retinal pigment epithelium differentiation. *Development* **130**, 1565-77.

Perron, M., Kanekar, S., Vetter, M. L. and Harris, W. A. (1998). The genetic sequence of retinal development in the ciliary margin of the Xenopus eye. *Dev Biol* **199**, 185-200.

Perrone, R. D., Bengele, H. H. and Alexander, E. A. (1986). Sodium retention after adrenal enucleation. *Am J Physiol* **250**, E1-12.

Peters, A. (1885). Regeneration des Epithels des Cornea, Inaugural Dissertation, Bonn., (ed.

Piatigorsky, J. (1998). Multifunctional lens crystallins and corneal enzymes. More than meets the eye. *Ann N Y Acad Sci* **842**, 7-15.

Plaza, S., Dozier, C., Langlois, M. C. and Saule, S. (1995). Identification and characterization of a neuroretina-specific enhancer element in the quail Pax-6 (Pax-QNR) gene. *Mol Cell Biol* **15**, 892-903.

Ponder, B. A., Schmidt, G. H., Wilkinson, M. M., Wood, M. J., Monk, M. and Reid, A. (1985). Derivation of mouse intestinal crypts from single progenitor cells. *Nature* **313**, 689-91.

Potten, C. S. and Loeffler, M. (1990). Stem cells: attributes, cycles, spirals, pitfalls and uncertainties. Lessons for and from the crypt. *Development* **110**, 1001-20.

Pratt, T., Sharp, L., Nichols, J., Price, D. J. and Mason, J. O. (2000). Embryonic stem cells and transgenic mice ubiquitously expressing a tau-tagged green fluorescent protein. *Dev Biol* **228**, 19-28.

Puangsricharern, V. and Tseng, S. C. (1995). Cytologic evidence of corneal diseases with limbal stem cell deficiency. *Ophthalmology* **102**, 1476-85.

Puschel, A. W., Gruss, P. and Westerfield, M. (1992). Sequence and expression pattern of pax-6 are highly conserved between zebrafish and mice. *Development* **114**, 643-51.

Quiring, R., Walldorf, U., Kloter, U. and Gehring, W. J. (1994). Homology of the eyeless gene of Drosophila to the Small eye gene in mice and Aniridia in humans. *Science* **265**, 785-9.

Ramaesh, T., Collinson, J. M., Ramaesh, K., Kaufman, M. H., West, J. D. and Dhillon, B. (2003). Corneal abnormalities in Pax6+/- small eye mice mimic human aniridia-related keratopathy. *Invest Ophthalmol Vis Sci* **44**, 1871-8.

Ramaesh, T., Ramaesh, K., Leask, R., Springbett, A., Riley, S. C., Dhillon, B. and West, J. D. (2006). Increased apoptosis and abnormal wound-healing responses in the heterozygous Pax6+/- mouse cornea. *Invest Ophthalmol Vis Sci* **47**, 1911-7.

Ramamurthi, S., Rahman, M. Q., Dutton, G. N. and Ramaesh, K. (2006). Pathogenesis, clinical features and management of recurrent corneal erosions. *Eye* **20**, 635-44.

Rando, T. A. (2006). Stem cells, ageing and the quest for immortality. *Nature* **441**, 1080-6.

Rasband, W. S. (1997-2006). ImageJ, (ed.: U. S. National Institutes of Health, Bethesda, Maryland, USA.

Rehbinder, C. (1978). Fine structure of the mouse cornea. *Z Versuchstierkd* **20**, 28-34.

Reid, B., Song, B., McCaig, C. D. and Zhao, M. (2005). Wound healing in rat cornea: the role of electric currents. *Faseb J* **19**, 379-86.

Ren, H. and Wilson, G. (1996). The cell shedding rate of the corneal epithelium--a comparison of collection methods. *Curr Eye Res* **15**, 1054-9.

Resnitzky, D., Gossen, M., Bujard, H. and Reed, S. I. (1994). Acceleration of the G1/S phase transition by expression of cyclins D1 and E with an inducible system. *Mol Cell Biol* **14**, 1669-79.

Roach, S. A. (1968). The theory of random clumping: London: Methuen.

Rodrigues, M. M., Fine, B. S., Laibson, P. R. and Zimmerman, L. E. (1974). Disorders of the corneal epithelium. A clinicopathologic study of dot, geographic, and fingerprint patterns. *Arch Ophthalmol* **92**, 475-82.

Ruiz i Altaba, A. (1999). The works of GLI and the power of hedgehog. *Nat Cell Biol* **1**, E147-8.

Saika, S., Muragaki, Y., Okada, Y., Miyamoto, T., Ohnishi, Y., Ooshima, A. and Kao, W. W. (2004). Sonic hedgehog expression and role in healing corneal epithelium. *Invest Ophthalmol Vis Sci* **45**, 2577-85.

Schedl, A., Ross, A., Lee, M., Engelkamp, D., Rashbass, P., van Heyningen, V. and Hastie, N. D. (1996). Influence of PAX6 gene dosage on development: overexpression causes severe eye abnormalities. *Cell* **86**, 71-82.

Schermer, A., Galvin, S. and Sun, T. T. (1986). Differentiation-related expression of a major 64K corneal keratin in vivo and in culture suggests limbal location of corneal epithelial stem cells. *J Cell Biol* **103**, 49-62.

Schmidt, G. H., Winton, D. J. and Ponder, B. A. (1988). Development of the pattern of cell renewal in the crypt-villus unit of chimaeric mouse small intestine. *Development* **103**, 785-90.

Serbedzija, G. N., Bronner-Fraser, M. and Fraser, S. E. (1992). Vital dye analysis of cranial neural crest cell migration in the mouse embryo. *Development* **116**, 297-307.

Sheng, G., Thouvenot, E., Schmucker, D., Wilson, D. S. and Desplan, C. (1997). Direct regulation of rhodopsin 1 by Pax-6/eyeless in Drosophila: evidence for a conserved function in photoreceptors. *Genes Dev* **11**, 1122-31.

Shi, Y., Tabesh, M. and Sugrue, S. P. (2000). Role of cell adhesion-associated protein, pinin (DRS/memA), in corneal epithelial migration. *Invest Ophthalmol Vis Sci* **41**, 1337-45.

Simpson, T. I. and Price, D. J. (2002). Pax6; a pleiotropic player in development. *Bioessays* **24**, 1041-51.

Sivak, J. M. and Fini, M. E. (2002). MMPs in the eye: emerging roles for matrix metalloproteinases in ocular physiology. *Prog Retin Eye Res* **21**, 1-14.

Sivak, J. M., Mohan, R., Rinehart, W. B., Xu, P. X., Maas, R. L. and Fini, M. E. (2000). Pax-6 expression and activity are induced in the reepithelializing cornea and control activity of the transcriptional promoter for matrix metalloproteinase gelatinase B. *Dev Biol* **222**, 41-54.

Skelton, F. R. (1959). Adrenal regeneration and adrenal-regeneration hypertension. *Physiol Rev* **39**, 162-82.

Smith, R. S., John S. W. M., Nishina, P. M., Sundberg, J. P. (2001). Systematic Evaluation of the Mouse Eye: Anatomy, Pathology, and Biomethods: Taylor and Francis, CRC Press.

Soucy, E., Wang, Y., Nirenberg, S., Nathans, J. and Meister, M. (1998). A novel signaling pathway from rod photoreceptors to ganglion cells in mammalian retina. *Neuron* **21**, 481-93.

Sta Iglesia, D. D. and Vanable, J. W., Jr. (1998). Endogenous lateral electric fields around bovine corneal lesions are necessary for and can enhance normal rates of wound healing. *Wound Repair Regen* **6**, 531-42.

Stepensky, D. (2007). FRETcalc plugin for calculation of FRET in non-continuous intracellular compartments. *Biochem Biophys Res Commun* **359**, 752-8.

Stepp, M. A., Zhu, L. and Cranfill, R. (1996). Changes in beta 4 integrin expression and localization in vivo in response to corneal epithelial injury. *Invest Ophthalmol Vis Sci* **37**, 1593-601.

Stepp, M. A., Zhu, L., Sheppard, D. and Cranfill, R. L. (1995). Localized distribution of alpha 9 integrin in the cornea and changes in expression during corneal epithelial cell differentiation. *J Histochem Cytochem* **43**, 353-62.

Steuhl, K. P. and Thiel, H. J. (1987). Histochemical and morphological study of the regenerating corneal epithelium after limbus-to-limbus denudation. *Graefes Arch Clin Exp Ophthalmol* **225**, 53-8.

Stoykova, A., Gotz, M., Gruss, P. and Price, J. (1997). Pax6-dependent regulation of adhesive patterning, R-cadherin expression and boundary formation in developing forebrain. *Development* **124**, 3765-77.

Stoykova, A., Treichel, D., Hallonet, M. and Gruss, P. (2000). Pax6 modulates the dorsoventral patterning of the mammalian telencephalon. *J Neurosci* **20**, 8042-50.

Streilein, J. W., Toews, G. B. and Bergstresser, P. R. (1980). Langerhans cells: functional aspects revealed by in vivo grafting studies. *J Invest Dermatol* **75**, 17-21.

Suzuki, K., Saito, J., Yanai, R., Yamada, N., Chikama, T., Seki, K. and Nishida, T. (2003). Cell-matrix and cell-cell interactions during corneal epithelial wound healing. *Prog Retin Eye Res* **22**, 113-33.

Szel, A., Csorba, G., Caffe, A. R., Szel, G., Rohlich, P. and van Veen, T. (1994). Different patterns of retinal cone topography in two genera of rodents, Mus and Apodemus. *Cell Tissue Res* **276**, 143-50.

Szel, A., Rohlich, P., Caffe, A. R., Juliusson, B., Aguirre, G. and Van Veen, T. (1992). Unique topographic separation of two spectral classes of cones in the mouse retina. *J Comp Neurol* **325**, 327-42.

Szel, A., Rohlich, P., Caffe, A. R. and van Veen, T. (1996). Distribution of cone photoreceptors in the mammalian retina. *Microsc Res Tech* **35**, 445-62.

Tachi, C. (1988). Quantitative evaluation of coat-color patterns in artificially produced chimeras of the mouse by means of a microcomputer-based video-image analysis system. *Dev Genet* **9**, 121-54.

Tan, S. S., Williams, E. A. and Tam, P. P. (1993). X-chromosome inactivation occurs at different times in different tissues of the post-implantation mouse embryo. *Nat Genet* **3**, 170-4.

Tanifuji-Terai, N., Terai, K., Hayashi, Y., Chikama, T. and Kao, W. W. (2006). Expression of keratin 12 and maturation of corneal epithelium during development and postnatal growth. *Invest Ophthalmol Vis Sci* **47**, 545-51.

Tesar, P. J., Chenoweth, J. G., Brook, F. A., Davies, T. J., Evans, E. P., Mack, D. L., Gardner, R. L. and McKay, R. D. (2007). New cell lines from mouse epiblast share defining features with human embryonic stem cells. *Nature*.

Theil, T., Kaesler, S., Grotewold, L., Bose, J. and Ruther, U. (1999). Gli genes and limb development. *Cell Tissue Res* **296**, 75-83.

Thoft, R. A. and Friend, J. (1983). The X, Y, Z hypothesis of corneal epithelial maintenance. *Invest Ophthalmol Vis Sci* **24**, 1442-3.

Tole, S., Ragsdale, C. W. and Grove, E. A. (2000). Dorsoventral patterning of the telencephalon is disrupted in the mouse mutant extra-toes(J). *Dev Biol* **217**, 254-65.

Ton, C. C., Hirvonen, H., Miwa, H., Weil, M. M., Monaghan, P., Jordan, T., van Heyningen, V., Hastie, N. D., Meijers-Heijboer, H., Drechsler, M. et al. (1991). Positional cloning and characterization of a paired box- and homeobox-containing gene from the aniridia region. *Cell* **67**, 1059-74.

Townsend, W. M. (1991). The limbal palisades of Vogt. *Trans Am Ophthalmol Soc* **89**, 721-56.

Trainor, P. A. and Tam, P. P. (1995). Cranial paraxial mesoderm and neural crest cells of the mouse embryo: co-distribution in the craniofacial mesenchyme but distinct segregation in branchial arches. *Development* **121**, 2569-82.

Tripathi, R. C. and Bron, A. J. (1972). Ultrastructural study of non-traumatic recurrent corneal erosion. *Br J Ophthalmol* **56**, 73-85.

Tumbar, T., Guasch, G., Greco, V., Blanpain, C., Lowry, W. E., Rendl, M. and Fuchs, E. (2004). Defining the epithelial stem cell niche in skin. *Science* **303**, 359-63.

Tyas, D. A., Pearson, H., Rashbass, P. and Price, D. J. (2003). Pax6 regulates cell adhesion during cortical development. *Cereb Cortex* **13**, 612-9.

Tzoulaki, I., White, I. M. and Hanson, I. M. (2005). PAX6 mutations: genotype-phenotype correlations. *BMC Genet* **6**, 27.

Ubels, J. L., Edelhauser, H. F. and Austin, K. H. (1982). A comparison of healing of corneal epithelial wounds stained with fluorescein or Richardson's stain. *Invest Ophthalmol Vis Sci* **23**, 127-31.

Ulbrich, H., Prech, P., Luxenburger, A. and Dannhardt, G. (2005). Characterization of a computerized assay for rapid and easy determination of leukocyte adhesion to endothelial cells. *Biol Pharm Bull* **28**, 718-24.

Velculescu, V. E., Zhang, L., Vogelstein, B. and Kinzler, K. W. (1995). Serial analysis of gene expression. *Science* **270**, 484-7.

Vincent, M. C., Pujo, A. L., Olivier, D. and Calvas, P. (2003). Screening for PAX6 gene mutations is consistent with haploinsufficiency as the main mechanism leading to various ocular defects. *Eur J Hum Genet* **11**, 163-9.

Walker, D. C., Hill, G., Wood, S. M., Smallwood, R. H. and Southgate, J. (2004). Agent-based computational modeling of wounded epithelial cell monolayers. *IEEE Trans Nanobioscience* **3**, 153-63.

Walther, C. and Gruss, P. (1991). Pax-6, a murine paired box gene, is expressed in the developing CNS. *Development* **113**, 1435-49.

Wang, B., Fallon, J. F. and Beachy, P. A. (2000). Hedgehog-regulated processing of Gli3 produces an anterior/posterior repressor gradient in the developing vertebrate limb. *Cell* **100**, 423-34.

Ware, C. I. (2003). A simple method to 'point count' silt using scanning electron microscopy aided by image analysis. *J Microsc* **212**, 205-8.

Watson, R. F., Abdel-Majid, R. M., Barnett, M. W., Willis, B. S., Katsnelson, A., Gillingwater, T. H., McKnight, G. S., Kind, P. C. and Neumann, P. E. (2006). Involvement of protein kinase A in patterning of the mouse somatosensory cortex. *J Neurosci* **26**, 5393-401.

Wawersik, S., Purcell, P., Rauchman, M., Dudley, A. T., Robertson, E. J. and Maas, R. (1999). BMP7 acts in murine lens placode development. *Dev Biol* **207**, 176-88.

Welker, E., Armstrong-James, M., Bronchti, G., Ourednik, W., Gheorghita-Baechler, F., Dubois, R., Guernsey, D. L., Van der Loos, H. and Neumann, P. E. (1996). Altered sensory processing in the somatosensory cortex of the mouse mutant barrelless. *Science* **271**, 1864-7.

West, J. D. (1976). Clonal development of the retinal epithelium in mouse chimeras and X-inactivation mosaics. *Journal of embryology and experimental morphology* **35**, 445-461.

West, J. D. (1978). Clonal growth versus cell mingling. *Basic Life Sci* **12**, 435-44.

West, J. D. (1999). Insights into development and genetics from mouse chimeras. *Curr Top Dev Biol* **44**, 21-66.

West, J. D., Hodson, B. A. and Keighren, M. A. (1997). Quantitative and spatial information on the composition of chimaeric fetal mouse eyes from single histological sections. *Dev Growth Differ* **39**, 305-17.

Winton, D. J. and Ponder, B. A. (1990). Stem-cell organization in mouse small intestine. *Proc Biol Sci* **241**, 13-8.

Wolosin, J. M., Budak, M. T. and Akinci, M. A. (2004). Ocular surface epithelial and stem cell development. *Int J Dev Biol* **48**, 981-91.

Wong, M. H., Saam, J. R., Stappenbeck, T. S., Rexer, C. H. and Gordon, J. I. (2000). Genetic mosaic analysis based on Cre recombinase and navigated laser capture microdissection. *Proc Natl Acad Sci U S A* **97**, 12601-6.

Wong, T. T., Sethi, C., Daniels, J. T., Limb, G. A., Murphy, G. and Khaw, P. T. (2002). Matrix metalloproteinases in disease and repair processes in the anterior segment. *Surv Ophthalmol* **47**, 239-56.

Woolsey, T. A. and Van der Loos, H. (1970). The structural organization of layer IV in the somatosensory region (SI) of mouse cerebral cortex. The description of a cortical field composed of discrete cytoarchitectonic units. *Brain Res* **17**, 205-42.

Yang, A. and McKeon, F. (2000). P63 and P73: P53 mimics, menaces and more. *Nat Rev Mol Cell Biol* **1**, 199-207.

Yueh, Y. G., Yaworsky, P. J. and Kappen, C. (2000). Herpes simplex virus transcriptional activator VP16 is detrimental to preimplantation development in mice. *Mol Reprod Dev* **55**, 37-46.

Zahm, J. M., Kaplan, H., Herard, A. L., Doriot, F., Pierrot, D., Somelette, P. and Puchelle, E. (1997). Cell migration and proliferation during the in vitro wound repair of the respiratory epithelium. *Cell Motil Cytoskeleton* **37**, 33-43.

Zajicek, G., Ariel, I. and Arber, N. (1986). The streaming adrenal cortex: direct evidence of centripetal migration of adrenocytes by estimation of cell turnover rate. *J Endocrinol* **111**, 477-82.

Zaki, P. A., Collinson, J. M., Toraiwa, J., Simpson, T. I., Price, D. J. and Quinn, J. C. (2006). Penetrance of eye defects in mice heterozygous for mutation of Gli3 is enhanced by heterozygous mutation of Pax6. *BMC Dev Biol* **6**, 46.

Zhang, X., Friedman, A., Heaney, S., Purcell, P. and Maas, R. L. (2002). Meis homeoproteins directly regulate Pax6 during vertebrate lens morphogenesis. *Genes Dev* **16**, 2097-107.

Zhao, B., Cooper, L. J., Brahma, A., MacNeil, S., Rimmer, S. and Fullwood, N. J. (2006a). Development of a three-dimensional organ culture model for corneal wound healing and corneal transplantation. *Invest Ophthalmol Vis Sci* **47**, 2840-6.

Zhao, M., Song, B., Pu, J., Forrester, J. V. and McCaig, C. D. (2003). Direct visualization of a stratified epithelium reveals that wounds heal by unified sliding of cell sheets. *Faseb J* **17**, 397-406.

Zhao, M., Song, B., Pu, J., Wada, T., Reid, B., Tai, G., Wang, F., Guo, A., Walczysko, P., Gu, Y. et al. (2006b). Electrical signals control wound healing through phosphatidylinositol-3-OH kinase-gamma and PTEN. *Nature* **442**, 457-60.

Zhou, M., Li, X. M. and Lavker, R. M. (2006). Transcriptional profiling of enriched populations of stem cells versus transient amplifying cells. A comparison of limbal and corneal epithelial basal cells. *J Biol Chem* **281**, 19600-9.

Zieske, J. D., Bukusoglu, G., Yankauckas, M. A., Wasson, M. E. and Keutmann, H. T. (1992). Alpha-enolase is restricted to basal cells of stratified squamous epithelium. *Dev Biol* **151**, 18-26.

Zieske, J. D., Francesconi, C. M. and Guo, X. (2004). Cell cycle regulators at the ocular surface. *Exp Eye Res* **78**, 447-56.

Zieske, J. D., Hutcheon, A. E., Guo, X., Chung, E. H. and Joyce, N. C. (2001). TGF-beta receptor types I and II are differentially expressed during corneal epithelial wound repair. *Invest Ophthalmol Vis Sci* **42**, 1465-71.

Zieske, J. D., Takahashi, H., Hutcheon, A. E. and Dalbone, A. C. (2000). Activation of epidermal growth factor receptor during corneal epithelial migration. *Invest Ophthalmol Vis Sci* **41**, 1346-55.

Zieske, J. D. and Wasson, M. (1993). Regional variation in distribution of EGF receptor in developing and adult corneal epithelium. *J Cell Sci* **106 (Pt 1)**, 145-52.